LAWRENCE
LIVERMORE
NATIONAL
LABORATORY

LLNL-TR-810225

Interpretation of Mineralogical Diagenesis for Assessment of Radionuclide Transport at Pahute Mesa, Nevada National Security Site

S. F. Carle

May 14, 2020

Disclaimer

This work performed under the auspices of the U.S. Department of Energy by Lawrence Livermore National Laboratory under Contract DE-AC52-07NA27344.

LLNL-TR-810225

Interpretation of Mineralogical Diagenesis for Assessment of Radionuclide Transport at Pahute Mesa, Nevada National Security Site

Steven F. Carle
Lawrence Livermore National Laboratory

July 2020

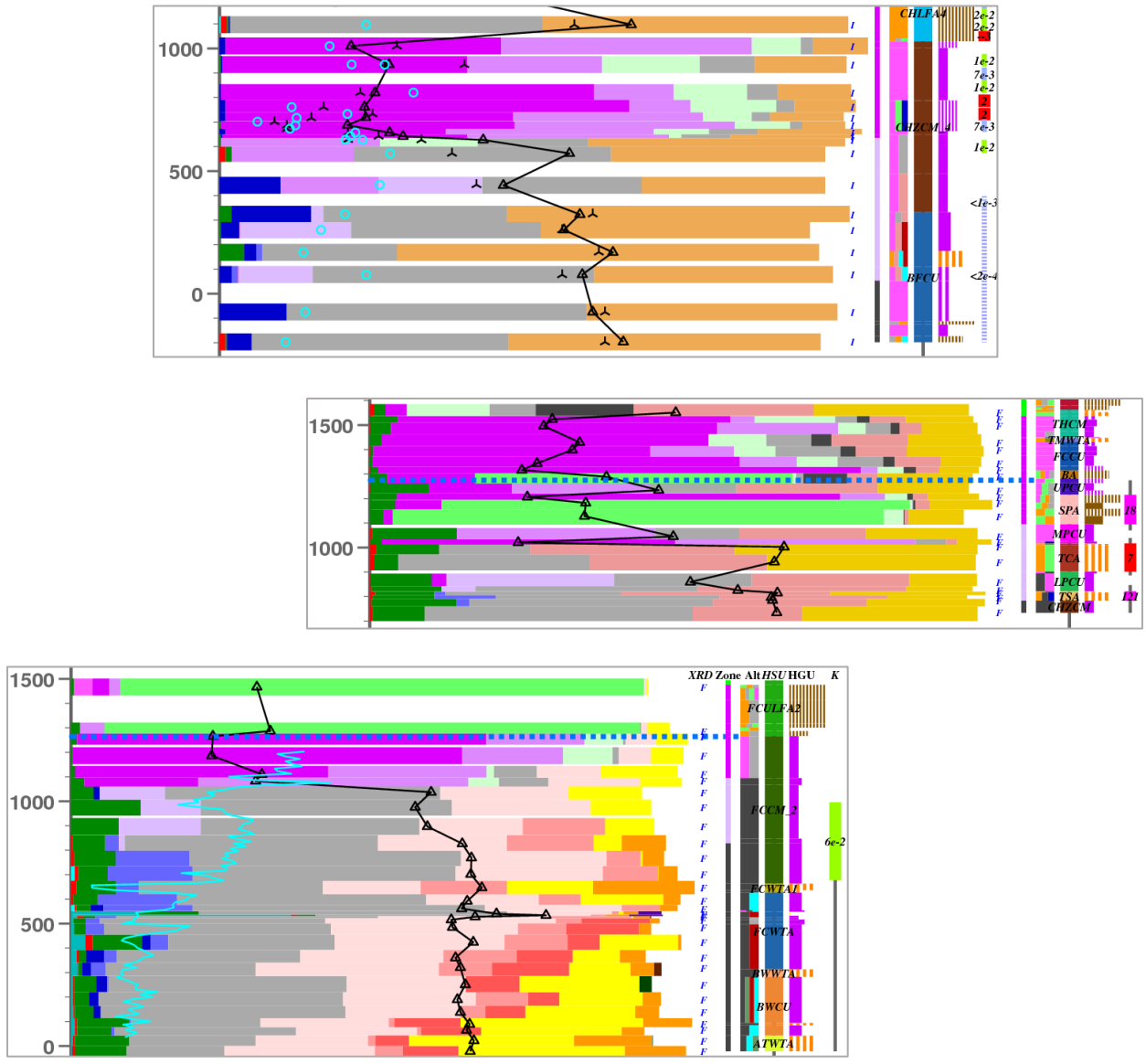

This work performed under the auspices of the U.S. Department of Energy by Lawrence Livermore National Laboratory under Contract DE-AC52-07NA27344.

Table of Contents

List of Figures

List of Tables

1 Background

1.1 Introduction

Pahute Mesa (PM) in southern Nevada was one of the four principal underground nuclear testing areas at the Nevada National Security Site (NNSS), known as the "Nevada Test Site" until 2010 (Figure 1). Eighty-two underground nuclear tests were conducted at PM in northwestern corner of NNSS (USDOE, 2015). The PM area of underground nuclear testing is located near the center of the Pahute Mesa and Oasis Valley (PM-OV) groundwater basin, which discharges to the southwest near Oasis Valley (OV) north of Beatty, Nevada (Fenelon et al. 2016; Jackson et al., 2020). Most of the PM tests were located at depths near or below the regional water table and, therefore, present potential sources of groundwater contamination from release of test-related radionuclides.

Geologically, the PM testing area is situated within and adjacent to the Silent Canyon caldera complex (SCCC). These Tertiary volcanic rocks are mostly rhyolites and quartz latites with silica content between 65 to 78% (Moncure et al., 1981; Broxton et al, 1989). Such silicic (or felsic) rocks have been subjected to physical, chemical, biological, and hydrothermal (heating, hydration, dehydration) processes to various extents over time and space. The resulting diagenetic effects impact nearly all rock properties relevant to groundwater flow and radionuclide transport (e.g. porosity, permeability, grain density, permeability, sorption).

The 82 higher yield tests conducted in vertical shafts at PM constitute about 60% of the radionuclide source term in curies for the 928 underground nuclear tests at NNSS (USDOE, 2015; Finnegan et al., 2016). Assessment of radionuclide transport in groundwater from PM test sources includes monitoring and computer modeling activities occurring under the auspices of a joint Federal Facility Agreement and Consent Order (FFACO) (1996, as amended) developed between the State of Nevada, U.S. Department of Energy (USDOE), and U.S. Department of Defense. Within this agreement, the 82 underground tests at PM are considered as individual contaminant sources grouped by location into two "Corrective Action Units" (Figure 1). Radionuclide transport is to be assessed over a 1000-year timeframe.

Transport models are expected to have a capability to account for sorption processes in the volcanic rocks at PM-OV, in addition to groundwater flow properties of porosity and permeability (Stoller Navarro Joint Venture, 2009). Within a caldera complex, the hydrogeological setting and physiochemical properties affecting sorption can be expected to vary significantly between the multiple source locations of contamination and along potential PM-OV transport pathways. The parameters needed for modeling sorption should be representative of the hydrogeological and geochemical conditions at PM-OV including the mineralogy, which is spatially variable and has undergone multiple stages of physical and chemical change or "diagenesis" (Moncure et al., 1981; Sawyer and Sargent, 1989; Broxton et al, 1989).

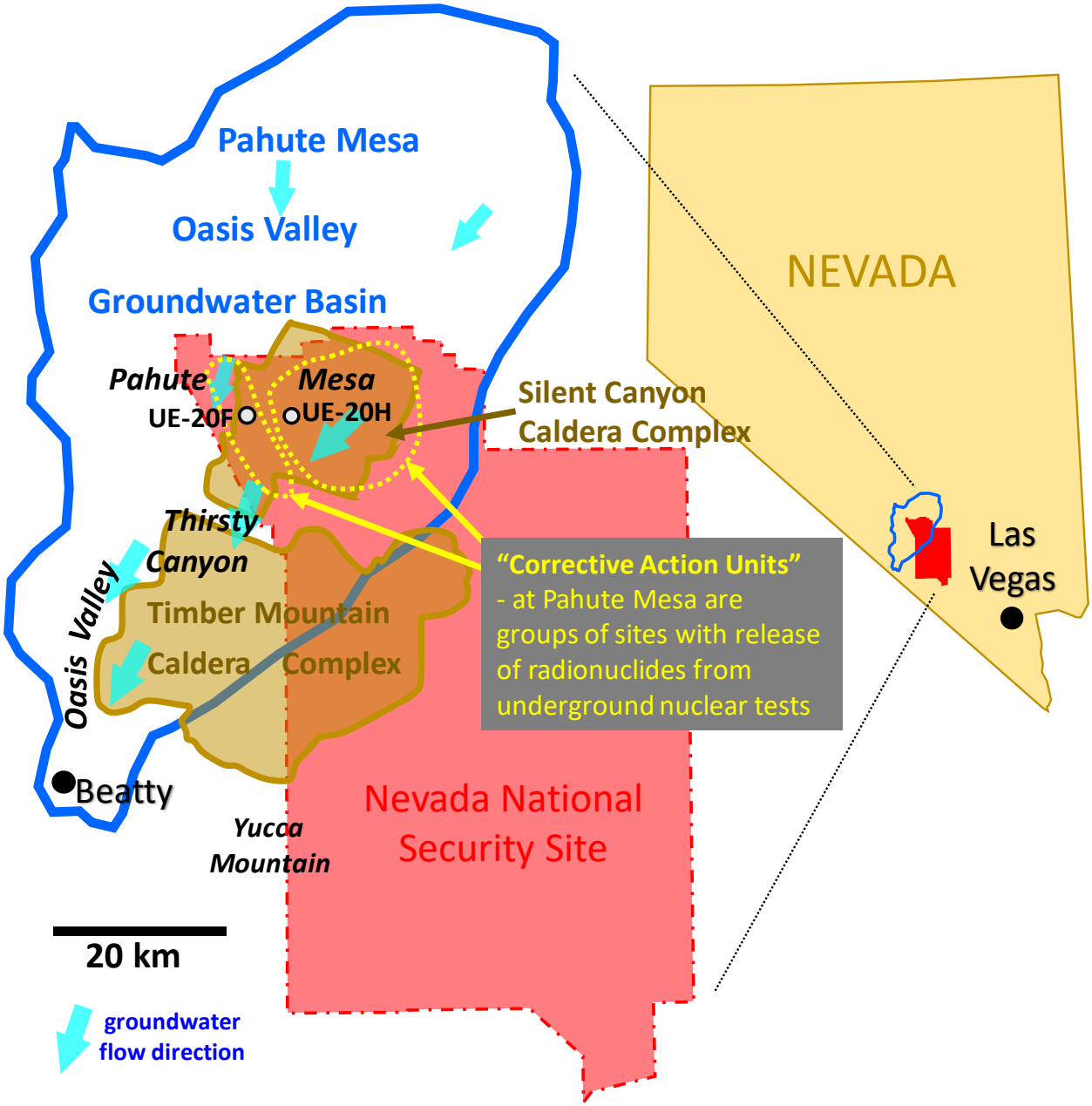

Figure 1. Location map showing Nevada National Security Site, Pahute Mesa-Oasis Valley groundwater basin, Pahute Mesa, and UE-20F and UE-20H boreholes discussed in Moncure et al. (1981).

Diagenesis in volcanic rocks at the (NNSS) and adjacent areas is often characterized by descriptions of secondary mineral alteration (or lack thereof) by terms such as glass, zeolitic, or devitrified (Bechtel Nevada, 2002; Prothro et al., 2009; USDOE, 2020). Descriptors of alteration and lithology are used to distinguish hydrogeologic units (e.g. vitric tuff aquifer, tuff confining unit, welded-tuff aquifer) or hydrostratigraphic units (e.g. vitric composite unit, zeolitic composite unit). Ash-fall or bedded tuff is often described as

either vitric (glassy) or zeolitic to distinguish unaltered tuff from tuff altered by hydration. The deeper volcanic rocks within and adjacent to the caldera complex at PM-OV have been subjected more extreme hydrothermal effects compared to elsewhere at NNSS (e.g. Rainier Mesa or Yucca Flat). Mineralogic zonation within tuff of Yucca Flat is largely attributable to temperatures less than 100°C (Prothro, 2005). The more extreme hydrothermal diagenesis evident at PM was first described in detail in a journal article titled "Zeolite Diagenesis Below Pahute Mesa, Nevada Test Site" (Moncure et al., 1981). Similar hydrothermal diagenesis at Yucca Mountain (YM), about 50 km south of PM and a few km south of the southern extent of the Timber Mountain caldera complex (TMCC), requires post-depositional temperatures of over 100 °C to at least 275 °C (Bish and Aronson, 1993).

Moncure et al. (1981) interpreted three diagenetic or "mineralogical" zones at PM based on rock chemistry and mineralogic mass fraction data derived from x-ray diffraction (XRD) at boreholes UE-20F and UE-20H (Figure 2). A third borehole shown in Figure 2, PM-1, had available only qualitative descriptions of the mineralogy with no quantitative breakdown of mineral mass fractions. Broxton et al. (1987) identified similar diagenetic zones in the silicic volcanic rocks at YM and added a fourth deeper zone with a groundmass dominated by quartz and feldspar (quartzofeldspathic), which is evident at PM-OV as well.

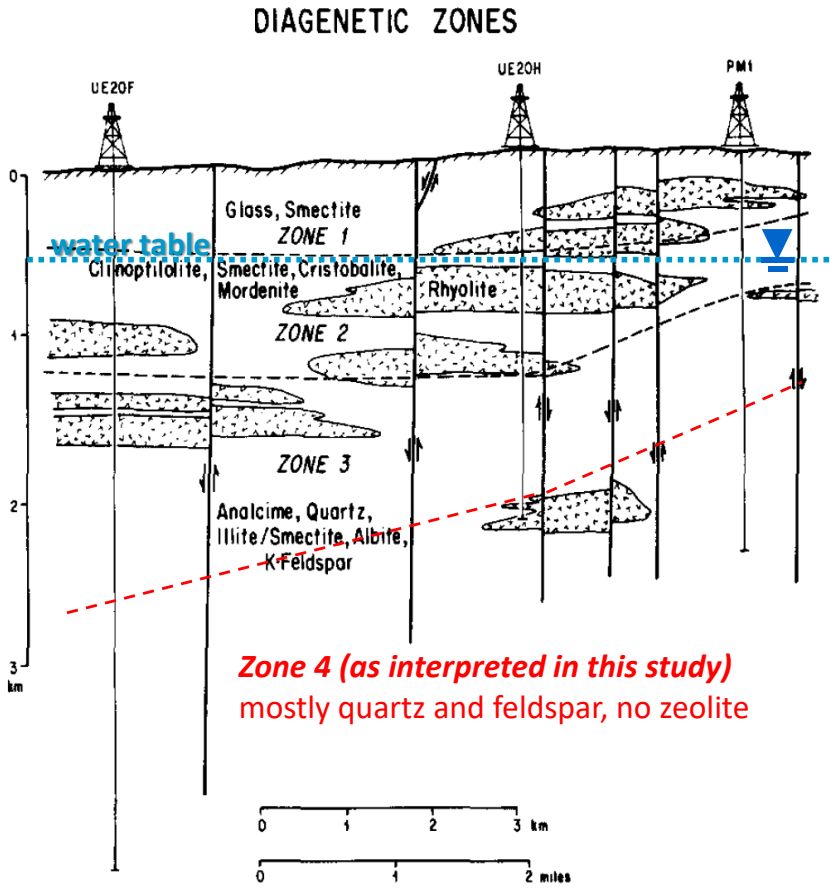

Figure 2. Schematic cross section through boreholes UE-20F, UE-20H, and PM-1 at Pahute Mesa. This study introduces Zone 4 below Zone 3. Modified from Moncure et al. (1981) and Orkild et al. (1969).

Given the need for sorption parameters in assessment of radionuclide transport, there is a need to extend the interpretation of mineralogic diagenesis across the PM testing areas and toward the southwest along groundwater flow paths from PM toward OV. This is possible because XRD have collected from over 100 boreholes in these areas (Warren et al, 2003; Wood, 2017).

Mineralogical zonation is directly relevant to assessment of radionuclide transport by its impact on physical (e.g. porosity, pore structure, and permeability) and chemical (e.g. sorption) properties. Diagenesis affects the spatial distribution of the mass fractions of primary and secondary minerals known to sorb radionuclides - calcite, hematite, mica, smectite, and the zeolites clinoptilolite, mordenite, and analcime (Zavarin and Bruton, 1999; Pawloski et al., 2001; Zavarin et al., 2004; Zavarin and Bruton, 2004a,b). In application to physical properties, differences in matrix permeability have been shown to be related to the diagenetic zones at PM (Moncure et al., 1981). Variation in grain density, a key parameter for determining porosity and bulk density, has been shown to directly relate to mineralogy derived from XRD data from similar volcanic rocks at YM and Rainier Mesa (Nelson et al. 1989; Carle, 2011).

Overall, diagenesis causes large-scale zonal spatial variability of rock properties that is not solely a function of depth or categorization by lithologic, stratigraphic, hydrogeologic, or hydrostratigraphic units. Diagenesis in PM-OV rocks should be considered in conceptualization of a spatial distribution of flow and radionuclide transport properties for both local (e.g. hydrologic source term) and regional flow and transport models.

1.2 Current Work

The current work presented here builds on previous interpretation of diagenetic zones at PM by Moncure et al. (1981). Cross-interpretation of rock property data is facilitated by graphical display of the current databases for XRD, hydrostratigraphic and hydrogeologic units (HSUs and HGUs), lithology, porosity, grain density, and hydraulic conductivity. This work covers the entire area of PM underground nuclear testing in Areas 19 and 20 of the NNSS and downgradient areas including the TMCC, Thirsty Canyon (TC), and OV (Figure 1). This work is directly relevant to any local or regional characterization or conceptualization of radionuclide transport at PM-OV. The interpretational framework of diagenetic zones may facilitate abstraction of insights from the relatively well-characterized PM test locations such as TYBO, BENHAM, and CHESHIRE (Pawloski et al, 2001; Wolfsberg et al., 2002) to the remaining 79 tests with little or no site-specific characterization and monitoring data.

The composite XRD dataset confirms that a vertical sequence of diagenetic zonation is evident throughout PM and hydrologically downgradient toward the TMCC and OV. The current work further supports conclusions by Moncure et al. (1981) that are relevant to conceptualization and assessment of flow and transport:

1. The diagenetic zonal contacts are generally sharp, although mineralogical elements of a shallower zone may be found well within a deeper zone.

2. The diagenetic zones vary in thickness and transgress stratigraphic boundaries (Hoover, 1968; Moncure et al., 1981); this means HSUs and HGUs alone are insufficient to characterize the spatial distribution of flow and transport properties.
3. Matrix porosity and permeability can be higher in the deeper Zone 3 as compared to Zone 2.

This work utilizes XRD data from 109 boreholes as compared to two boreholes (UE-20F and UE-20H) in Moncure et al. (1981). A central objective is to extend interpretation of mineralogic diagenesis to the entire areas of PM testing within and adjacent to the SCCC (>15.2 to 13.4 Ma) (Sawyer and Sargent, 1989) and downgradient areas of the PM-OV groundwater basin including the TMCC (>14.3 to 11.4 Ma) (Broxton et al., 1989). An important question to address is whether significant differences exist in the mineralogy of the tuffaceous rocks sourced from the SCCC and TMCC, considering that transport pathways would originate largely in rocks of the SCCC and could potentially enter rocks of the TMCC. This work further integrates porosity, grain density, HSU, HGU, lithology, alteration, and hydraulic conductivity databases to improve understanding of spatial variability of rock properties (i.e. heterogeneity). An extension in this current work is to add a deeper quartzofeldspathic zone (Zone 4) where zeolitic minerals are absent and largely replaced by quartz and feldspar, which are currently interpreted as non-sorbing to all radionuclides.

1.3 Characteristics of the Diagenetic Zones

Figure 3 summarizes the mineralogic and alteration characteristics of the diagenetic zones. The four diagenetic zones are defined by the characteristics of silicate minerals at deposition and the subsequent authigenic mineral phases and assemblages resulting from hydration and further stages of hydrothermal alteration:

- **Zone 1 (vitric):** characterized by abundance of unaltered or incipiently altered glass in bedded or ash-fall tuff (i.e. vitric tuff). Welded tuffs may include glass or devitrified tuff, which is mostly composed of feldspar with lesser quartz. Secondary calcite is sporadically deposited by downward percolation of meteoric water in the unsaturated zone at low to moderate temperatures (Smith et al., 1999).
- **Zone 2 (zeolitic):** characterized by hydration effects on glass resulting zeolitization primarily to clinoptilolite and a lesser fraction of mordenite that increases in abundance with depth.
- **Zone 3 (transitional):** characterized by dehydration and thermal effects causing further transition in zeolite minerals to mordenite and analcime. Zeolite decreases and quartz and feldspar increase in abundance with depth. Secondary calcite is deposited under higher paleo-geothermal gradients with paleo-temperatures of 72 to 170°C (Smith et al., 1999).
- **Zone 4 (quartzofeldspathic):** characterized by absence of any mineral phase of zeolite or glass; dominant minerals are quartz and feldspar. Secondary calcite is present, as in Zone 3. Kaolinite occurs from hydrothermal alteration of feldspar (Moncure et al., 1981). XRD indicates kaolinite is the dominant clay in Zone 4 southwest of PM toward the northwest portion of the TMCC, whereas smectite remains prevalent over kaolinite at PM and the SCCC.

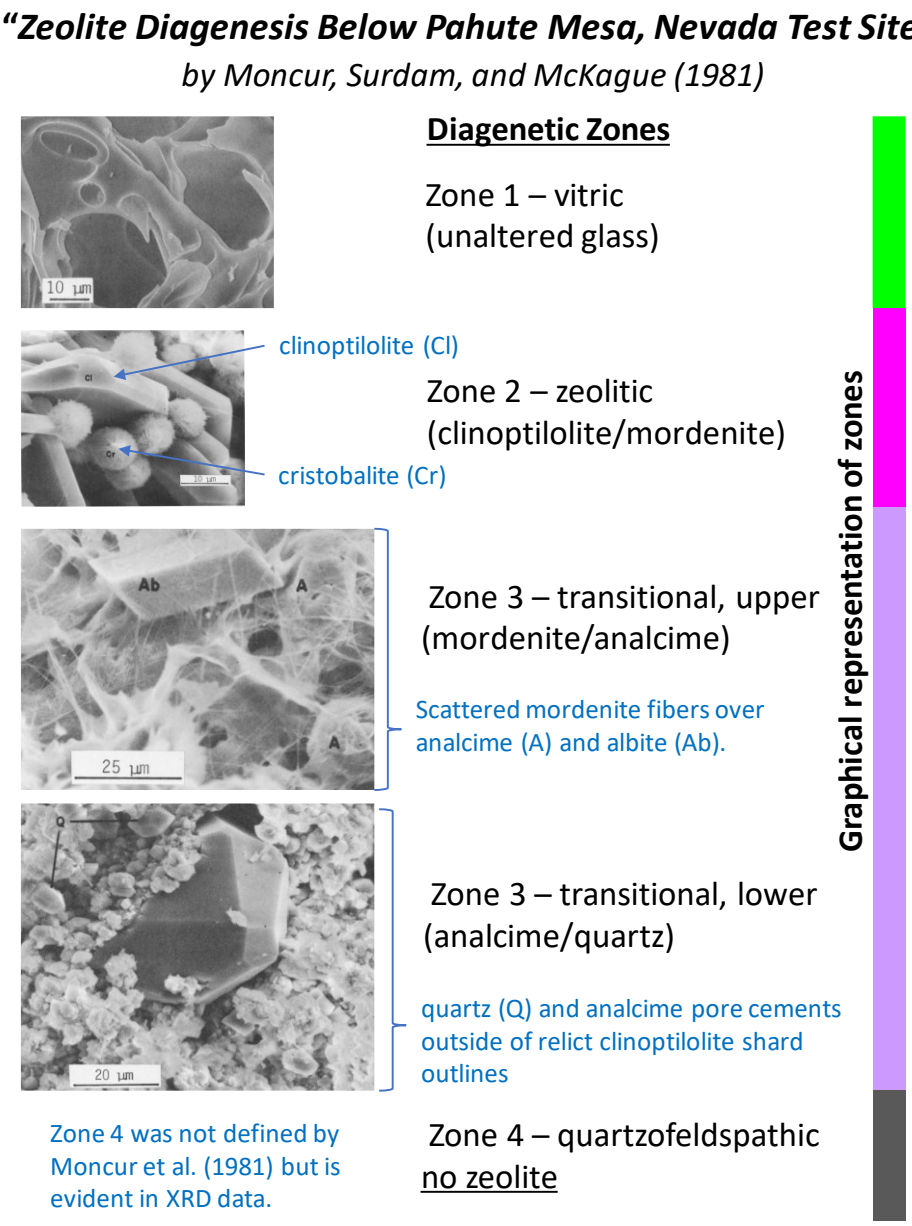

Figure 3. Mineralogic characteristics of diagenetic zones in Pahute Mesa volcanic rocks. Scanning electron micrographs (left) from Moncure et al. (1981).

The scanning electron micrographs in Figure 3 from Moncure et al. (1981) illustrate how zeolite minerals vary in morphology (i.e. clinoptilolite is crystal-like; mordenite is fibrous; analcime is flaky). In addition to transition in zeolite mineral abundance, other mineralogic characteristics of the diagenetic zones are directly relevant to radionuclide transport because of the changes in abundance of the reactive minerals:

- Calcite is usually present only in Zones 3 and 4.
- Hematite is more abundant in Zones 1, 3, and 4 and less abundant where zeolitic.
- Mica (i.e. the micaceous minerals biotite, illite) increases in abundance with depth.
- Smectite occurrence is variable – either continuous, spotty, or completely absent.

About twenty descriptors of alteration characteristics are included in PM-OV rock property database (e.g. “GL” = glass, “ZE” = zeolitic, “QF” = quartzofeldspathic), many of which are directly related to the mineralogy or diagenesis. The four diagenetic zones provide a systematic framework for integrating XRD data with the descriptors of alteration to collectively identify large-scale zonal differences in physical and chemical properties of the volcanic rocks at PM-OV.

1.4 XRD Database

This study examines all available XRD data, regardless of origin and quality, for the PM testing areas and downgradient areas of the PM-OV groundwater basin. Since 1981, various activities of the Environmental Restoration Project at NNSS (FFACO, 1996), including those of the Underground Test Area (UGTA) for assessment of radionuclide transport in groundwater, have produced an immense quantitative dataset for the mass fraction of minerals in rocks in and adjacent to NNSS as measured by various XRD methods (Warren et al., 2003; Wood, 2017). XRD data in the U.S. Geological Survey (USGS) Data Series 297 publication (Wood, 2017) largely consists of the XRD database compiled by Warren et al. (2003). The current XRD database consists of over 70,000 records, of which about 20,000 are from the PM-OV area.

The new higher quality XRD data were obtained by “internal standard” (I) and “full spectrum” (F) methods (Chipera and Bish, 1989; Chipera and Bish, 2002). Older “subjective” (S) and “external standard” (E) XRD data from the 1980s and earlier have mass fraction resolution on the order of 5% or greater, whereas the newer F and I methods have much higher resolution on the order of 0.1% and 1%, respectively. While S and E data resolve some mineral fractions down to 1%, shortcomings persist in resolution and differentiation of the overall mineralogical profile including the different feldspar and zeolite minerals.

The improved XRD resolution of the F and I data is immensely important to assessment of radionuclide transport because very small fractions of calcite, smectite, or hematite in volcanic rocks can profoundly retard radionuclide mobility. The quantity and spatial distribution of these “reactive minerals” including micas and zeolites is of first-order importance to assessment of sorbing radionuclides such as plutonium, cesium, strontium, and uranium (Pawloski et al., 2001; Zavarin et al., 2004; Stoller-Navarro Joint Venture, 2007, 2008, 2009; Carle et al., 2008; Carle, 2011). This study also includes recently collected F XRD data for ER-20-12 (WoldeGabriel et al., 2016). The older E and S XRD data could rarely detect the important radionuclide sorbing minerals calcite, hematite, mica, and smectite or differentiate the zeolite minerals clinoptilolite, mordenite, and analcime. However, the older data can still help identify diagenetic zones, particularly when combined with alteration descriptions (Bechtel Nevada, 2002; USDOE, 2020).

Figure 4 shows 42 locations where newer F and I XRD data have been collected within the PM testing Areas 19 and 20 at the NNSS and further downgradient southwest of PM through the TMCC to OV. The XRD data collected southwest of the testing areas enable

identification of the diagenetic zones along downgradient flow paths. The XRD data collected outside NNSS provide a large-scale framework for distribution of physical properties (e.g., porosity and grain density) that have been measured directly on core only within the NNSS testing areas for evaluation of site characteristics.

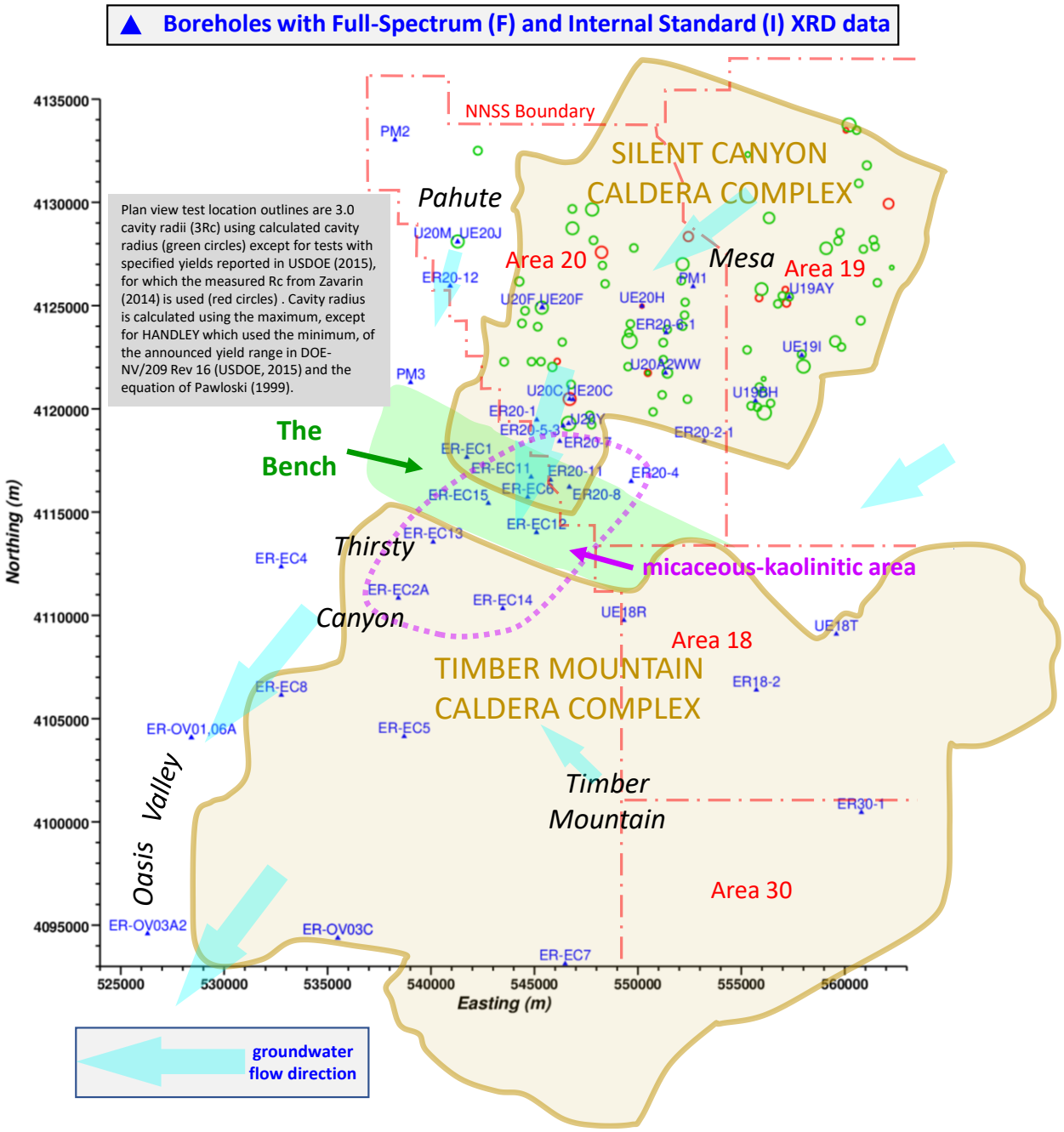

Figure 4. Map showing boreholes with newer F and I XRD data including downgradient areas to southwest of Pahute Mesa detonation locations.

Figure 5 shows the locations of boreholes with newer XRD data, labeled in blue, and older XRD data largely collected for test site characterization at PM, labeled in orange. In Areas 19 and 20 of the NNSS, most of the newer F and I XRD data are obtained from boreholes with the "ER" prefix (labeled as ER20* on Figures 4 and 5). Additional F and I XRD data were obtained from some of the test emplacement and exploration boreholes (with "U", "UE" or "PM" prefix). However, the majority of XRD data from the U, UE, and PM boreholes consist of the lower quality E or S XRD data. All of the XRD data are useful for identifying the diagenetic zones.

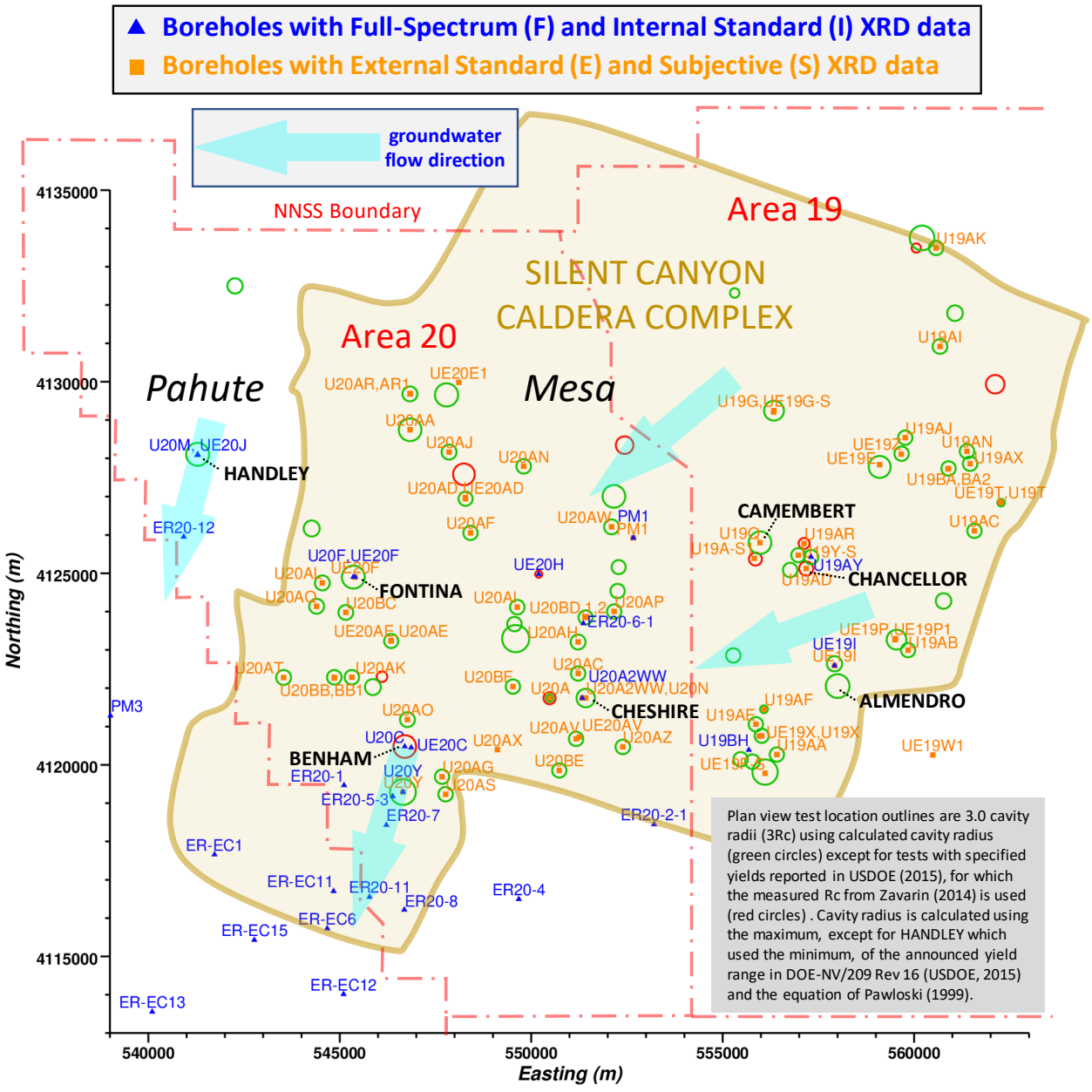

Figure 5. Map showing boreholes with XRD data near Pahute Mesa detonation locations.

In Figures 4 and 5, locations of PM underground nuclear tests are outlined by 3 cavity radii (3Rc) circles (see Figures 4 and 5 for definition of 3Rc). The 3Rc outline represents the "exchange zone" (EZ), a term used in assessment of radionuclide transport at PM to define an estimate of the outer limit of initial radionuclide contamination (USDOE 2018; Carle et al., 2020). The 3Rc outlines convey the approximate spatial extent of the local sources of contamination on PM. Figure 4 also maps two areas called "The Bench" and "micaceous-kaolinitic area," which will be discussed later beginning in Section 3.4 and continuing through Chapter 5.

1.5 Relationship Between Mineralogy and Radionuclide Sorption

Most of the 82 underground nuclear tests detonated at PM between 1968 and 1991 were located near or below the water table (USDOE, 2015). All 82 PM underground tests involved a single detonation, so the words "test" and "detonation" are used interchangeably in the following discussion. The radionuclide inventory for the 82 PM tests lists 43 radionuclide species (Finnegan et al., 2016). Of the sorbing radionuclides (i.e. those radionuclides that will readily partition into the solid phase of the rock), isotopes of strontium, cesium, uranium, and plutonium present the primary concern for radionuclide contamination from underground nuclear testing at PM (Carle et al., 2020). These radionuclides sorb to the reactive minerals calcite, hematite, mica, smectite, and zeolite to various degrees based on laboratory experiments and mechanistic modeling of reactive chemistry (Zavarin et al., 2004; Zavarin and Bruton, 2004a,b; Zavarin et al., 2005; Zavarin et al. 2007; Begg et al., 2015).

For each radionuclide, a linear sorption coefficient (K_d) for a rock type is estimated by a "component additivity approach" as the sum of the products of mass fraction (X) of the reactive mineral in the rock type and K_d of the reactive mineral for the radionuclide (Davis et al., 1999; Zavarin et al., 2004):

$$K_{d,radionuclide,rock} = \sum_{1}^{\substack{number\ of \\ reactive\ minerals}} X_{reactive\ mineral,rock} K_{d,radionuclide,reactive\ mineral}$$

Consequently, characterization of the spatial distribution of the mineralogy, particularly presence/absence and mass fraction of reactive minerals within rock units or zones, is of first-order importance to assessment of transport for sorbing radionuclides at PM.

Table 1 shows estimates for average Log_{10} K_d for strontium, cesium, uranium, and plutonium transport within each reactive mineral as determined by mechanistic modeling for PM groundwater chemistry (Carle et al., 2020). Such K_d estimates are expected to vary by an order of magnitude or more depending on water chemistry, pH, and model uncertainty. Importantly, each radionuclide is expected to sorb primarily to three of the

five reactive minerals. Strontium and cesium sorb primarily to mica, smectite, and zeolite. Uranium and plutonium sorb primarily to calcite, hematite, and smectite.

Table 1. Estimates of average Log_{10} K_d for strontium, cesium, uranium, and plutonium for 100% mass fraction of sorbing mineral.

Reactive Mineral	Log_{10}Kd for Radionuclide per 100% mass fraction			
	Strontium	Cesium	Uranium	Plutonium
Calcite	-1.12	----	0.50	4.19
Hematite	-1.13	----	2.41	3.17
Mica/Illite	2.78	5.67	----	----
Smectite	2.72	3.06	1.70	3.49
Zeolite	3.66	3.66	----	----

Differences in sorption properties of reactive minerals will cause dependency of radionuclide redistribution and mobility parameters (i.e. transport properties) on the mineralogical conditions, which will certainly vary between different PM detonation locations and along downgradient PM-OV flow paths. For example, many of the 82 PM detonations are located near the water table in zeolitic tuff of Zone 2. However, uranium and plutonium are not known to sorb to zeolite in the groundwater chemistry conditions at YM or PM (Vaniman and Bish, 1993; Duff et al., 1999; Zavarin and Bruton, 2004a; Zavarin et al., 2004, 2007). Only smectite strongly sorbs all four of these radionuclides (Zavarin and Bruton, 2004b; Zavarin et al., 2004, 2007).

The ability to resolve small percentages of the reactive minerals is crucial to estimation of K_d coefficients. The F and I XRD indicate that hematite commonly occurs on the order of 1% mass fraction (except perhaps in highly zeolitic rock, where it may be absent). A 1% mass fraction of hematite will significantly decrease uranium and plutonium mobility. The mica group minerals (including illite) typically represent a few percent of the mass fraction and, therefore, are often not resolved by the poorer quality S and E XRD data. The F and I XRD data reveal a nearly ubiquitous presence and depth increase of mica, which is highly relevant to assessment of strontium and cesium transport. Because of the strong sorption effects from trace quantities of reactive minerals, the higher quality F and I XRD data are preferable for estimation of K_d coefficients by the component additivity approach.

1.6 Plutonium Example

Pu-239 and Pu-240 are two of the 43 radioisotopes in the radionuclide inventory of underground nuclear detonations at PM (Finnegan et al., 2016). Measurements of total Pu-239 and Pu-240 (Pu-239/240) are available for the source or adjacent plumes of six PM contaminant sources - BENHAM, BULLION, CHANCELLOR, CAMEMBERT, ALMENDRO, and CHESHIRE (Navarro-Intera, LLC., 2013). Figure 6 compares the highest measured concentration of Pu-239/240 associated with each these contaminant sources (sampling location in parentheses). The measurements are compared to the maximum contaminant level (MCL) standard of 15 pCi/L for gross alpha particle activity (USEPA, 2002). For most contaminant sources, only trace concentrations of Pu-239/240 are found. The exceptions are CHANCELLOR and ALMENDRO. These two detonations have rather unique characteristics. CHANCELLOR is located near the water table in Zone 1 where rocks are largely unaltered. The other six detonations with plutonium data are located hundreds of meters below the water table in either Zone 2 or Zone 3. ALMENDRO appears to be hydrologically isolated as evidenced by enduring test heat and slow water level recovery lasting 25 years (Carle et al., 2003). The CHANCELLOR and ALMENDRO plutonium data raise the question of whether local detonation site characteristics, including mineralogy, can lead to unusually high radionuclide source concentrations.

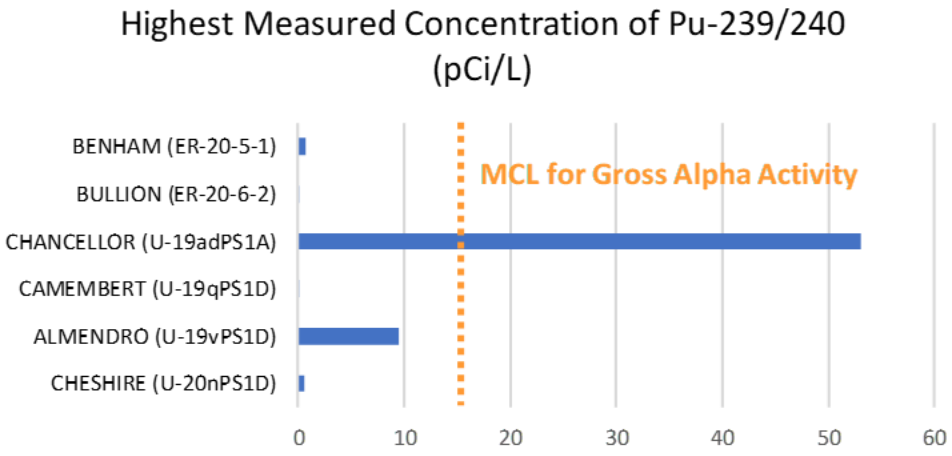

Figure 6. Highest measured concentrations of Pu-239/240 at PM source/plume locations.

2 Graphical Representation of XRD and Related Rock Properties – Example at Borehole UE-20H

The UGTA program has assembled many large databases useful to characterization of rock properties at PM-OV (Wood, 2017). The XRD database is particularly relevant to assessment of radionuclide transport for several reasons:

- The mass-fractional abundances of the reactive minerals (calcite, hematite, mica, smectite, and zeolite) are directly measured by XRD.
- Diagenesis is evident in not just abundance of zeolite, but also abundances of chemically inert or "non-reactive" minerals (e.g. quartz and feldspar).
- The newer high-quality XRD data provide insights to interpretation of older low-quality XRD data; this is important to abstraction of modeling results from Area 20 to Area 19, for example, because Area 19 has very few high-quality XRD data.
- Recognition of the diagenetic zones enables systematic identification of smaller-scale spatial variations in rock properties between different HGUs or lithologies; this provides a sound basis for characterization and conceptualization of multi-scale heterogeneity evident at PM.

This study uses a graphical method to display multiple rock property datasets available at each borehole, all of which are directly applicable to development of groundwater flow and radionuclide transport models. The graphical display enables cross-interpretation of data on one page without resorting to manual comparison tabular values given in the various formats of these separate datasets.

As an initial example of the graphical display, Figure 7 presents data for borehole UE-20H with added explanation. From left to right, thirteen data sets are presented on Figure 7:

1. **XRD data**, shown as color-coded horizonal bar graph segments proportional in length to the mass fraction of the mineral, with mineral component abbreviation shown in the legend (see Table 2).
2. **Porosity measurements**, shown as light blue circles in units of percent.
3. **Grain density measurements**, shown as black 3-point stars in units of g/cc × 100 – 200 (i.e., a value of 63 on the x-axis of the graph represents 2.63 g/cc).
4. **Grain density derived from XRD**, shown as black triangles connected by line segments in units of g/cc × 100 – 200 (i.e., a value of 63 on the x-axis of the graph represents 2.63 g/cc).
5. **3Rc outline**, shown as a red circle for detonations with specified yield or a green circle for detonations with an announced yield range (see explanation on Figure 7). If the borehole is not an emplacement hole and is within 5Rc of the detonation, an approximate distance in meters is appended to the detonation name.
6. **Water level**, shown as horizontal dashed blue line at water level elevation.
7. **XRD method,** colored blue for F and I methods and orange for E and S methods.
8. **Diagenetic zone (as interpreted in this report)**, with Zone 1 (green), Zone 2 (magenta), Zone 3 (light purple), Zone 4 (grey).

9. **Alteration**, color codes identified by lower-case descriptors in legend (see Table 3 for index of descriptors). Multiple colors at the same elevation interval denote the multiple alteration descriptors given in the PM-OV hydrostratigraphic database.
10. **Hydrostratigraphic unit (HSU)**, with labels shown.
11. **Hydrogeologic unit (HGU)**, color coded as AA (yellow), VTA (green), WTA (orange), TCU (magenta), LFA (brown), ICU (red).
12. **Lithology**, coded by the width and dashing on the hydrogeologic section (see Figure 8 for explanation).
13. **Hydraulic conductivity**, given in units of m/d and color coded as >10 (magenta), >1 (red), > 0.1 (yellow), >0.01 (green), > 0.001 (light blue), > 0.0001 (dark blue), zero (black). Dashing indicates the interpreted value is a range less than an upper limit. Thicker lines represent pumping test estimates; thinner lines represent slug test estimates. A thin grey line represents an open interval not tested or interpreted not to be contributing to flow.
14. **Fracture frequency and openness**, with frequency represented by color (warmer = more frequent, colder = less frequent) and openness represented by width (closed = thin, open = wide, partially open = mid).

Table 1 provides an index of basic information for the twelve boreholes with XRD data discussed in Sections 2 and 3 of this report. Tables A.1 through A.6 provide corresponding information for the remaining 98 boreholes with XRD data discussed in the Appendix.

Table 1. Index of boreholes with XRD data discussed in main body of report.

Borehole	Geographical Location	Geological Location	XRD Method(s)	Adjacent Test (distance to)	Figure
UE-20H	PM Area 20, NNSS	SCCC	I	REX	7
UE-20F	PM Area 20, NNSS	SCCC	F, I, S	FONTINA (50 m)	9
UE-20J	PM Area 20, NNSS	NW of SCCC	I	HANDLEY (20 m)	10
U-20M	PM Area 20, NNSS	NW of SCCC	I	HANDLEY	11
UE-20C	PM Area 20, NNSS	SCCC	I	BENHAM (170 m)	12
U-20C	PM Area 20, NNSS	SCCC	I	BENHAM	13
ER-20-5-3	PM Area 20, NNSS	SCCC	I	TYBO (290 m)	14
U-20Y	PM Area 20, NNSS	SCCC	I, S	TYBO	15
ER-20-7	PM Area 20, NNSS	SCCC	F	---	16
ER-EC-11	Thirsty Canyon	The Bench	F	---	17
ER-EC-6	Thirsty Canyon	The Bench	I	---	18
ER-EC-2A	Thirsty Canyon	TMCC	F	---	19

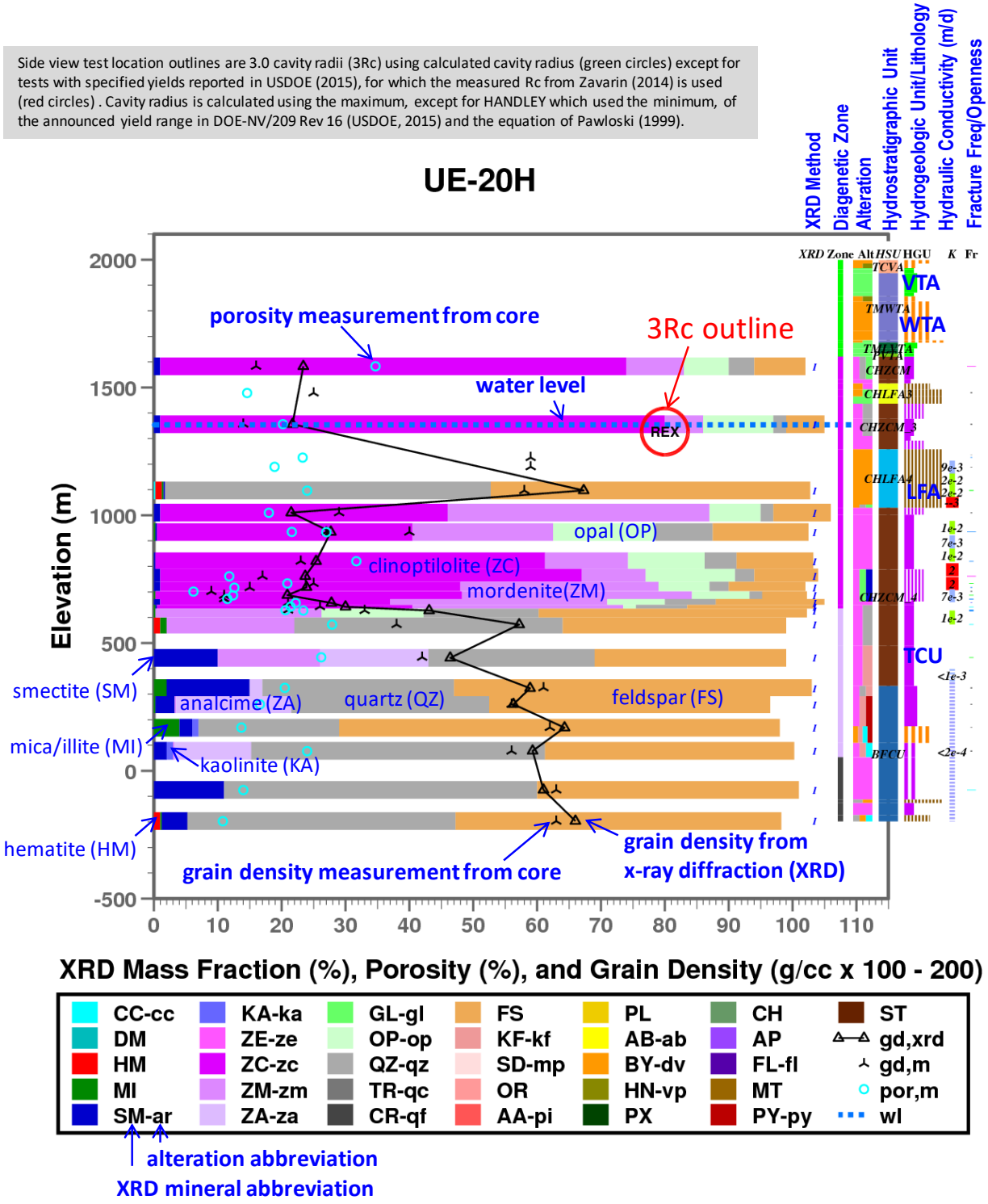

Figure 7. Graphical representation of rock property data for borehole UE-20H, SCCC, PM, east-central Area 20, NNSS.

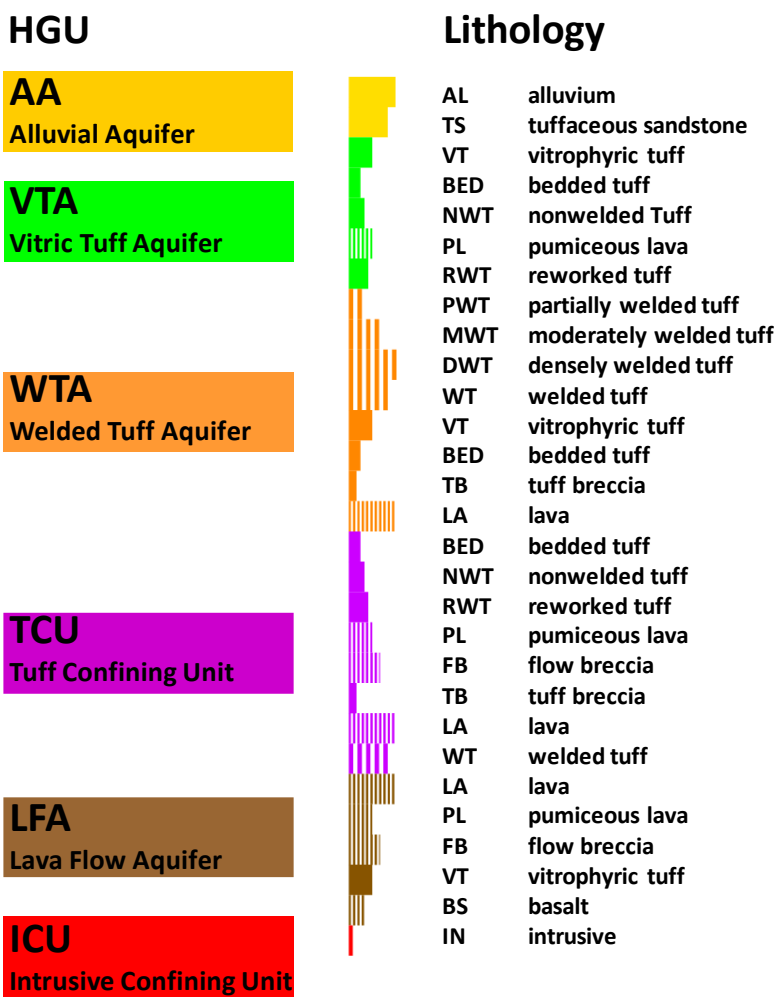

Figure 8. Explanation of graphical display for hydrogeologic unit (HGU) and lithology. Note: the same lithology can occur in multiple HGUs of the PM-OV hydrostratigraphic database.

Table 2. Index of mineral component abbreviations from XRD database.

Mineral									
CA	calcite	ZE	zeolite	QZ	quartz	OR	orthoclase	HN	hornblende
DM	dolomite	ZC	clinoptilolite	TR	tridymite	AA	adularia	CH	chlorite
HM	hematite	ZM	mordenite	CR	cristobalite	PL	plagioclase	AP	apatite
MI	mica	ZA	analcime	FS	feldspar	AB	albite	FL	fluorite
SM	smectite	GL	glass	KF	K-feldspar	BY	bytownite	MT	magnetite
KA	kaolinite	OP	opal	SD	sanidine	CX	clinopyroxene	PY	pyrite

2.1 XRD

As discussed previously, UE-20H is one of two boreholes with XRD data examined in detail by Moncure et al. (1981). Table 2 provides an index of XRD mineral component

abbreviations. Figure 7 includes extra labeling to help explain the graphical display of the XRD data:

- In Zone 2, tuff confining units (TCU) rocks are composed of about 65 to 90% zeolite, with clinoptilolite and mordenite the prevalent zeolitic minerals. Opal, feldspar, and quartz account for most of the remainder, along with trace smectite. The one XRD sample in the CHLFA4 lava flow aquifer (LFA) indicates mostly quartz and feldspar with trace hematite and smectite.
- In Zone 3, TCU rocks are less zeolitic, with only mordenite and analcime present. Most of the TCU rock is quartz and feldspar, with increased smectite relative to Zone 2. Traces of hematite, mica, and kaolinite are present.
- In Zone 4, TCU rocks contain no zeolite. 90% or more of the rock is quartz and feldspar. Some smectite is present as are traces of hematite.
- LFAs and WTAs are higher in quartz and feldspar compared to TCUs, as characteristic of devitrified (dv) and vapor phase (vp) alteration occurring shortly after deposition.

A few specifics on the XRD mineralogy:

- "ZE" refers to undifferentiated zeolite; clinoptilolite (ZC), mordenite (ZM), and analcime (ZA) are the only three zeolite minerals identified on PM.
- "FS" refers to undifferentiated feldspar; "KF" and "PL" are sometimes differentiated. KF is sometimes differentiated into "SD", "OR", and "AA"; "PL" is sometimes differentiated into "AB", "BY" and "CX".
- For all zeolite and feldspar mineral components, the mass fractions shown in the bar graphs account for the level of mineralogical differentiation in the XRD data.

2.2 Porosity and Grain Density Measurement Comparison to XRD

The porosity and grain density measurements are obtained from the rock properties database given in the USGS Data Series 297 report (Wood, 2017). At UE-20H, porosity hovers around 20 to 30% in most of the TCUs of Zone 2 (the CHZCM, CHZCM_3, and upper CHZCM_4 HSUs). Lower porosity is evident where a pumiceous lava occurs at about 700 m elevation. TCU porosity decreases downward through Zone 3.

The XRD-derived grain density is determined using widely published specific gravity values for each mineral (e.g. Deer et al., 1966; Nelson and Anderson, 1992). Grain density measurements from the rock properties database compare closely to XRD-derived grain density. The XRD-derived grain density should be very accurate for newer XRD data using F and I methods. The collective data show that grain density of zeolitic TCU in Zone 2 is typically 2.2 to 2.4 g/cc. The TCU in zone 4 is distinguished by much higher grain density of 2.60 g/cc or greater. Grain density in the LFA and WTA HGUs is usually on the order of 2.60 g/cc, with lower values where vitric or zeolitic.

The largest discrepancies between measured and XRD-derived grain density result from the inability of rock property measurement methods to account for "bound water" incorporated into the mineral structure of hydrated minerals. Bound water refers to water molecules incorporated into mineral structure, which can include significant mass fraction

of water – clinoptilolite 15.3 to 15.6%, mordenite 12.2%, smectite 9.2%, analcime 8.2%. Bound water is released by heating or exposure to low humidity. Typical methods for rock property measurement do not account for bound water. Methods using oven drying cause dehydration of a large fraction of the bound water. Water or gas pycnometry methods involving fluid volume displacement do not account for rehydration of dehydrated minerals or penetration of gas into the dehydrated volume. Dehydration and rehydration of hydrated minerals such as zeolite and smectite is a long-recognized difficulty to measurement of rock properties at NNSS (Catalano, 1969; Knowlton and McKague, 1976; Knowlton et al, 1981; Martin et al., 1993; Carle, 2011) and YM (Kranz et al., 1989; Nelson and Anderson, 1992; Boyd et al., 1995; Bish et al., 2003).

Many tests on PM were situated in the zeolitic Zone 2. In "site characteristics reports" for some of the latest test site evaluation work completed on PM between 1988 and 1991, rock property measurements were presented with the caveat that the effects of bound water cause overestimation of grain density, saturation, and porosity and underestimation of gas porosity (Newmark and McKague, 1988; McKague and Newmark, 1989; Newmark and Wagoner 1990; McKague et al. 1990; McKague and Hearst, 1991). Considering that Zone 2 minerals often consist of mostly hydrated minerals - clinoptilolite, mordenite, and smectite – grain density were usually overestimated, and, similarly, dry bulk density measurements were usually underestimated on the order of 10%. These errors propagate into the standard equations for porosity, saturation, and gas porosity. For example, McKague et al. (1990) estimated up to 13% mass fraction bound water in Zone 2 rocks at U-20BF on PM, causing overestimation of saturation by up to 61 volume percent and underestimation of gas porosity by 14 volume percent.

It is reasonable to expect that effects of bound water significantly impact most rock property data for the highly zeolitic and argillic rocks in the rock property database for NNSS (Wood, 2017). In the graphical representation of rock properties, the effects of bound water are evident in grain density data, with those derived from direct measurements clearly exceeding those derived from XRD by 0.2 g/cc or greater in zeolitic rocks. This topic is further discussed in Section 3.1 for the U-20F (FONTINA) site and in the Appendix for other locations with XRD on PM.

2.3 HSU, HGU, Lithology, and Alteration

The HSU, HGU, lithology, and alteration descriptors used in this study are obtained from the PM-OV hydrostratigraphic database current to 9/17/2018. In previous radionuclide transport assessments at NNSS, HSUs and HGUs have provided a reasonable framework to spatially compartmentalize hydraulic and transport properties (Prothro et al., 2009). This approach may require further refinement at PM-OV considering the spatial variability (i.e. heterogeneity) evident by cross-interpretation of HSU, HGU, lithology, and alteration in multiple rock property datasets. It should be recognized that several HGUs can occur within one HSU, and several lithologies can occur in one HGU. In some instances, the lithology within an HGU appears inconsistent, for example: lava in welded tuff aquifer (WTA), lava in tuff confining unit (TCU), welded tuff in lava flow aquifer (LFA), or welded

tuff in TCU. Alteration often varies within the same lithology or HGU. Table 3 shows the abbreviations for alteration described at PM-OV. Collectively, the rock property data within a HSU, HGU, lithology, or alteration interval exhibit both systematic and random spatial variation. The random spatial variation results from fine-scale variability and measurement error or uncertainty.

Table 3. Index of alteration abbreviations from Pahute Mesa-Oasis Valley drill hole database.

Alteration							
cc	calcite	zm	mordenite	qc	chalcedony	ab	albitic
ar	argillic	za	analcime	qf	quartzofeldspathic	dv	devitrified
ka	kaolinitic	gl	vitric	kf	potassic	vp	vapor phase
ze	zeolitic	op	opaline	mp	microporphyritic	fl	fluoritic
zc	clinoptilolite	qz	silicic	pl	pilotaxitic	py	pyritic

2.4 Hydraulic Conductivity

The graphical display enables direct comparison of interval hydraulic conductivity (K) data to the vertical profile of HSUs, HGUs, lithology, and alteration. The K data are derived from transmissivity data from slug and pumping tests over vertical intervals given in Jackson et al. (2020). Two important points stressed in Jackson et al. (2020) are (1) the flowing portion of the aquifer is typically only a small fraction of the total aquifer, and (2) the tuff confining units can also contain high-conductivity intervals. Both points are evident in the UE-20H data (Figure 7). These interval-specific K data are further evidence that categorization of properties solely by HGU or HSU will not adequately characterize the spatial variation of flow and transport property heterogeneities relevant to assessment of radionuclide transport.

2.5 Fracture Frequency and Openness

Data on fracture frequency and openness are provided in the USGS Series 297 report (Wood, 2017). These data apply to short segments of the borehole typically less than 3 meters long. As introduced at the beginning of Section 2, the graphical representation plots the fracture frequency by color and the fracture openness by line width. The line segment length along the vertical represents the fracture data interval (i.e. from top to bottom). The graphical plot emphasizes the fact that only a small fraction of the total length of the borehole was sampled for fracture data. At UE-20H, the fracture data suggest that open fractures exist in the high-K interval in the pumiceous lava with the TCU at the base of Zone 2. Fractures are often infrequent and closed in low-K intervals, as expected. These fracture data are not continuous enough along the borehole to adequately characterize the true spatial distribution of fractures at UE-20H; the same shortcoming is evident for other PM-OV boreholes with fracture data. In general, the available data for fracture frequency and openness should be interpreted as supplementary to other data or models used for fracture characterization at PM-OV.

3 XRD and Rock Properties Near and Downgradient of PM Detonations

This section examines rock properties at several locations of interest to assessment of radionuclide transport at PM-OV: the detonation locations FONTINA, HANDLEY, BENHAM, and TYBO and several downgradient boreholes southwest of PM.

3.1 UE-20F near FONTINA

Borehole UE-20F is the deepest borehole at PM. UE-20F has extensive XRD, porosity, and grain density data and was one of the two boreholes examined in detail by Moncure et al. (1981). The XRD data at UE-20F (Figure 9) show a profile of zeolite transformation similar to UE-20H: a pronounced clinoptilolite-rich Zone 2, a transition from mordenite to analcime in Zone 3, and a complete absence of zeolite in Zone 4. Glass is evident at the base of the CHLFA5 HSU. For smectite, the XRD data at UE-20F show a depth distribution nearly opposite to UE-20H; smectite is more abundant in the upper portion of the borehole, particularly in Zone 2. For mica, the XRD data show increasing abundance with depth, a trend that is consistently seen elsewhere at PM-OV.

Similar to UE-20H, porosity data in TCUs at UE-20F show higher porosity in Zone 2 and a decreasing trend in porosity with depth in Zone 3. Grain density derived from measurements and XRD are in generally good agreement except in Zone 2. Many of the grain density measurements are suspiciously high in the highly-zeolitized rocks. This results from faulty grain density and porosity measurement methods discussed in Section 2.2. The combined XRD and rock property data at UE-20F show how rocks are more heterogeneous in Zones 2 and 3 as compared to Zone 4.

Zone 4 in the deepest 1,750 meters of UE-20F consists primarily of the BRA and PBRCM HSUs, which occur here as composite units of LFA, WTA, and TCU HGUs within the SCCC (USDOE, 2020). Within Zone 4 at UE-20F, the mineralogy of the BRA and PBRCM composite units becomes uniformly quartzofeldspathic. However, the sequence of mineralogical diagenesis evident at UE-20F is certainly not uniform across PM and not directly related to HSUs or HGUs, as clearly evident in the BRA.

Elsewhere at PM, the BRA occurs as either WTA, TCU, or LFA HGUs in all four diagenetic zones. For example, to the northeast of SCCC at borehole PM-2 and toward the western margin of the PM-OV groundwater basin at Rainier Mesa, the BRA occurs predominately as unaltered welded tuff in the vitric Zone 1 (USDOE, 2018). Near the HANDLEY test northwest of the SCCC, the BRA occurs as a WTA within the zeolitic Zone 2. At UE-20F, the BRA is almost entirely lava flows lacking any glass or zeolite, having undergone quartzofeldspathic diagenesis. In Area 19 of PM, the BRA typically occurs as thick composite units of WTA, TCU, and LFAs spanning the Zones 2 and 3. The lithologic and diagenetic variation evident in the BRA is a leading example for why flow and transport property variation cannot be entirely attributed to HSU or HGU.

Figure 9 also shows the 3Rc outline for the FONTINA detonation located about 50 m horizontal distance from UE-20F in the emplacement hole U-20F (see explanation of 3Rc value on Figure 9). The 3Rc EZ for FONTINA is primarily situated in Zone 3. The upper EZ extends into the bottom portion of Zone 2, mostly composed of the glassy base of the CHLFA5 HSU. The most prevalent sorbing minerals near the FONTINA detonation are mica, smectite, and zeolite (mostly as mordenite or analcime in Zone 3). Some calcite is sporadically present. The XRD data indicate a lack of hematite at UE-20F, similar to UE-20H. Detection of trace calcite and hematite depends heavily on the XRD method, for which the "I" method is not adequate to detect to a mass fraction of less than 1%. This is consistent with rock chemistry data for "upper rhyolitic lavas of Area 20" (Calico Hills lavas) showing an average of 0.8% or less Fe_2O_3 (Sargent, 1969). It may be advisable to utilize rock chemistry data to improve estimation hematite mass fraction.

The XRD data for UE-20F provide the deepest vertical section of mineralogy at PM-OV. Smectite is noticeably absent below the middle of Zone 3. Moncure et al. (1981) note the presence of mixed-layered illite-smectite in Zone 3. Illite is usually formed by alteration of muscovite (a mica). In XRD data, illite is typically lumped together with the mica group or "micaceous" minerals, which have similar chemical composition. In rhyolitic rocks, illite can also be formed by hydrothermal alteration of smectite, with the proportion of illite increasing in mixed-layer illite-smectite as a function of increased temperature, time, and burial depth (Bish and Aronson, 1993; Bauluz et al., 2002). Thus, the apparent absence of smectite and abundance of mica at depth in UE-20F is attributable to the extent of hydrothermal alteration. Smith and Aronson (1993) attribute a similar transition of illite/smectite layers to nearly 100% illite in borehole USW G-2 at YM to higher paleothermal gradient and temperature caused by proximity to hydrothermal upflow near the southern margin of the Claim Canyon caldera within the TMCC.

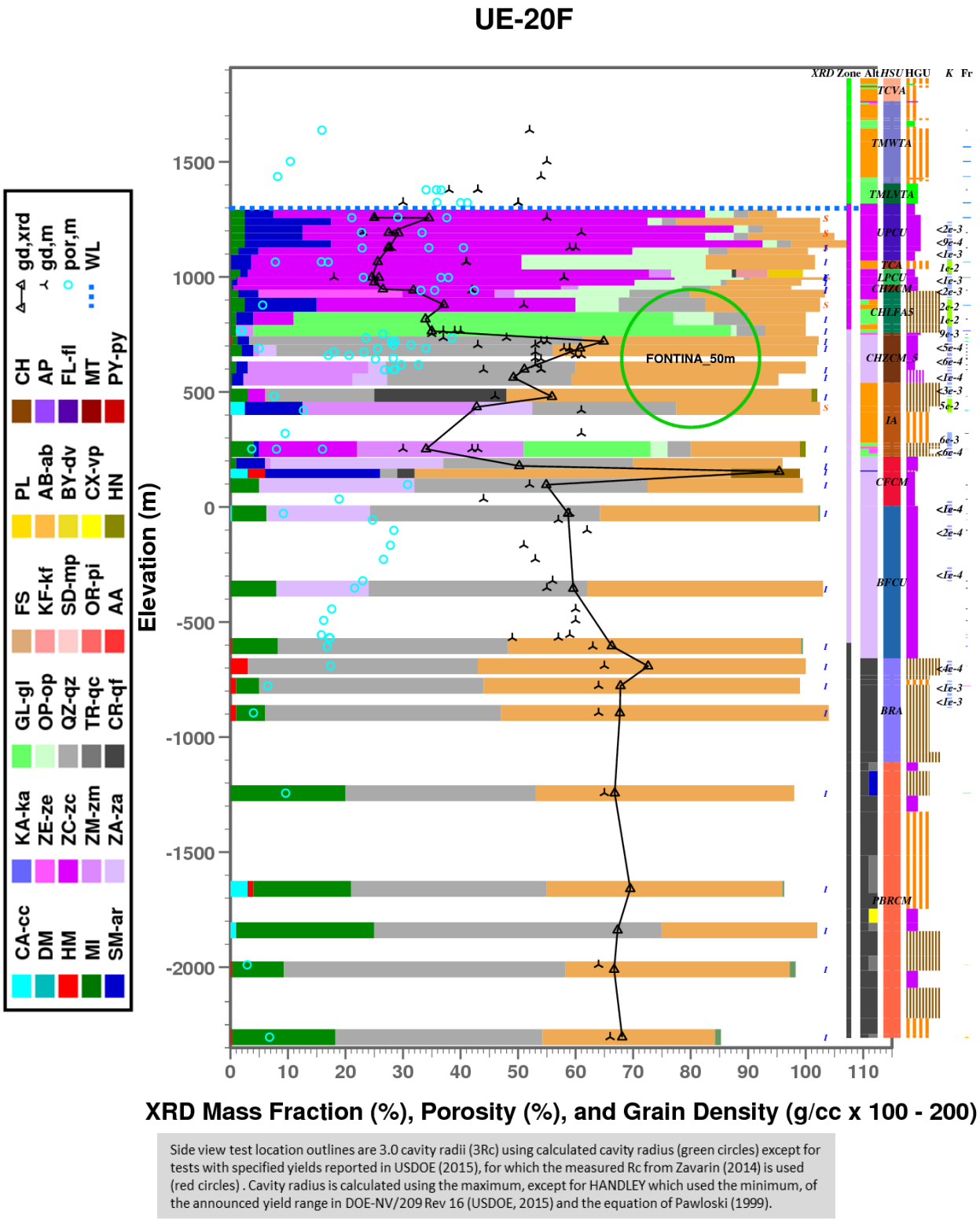

Side view test location outlines are 3.0 cavity radii (3Rc) using calculated cavity radius (green circles) except for tests with specified yields reported in USDOE (2015), for which the measured Rc from Zavarin (2014) is used (red circles) . Cavity radius is calculated using the maximum, except for HANDLEY which used the minimum, of the announced yield range in DOE-NV/209 Rev 16 (USDOE, 2015) and the equation of Pawloski (1999).

Figure 9. Graphical representation of rock property data for borehole UE-20F (about 50 m distance from FONTINA), SCCC, PM, west-central Area 20, NNSS.

3.2 UE-20J and U20M near HANDLEY

Borehole UE-20J is located 20 m distant from the HANDLEY detonation, which was located in the emplacement hole U-20M. A moderate amount of rock property data is available for UE-20J (Figure 10). Less extensive XRD and rock property data are available for U-20M (Figure 11).

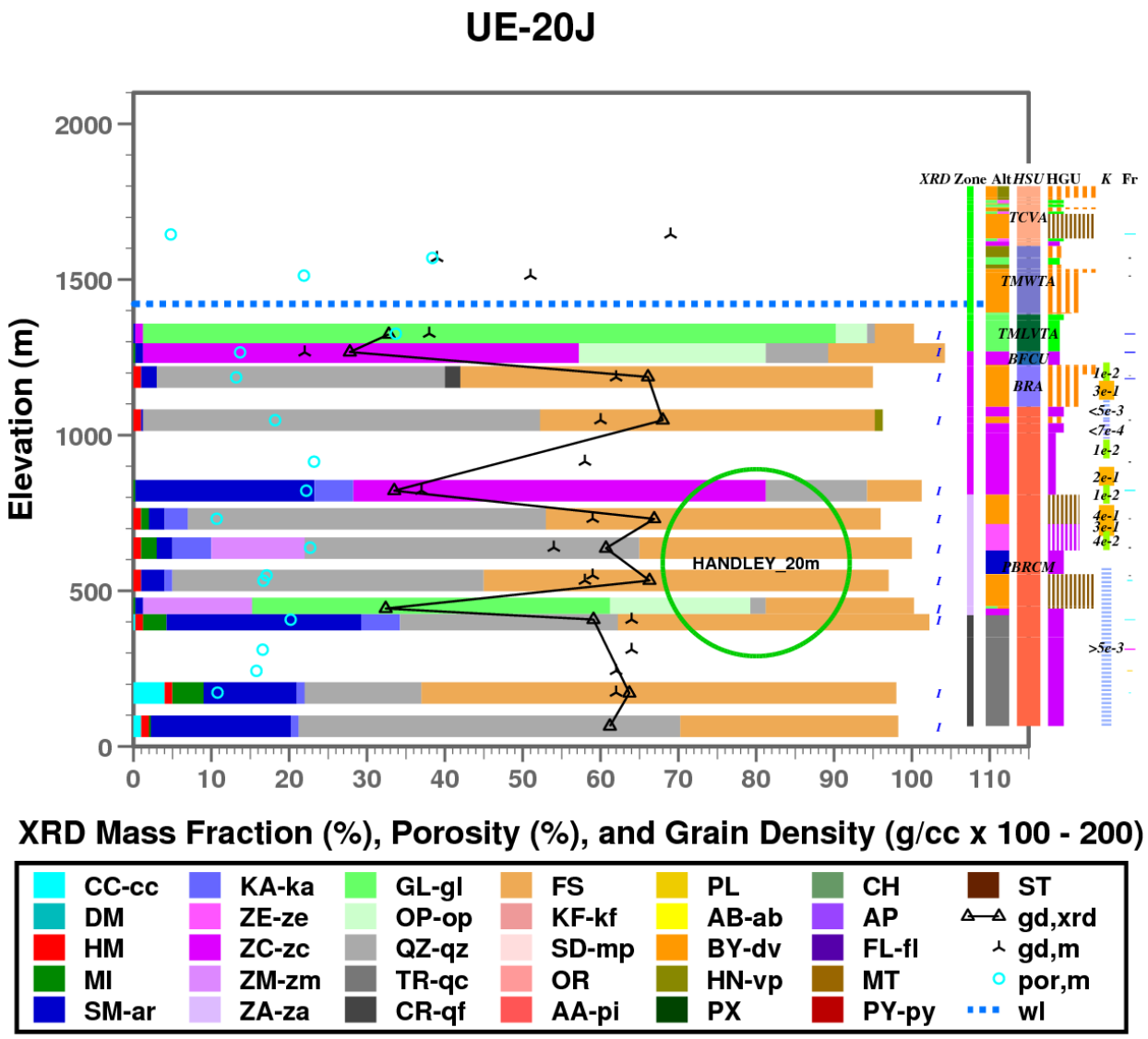

Side view test location outlines are 3.0 cavity radii (3Rc) using calculated cavity radius (green circles) except for tests with specified yields reported in USDOE (2015), for which the measured Rc from Zavarin (2014) is used (red circles) . Cavity radius is calculated using the maximum, except for HANDLEY which used the minimum, of the announced yield range in DOE-NV/209 Rev 16 (USDOE, 2015) and the equation of Pawloski (1999).

Figure 10. Graphical representation of rock property data for borehole UE-20J (about 20 m distance from HANDLEY), west of SCCC, PM, northwest Area 20, NNSS.

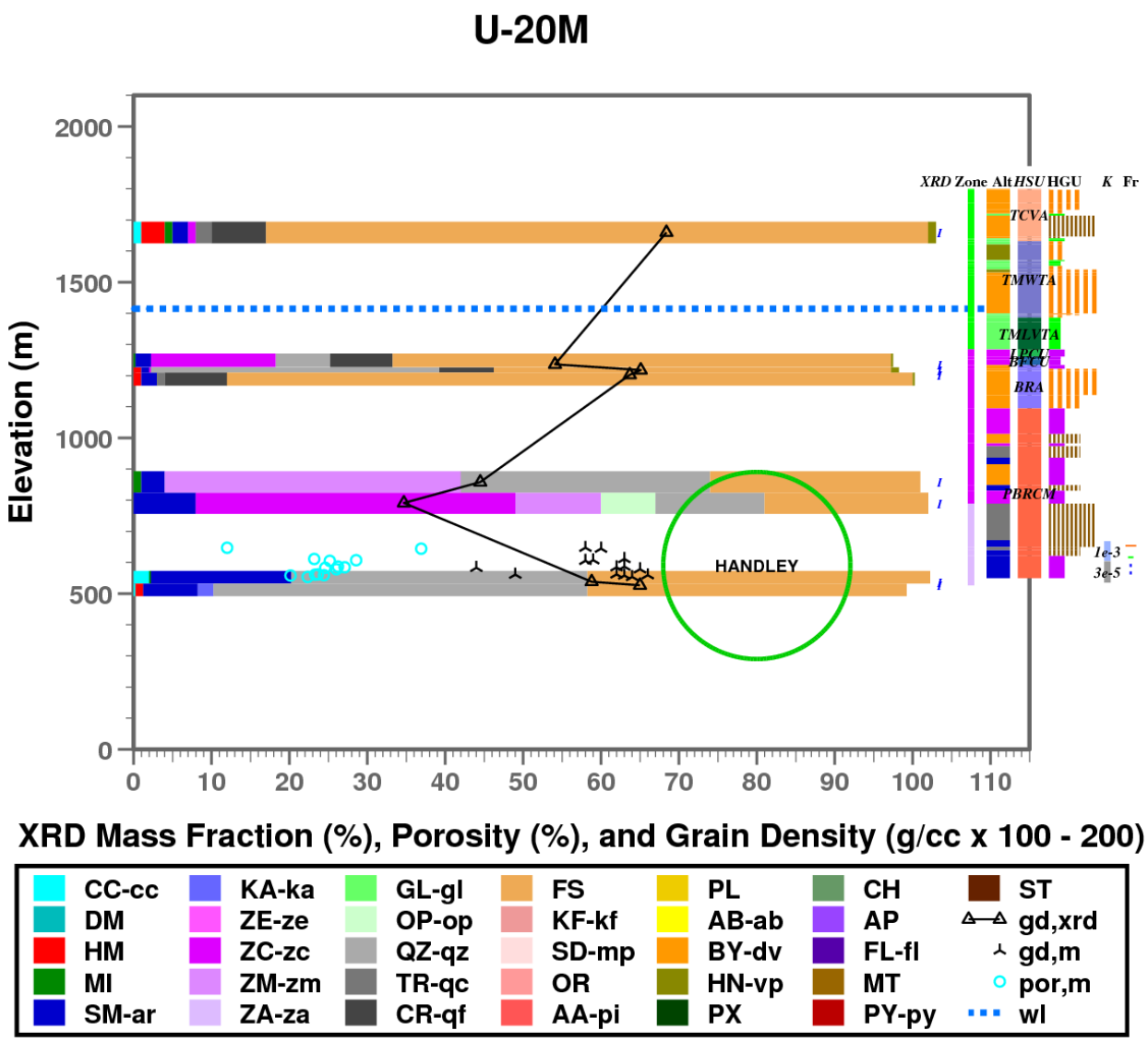

Side view test location outlines are 3.0 cavity radii (3Rc) using calculated cavity radius (green circles) except for tests with specified yields reported in USDOE (2015), for which the measured Rc from Zavarin (2014) is used (red circles) . Cavity radius is calculated using the maximum, except for HANDLEY which used the minimum, of the announced yield range in DOE-NV/209 Rev 16 (USDOE, 2015) and the equation of Pawloski (1999).

Figure 11. Graphical representation of rock property data for borehole U-20M (HANDLEY), west of SCCC, PM, northwest Area 20, NNSS.

Most of the HANDLEY 3Rc EZ, including the working point, is located in Zone 3. Smectite is relatively abundant. Hematite is pervasive except where clinoptilolite is abundant. Mica is less abundant at HANDLEY compared to at FONTINA; hematite is more abundant at HANDLEY compared to FONTINA; this is attributable to a higher mass fraction of Fe_2O_3 of over 2% in rhyolitic lavas of Quartet Dome (Sargent, 1969). Three relatively high-K intervals (> 0.1 m/d) are evident from K data above the working point. Low hydraulic conductivity persists below the working point in Zone 4, where the smectite mass fraction appears to be high at 10 to 25%. Zone 1 extends below the water table, including welded tuff of the TMWTA HSU.

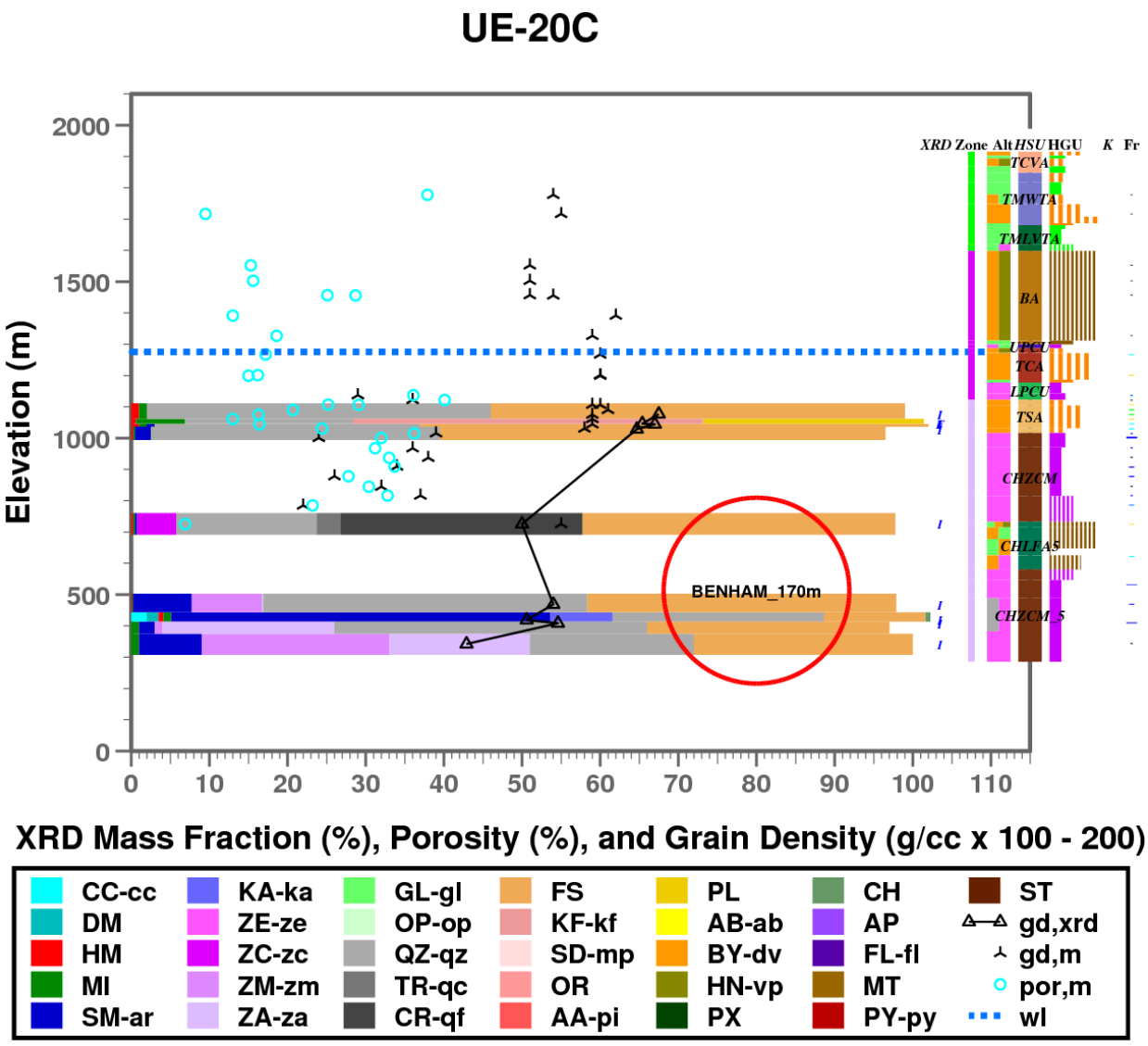

Side view test location outlines are 3.0 cavity radii (3Rc) using calculated cavity radius (green circles) except for tests with specified yields reported in USDOE (2015), for which the measured Rc from Zavarin (2014) is used (red circles) . Cavity radius is calculated using the maximum, except for HANDLEY which used the minimum, of the announced yield range in DOE-NV/209 Rev 16 (USDOE, 2015) and the equation of Pawloski (1999).

Figure 12. Graphical representation of rock property data for borehole UE-20C (about 170 m distance from BENHAM), SCCC, PM, southwest Area 20, NNSS.

3.3 UE-20C, U-20C, ER-20-5-3, and U-20Y near BENHAM and TYBO

XRD data for the UE-20C, U-20C, ER-20-5-3, and U-20Y boreholes (Figures 12, 13, 14, and 15) are relatively sparse but important to characterization of the TYBO and BENHAM sources of radionuclide contamination. The XRD data indicate that the BENHAM and TYBO working points are situated in Zone 3 with one embedded interval in the upper CHZCM5 (and possibly the CHLFA5), having characteristics of Zone 2, with opal present and abundant clinoptilolite (Figures 13 and 15).

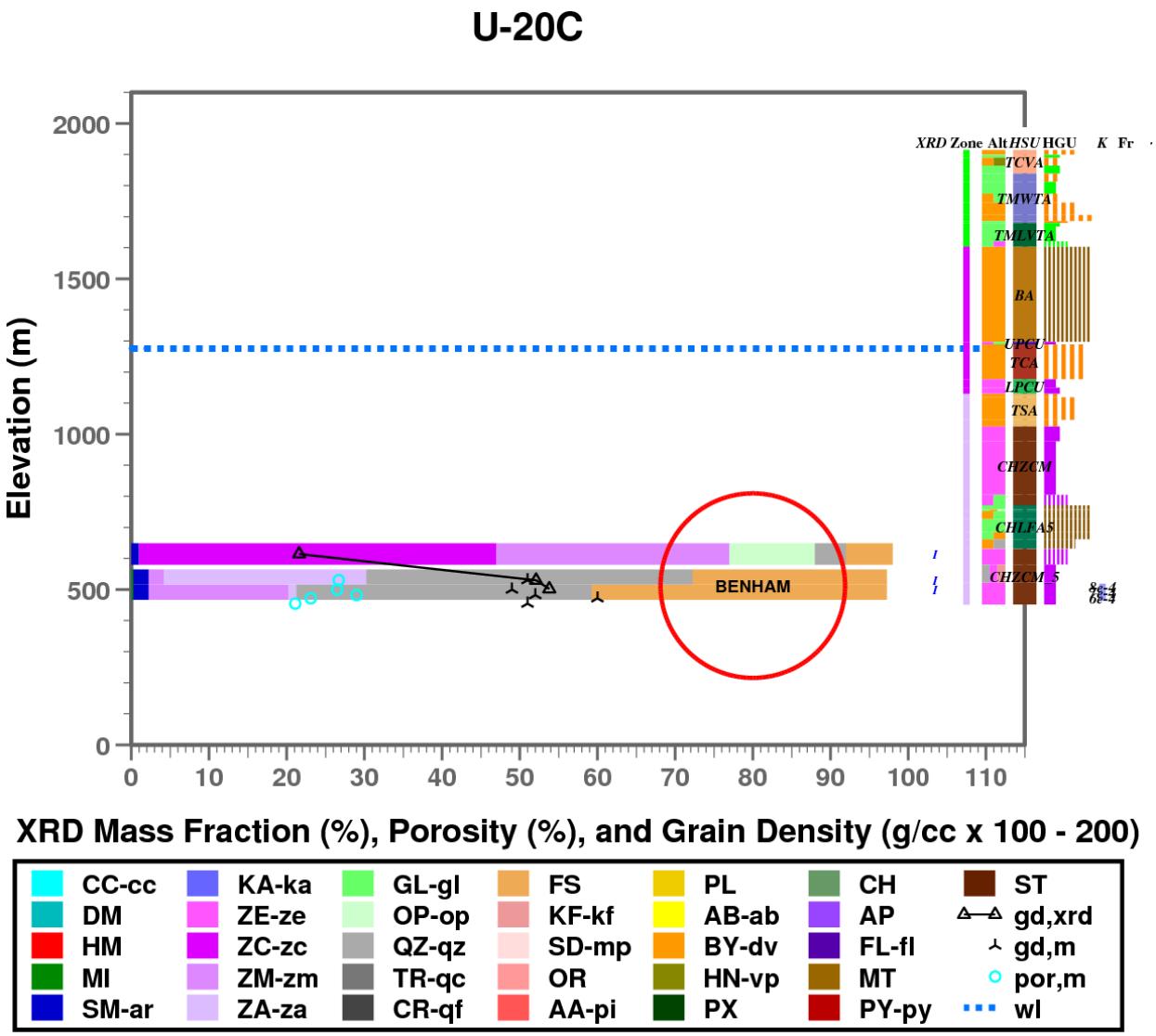

Side view test location outlines are 3.0 cavity radii (3Rc) using calculated cavity radius (green circles) except for tests with specified yields reported in USDOE (2015), for which the measured Rc from Zavarin (2014) is used (red circles) . Cavity radius is calculated using the maximum, except for HANDLEY which used the minimum, of the announced yield range in DOE-NV/209 Rev 16 (USDOE, 2015) and the equation of Pawloski (1999).

Figure 13. Graphical representation of rock property data for borehole U-20C (BENHAM), SCCC, PM, southwest Area 20, NNSS.

At BENHAM, zeolite in the middle and lower portions of the EZ is mordenite and analcime, and zeolite is mostly clinoptilolite within pumiceous lava in the upper EZ (Figures 12 and 13). Zone 3 extends upward through the CHZCM and TSA HSUs, where zeolite is analcime and mordenite with no clinoptilolite, as evident from XRD data at ER-20-5-3 and U-20Y (Figures 14 and 15). Similar to HANDLEY, smectite is present, and mica is less abundant than at FONTINA. Hematite is rarely detected, but likely mostly in lava flows and welded tuffs at <1%. Overall, the mineralogical setting at TYBO and BENHAM is a clear example where elements of Zone 2 are present in the transitional Zone 3 (Section 1.2).

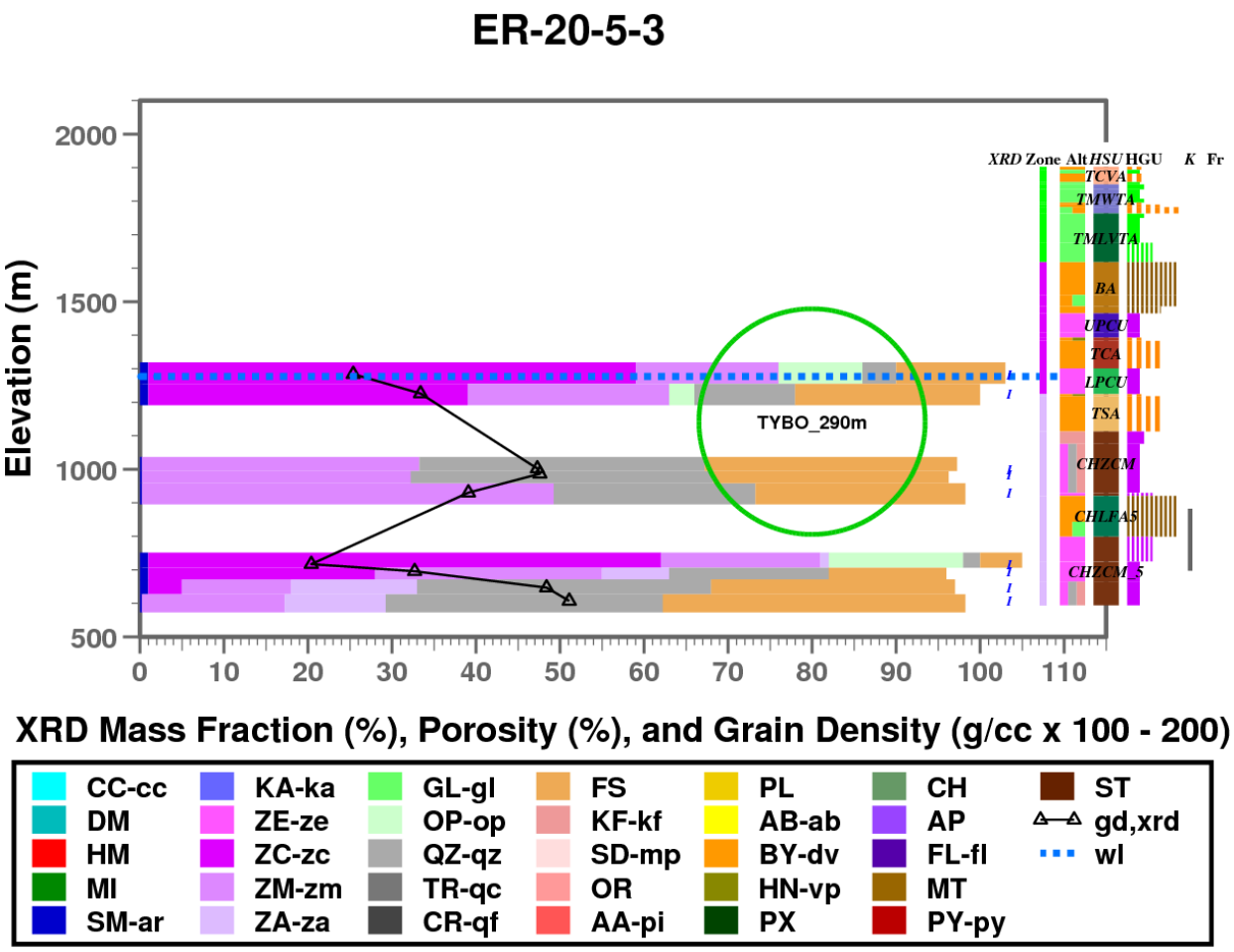

Side view test location outlines are 3.0 cavity radii (3Rc) using calculated cavity radius (green circles) except for tests with specified yields reported in USDOE (2015), for which the measured Rc from Zavarin (2014) is used (red circles) . Cavity radius is calculated using the maximum, except for HANDLEY which used the minimum, of the announced yield range in DOE-NV/209 Rev 16 (USDOE, 2015) and the equation of Pawloski (1999).

Figure 14. Graphical representation of rock property data for borehole ER-20-5-3 (about 290 m distance from TYBO), SCCC, PM, southwest Area 20, NNSS.

The mineralogical setting near radionuclide sources such as TYBO and BENHAM should be integrated with interpretation of colloid-facilitated transport at NNSS (e.g. Kersting et al, 1999; Kersting and Zavarin, 2011; Zavarin et al., 2019). Plutonium isotopes sampled in both the shallow ER-20-5-1 and deep ER-20-5-3 downgradient observation wells were traced to a BEHNAM source despite the closer proximity to a TYBO source (Kersting et al., 1999). Colloids filtered from groundwater samples are predominately mordenite in ER-20-5-1 and unspecified clay (illite/smectite) in ER-20-5-3 (Brachmann and Kersting, 2003). The limited XRD data for UE-20C and U-20C (Figures 12 and 13) indicate an abundance of mordenite and smectite near the BENHAM EZ. Thus, mordenite and smectite would be reasonable minerals to incorporate into assessment of plutonium transport sourced from TYBO and BENHAM.

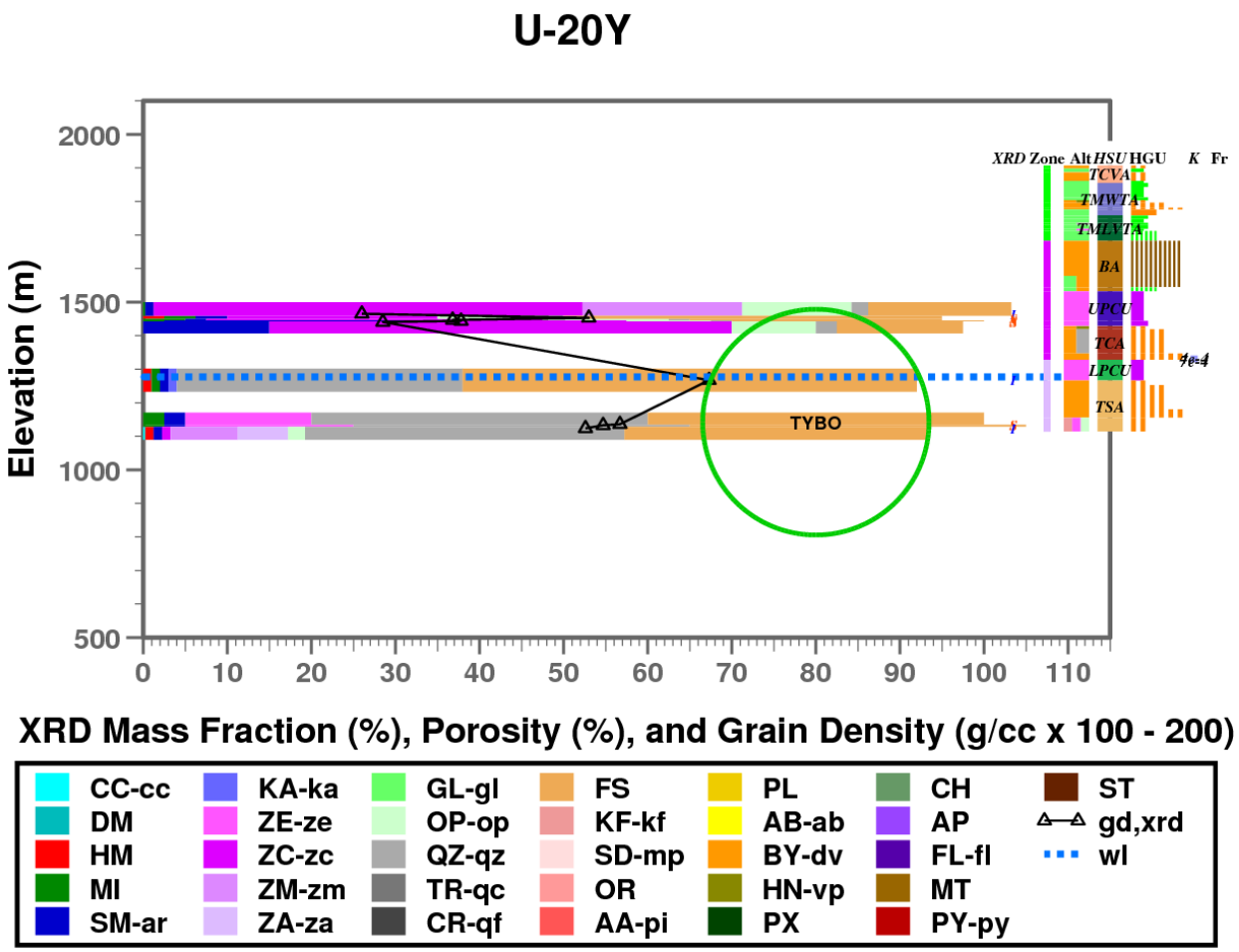

Figure 15. Graphical representation of rock property data for borehole U-20Y (TYBO), SCCC, PM, southwest Area 20, NNSS.

3.4 Boreholes Downgradient of PM Detonations

The newer XRD data collected by F and I methods provide excellent characterization of the mineralogy and diagenetic zones southwest (downgradient) of PM radionuclide contamination sources. These data confirm that the diagenetic zones extend into OV southwest of Areas 19 and 20 of PM. Boreholes ER-20-7, ER-EC-11, ER-EC-6, and ER-EC2A are positioned along a downgradient transect.

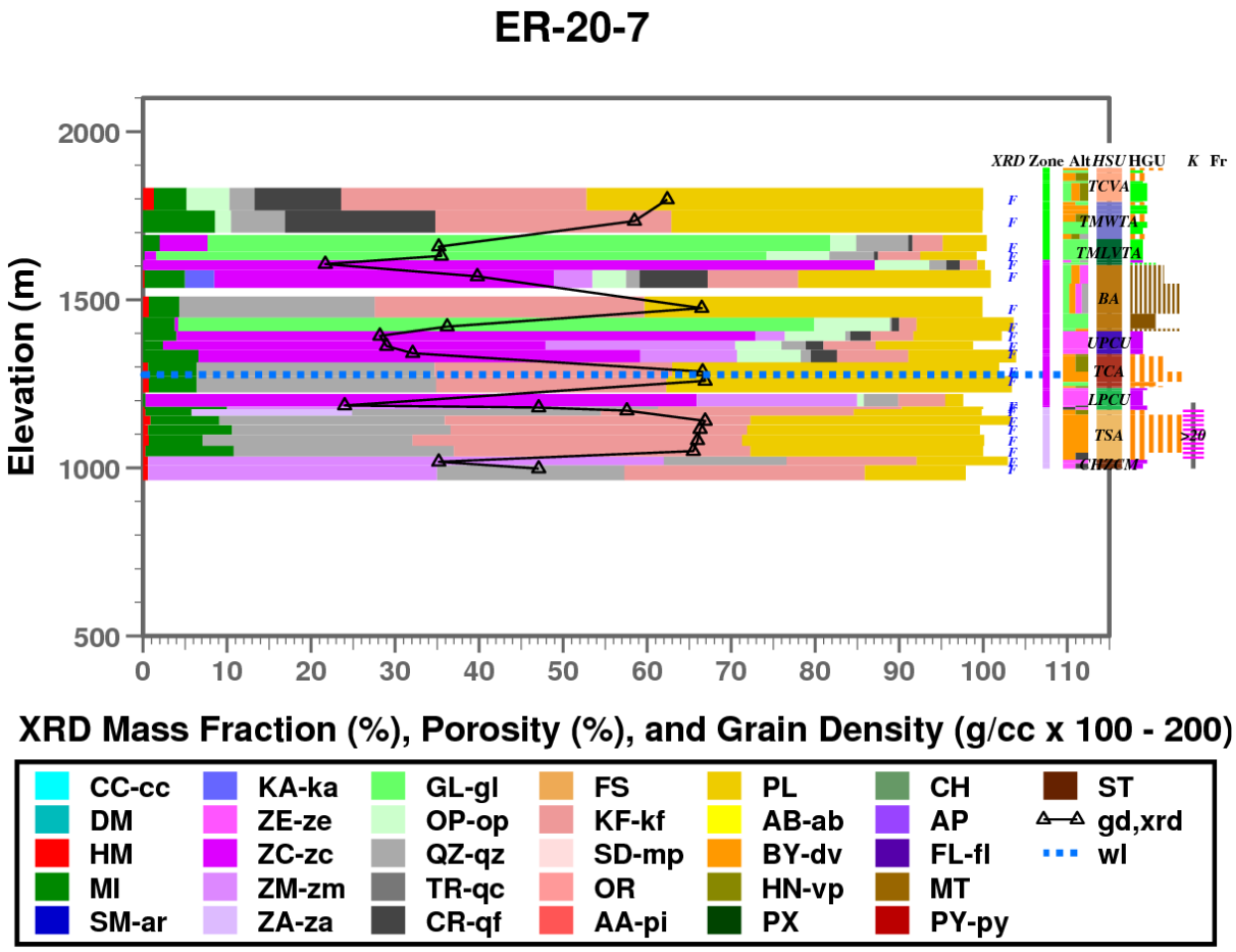

Figure 16. Graphical representation of rock property data for borehole ER-20-7, SCCC, PM, southwest Area 20, NNSS.

At ER-20-7 (Figure 16), Zone 1 terminates at the top of the BA HSU, where clinoptilolite becomes abundant. Zone 2 extends to the top of the TSA HSU, where analcime is present. Zone 3 extends to the base of ER-20-7 in CHZCM HSU, where the zeolite component is mordenite with no clinoptilolite. At ER-20-7, hematite is nearly ubiquitous except in TCUs of Zone 2 having abundant clinoptilolite. Notably hydraulic conductivity is high in the TSA HSU, which is interpreted to be located in Zone 3 by presence of analcime. Hematite regularly occurs where the rocks are lacking in glass or clinoptilolite, a pattern common to other PM boreholes.

Overall, the mineralogical profile at ER-20-7 is consistent with other boreholes near PM detonations except for absence of smectite, which if true, is of direct importance to assessment of radionuclide transport assessment. As will be discussed later in Section 5.2, smectite is lacking in abundance in an area southwest of PM on the Bench and in northwestern TMCC, which is labeled as the "micaceous-kaolinitic area" on Figure 4.

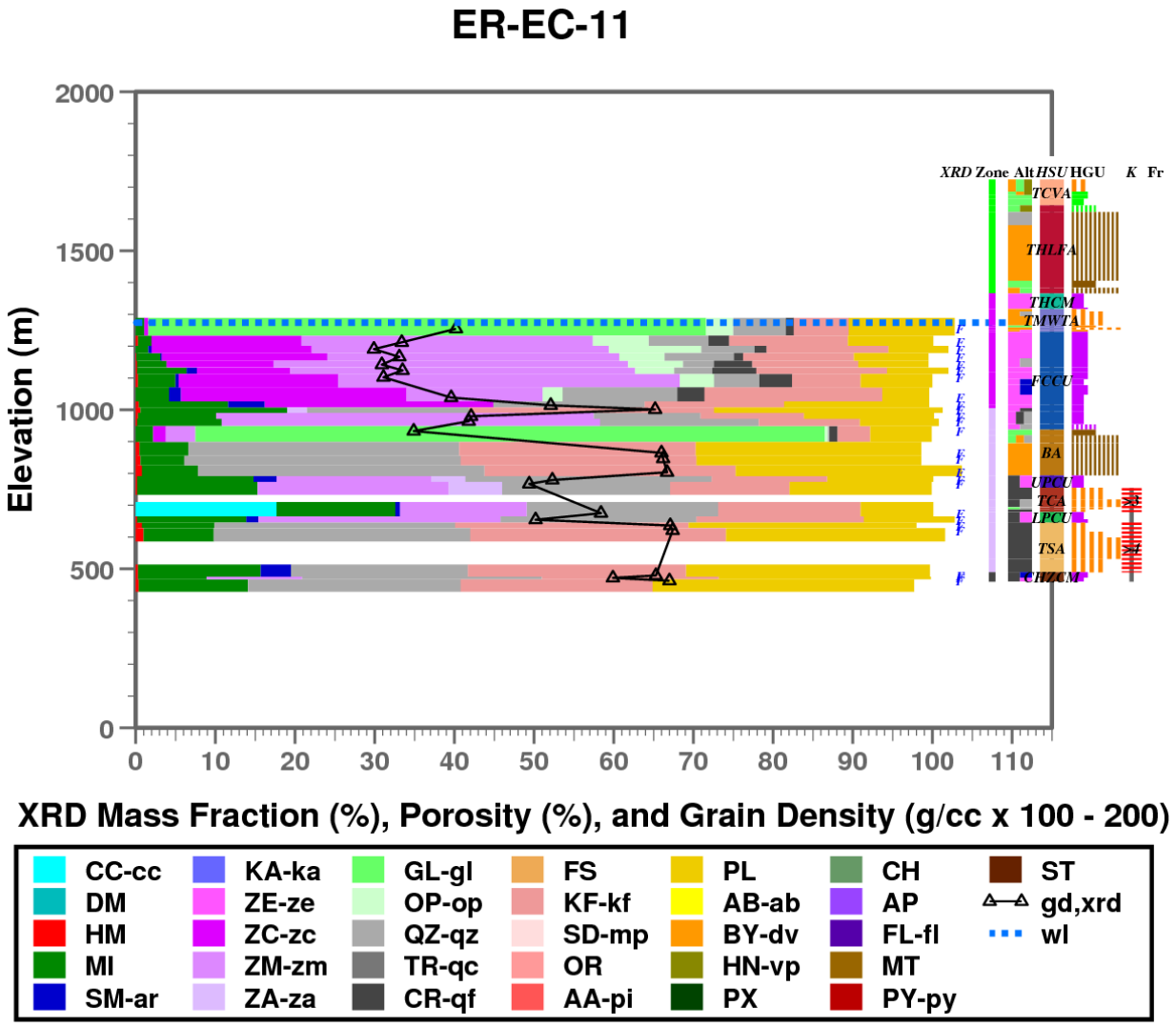

Figure 17. Graphical representation of rock property data for borehole ER-EC-11, the Bench, SCCC, PM.

At ER-EC-11 (Figure 17), the base of Zone 2 is higher stratigraphically than at ER-20-7, 2 km to the northeast. In Zone 3, mordenite and analcime are the prevalent zeolite minerals below 1,000 m elevation toward the base of the FCCU HSU. The top of Zone 4 is interpreted where zeolite appears to be absent in the CHZCM HSU at the base of ER-EC-11. As at ER-20-7, hematite regularly occurs where the rocks are lacking in glass or clinoptilolite. Smectite is relatively sparse at ER-EC-11 compared to Area 20 test locations on PM. Like ER-20-7, ER-EC-11 is interpreted to be within the "micaceous-kaolinitic" area shown on Figure 4 based on the low fraction of smectite. Mica increases in abundance with depth, while smectite occurs sporadically. Thin occurrences of glass within the TMWTA and BA HSUs appear to be associated with vitric tuff, as also evident at ER-20-7. Notably, hydraulic conductivity is high in both the TSA and TCA HSUs, both of which are WTAs.

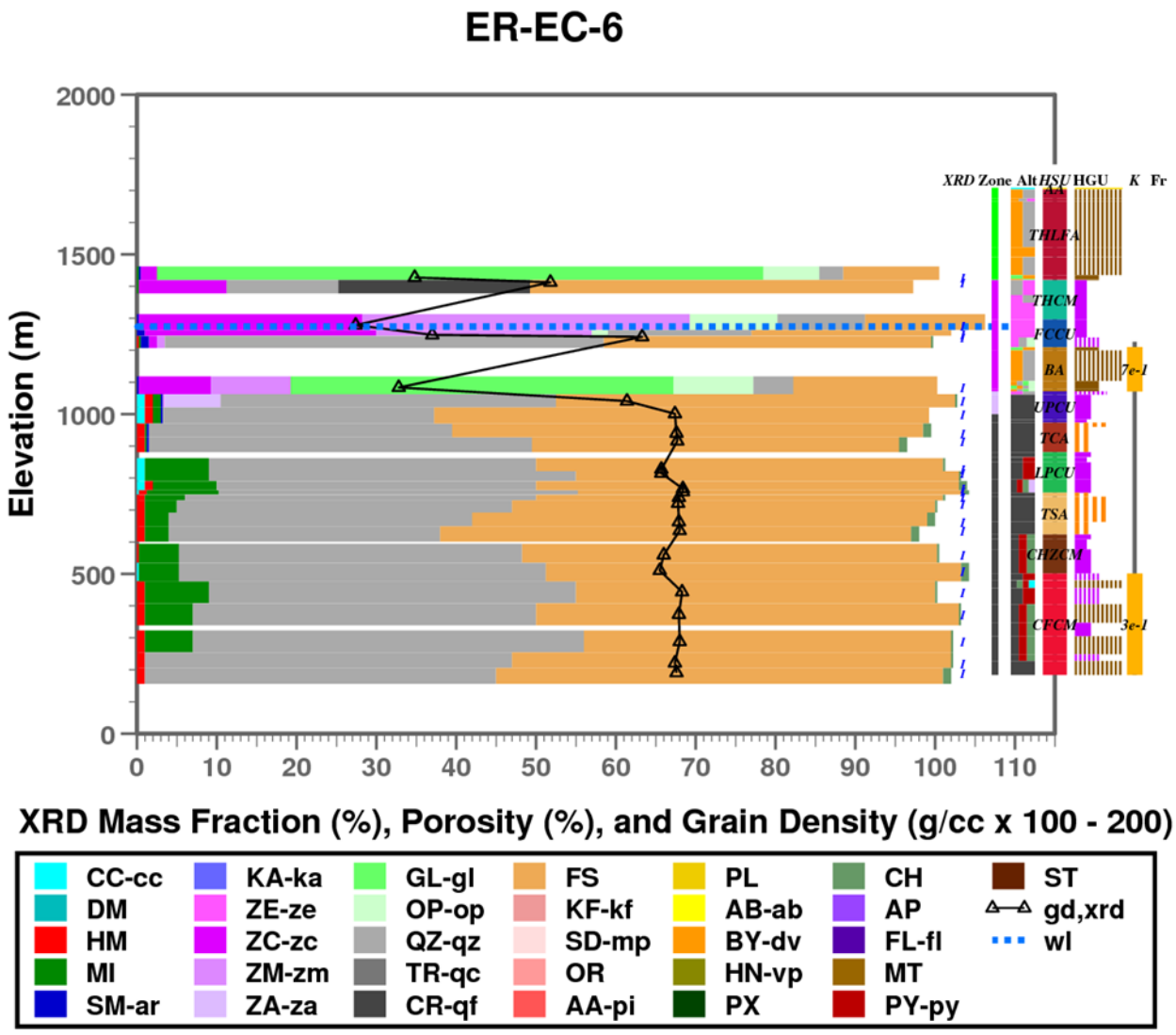

Figure 18. Graphical representation of rock property data for borehole ER-EC-6, the Bench, SCCC, PM.

At ER-EC-6 (Figure 18), one km southwest of ER-EC-11, the presence of Zone 4 is quite pronounced below 1,000 m elevation. Zone 3 is thin, evident by zeolitic transition to mordenite and analcime near the base of the BA HSU and the top of the UPCU. This mineralogic profile is particularly demonstrative of the impact of diagenesis on rock properties. Here, the Calico Hills zeolitic composite unit (CHZCM) is clearly lacking zeolite. Similarly, zeolite is lacking in the UPCU and LPCU in Zones 3 and 4. The UPCU and LPCU would otherwise have abundant clinoptilolite in Zone 2. Another subtle pattern is the lack or reduced abundance of hematite in the TCUs. This is important to assessment of radionuclide transport because hematite is a strong sorber of uranium and plutonium. The apparent low abundance of smectite (as also evident in the upgradient ER-20-7 and ER-EC-11 boreholes) is pertinent to assessment of transport for all sorbing radionuclides. The

XRD data for ER-EC-6 provide another good example of how the diagenetic zones transgress stratigraphic boundaries (Moncure et al., 1981).

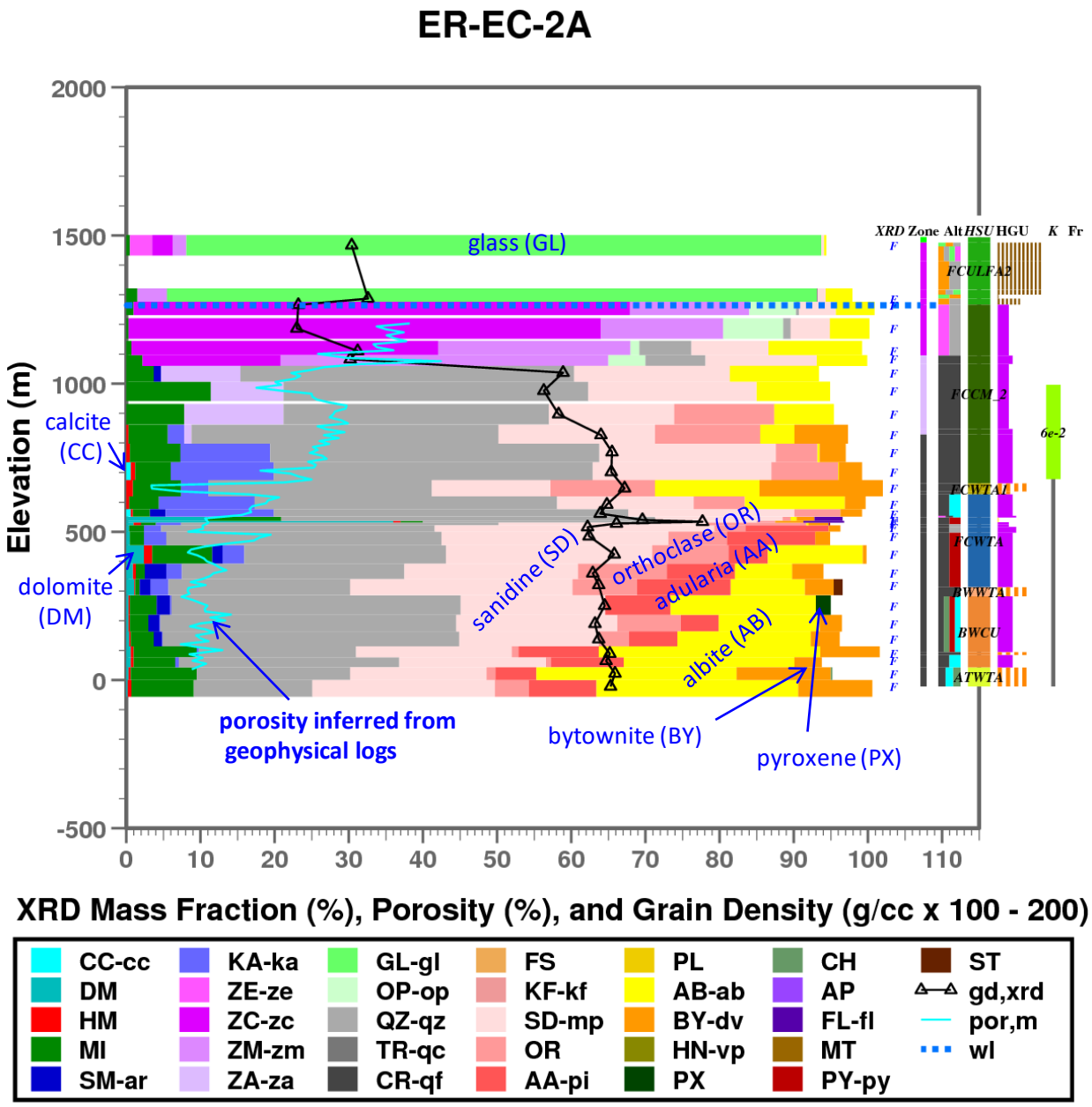

Figure 19. Graphical representation of rock property data for borehole ER-EC-2A, TMCC.

The XRD data at ER-EC-2A (Figure 19), 8 km southwest of ER-EC-6, is the most detailed mineralogical dataset available at PM-OV. Feldspar minerals are differentiated into the K-spar minerals sanidine, orthoclase, and adularia and the plagioclase minerals albite, bytownite, and clinopyroxene. As is the case for all ER-prefix boreholes, rock property measurements from core are lacking.

In Figure 19, porosity is inferred geophysical logs assuming a grain density of 2.4 g/cc as assumed in USDOE (2019). This example illustrates how porosity might be overestimated or underestimated at different depth intervals by assuming a fixed grain density. The XRD profile of mineralogy at ER-EC-2A, within the TMCC about 10 km southwest of the NNSS boundary, clearly exhibits the same zones of zeolite diagenesis as those identified by Moncure et al. (1981) at PM within the SCCC. A major difference is that Zone 4, where zeolite is absent, occurs much higher at about +800 m elevation as compared to about 0 m elevation at UE-20H and -550 m elevation at UE-20F. Possibly the rocks infilling the northwestern TMCC were subjected to more extreme hydrothermal alteration the rock infilling the western SCCC.

Kaolinite, evident between 300 to 800 m elevation at ER-EC-2A, is formed by hydrothermal alteration of feldspar (Deer et al., 1966; Yuan et al. 2014). A relatively low abundance of smectite, particularly in Zones 3 and 4, apparently persists in this northwest area of the TMCC. Similar to at ER-EC-2A, XRD data at boreholes ER-20-4, ER-20-8, ER-EC-12, ER-EC-13, ER-EC-14, and ER-EC-15 (see Appendix) indicate kaolinite is the prevalent clay in Zone 4 of the northwest TMCC (the "micaceous-kaolinitic area" in Figure 4). This is in contrast to Areas 19 and 20 on PM, where kaolinite is apparently rare, and smectite is the prevalent clay in Zone 4, as observed UE-20H. Prevalence of kaolinite or smectite is dependent on the physiochemical conditions of hydrothermal alteration (Simeone et al., 2005), which appears to be divided across the Bench and the boundary between the SCCC and the northwest TMCC.

3.5 Rock Chemistry of SCCC and TMCC

Some of the larger-scale differences in mineralogy can be attributed the source rock chemistry of the volcanic rocks. Rock chemistry of the SCCC is peralkaline (Sawyer and Sargent, 1989), whereas rock chemistry of the TMCC is calc-alkaline (Broxton et al., 1989). In Figure 20, rock chemistry of the SCCC and TMCC is shown to be distinct in an alkaline-iron-magnesium (AFM) ternary diagram using relative mass fractions of Na_2O+K_2O, total FeO, and MgO, as commonly applied to categorization of volcanic rocks (Kuno, 1968). Besides high silica content, the rhyolitic character of the SCCC and TMCC rocks is evident in the AFM diagram by the high mass fraction of Na_2O+K_2O (alkalies) as compared to dacite, andesite, or basalt (Sen, 2014). The relatively high FeO/MgO ratio of SCCC rocks is characteristic of peralkaline rhyolite. Obviously, such fundamental differences in rock chemistry would contribute to differences in the mineralogy across the two caldera complexes. Rock chemistry is relevant to radionuclide transport at PM-OV because, for example, the higher total FeO mass proportion in rocks sourced from the SCCC would favor greater retardation of plutonium and uranium transport as compared to rocks sourced from the TMCC.

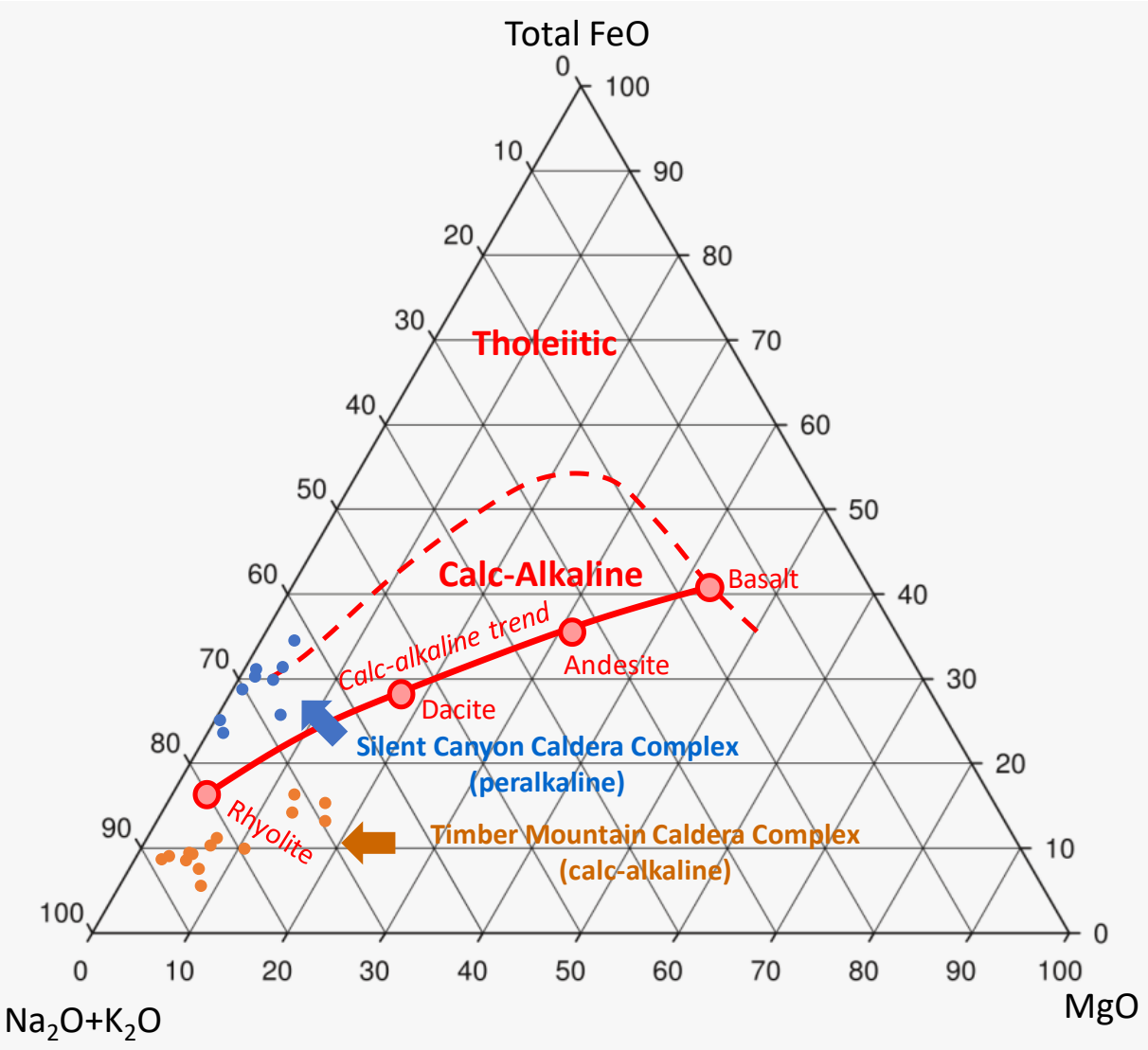

Figure 20. Ternary diagram for relative mass fractions of Na_2O+K_2O, FeO, and MgO components (scaled in percent).

3.6 Addressing Data Scarcity and Quality

The highest quality and most vertically abundant XRD data were obtained primarily from newer boreholes mostly situated along downgradient flow paths. Older XRD data obtained primarily for Area 19 and 20 test site characterization tend to be scarce and irregularly sampled outside of the test location. Although XRD data for Area 19 tests are generally obtained from lower quality subjective (S) methods, these data are useful to interpretation of the diagenetic zones (see Appendix for graphical representation of data). Of direct relevance to assessment of groundwater flow and radionuclide transport, many Area 19 tests were situated at similar elevation near the water table but in three different diagenetic zones. Examples are AMARILLO and CHANCELLOR in Zone 1 (Figure A.12), TOWANDA and BACKBEACH in Zone 2 (Figures A.14 and A.17), and FONDUTTA in Zone 3

(Figure A.4). Diagenetic zonation could partly explain why concentration of plutonium in groundwater is much higher at the relatively shallow CHANCELLOR detonation located in Zone 1 as compared to six deeper detonations located in Zones 2 and 3. Overall, the framework of diagenetic zones is helpful to extension of interpretation of rock properties from areas with abundant high-quality data to areas with scarce low-quality data.

4 Hydrostratigraphic Sections Showing Diagenetic Zones

As derived from the hydrostratigraphic framework model (HFM) for PM (USDOE, 2020), the USGS has produced some excellent hydrostratigraphic sections along flow paths through or nearby the underground nuclear detonations at PM-OV (Jackson et al., 2020). Using the methods for interpretation of rock property databases discussed previously, the following presents 2-D interpretations of the diagenetic zones along segments of the USGS sections (Figure 21). An effort is made here to interpret the structure of the diagenetic zonation throughout the areas of the underground nuclear testing at PM.

At locations of the detonations shown in Figure 22 to 28, side view outlines are 3.0 cavity radii (3Rc) using calculated cavity radius except for tests with specified yields reported in USDOE (2015), for which the measured Rc from Zavarin (2014) is used. Cavity radius is calculated using the maximum, except for HANDLEY which used the minimum, of the announced yield range in DOE-NV/209 Rev 16 (USDOE, 2015) and the equation of Pawloski (1999).

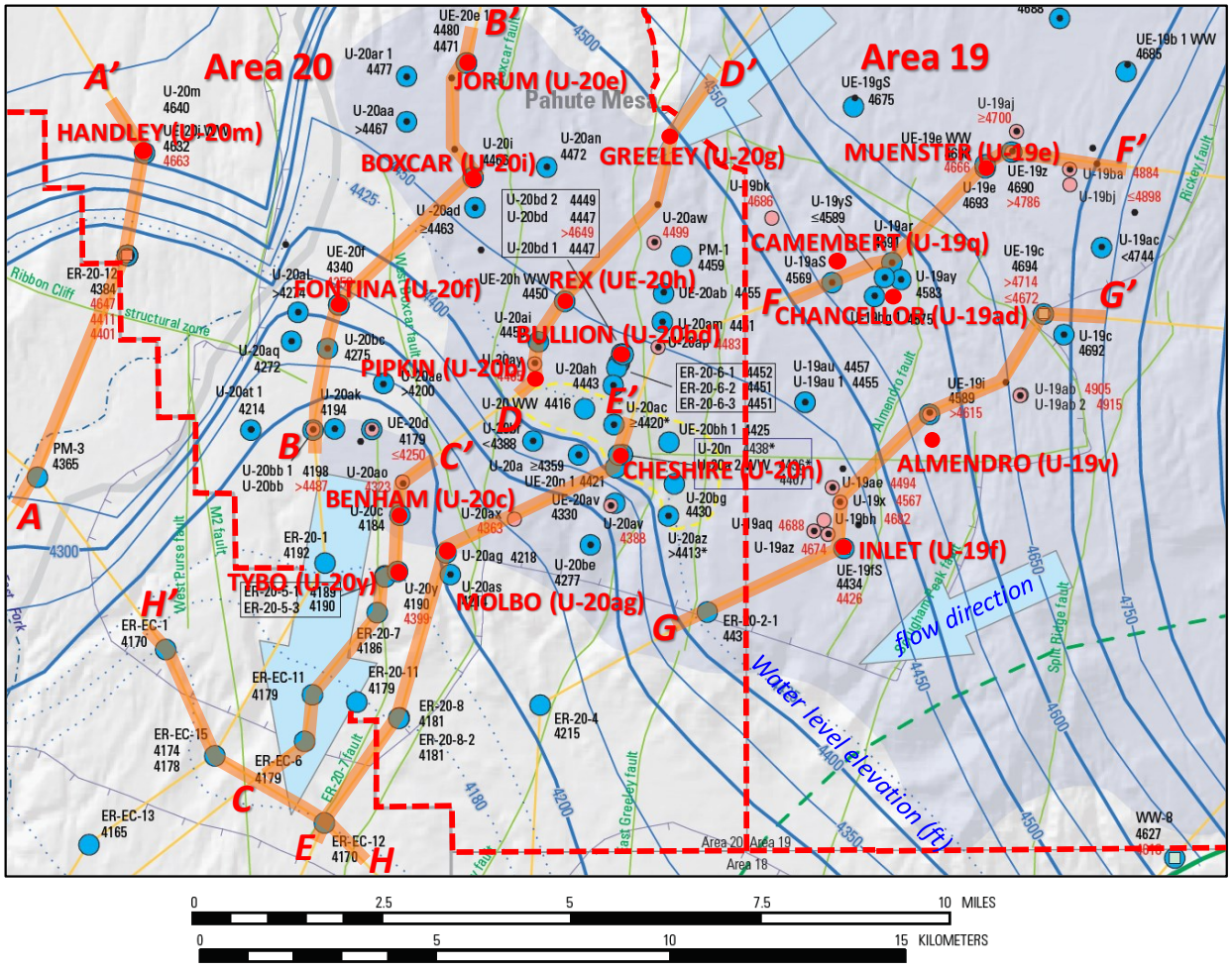

Figure 21. Map showing location of segments (AA', BB', CC', etc.) where diagenetic zones are interpreted along USGS hydrostratigraphic sections and selected PM detonations. Modified from Plate 1 of Jackson et al. (2020).

4.1 HANDLEY

XRD and other rock properties data are available for boreholes UE-20J, U-20M, ER-20-12, and PM-3, which are aligned along likely downgradient pathway from the HANDLEY detonation (Figure 22). The top of Zone 2 is located at the base of the TMLVTA HSU, consistent with the boundary between vitric and zeolitic rocks at NNSS. The tops of Zone 3 and Zone 4 transgress multiple stratigraphic units within the PBRCM HSU. At PM-3, the top of Zone 3 is inferred to be in the CHZCM by presence of secondary calcite (Smith et al, 1999). At ER-20-12, the top of Zone 3 is interpreted by presence of analcime.

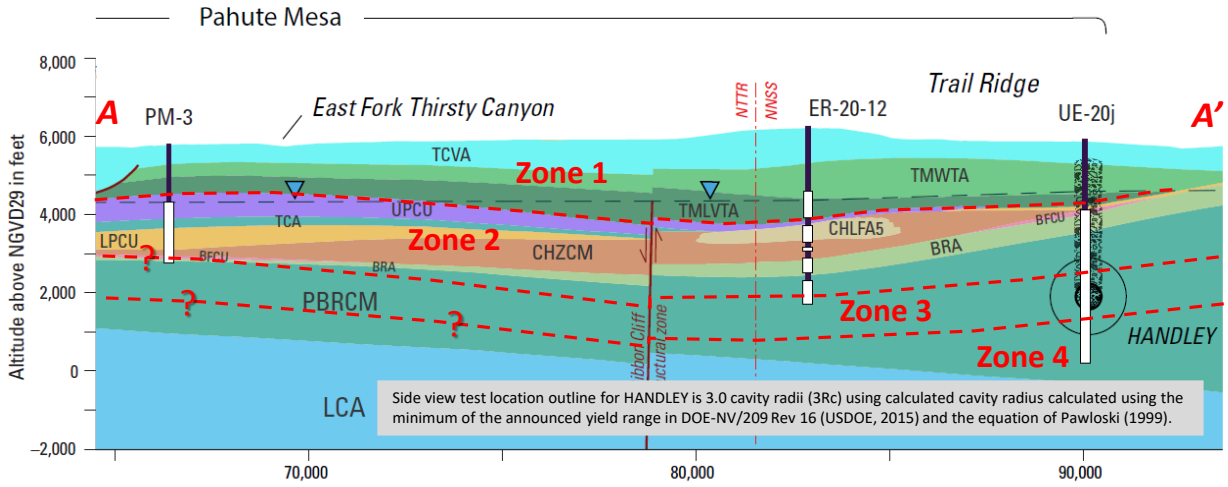

Figure 22. Section AA' through HANDLEY detonation showing HSUs and interpretations of diagenetic zones. Modified from Plate 2 of Jackson et al. (2020).

4.2 FONTINA

XRD and rock properties data are available for boreholes U-20BB, U-20BC, UE-20F, U-20F, U-20AJ, and UE-20E, which are aligned along a likely flow path through the FONTINA detonation (Figure 23). The top of Zone 2 is consistently located by the base of the TMLVTA. The top of Zone 3 appears to occur near the base of the CHLFA5. The top of Zone 4 transgresses stratigraphic units within either the BFCU or BRA. From this interpretation, it is evident that the deeper detonations of FONTINA, BOXCAR, and JORUM are situated in similar mineralogical regimes near the Zone 2/Zone 3 transition.

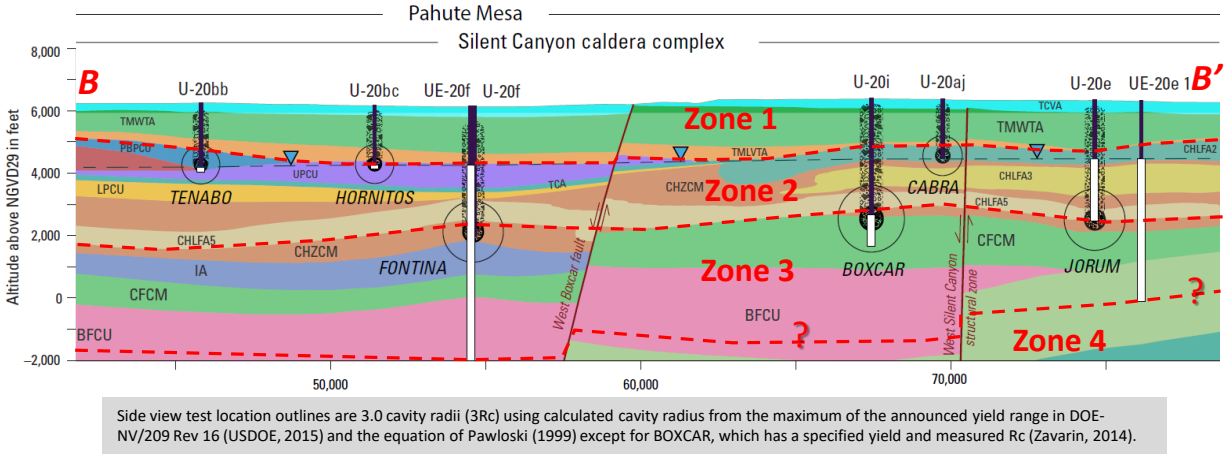

Figure 23. Section BB' through FONTINA detonation showing HSUs and interpretations of diagenetic zones. Modified from Plate 2 of Jackson et al. (2020).

4.3 TYBO and BENHAM

XRD and some rock properties data are available for boreholes ER-EC-6, ER-EC-11, ER-20-7, ER-20-5-3, U-20Y, U-20C, UE-20C, and UE-20ao, which are aligned along a likely flow path through the TYBO and BENHAM detonations (Figure 24). The top of Zone 2 is consistently located by the base of the THLFA and TMLVTA. The top of Zone 3 tends to transgress hydrostratigraphic boundaries. Data for Zone 4 is limited to ER-EC-6 and ER-EC-11, where Zone 4 is highest in elevation, particularly at "The Bench." Along this profile of Area 20, the top of Zone 4 likely deepens to the north.

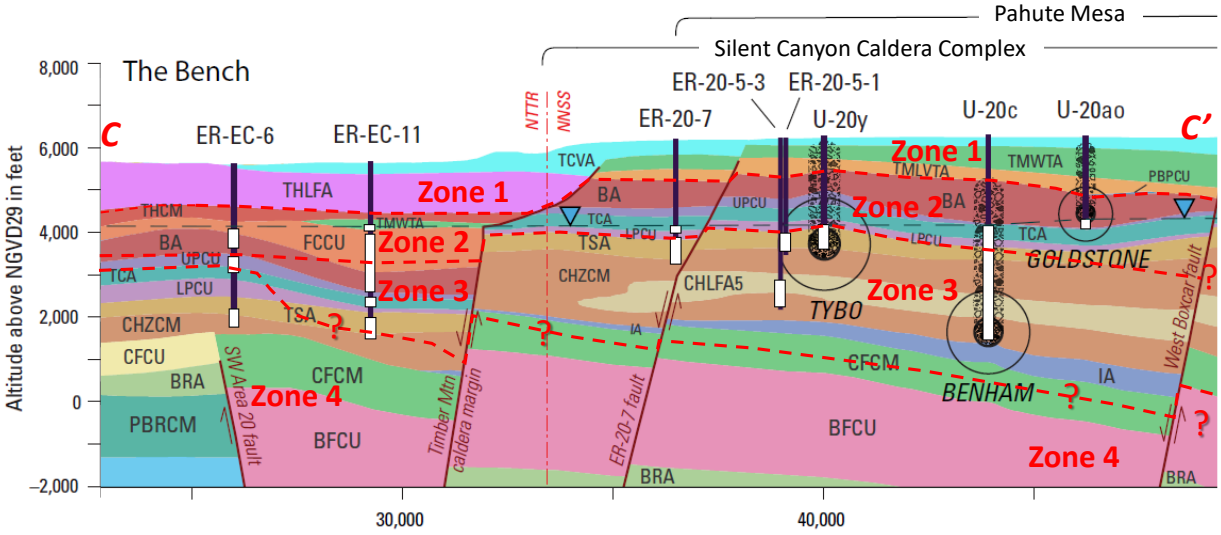

Side view test location outlines are 3.0 cavity radii (3Rc) using calculated cavity radius from the maximum of the announced yield range in DOE-NV/209 Rev 16 (USDOE, 2015) and the equation of Pawloski (1999) except for BENHAM, which has a specified yield and measured Rc (Zavarin, 2014).

Figure 24. Section CC' through FONTINA detonation showing HSUs and interpretations of diagenetic zones. Modified from Plate 2 of Jackson et al. (2020).

4.4 PIPKIN, KASSERI, and GREELEY

XRD and rock properties data are available for boreholes U-20AI and UE-20H, which are aligned along a likely flow path through the PIPKIN, KASSERI, and GREELEY detonations (Figure 25). The top of Zone 2 is consistently located by the base of the TMLVTA, PLFA, and CHVTA. The top of Zone 3 transgresses Calico Hills units near UE-20H and occurs at the top of the BFCU near U-20Z and U-20G. Along this profile of Area 20, the top of Zone 4 likely transgresses stratigraphic units within the CFCU, BFCU, and BRA.

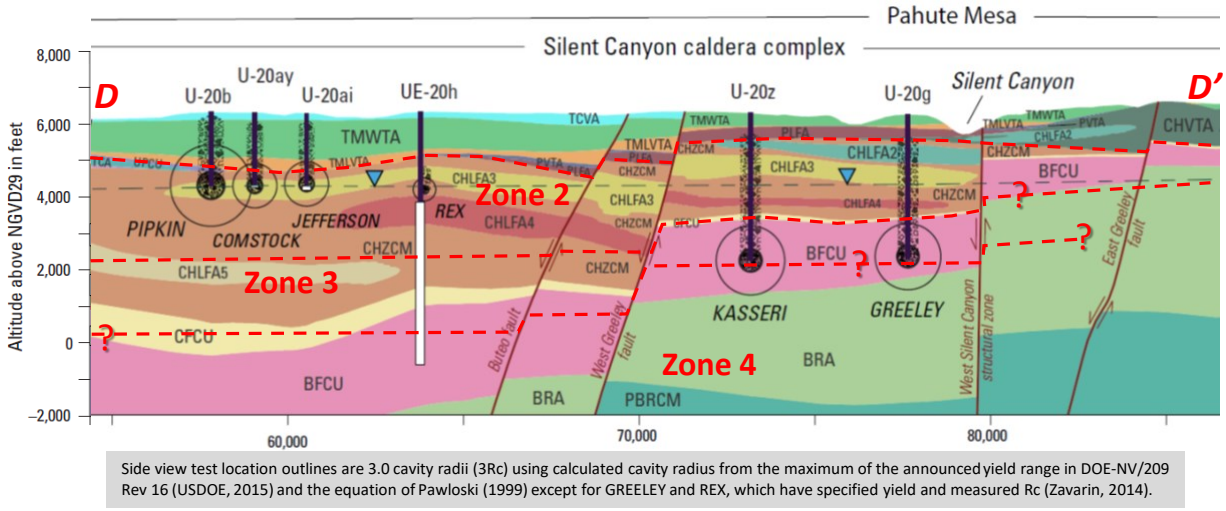

Side view test location outlines are 3.0 cavity radii (3Rc) using calculated cavity radius from the maximum of the announced yield range in DOE-NV/209 Rev 16 (USDOE, 2015) and the equation of Pawloski (1999) except for GREELEY and REX, which have specified yield and measured Rc (Zavarin, 2014).

Figure 25. Section DD' through PIPKIN detonation showing HSUs and interpretations of diagenetic zones. Modified from Plate 2 of Jackson et al. (2020).

4.5 CHESHIRE and MOLBO

XRD and some rock properties data are available for boreholes ER-EC-12, ER-20-8, U-20AG, U-20AX and U-20A2WW, which are aligned along a likely flow path downgradient from the MOLBO and CHESHIRE detonations (Figure 26). The top of Zone 2 is consistently located by the base of the TMLVTA and WWA HSUs, except at "The Bench," where the top of Zone 2 transgresses the THLFA HSU. Along this profile through Area 20, the tops of Zone 3 and Zone 4 tend to transgress hydrostratigraphic boundaries and deepen toward the north. Toward the southwest at the Bench, the top of Zone 3 rises to near the water table at ER-EC-12.

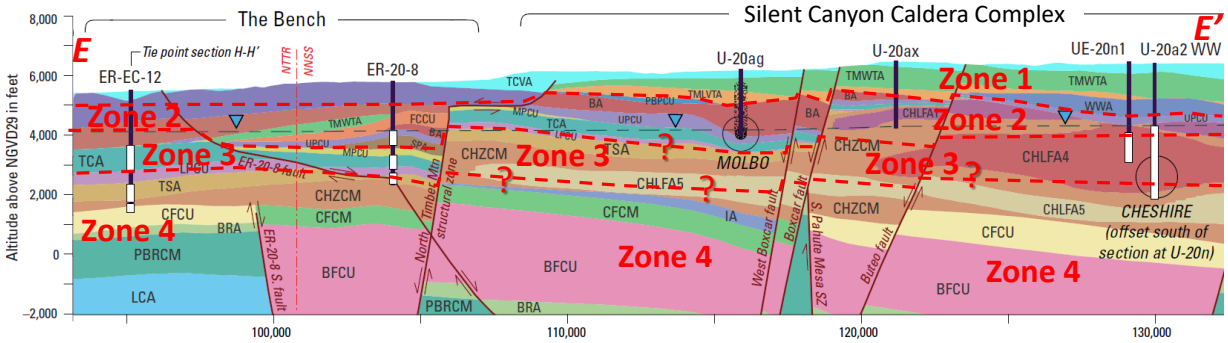

Side view test location outlines are 3.0 cavity radii (3Rc) using calculated cavity radius from the maximum of the announced yield range in DOE-NV/209 Rev 16 (USDOE, 2015) and the equation of Pawloski (1999).

Figure 26. Section EE' through CHESHIRE detonation showing HSUs and interpretations of diagenetic zones. Modified from Plate 2 of Jackson et al. (2020).

4.6 Area 19

XRD data are relatively sparse and of poorer quality in Area 19, making evaluation of local rock properties more challenging. It is nonetheless useful to interpret the available XRD

and rock property data from Area 19 to map out the diagenetic zones. The zonal framework justifies transfer of physical or chemical properties (i.e. K_d coefficients) from areas of PM-OV with more abundant and high-quality XRD data. Regional-scale radionuclide transport assessment will involve abstraction of source term model parameters derived from locations with more abundant characterization data, such as near CHESHIRE, HANDLEY, and TYBO/BENHAM in Area 20, to areas with sparse characterization and radionuclide data as typical in Area 19.

XRD and some rock properties data are available for boreholes U-19AR, UE-19E, UE-19Z, and U-19AX, which are aligned along a profile in Area 19 through the CYBAR, MUENSTER, FONDUTTA, and KEARSARGE detonations (Figure 27). Along this profile, the top of Zone 2 occurs at the base of the CHVTA. The top of Zone 3 transgresses the BFCU and BRA, with an apparent step-up between MUENSTER to FONDUTTA. This step-up in the top of Zone 3 remains questionable because of poor quality of the XRD data. However, hydrothermal upflow could produce such an upward step in alteration. The location of the top of Zone 4 is uncertain but can be reasonably expected at occur near an elevation of zero.

The CHANCELLOR (U-19AD) detonation near U-19AR (CYBAR) is of particular interest to radionuclide transport, having the highest plutonium and gross alpha radioactivity observed at Pahute Mesa (Navarro, 2013). At CHANCELLOR and CYBAR, the water table is well above the base of Zone 1, and the 3Rc EZ is within the vitric Zone 1. These relatively shallow detonations are situated in vastly different mineralogy compared to most PM detonations located in Zones 2 and 3. Radionuclide transport assessment at PM should consider that local site conditions including saturation, porosity, and mineralogy could lead to large differences in radionuclide concentrations at different PM detonations.

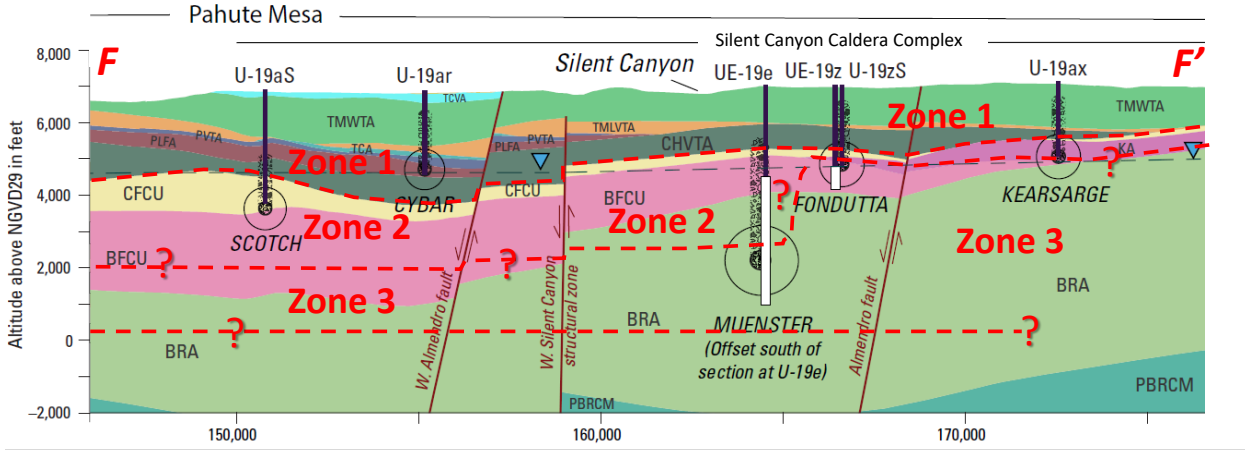

Side view test location outlines are 3.0 cavity radii (3Rc) using calculated cavity radius from the maximum of the announced yield range in DOE-NV/209 Rev 16 (USDOE, 2015) and the equation of Pawloski (1999) except for SCOTCH and CYBAR, which have specified yield and measured Rc (Zavarin, 2014).

Figure 27. Section FF' through Area 19 detonations SCOTCH, CYBAR, MUENSTER, FONDUTTA, and KEARSARGE showing HSUs and interpretations of diagenetic zones. Modified from Plate 2 of Jackson et al. (2020).

XRD and some rock properties data are available for boreholes ER-20-2-1, UE-19FS, U-19X, and UE-19I along a profile through the INLET, BACKBEACH, SLED, and POOL detonations of Area 19 (Figure 28). Here the top of Zone 2 corresponds to the base of either the PLFA or CHVTA. The top of Zone 3 is near the top of the IA at the INLET and BACKBEACH detonations. Toward the north, the top of Zone 3 transgresses through the BFCU and BRA. The top of Zone 4 appears to be near the top of the CFCU toward the south and within the BRA toward the north.

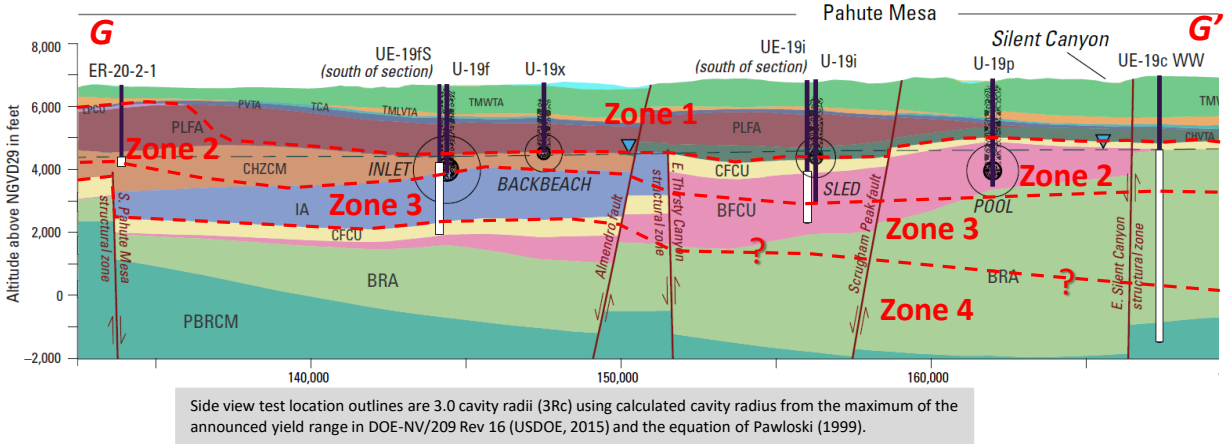

Figure 28. Section GG' through Area 19 detonations INLET, BACKBEACH, SLED, and POOL showing HSUs and interpretations of diagenetic zones. Modified from Plate 2 of Jackson et al. (2020).

4.7 The Bench

XRD data are available for boreholes ER-EC-12, ER-EC-15, and ER-EC-1, which are aligned along the Bench southwest of PM in an area between the margins of the TMCC and SCCC (Figures 4 and 29). The Bench area is of particular interest to radionuclide transport assessment because flow paths downgradient of PM radionuclide contamination sources focus into thin but high-permeability welded tuff and lava flow aquifers within the Bench (Fenelon et al., 2016). Section HH' is roughly perpendicular to these flow paths. The tops of Zones 2 and 4 appear to be higher across than Bench compared to at PM. Toward PM, the top of Zone 2 is below the THLFA. Toward the Bench, the top of Zone 2 transgresses through the THLFA and most of the TCVA. Toward PM, the top of Zone 3 is the top of the UPCU, and toward the Bench, the top of Zone 3 transgresses upward across several HSUs to the southwest. Within the Bench, the top of Zone 4 appears to correspond with the top of the LPCU. Toward PM, the top of Zone 4 is uncertain but may be near the top of the BFCU. Toward PM, Zone 3 appears to be as much as 1,000 m thicker and, correspondingly, the top of Zone 4 is as much as 1,000 m lower in elevation. The boundaries of the diagenetic zones appear to be more variable along the caldera margins, likely influenced by combined effects of hydrothermal convection and caldera collapse.

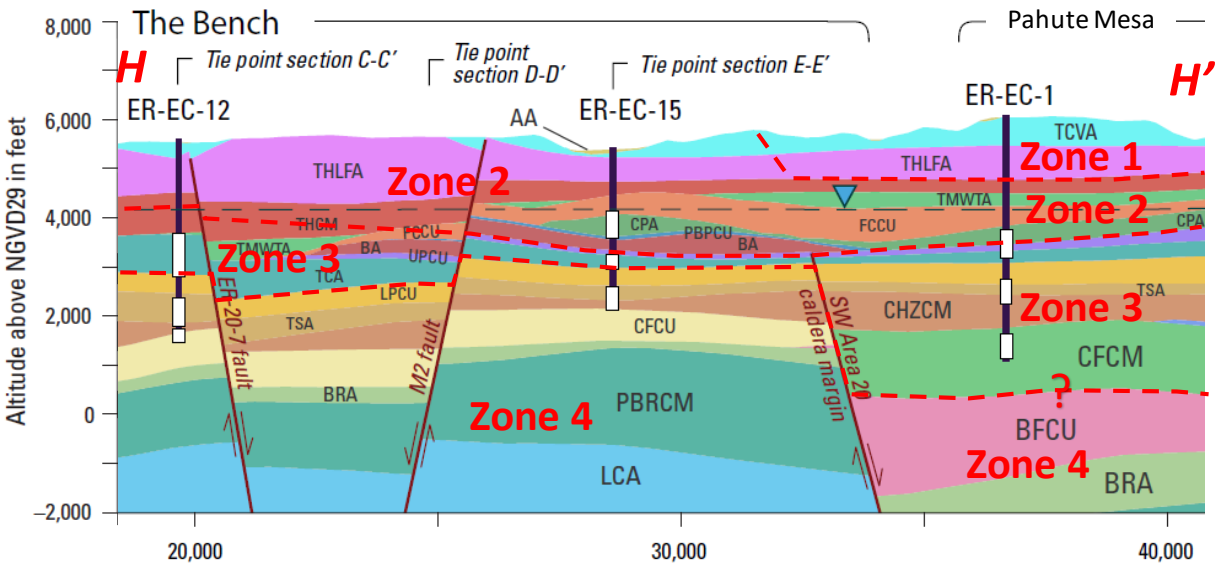

Figure 29. Section HH' through "The Bench" southwest of Pahute Mesa showing HSUs and interpretations of diagenetic zones. Modified from Plate 2 of Jackson et al. (2020).

5 Discussion

"*Probably nowhere else the world as so much effort been invested in the study of a volcanic field.*" (Byers et al., 1989)

This quote refers to the southwestern Nevada volcanic field including the SCCC, TMCC, and PM-OV groundwater basin – over thirty years ago. Subsequently, a large quantity of high-quality XRD data have been collected at PM-OV. However, in some areas of PM-OV such as Area 19 at NNSS, the mineralogical data needed for characterization of sorption and other rock properties for assessment of radionuclide transport are relatively sparse or of low quality. At PM-OV there remains a need for a framework of understanding for how rock properties are affected by mineralogical diagenesis.

5.1 Diagenetic Zones and Hydrothermal Alteration

This work builds on the interpretation of diagenetic zones by Moncure et al. (1981) at PM and Broxton et al. (1989) at YM to establish categories of volcanic rock at PM-OV that have undergone different stages of diagenesis (physical and chemical change) leading to distinct mineralogical characteristics and rock properties. Integrated graphical presentation of extensive XRD data and rock property databases for PM-OV facilitates identification of four diagenetic zones – vitric, zeolitic, transitional, and quartzofeldspathic – that are consistently present at variable vertical and stratigraphic position with the volcanic rocks for the PM-OV groundwater basin. The boundaries of the diagenetic zones transgress stratigraphic boundaries (Hoover 1968; Moncure et al., 1981) and, therefore, transgress lithologies, HGUs, and HSUs.

The diagenetic zones are related to paleo-temperature regimes during hydrothermal alteration. Clinoptilolite forms by hydration and dissolution of glass under saturated or near-saturated conditions (Moncure et al., 1981; Broxton et al., 1987). In studies of YM rhyolitic tuff by Bish and Aronson (1993), clinoptilolite becomes unstable at 100°C, mordenite was not a major phase above 130°C, analcime transformed to albite (a feldspar) above 175-200°C, and illite (a mica) dominates smectite/illite interlayers at or above 275°C. Assuming similar paleowater chemistry conditions for YM and PM-OV, the base of the zeolitic zone (Zone 2) represents paleo-temperatures of about 100 to 130 °C, and the base of the transitional zone (Zone 3) represents paleo-temperatures of about 175-200°C. Based on mineralogical conditions in some portions of the quartzofeldspathic zone (Zone 4), paleo-temperatures of at least 275°C likely existed in the deepest 1750 m of UE-20F and within the kaolinitic-micaceous area near the Bench and the northwest portion of the TMCC (Figure 4), which is further discussed in Section 5.4. Hydrothermal kaolinite may form in rhyolite within a paleo-temperature range of 270 °C to 350 °C (Yuan et al., 2014). Additional study of mineralogical and geochemical conditions would be needed to constrain further interpretation of past hydrothermal conditions to the PM testing areas and downgradient flow paths. Nonetheless, the available XRD data show clear evidence of much higher temperature hydrothermal alteration at PM compared to other NNSS testing areas.

The diagenetic zones provide a consistent framework for addressing large-scale spatial variation in rock properties – both physical and chemical – as relevant to assessment of radionuclide transport at PM-OV. High-quality XRD data with resolution of 1% or less mineral mass fraction has enabled detection of the important radionuclide-sorbing or "reactive" minerals calcite, clinoptilolite, hematite, mica, smectite, and zeolite and their patterns of occurrence within and between the different diagenetic zones. For example, clinoptilolite, the prevalent zeolite mineral at many PM detonation locations near the water table, is largely if not completely replaced by other zeolite minerals (mordenite or analcime) or quartz and feldspar near the locations of deeper detonations such as HANDLEY, BENHAM, and TYBO. Some portions of a "zeolitic" HSU (e.g. CHZCM) can be devoid of zeolite as a result of hydrothermal alteration. The subsurface distribution of zeolite mineralogy is particularly important to assessment of cesium and strontium transport.

5.2 Distribution of Reactive Minerals

While zeolite minerals largely distinguish the four diagenetic zones, spatial characterization of calcite, hematite, mica, and smectite is also necessary to radionuclide transport assessment (Zavarin and Bruton 1999, 2004a,b; Pawloski et al., 2001; Zavarin et al., 2004, 2005, 2007). Because of high reactivity, mass fractions on the order of 1% or less of hematite and calcite could play a leading role in sorption of plutonium and uranium. Occurrence of hematite, the strongest sorber of plutonium, largely depends on parent rock and lithology, with greater abundance in welded tuffs and lava flows and lesser abundance in bedded or ash-fall tuffs. Rock chemistry including iron oxide mass fraction is also known

to vary for different groups of rhyolitic lavas and stratigraphic units at Pahute Mesa and between the SCCC and TMCC (Sargent et al., 1969; Broxton et al., 1989; Sawyer and Sargent, 1989). Source rock chemistry, HSU, HGU, lithology, and diagenesis all play a role in the spatial distribution of hematite.

Calcite, the strongest sorber of plutonium by mass fraction, is more abundant in the deeper diagenetic Zones 3 and 4 as a result of secondary mineralization. The diagenetic zones are a reasonable framework for addressing large-scale spatial variability of calcite abundance.

Mica group minerals including biotite and illite are relatively ubiquitous and appear to increase in abundance with depth in XRD measurements. Biotite abundance varies with stratigraphic unit, with a tendency to increase in abundance with depth (or age) within a stratigraphic unit in the TMCC (Broxton et al., 1989). In the deeper Zones 3 and 4, the apparent abundance of mica minerals derived from XRD is partly attributable to increasing illite content within mixed-layer smectite-illite and hydrothermal alteration of smectite to illite (Bish and Aronson, 1993; Bauluz et al., 2002). Large-scale spatial variability of mica can be reasonably characterized by HSU and diagenetic zone. Characterization of mica abundance is important to radionuclide transport because, in addition to zeolite, mica will further retard cesium and strontium transport.

Characterization of the spatial variability of smectite is not straightforward. Smectite can be quite ubiquitous, spotty, or absent according to the XRD data. Smectite, which sorbs cesium, strontium, plutonium, and uranium, appears to be more consistently present on PM, but sparse or absent across an of the area of the extreme southern SCCC, across the Bench, and into the northwestern TMCC. Smectite appears to be more abundant in unsaturated intervals of Zone 1 in Area 19 (e.g. U-19AF, U-19AE, U-19AR, UE-19T, UE-19X; see Section A.1) and near the caldera margins (e.g. U19AK, UE-18T; see Sections A.1 and A.6). Some of the apparent variability in smectite abundance from XRD data may be attributable to difficulty in resolving mixed-layer smectite and illite known to occur in Zones 3 and 4 at PM (Moncure et al., 1981) and YM (Bish and Aronson, 1993).

5.3 Geometric Complexities of Diagenetic Zonation

The topography of the diagenetic zone boundaries deviates from horizontal for a variety of interrelated reasons including spatial variability of rock properties and parent rock mineralogy, structural displacement (e.g. multiple caldera collapses, faulting), past saturation and hydrothermal conditions (e.g. water table location, hydrothermal circulation, paleo-temperatures, paleo-temperature gradients), and slope angles of deposition. The diagenetic boundaries are often closely or partially associated with segments of HSU, HGU, or lithologic boundaries because of the inherent contrasts in rock properties. Zones of hydrothermal upflow may elevate the boundaries of mineralogic alteration (Bish and Aronson, 1993). Elements of one zone may be within another zone as a result of the complexities discussed above.

For assessment of groundwater flow and radionuclide transport, the water table is a particularly relevant reference plane. At PM, the water table is usually within the zeolitic rocks of Zone 2. Exceptions are mostly in Area 19 (see Appendix Section A.1), where the water table is in Zone 1 in west-central Area 19 (e.g. at U-19Q, U-19AD, and UE-19I) and in Zone 3 in northern and north-central Area 19 (e.g. at U-19AK and UE-19Z). The water table is in Zone 3 along some downgradient flow paths through the Bench and the TMCC (e.g. at ER-EC-5, ER-EC-7, and ER-EC-12; see Section A.4). The water table is within Zone 4 at UE-19W1 southeast of SCCC (see Figure A.20 in Section A.1). Throughout the PM-OV groundwater basin, the water table intersects all four diagenetic zones. Consequently, the spatial distributions of flow and transport properties at PM-OV cannot be simply conceptualized as a function of depth below the water table.

5.4 Regional Scale Variability

Some large-scale differences in mean abundance of calcite, smectite, mica, and zeolite are not completely attributable to diagenetic zonation. Regional scale differences in reactive mineral abundances can result from differences in hydrothermal and physiochemical conditions between the SCCC, across the Bench, and into the TMCC. Such regional scale differences in mineralogy, in addition to inter-zonal differences, should be considered in modeling of radionuclide transport.

A "micaceous-kaolinitic area" is outlined in northwestern TMCC where smectite appears to be less abundant or absent and kaolinite and mica (likely illite) more prevalent in Zones 3 and 4 (Figure 4). High-temperature hydrothermal alteration can lead to prevalence of kaolinite instead of smectite (Simeone et al., 2005; Yuan et al., 2014). This micaceous-kaolinitic area is defined by high-quality F XRD data for boreholes ER-20-4, ER-20-7, ER-20-8, ER-20-11, ER-EC-2A, ER-EC-6, ER-EC-11, ER-EC-12, ER-EC-13, ER-EC-14 (see Figure 4 and Sections 3.4, A.3, and A.4). Considering that downgradient flow paths from PM sites of contamination focus to the southwest across the Bench and into northwestern TMCC (Fenelon et al, 2016), these measured spatial variations of the reactive minerals should be factored into assessment of radionuclide transport.

5.5 Impact of Diagenesis on Rock Properties

This study focuses on the mineralogical aspects including diagenesis that impact sorption and porosity/permeability relationships directly relevant to assessment of radionuclide transport using models. Mineralogic diagenesis also ties into rock property evaluation of porosity, saturation and grain density. Clay and zeolite minerals that distinguish Zones 2 and 3 at PM-OV include a large fraction of chemically bound water in their mineral structure. Large errors in grain density, bulk density, porosity, and saturation estimation result from ignoring effects of bound water dehydration and rehydration in rock property measurement methods. The comprehensive mineral mass fraction distribution obtained from XRD data offers a more accurate estimate of grain density, which can subsequently be used to correct measurements of porosity and saturation.

Transport modeling of sorbing radionuclides such as strontium, cesium, uranium, or plutonium requires realistic sorption parameters consistent with spatial the distribution of the reactive minerals at PM-OV. This requires understanding of the underlying causes of spatial variability in the mineralogy and related rock properties. Local scale (e.g. hydrologic source term) and regional scale transport models need to consider that local test settings and downgradient flow paths straddle multiple intervals of diagenetically altered rock. Alteration of PM-OV rocks includes not only hydration processes (e.g. of glass to zeolite), but extends to more extreme hydrothermal-dehydration processes characteristic of silicic calderas. Individual test settings should be considered in implementation of the source term because, for example, the diagenetic zonation is not always the same between tests located at similar elevation or vertical distance from the water table. Downstream transport pathways will inevitably transgress different diagenetic zones with inherently different mineralogical and permeability/porosity characteristics. Diagenetic zonation is an overarching hydrogeochemical framework that should be added to consideration of lithology, HGU, or HSU in characterization of rock properties and assessment of radionuclide transport at PM-OV.

6 References

Bauluz, B., D.R. Peacor, and R.F. Ylagan (2002), Transmission Electron Microscopy Study of Smectite Illitization during Hydrothermal Alteration of Rhyolitic Hyaloclastite from Ponza, Italy, Clays and Clay Minerals, v. 50, n. 2, p. 157-173.

Bechtel Nevada (2002), A Hydrostratigraphic Model and Alternatives for the Groundwater Flow and Transport Model of Corrective Action Units 101 and 102: Central and Western Pahute Mesa, Nye County, Nevada, DOE/NV/11718—706, Las Vegas, NV.

Begg, J. D., M. Zavarin, S.J. Tumey, and A.B. Kersting (2015), Plutonium Sorption and Desorption Behavior on Bentonite, Journal of Environmental Chemistry, v. 141, p 106-114.

Bish, D.L. and J.L. Aronson (1993), Paleogeothermal and Paleohydrologic Conditions in Silicic Tuff from Yucca Mountain, Nevada, Clays and Clay Minerals, v. 41, n. 2, p. 148-161.

Bish, D.L., D.T Vaniman, S.J. Chipera, and W.J. Carey (2003), The Distribution of Zeolites and Their Effects on the Performance of a Nuclear Waste Repository at Yucca Mountain, Nevada, U.S.A., American Mineralogist, v. 88, p. 1889-1902.

Boyd, P. J., R.J. Martin, and R.H. Price (1994), An Experimental Comparison of Laboratory Techniques in Determining Bulk Properties of Tuffaceous Rocks, Sand92-0119, Sandia National Laboratories, Albuquerque, NM.

Brachmann, A., and A.B. Kersting (2003), Colloid-Facilitated Transport of Low-Solubility Radionuclides: A Field, Experimental, and Modeling Investigation. In: Kersting AB, Reimus PW (eds) Lawrence Livermore National Laboratory. UCRL-ID-149688

Broxton, D.E., D.L. Bish, and R.G. Warren (1987), Distribution and Chemistry of Diagenetic Minerals at Yucca Mountain, Nye County, Nevada, Clays and Clay Minerals, v. 35, n. 2, p. 89-110.

Broxton, D.E., R.G. Warren, F. M. Byers, and R.B. Scott (1989), Mineralogic Trends Within the Timber Mountain-Oasis Valley Caldera Complex, Nevada: Evidence for Multiple Cycles of Chemical Evolution in a Long-Lived Silicic Magma System, Journal of Geophysical Research, v. 94, n. B5, p. 5961-5985.

Carle, S.F. (2011), Hydrologic Source Term Processes and Models for the Clearwater and Wineskin Tests, Rainier Mesa, Nevada Test Site, LLNL-TR-483651, Lawrence Livermore National Laboratory, Livermore, CA.

Carle, S. F., R. M. Maxwell, and G.A. Pawloski (2003), Impact of Heat on Groundwater Flow at Pahute Mesa, Nevada Test Site, UCRL-ID-152599, Lawrence Livermore National Laboratory, Livermore, CA.

Carle, S.F., M. Zavarin, and G.A. Pawloski (2008), Spatial Variability of Reactive Mineral and Radionuclide K_d Distributions in the Tuff Confining Unit: Yucca Flat, Nevada Test Site, LLNL-TR-402227, Lawrence Livermore National Laboratory, Livermore, CA.

Carle, S.F., A.F.B. Tompson, and M. Zavarin (2020), Radionuclide Screening Analysis and Transport Parameters for Pahute Mesa Detonations, Nevada National Security Site, LLNL-TR-812351, Lawrence Livermore National Laboratory, Livermore, CA.

Catalano, E. (1969), Comments on Some of the Physical Chemical Questions Associated with the Analysis of Water in Earth Materials, UCRL-50630, Lawrence Radiation Laboratory, Livermore, CA.

Chipera, S. J., and D.L. Bish (1989), Quantitative X-Ray Diffraction Analyses of Samples Used for Sorption Studies by the Isotope and Nuclear Chemistry Division, LA—11669-MS, Los Alamos National Laboratory, Los Alamos, NM.

Chipera, S. J., and D.L. Bish (2002), FULLPAT: A Full-Pattern Quantitative Analysis Program for X-Ray Powder Diffraction Using Measured and Calculated Patterns, Journal of Applied Crystallography, v. 35, p. 744-749

Davis J. A., J.A. Coston, D.B. Kent D. B., and C.C. Fuller (1998), Application of the Surface Complexation Concept to Complex Mineral Assemblages, Environmental Science & Technology, v. 32, n. 19, p. 2820−2828.

Duff, M. C., M. Newville, D. B. Hunter, P. M. Bertsch, S. R. Sutton, I. R. Triay, D. T. Vaniman, P. Eng, and M. L. Rivers (1999), Micro-XAS Studies with Sorbed Plutonium on Tuff, Journal of Synchrotron Radiation, v. 6, n. 3, p. 350-352.

Deer, W.A., Howie, R.A., and J. Zussman (1966), An Introduction to the Rock Forming Minerals, Longman Group Limited, Burnt Mill, Harlow, Essex, England.

Fenelon, J.M., K.J. Halford, and M.T. Moreo (2016), Delineation of the Pahute Mesa–Oasis Valley Groundwater Basin, Nevada (ver. 1.1, May 2016), U.S. Geological Survey Scientific Investigations Report 2015–5175, 40 p.

Finnegan, D. L., M. S. Bowen, J. L. Thompson, C. M. Miller, P. L. Baca, L. F. Olivas, C. G. Geoffrion, D. K. Smith, W. Goishi, B. K. Esser, J. W. Meadows, N. Namboodiri, J. F. Wild (2016), Nevada National Security Site Underground Radionuclide Inventory,1951-1992: Accounting for Radionuclide Decay through September 30, 2012, LA-UR-16-21749, Los Alamos National Laboratory, NM.

FFACO (1996), Federal Facility Agreement and Consent Order (as amended March 2010). Agreed to by the State of Nevada; U.S. Department of Energy, Environmental Management; U.S. Department of Defense; and U.S. Department of Energy, Legacy Management. Appendix VI, which contains the Underground Test Area Strategy, was last modified June 2014, Revision No. 5.

Hoover, D.L., (1968), Genesis of Zeolites, Nevada Test Site, Geol. Soc. Amer. Mem. v. 110, p. 275-284.

Jackson, T.R., Fenelon, J.M., R.L. Paylor (2020), Groundwater Flow Conceptualization of the Pahute Mesa–Oasis Valley Groundwater Basin, Nevada: U.S. Geological Survey Scientific Investigations Report 2020–XXXX, *in preparation*.

Kersting, A.B., D.W. Efurd, D.L. Finnegan, D.J. Rokop, D.K. Smith, and J.L. Thompson (1999), Migration of Plutonium in Ground Water at the Nevada Test Site, Nature, v. 397, p. 56-59.

Kersting, A.B., and M. Zavarin (2011), Colloid Facilitated Transport of Plutonium at the Nevada Test Site, NV USA, LLNL-BOOK-466498, Lawrence Livermore Laboratory, Livermore, CA.

Kuno, H. (1968), Differentiation of basalt magmas, in: Hess, H.H. and A.A. Poldervaart (eds), Basalts: The Poldervaart Treatise on Rocks of Basaltic Composition, 2. NewYork: Interscience, p. 623-688.

Kranz, R. L., D.L. Bish, and J.E. Blacic (1989), Hydration and Dehydration of Zeolitic Tuff from Yucca Mountain, Nevada, Geophysical Research Letters, v. 16, n. 10, p. 1113-1116.

Knowlton, G. D., and H.L. McKague (1976), A Study of the Water Content in Zeolitic Tuffs from the Nevada Test Site, UCRL-78013, Lawrence Livermore Laboratory, Livermore, CA.

Knowlton, G. D., T.R. White, and H.L. McKague (1981), Thermal Study of Types of Water Associated with Clinoptilolite, Clays and Minerals, v. 29, n. 5, p. 403-411.

Martin, J. W., C.W. Felice, and S.J. Green (1993), Grain Density of Zeolitized Tuff - TerraTek Investigations Volume II, TR93-48, TerraTek, Inc., Salt Lake City, UT.

McKague, L., and J.R. Hearst (1991), U20ax Site Characteristics Report, CP 91-121, Lawrence Livermore Laboratory, Livermore, CA

McKague, L., and R.L. Newmark (1989), U20bd Site Characteristics Report, CP 89-167, Lawrence Livermore Laboratory, Livermore, CA

McKague, L., R.L. Newmark, and W. B. McKinnis (1989), U20bf Site Characteristics Report, CP 90-216, Lawrence Livermore Laboratory, Livermore, CA

Moncure, G. K., R. C. Surdam, H. L. McKague (1981), Zeolite Diagenesis Below Pahute Mesa, Clays and Clay Minerals, v. 29, n. 5, p. 385-396.

Navarro-Intera, LLC. (2013), Written communication. Subject: "UGTA Geochemistry Database," UGTA Technical Data Repository Database Identification Number UGTA-4-129, Las Vegas, NV.

Nelson, P. H., and L.A. Anderson (1992), Physical Properties of Ash Flow Tuff from Yucca Mountain, Nevada, Journal of Geophysical Research, v 97, n B5, p. 6823-6841.

Newmark, R.L., and L. McKague (1988), U20aw Site Characteristics Report, CP 88-201, Lawrence Livermore Laboratory, Livermore, CA.

Newmark, R.L., and J.L. Wagoner (1990), U20bb Site Characteristics Report, CP 90-72, Lawrence Livermore Laboratory, Livermore, CA.

Nelson, P.H., and L. A. Anderson (1992), Physical Properties of Ash Flow Tuff from Yucca Mountain, Journal of Geophysical Research, v. 97, n. B5, p. 6823-6841.

Orkild, P.P., Sargent, K.A., and R.P. Snyder (1969), Geologic Map of Pahute Mesa, Nevada Test Site and Vicinity, Nye County, Nevada, U.S. Geological Survey Misc. Geol. Invest. Map I-567.

Pawloski, G. A. (1999), Development of Phenomenological Models of Underground Nuclear Tests on Pahute Mesa, Nevada Test Site: Benham and Tybo, UCRL-ID-136003, Lawrence Livermore National Laboratory, Livermore, CA.

Pawloski, G. A., A.F.B. Tompson, and S.F. Carle, Eds. (2001), Evaluation of the Hydrologic Source Term from Underground Nuclear Tests on Pahute Mesa at the Nevada National Security Site: The CHESHIRE Test, UCRL-ID-147023, Lawrence Livermore National Laboratory, Livermore, CA.

Prothro, L. B. (2005), Mineralogic Zonation Within the Tuff Confining Unit, Yucca Flat, Nevada Test Site, DOE/NV/11718—995, Bechtel Nevada, Las Vegas, NV.

Prothro, L.B., S.L. Drellack Jr., and J.M. Mercadante (2009), A Hydrostratigraphic System for Modeling Groundwater Flow and Radionuclide Migration at the Corrective Action Unit Scale, Nevada Test Site and Surrounding Areas, Clark, Lincoln, and Nye Counties, Nevada, U.S. Department of Energy Report DOE/NV/25946--630, 145 p.

Sargent, K.A. (1969), Petrography and Heavy Minerals of Three Groups of Rhyolitic Lavas, Pahute Mesa, Nevada Test Site, Geological Survey Research 1969, Professional Paper 650-C, p. C18-C24, U.S. Geological Survey, Washington, DC.

Sen, G. (2014), Igneous Rock Series: Basalt Magma Evolution, in: Petrology, Springer, Berlin, Heidelberg.

Simeone, R., J.H. Dilles, G. Padalino, and M. Palomba (2005), Mineralogical and Stable Isotope Studies of Kaolin Deposits: Shallow Epithermal Systems of Western Sardinia, Italy, Economic Geology, v. 100, n. 1, p. 115-130.

Smith, D.K., G.F. Eaton, F.C. Benedict, R.E. Criss, M.L. Davisson, G.B. Hudson, J.M. Kenneally, and T.P. Rose (1999), Hydrologic Resources Management Program and Underground Test Area FY 1998 Progress Report, UCRL-ID-135170, Lawrence Livermore National Laboratory, Livermore, CA.

Stoller-Navarro Joint Venture (2007), Phase I Contaminant Transport Parameters for the Groundwater Flow and Contaminant Transport Model of Corrective Action Unit 97: Yucca Flat/Climax Mine, Nevada Test Site, Nye County, Nevada, Rev. 0, S-N/99205—096, Las Vegas, NV.

Stoller-Navarro Joint Venture (2008), Phase I Contaminant Transport Parameters for the Groundwater Flow and Contaminant Transport Model of Corrective Action Unit 99: Rainier Mesa/Shoshone Mountain, Nevada Test Site, Nye County, Nevada, Rev. 1, S-N/99205—102, Las Vegas, NV.

Stoller-Navarro Joint Venture (2009), Phase I Transport Model of Corrective Action Units 101 and 102: Central and Western Pahute Mesa, Nevada Test Site, Nye County, Nevada, Rev. 1, S-N/99205—111, Las Vegas, NV.

USEPA (2002), Radionuclides in Drinking Water: A Small Entity Compliance Guide. Office of Ground Water and Drinking Water, U.S. Environmental Protection Agency, Washington, DC. EPA 815-R-02-001.

USDOE (2015), United States Nuclear Tests, July 1945 through September 1992, DOE/NV--209-REV 16, National Nuclear Security Administration Nevada Field Office, U.S. Department of Energy, Las Vegas, NV.

USDOE (2018), Rainer Mesa/Shoshone Mountain Flow and Transport Model Report, Nevada National Security Site, Nevada, DOE/NV—1588, U.S. Department of Energy, Environmental Management Nevada Program, Las Vegas, NV.

USDOE (2019), written communication, "Pahute Mesa Geophysical Log Evaluation for Matrix Porosity, March 2019," U.S. Department of Energy, Environmental Management Nevada Program, Las Vegas, NV.

USDOE (2020), Pahute Mesa-Oasis Valley Hydrostratigraphic Framework Model for Corrective Action Units 101 and 102: Central and Western Pahute Mesa, Nye County, Nevada, Revision No.: 0. DOE/EMNV--0014, Environmental Management Nevada Program, U.S. Department of Energy, Las Vegas, NV.

Vaniman, D. T., and D.L. Bish (1993), The Importance of Zeolites in the Potential High-Level Radioactive Waste Repository at Yucca Mountain, Nevada, LA-UR-93-2326; CONF-9306100-2, Los Alamos National Laboratory, Los Alamos, NM.

Warren, R. G., G. L. Cole, and D. Walther (2000), A Structural Block Model for the Three-Dimensional Geology of the Southwestern Nevada Volcanic Field, LA-UR-00-5866, Los Alamos National Laboratory, Los Alamos, NM.

Warren, R.G., Sawyer, D.A., Byers, F.M., and Cole, G.L. (2003), A Petrographic, Geochemical, and Geophysical Database, and Stratigraphic Framework for the Southwestern Nevada Volcanic Field, LA-UR-03-1503, Los Alamos National Laboratory, Los Alamos, NM.

WoldeGabriel, G., H. Xu, and E. Kluk (2016), Mineralogical and Geochemical Data Report for Samples of Lava and Tuff Cuttings from ER-20-12, LA-UR-16-25473, Los Alamos National Laboratory, Los Alamos, NM.

Wolfsberg, A., L. Glascoe, G. Lu, A. Olson, P. Lichtner, M. McGraw, T. Cherry, and G. Roemer (2002), TYBO/BENHAM: Model Analysis of Groundwater Flow and Radionuclide Migration from Underground Nuclear Tests in Southwestern Pahute Mesa, Nevada, LA-13977, Los Alamos National Laboratory, Los Alamos, NM.

Wood, D. B., (2017), Digitally Available Interval-Specific Rock-Sample Data Compiled from Historical Records, Nevada National Security Site and Vicinity, Nye County, Nevada, Data Series 297, Version 2.2, February 2017, U.S. Geological Survey, Reston, VA.

Yuan, Y., G. Shi, M. Yang, Y. Wu, Z. Zhang, A. Huang, and J. Zhang (2014), Formation of a Hydrothermal Kaolinite Deposit from Rhyolitic Tuff in Jiangxi, China, Journal of Earth Science, v. 25, n. 3, p. 495-505.

Zavarin, M., (2014), Yields and Cavity Radii of Underground Nuclear Tests with Specified Yields Reported in DOE/NV—209-REV 15 (2000), LLNL-TR-664664, Lawrence Livermore National Laboratory, Livermore, CA.

Zavarin, M. and C. J. Bruton (1999), A Non-Electrostatic Surface Complexation Approach to Modeling Radionuclide Migration: The Role of Iron Oxides and Carbonates, UCRL-JC-133474, Lawrence Livermore National Laboratory, Livermore, California.

Zavarin, M. and C. J. Bruton (2004a), A Non-Electrostatic Surface Complexation Approach to Modeling Radionuclide Migration at the Nevada Test Site: Aluminosilicates, UCRL-TR-208672, Lawrence Livermore National Laboratory, Livermore, California.

Zavarin, M. and C. J. Bruton (2004b), A Non-Electrostatic Surface Complexation Approach to Modeling Radionuclide Migration at the Nevada Test Site: Iron Oxides and Calcite, UCRL-TR-208673, Lawrence Livermore National Laboratory, Livermore, California.

Zavarin, M., S. F. Carle, and R. M. Maxwell (2004), Upscaling Radionuclide Retardation – Linking the Surface Complexation and Ion Exchange Mechanistic Approach to a Linear K_d Approach, UCRL-TR-204713, Lawrence Livermore National Laboratory, CA.

Zavarin, M., M. R. Johnson, S. K. Roberts, R. Pletcher, T. P. Rose, A. B. Kersting, G. Eaton, Q. Hu, E. Ramon, J. Walensky and P. Zhao (2005), Radionuclide Transport in Tuff and Carbonate Fractures from Yucca Flat, Nevada Test Site, UCRL-TR-219836, Lawrence Livermore National Laboratory, Livermore, CA.

Zavarin, M., Roberts, S., Reimus, P., and M. Johnson (2007), Summary of Radionuclide Reactive Transport Experiments in Fractured Tuff and Carbonate Rocks from Yucca Flat, Nevada Test Site, UCRL-TR-225271, Lawrence Livermore National Laboratory, Livermore, CA.

Zavarin, M., P. Zhao, C. Joseph, J.D. Begg, M.A. Boggs, Z. Dai, and A.B. Kersting (2019), Hydrothermal Alteration of Nuclear Melt Glass, Colloid Formation, and Plutonium Mobilization at the Nevada National Security Site, U.S.A., Environmental Science and Technology, v. 53, p. 7363-7370.

Appendix: Additional PM-OV Boreholes with XRD and Rock Property Data

This appendix assembles graphical representations of XRD and rock property data for 97 PM-OV boreholes in addition to the twelve included in Sections 2 and 3 of this report. The objective is to include in this report all 109 boreholes with XRD data in the PM testing areas, the downgradient areas of the PM-OV groundwater basin, and the TMCC. Discussion is included on interpretation of diagenetic zonation as related to characterization of local test settings in the context of assessment of radionuclide transport.

The sections of the appendix are organized into geographical areas from northeast to southwest (generally along the groundwater flow paths). Inside the NNSS, the Appendix sections are organized by the testing areas (Areas 19 and 20) and the Corrective Action Units (CAUs) of FFACO (1996). Outside the NNSS, Appendix sections are organized by borehole name prefix (EC and ER-OV). Within each section, the data presentation is ordered by borehole location generally from north to south with an effort to place nearby boreholes next to each other to ease comparison.

For most of the U, UE, and PM boreholes in Area 19 and Area 20, most of the XRD data consist of the lower quality S and E methods. Nonetheless, S and E XRD data are found to be useful for characterization of test settings. The quality of the XRD data varies from borehole to borehole and within each method. Importantly, all rock property data for grain density and porosity are obtained from the Area 19 and 20 boreholes with U, UE, and PM borehole name prefixes. The grain density data are useful for comparison to XRD-calculated grain density. For the reasons discussed in Section 2.2, measured grain density is often overestimated by up to 0.3 g/cc in the zeolitic zone where the clinoptilolite mass fraction is typically greater than 50%. The graphical representations make this evident. Section A.1 includes Area 19 boreholes, and Sections A.2 and A.3 include Area 20 boreholes divided by CAU.

Newer XRD data obtained primarily from the ER, ER-EC, and ER-OV boreholes are mostly obtained by the highest quality F method, with the remaining XRD obtained by the I method. These high-quality XRD data are extremely useful to radionuclide assessment by resolution of very low mass fractions (0.1% or greater) of the reactive minerals. These data provide much insight into the effects of geothermal alteration in the PM-OV area. Sections A.2 and A.3 includes the ER boreholes by location in Area 20. Sections A.4 and A.5 include the ER-EC and ER-OV boreholes, respectively.

Section A.6 includes four more boreholes with XRD data located within the TMCC in Areas 18 and 30 of the NNSS.

A.1 Area 19 Boreholes – Central Pahute Mesa CAU

This section includes XRD data for 32 boreholes in Area 19 of NNSS and the Central Pahute Mesa CAU. The XRD data were mostly derived from the lowest quality S method with the remainder obtained by E and I methods. Many of the S and E data distinguish the transitional zeolites mordenite and analcime, so these lower quality XRD data are still useful for identification of diagenetic zones. Table A.1 lists Area 19 boreholes with XRD data, general location (see Figure 5 for exact locations), XRD method, adjacent PM test (if emplacement hole or nearby exploration hole), and report figure reference.

Table A.1. List of 32 boreholes with XRD data in PM Area 19, Central Pahute Mesa CAU, NNSS.

Borehole	Location in Area 19	XRD Method(s)	Adjacent PM Test (distance to)	Figure
U-19AK	northern	S	HOSTA	A.1
U-19AI	northern	S	SERPA	A.1
UE-19G-S	northwestern	S	ESTUARY (190 m)	A.2
U-19G	northwestern	S	ESTUARY	A.3
U-19AJ	north-central	S	HARZER	A.4
UE-19Z	north-central	S	FONDUTTA (10 m)	A.4
UE-19E	north-central	S	MUENSTER (60 m)	A.5
U-19AN	north-central	S	LABQUARK	A.6
U-19AX	north-central	S	KEARSARGE	A.6
U-19BA2	north-central	S	BEXAR (20 m)	A.7
U-19BA	north-central	S	BEXAR	A.7
U-19T	north-central	S	EMMENTHAL	A.8
UE-19T	north-central	S	EMMENTHAL (30 m)	A.8
U-19AC	north-central	S	TIERRA	A.9
U-19Q	west-central	S	CAMEMBERT	A.10
U-19A-S1	west-central	S	SCOTCH (30 m)	A.10
U-19AR	west-central	S	CYBAR	A.11
U-19Y-S	west-central	S	PANIR	A.11
U-19AY	west-central	I	AMARILLO	A.12
U-19AD	west-central	S	CHANCELLOR	A.12
UE-19P1	south-central	S	POOL (40m)	A.13
UE-19P	south-central	S	POOL (30m)	A.13
U-19AB	south-central	S	TOWANDA	A.14
UE-19I	south-central	I, S	SLED	A.15
U-19AF	southwestern	S	GALVESTON	A.16
U-19AE	southwestern	S	NEBBIOLO	A.16
UE-19X	southwestern	S	BACKBEACH (60 m)	A.17
U-19X	southwestern	S	BACKBEACH	A.17
U-19BH	southwestern	I	---	A.18
U-19AA	southwestern	S	SHEEPSHEAD	A.18
UE-19F-S	southwestern	S	INLET	A.19
UE-19W1	southern	S	---	A.20

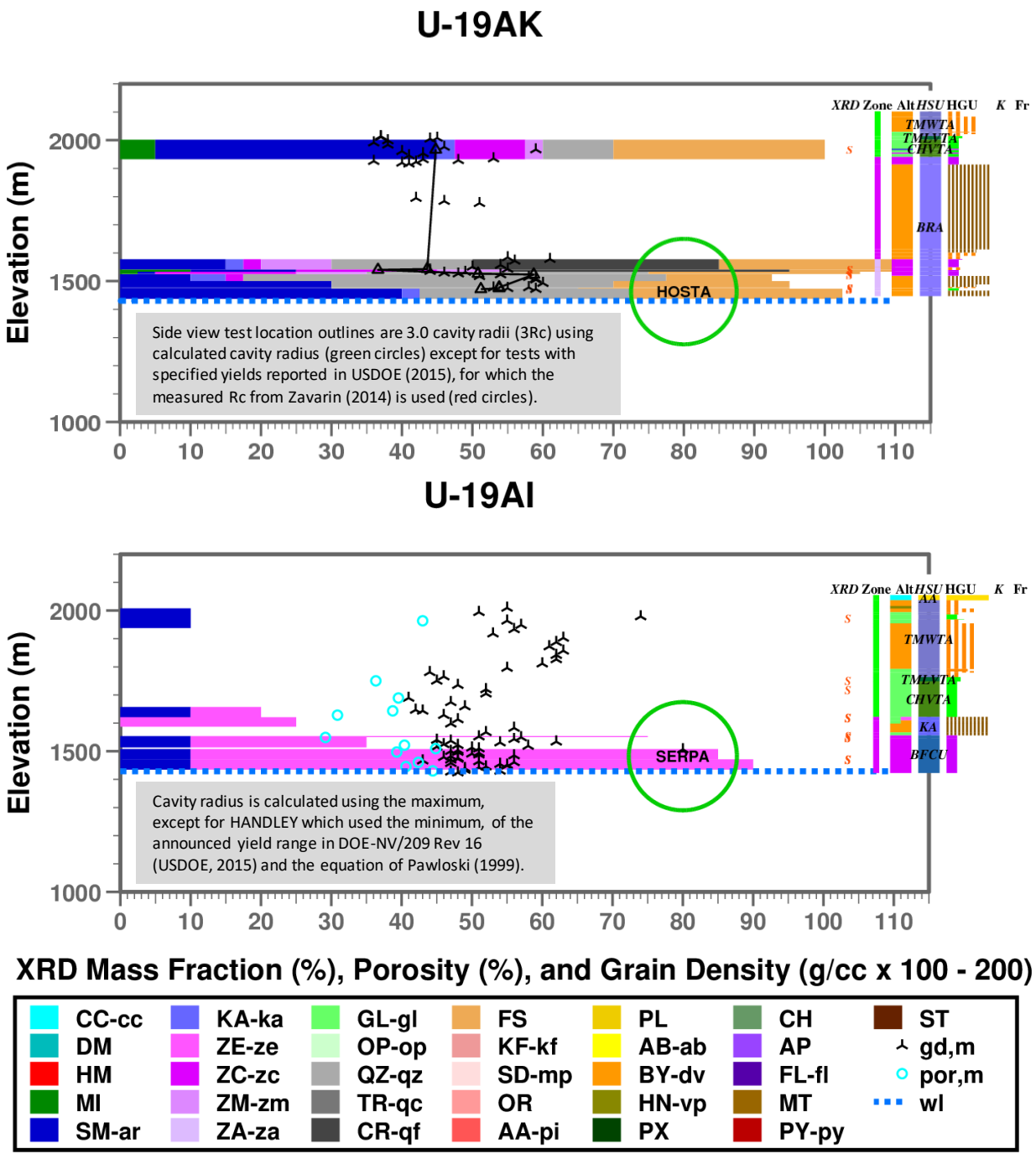

Figure A.1. Graphical representation of XRD and rock property data for boreholes U-19AK (HOSTA) and U-19AI (SERPA), SCCC, PM, northern Area 19, NNSS.

Borehole U-19AK is located in northern Area 19 very close to the northern margin of the SCCC. The relatively high smectite mass fraction could be attributed to this unusual geological setting. The HOSTA EZ is interpreted to be mostly in Zone 3 based on XRD, alteration description. Borehole U-19AI is located in northern Area 19 about 2.5 km south of Borehole U-19AK. THE SERPA EZ is interpreted to be mostly in Zone 2 based on XRD and alteration.

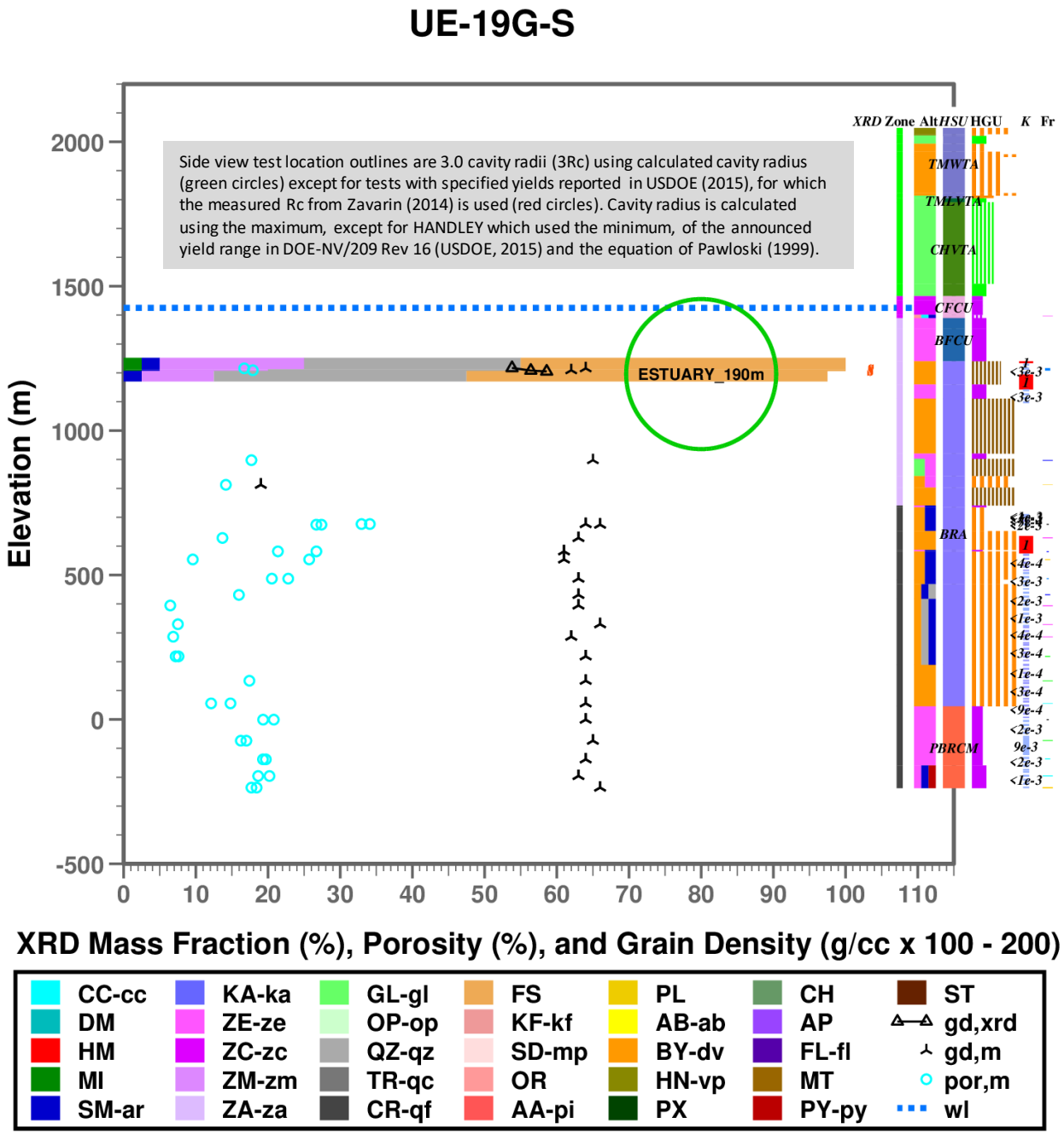

Figure A.2. Graphical representation of XRD and rock property data for borehole UE-19G-S, SCCC, PM, northwestern Area 19, NNSS.

XRD data for UE-19G-S and U-19G (Figure A.3) and indicate the ESTUARY EZ is situated mostly in Zone 3 based primarily on absence of clinoptilolite and prevalence of mordenite.

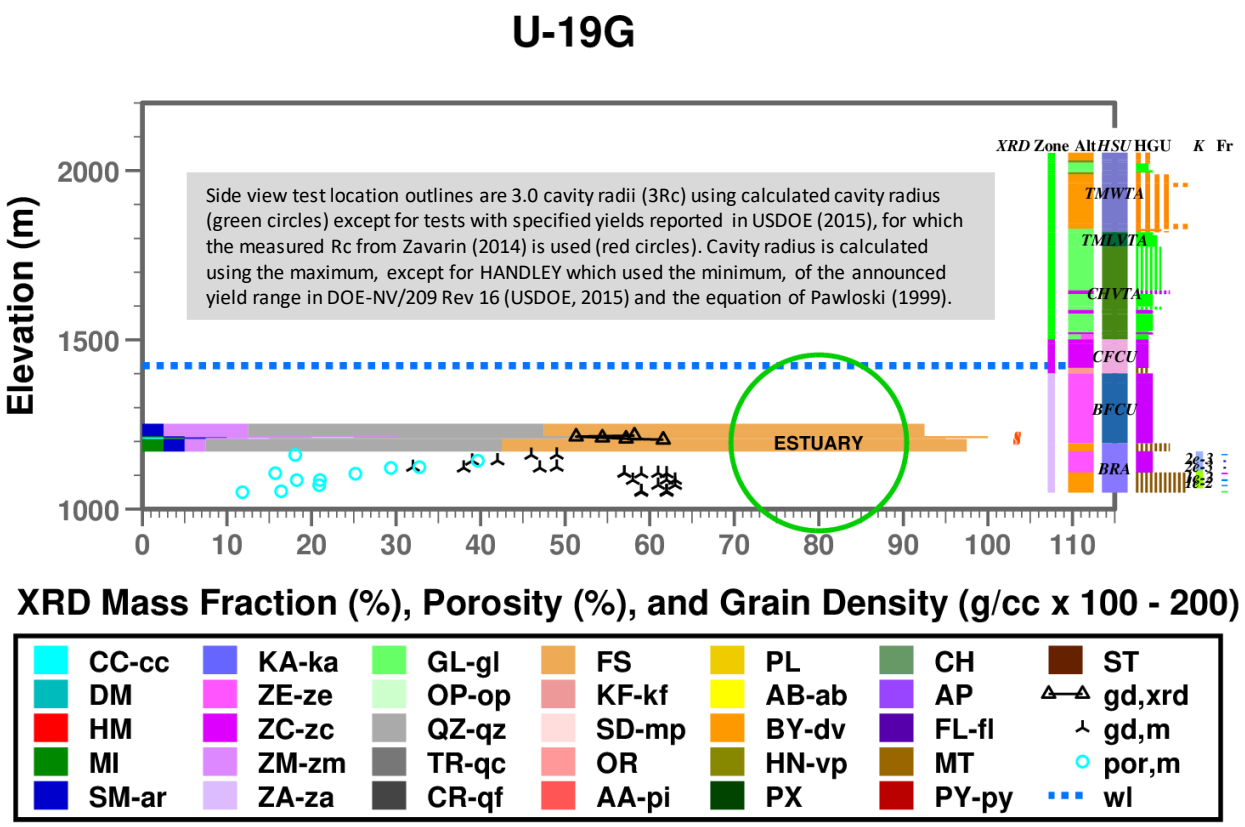

Figure A.3. Graphical representation of XRD and rock property data for borehole U19G, SCCC, PM, northwestern Area 19, NNSS.

XRD data for U-19G and UE-19G-S (Figure A.2) indicate the ESTUARY EZ is situated mostly in Zone 3 based primarily on absence of clinoptilolite and prevalence of mordenite.

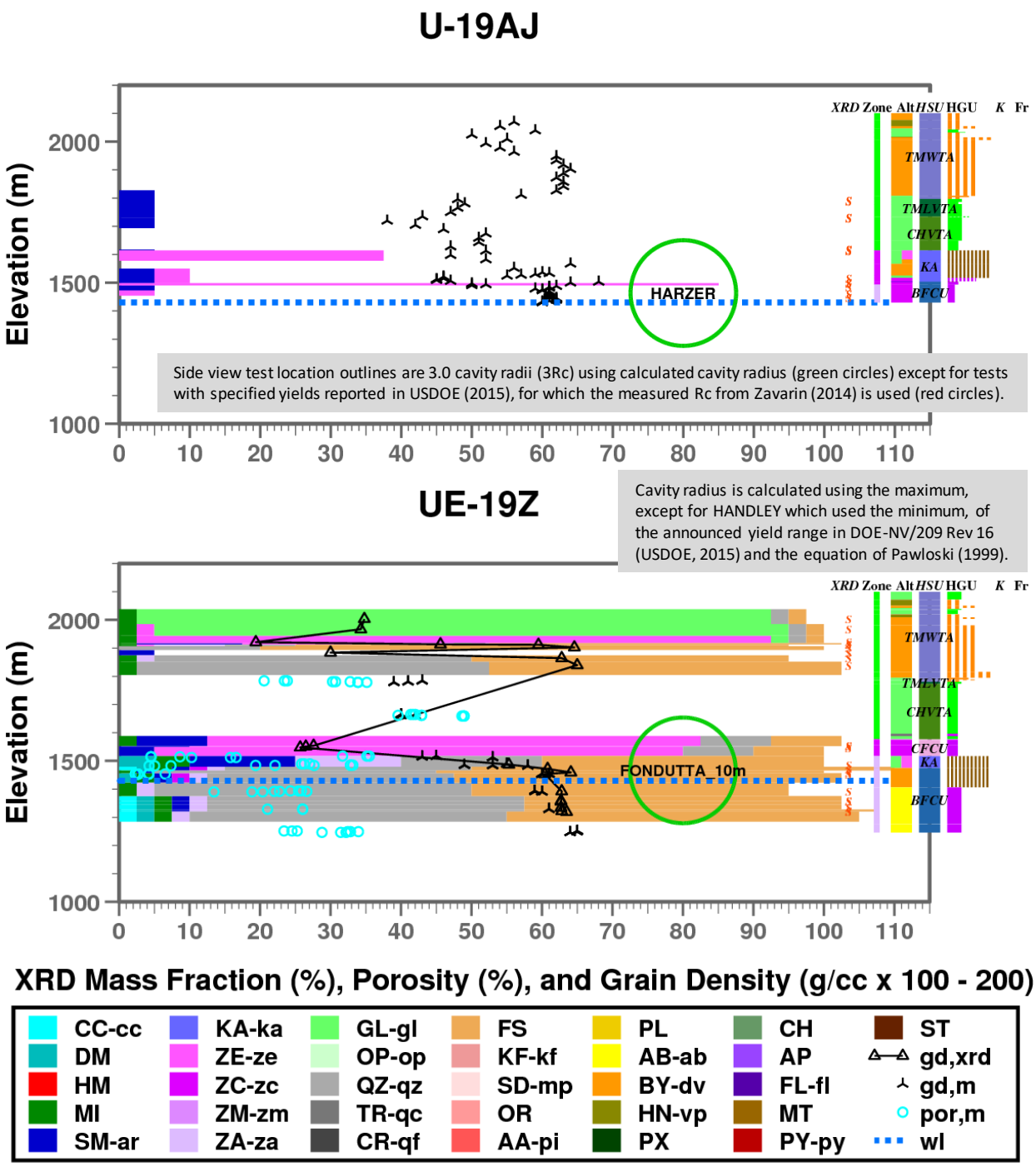

Figure A.4. Graphical representation of XRD and rock property data for boreholes U-19AJ and UE-19Z, SCCC, PM, north-central Area 19, NNSS.

Limited XRD data for U-19AJ indicate the HARZER test is located in Zones 2 and 3, with the BFCU interpreted to be in Zone 3 based on XRD data at nearby UE-19Z to the south. XRD data for UE-19Z indicate the FONDUTTA test working point was located in Zone 3 with presence of analcime. The upper portion of the FONDUTTA EZ spans Zones 1, 2, and 3 in the unsaturated zone, whereas saturated portion of the EZ is entirely in Zone 3.

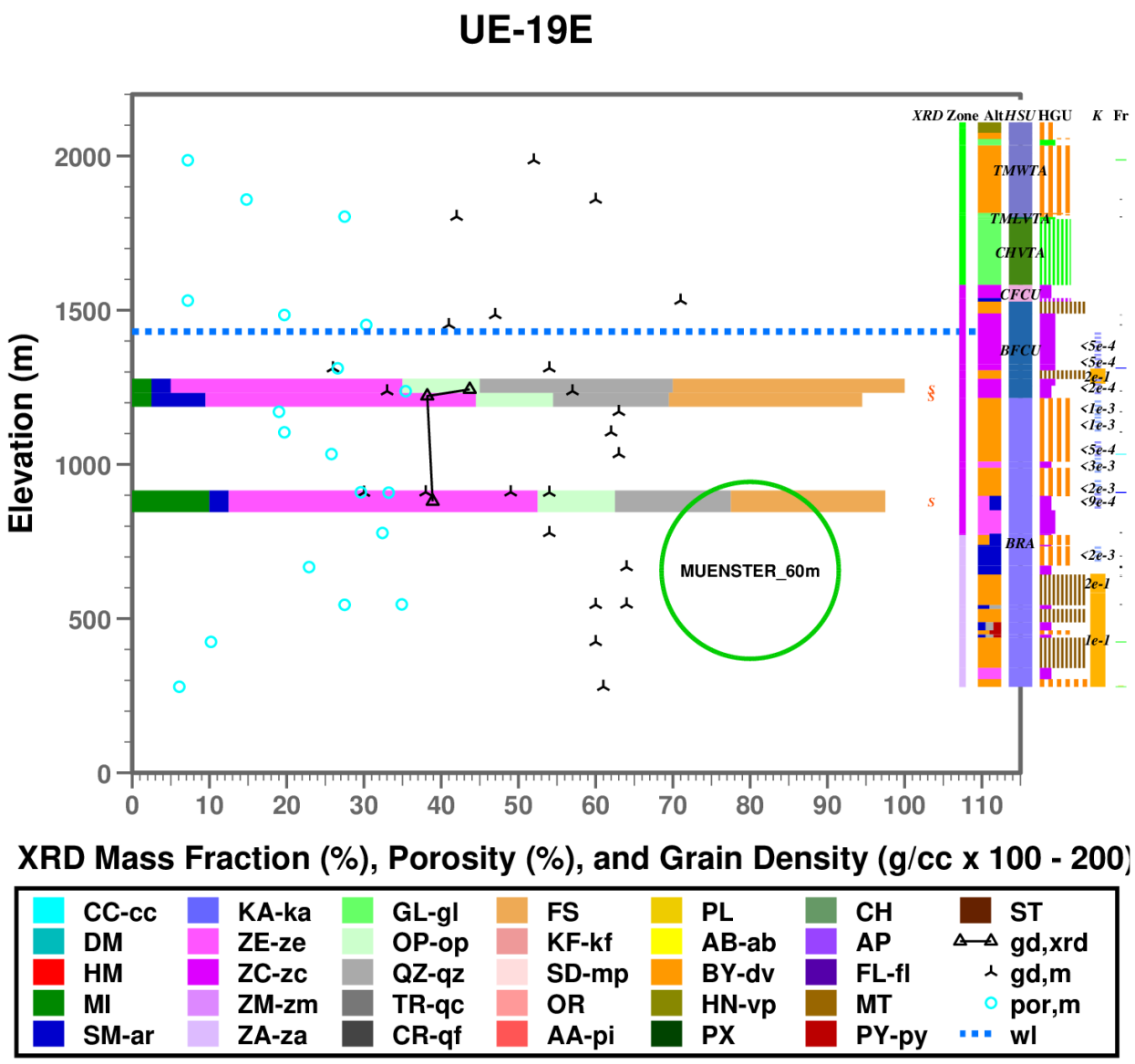

Side view test location outlines are 3.0 cavity radii (3Rc) using calculated cavity radius (green circles) except for tests with specified yields reported in USDOE (2015), for which the measured Rc from Zavarin (2014) is used (red circles). Cavity radius is calculated using the maximum, except for HANDLEY which used the minimum, of the announced yield range in DOE-NV/209 Rev 16 (USDOE, 2015) and the equation of Pawloski (1999).

Figure A.5. Graphical representation of XRD and rock property data for borehole UE-19E, SCCC, PM, north-central Area 19, NNSS.

The XRD data for UE-19E are sparse but support the presence of Zone 2 in the upper portion of the MUENSTER EZ. A key indicator of Zone 2 is the presence of opal. Increased grain density and argillic alteration indicate the lower portion of the MUENSTER EZ is in Zone 3. The MUENSTER setting appears to have a much thicker Zone 2 compared to at FONDUTTA (Figure A.4), only a few hundred meters to the northeast

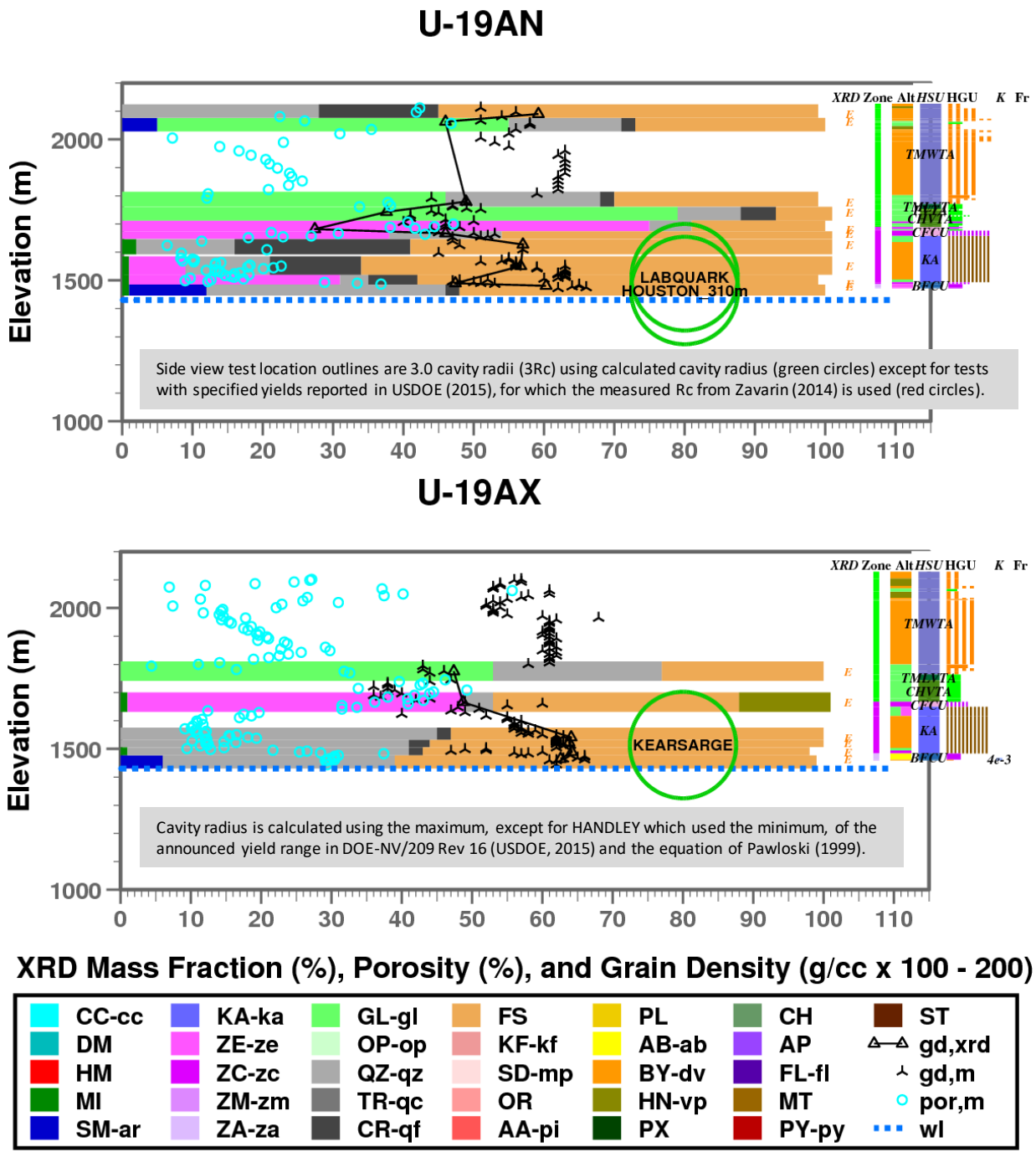

Figure A.6. Graphical representation of XRD and rock property data for boreholes U-19AN (LABQUARK) and U-19AX (KEARSARGE), SCCC, PM, north-central Area 19, NNSS.

The LABQUARK and KEARSAGE tests are in similar settings – above the water table in Zone 2 within a lava flow of the KA HSU. The underlying BFCU is interpreted to be in Zone 3 based on XRD at UE-19Z (Figure A.4) less than 2 km to the west.

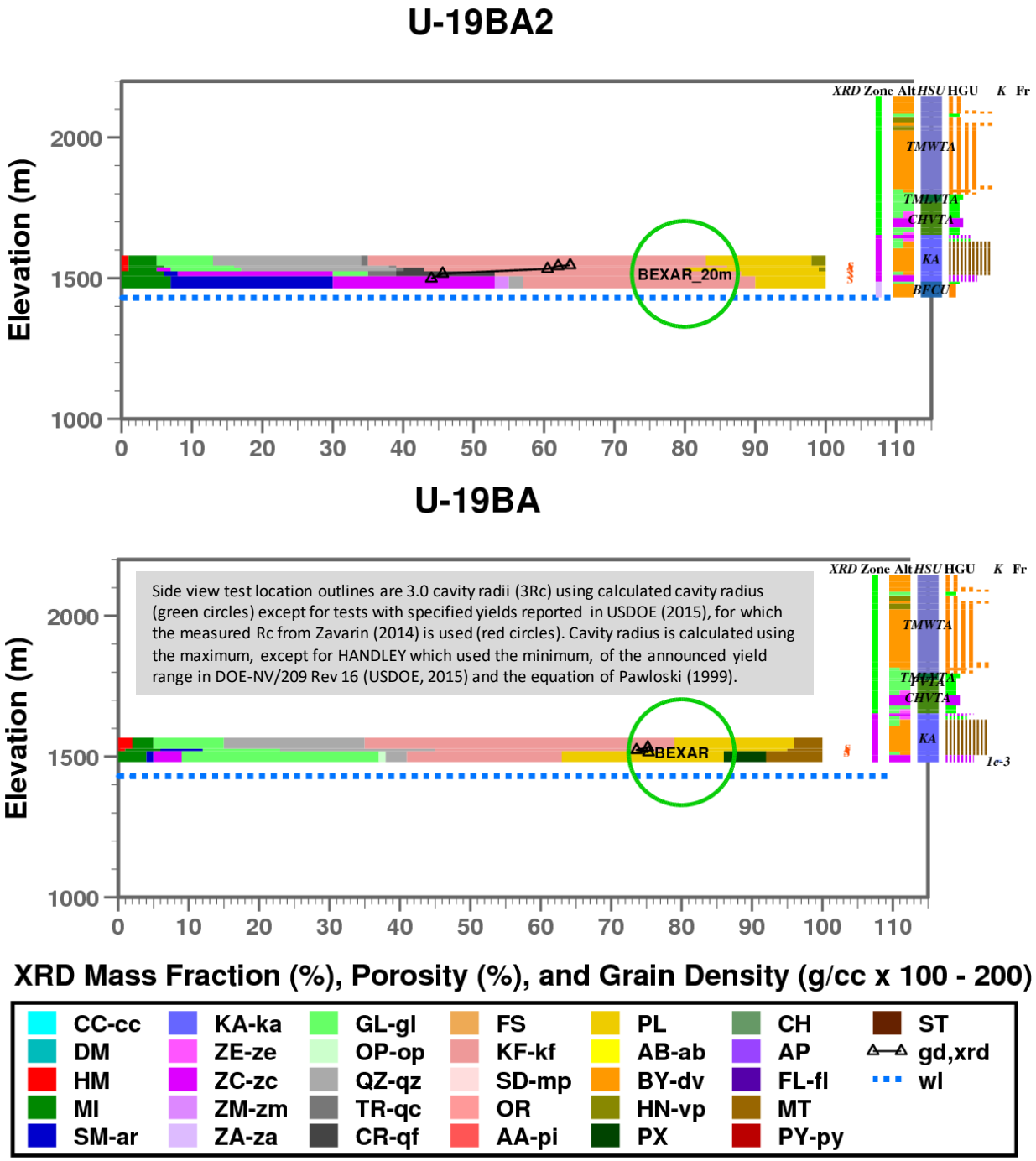

Figure A.7. Graphical representation of XRD and rock property data for boreholes U-19BA2 and U-19BA (BEXAR), SCCC, PM, north-central Area 19, NNSS.

The BEXAR test is in a similar setting to the LABQUARK and KEARSARGE tests. The BEXAR EZ may span Zones 1, 2, and 3. The BFCU is interpreted to be in Zone 3 based on XRD at UE-19Z (Figure A.4) about 1.5 km to the northwest.

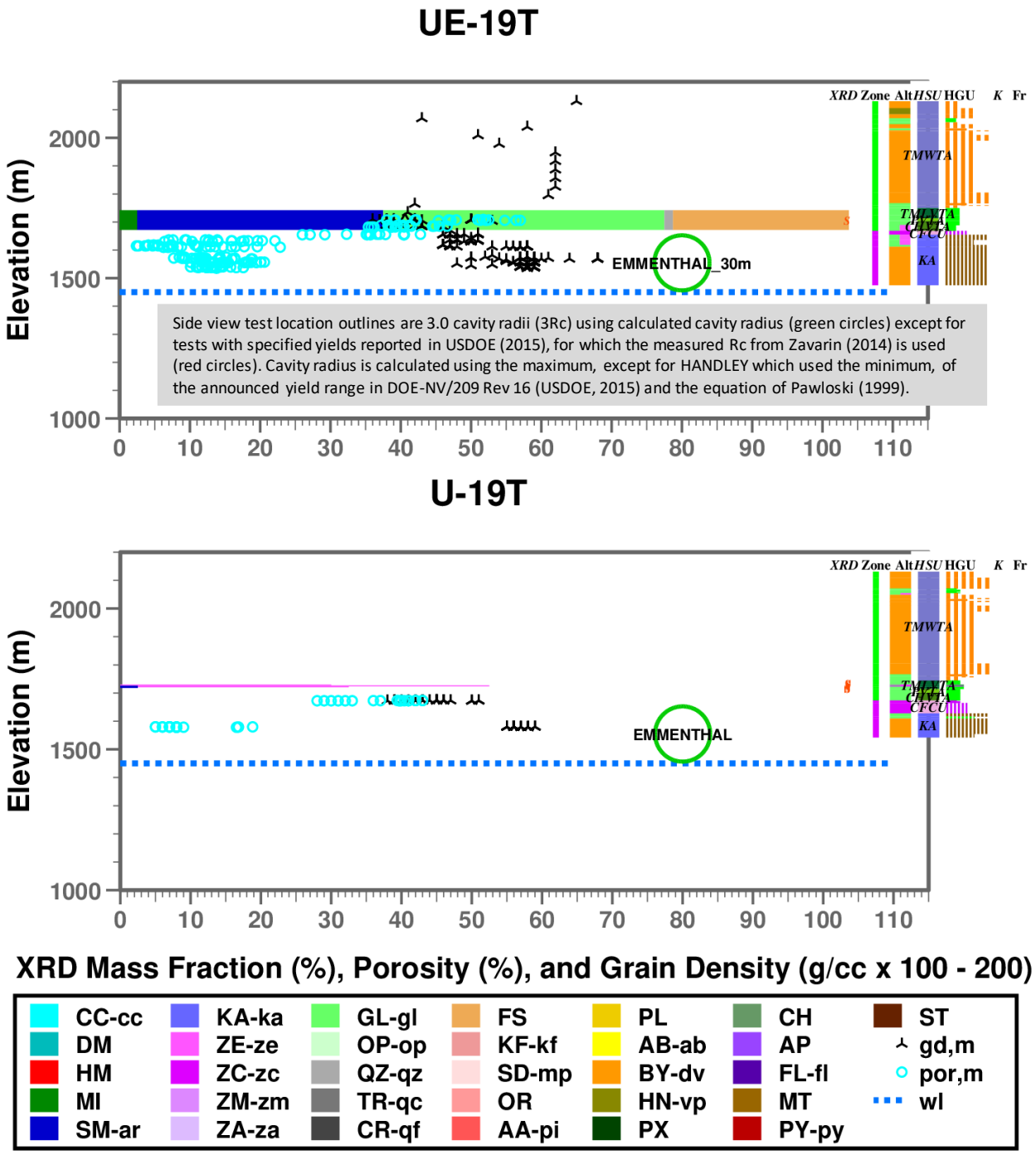

Figure A.8. Graphical representation of XRD and rock property data for boreholes UE-19T and U-19T (EMMENTHAL), SCCC, PM, north-central Area 19, NNSS.

The EMMENTHAL test appears to be in a similar setting as the LABQUARK, KEARSARGE, and BEXAR tests (see Figures A.6 and A.7). However, the EMMENTHAL EZ is entirely above the water table.

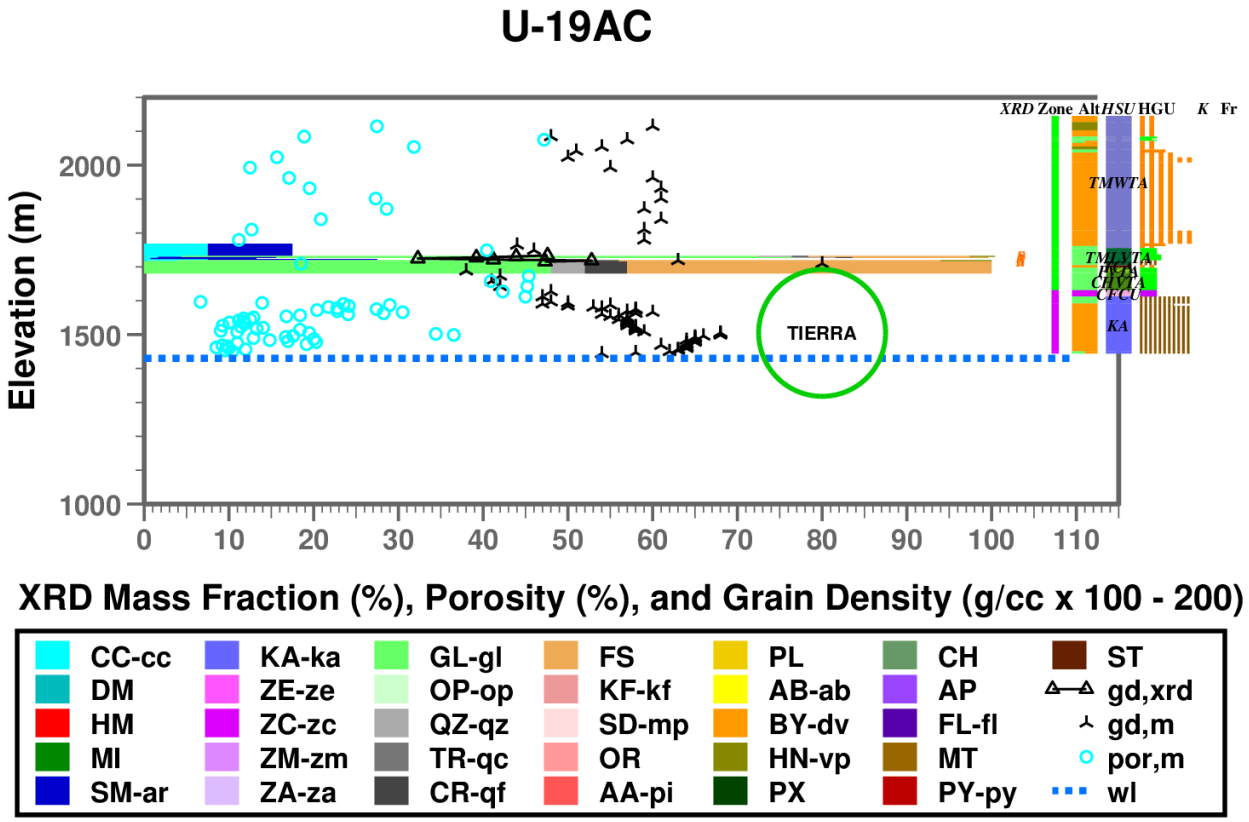

Side view test location outlines are 3.0 cavity radii (3Rc) using calculated cavity radius (green circles) except for tests with specified yields reported in USDOE (2015), for which the measured Rc from Zavarin (2014) is used (red circles). Cavity radius is calculated using the maximum, except for HANDLEY which used the minimum, of the announced yield range in DOE-NV/209 Rev 16 (USDOE, 2015) and the equation of Pawloski (1999).

Figure A.9. Graphical representation of XRD and rock property data for borehole U-19AC (TIERRA), SCCC, PM, north-central Area 19, NNSS.

None of the limited XRD data for U-19AC are within the TIERRA EZ. However, the TIERRA test appears to be in a similar setting as the LABQUARK, KEARSARGE, and BEXAR tests (see Figures A.6 and A.7).

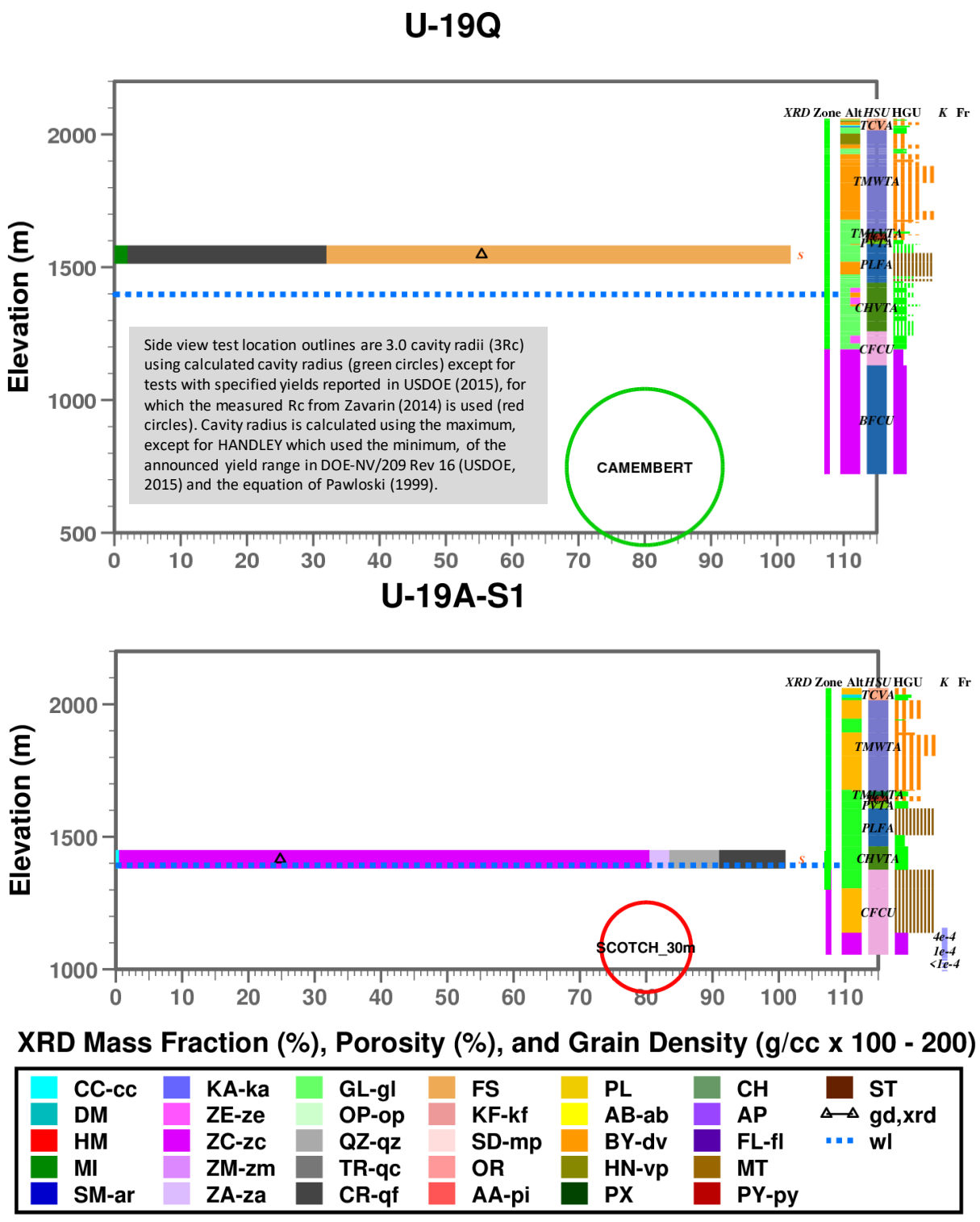

Figure A.10. Graphical representation of XRD and rock property data for boreholes U-19Q and U-19A-S1, SCCC, PM, west-central Area 19, NNSS.

The CAMEMBERT and SCOTCH tests are interpreted to be in Zone 2 based on alteration description and HSU. The XRD datum for U-19A-S1 is suspect, perhaps because of an error in depth. The lower portion of the CAMEMBERT EZ may be in Zone 3.

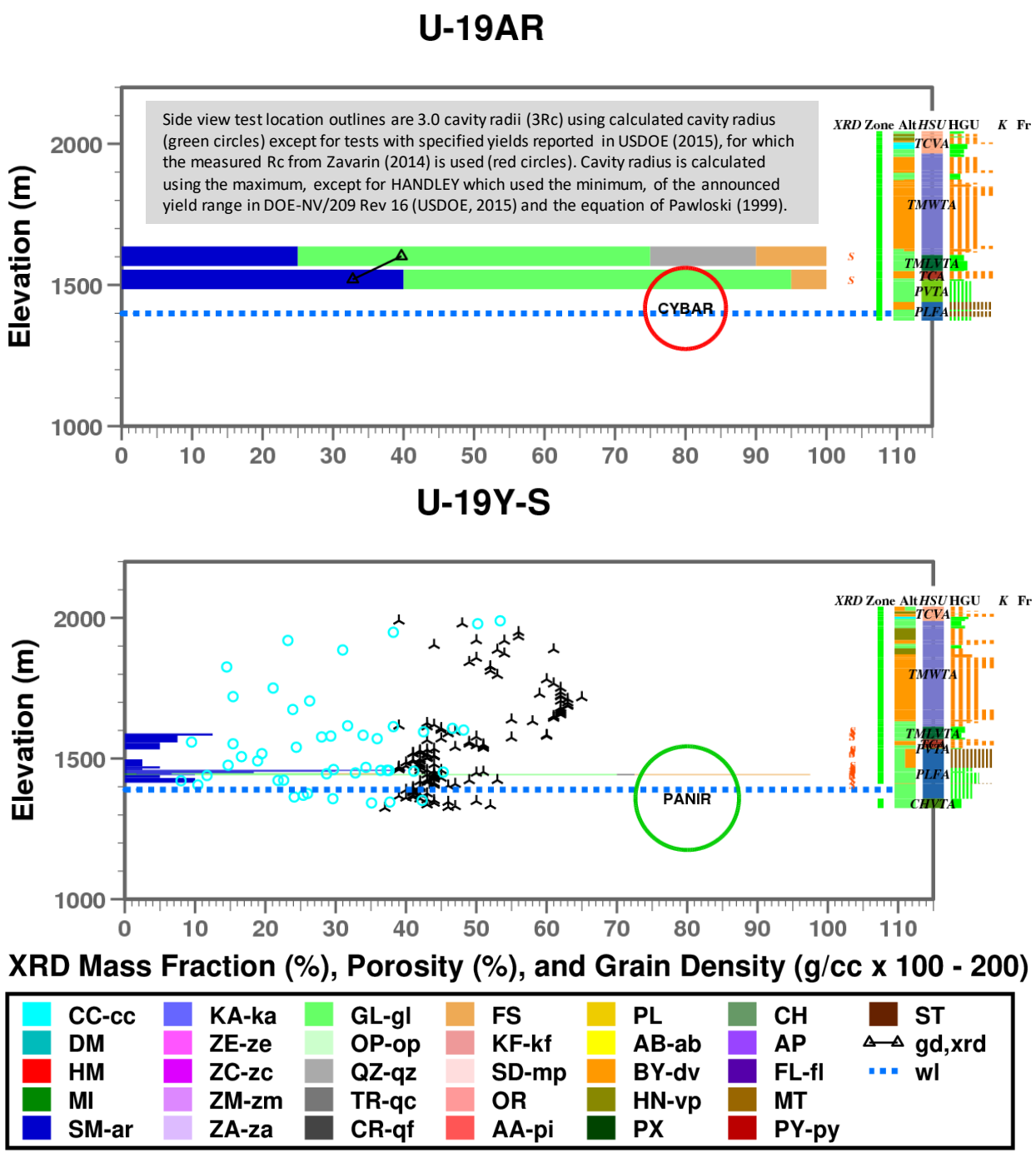

Figure A.11. Graphical representation of XRD and rock property data for boreholes U-19AR and U-19Y-S, SCCC, PM, west-central Area 19, NNSS.

Most or all of the EZ for the CYBAR and PANIR tests is interpreted to be in Zone 1 based on XRD and alteration description as well as HSU and HGU. The CYBAR and PANIR tests are in a similar setting as the AMARILLO and CHANCELLOR tests (Figure A.12).

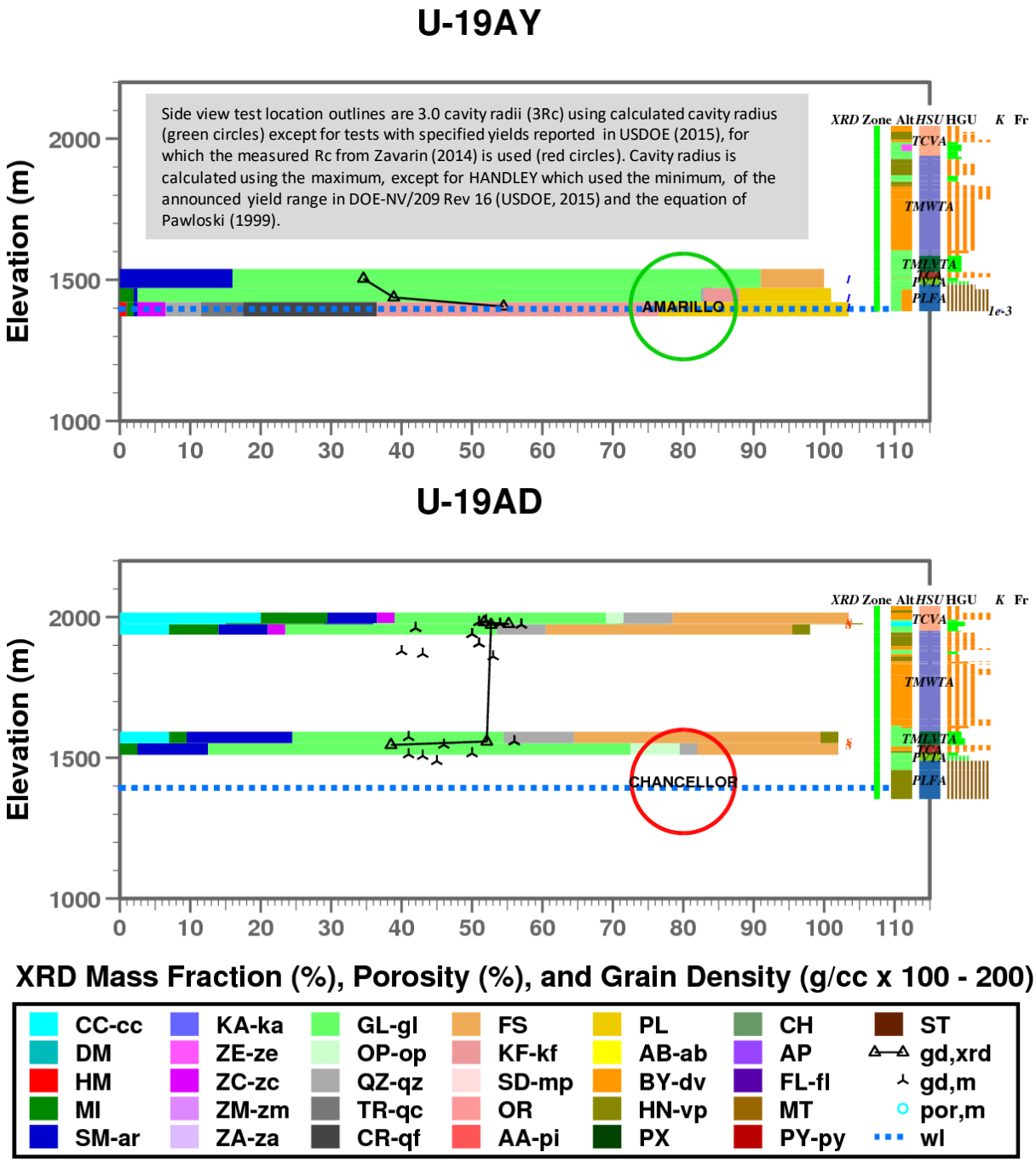

Figure A.12. Graphical representation of XRD and rock property data for boreholes U-19AY (AMARILLO) and U-19AY (CHANCELLOR), SCCC, PM, west-central Area 19, NNSS.

Most or all of the EZ for the PANIR and CHANCELLOR tests is interpreted to be in Zone 1 based on XRD and alteration description as well as HSU and HGU. The AMARILLO and CHANCELLOR tests are in a similar setting as the CYBAR and PANIR tests (Figure A.11).

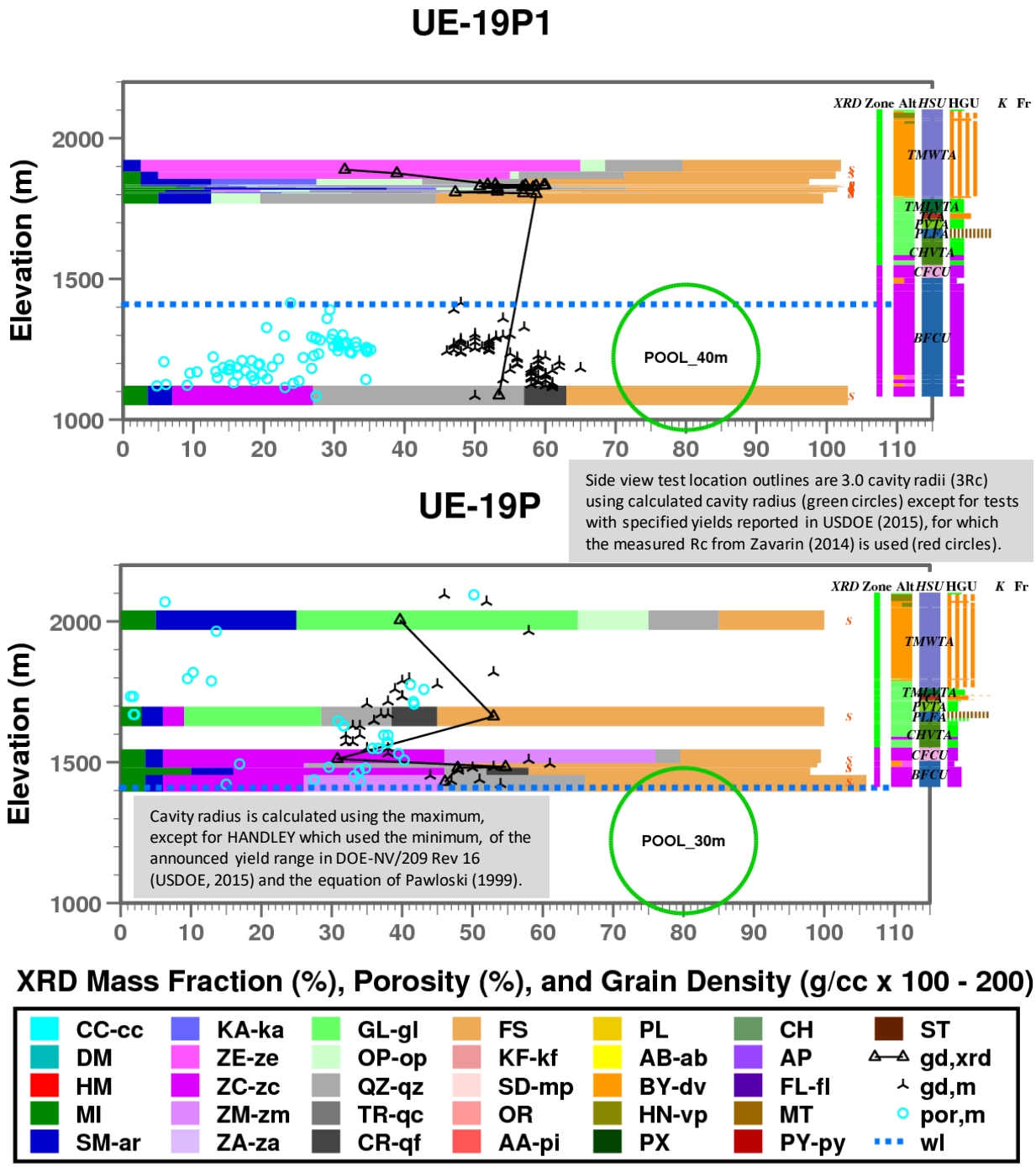

Figure A.13. Graphical representation of XRD and rock property data for boreholes UE-19P1 and UE-19P, SCCC, PM, south-central Area 19, NNSS.

Most or all of the POOL EZ is interpreted to be in Zone 2 based on XRD and alteration description. XRD data for UE-19P1 indicate a zeolitized interval at the base of the TMWTA. This is an example of an element of a deeper zone (Zone 2) present in a shallower zone (Zone 1).

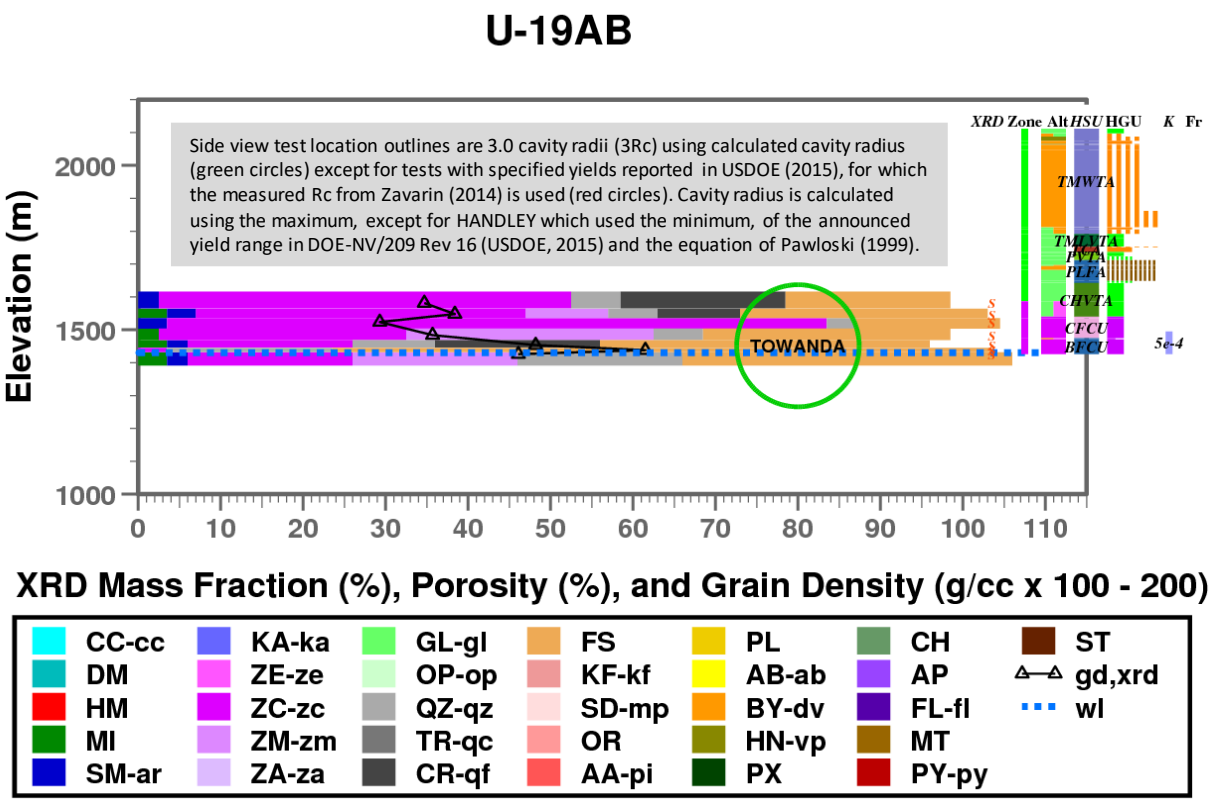

Figure A.14. Graphical representation of XRD and rock property data for borehole U-19AB (TOWANDA), SCCC, PM, south-central Area 19, NNSS.

The middle and upper portions of the TOWANDA EZ is interpreted to be in Zone 2 based on XRD and alteration description. The lower portion of the TOWANDA EZ is expected to remain in Zone 2 based on the XRD for nearby UE-19P1 showing clinoptilolite at about 900 m elevation (Figure A.13)

These S XRD data appear to be of better quality because mica, smectite, mordenite, and cristobalite are resolved. XRD data for U-19AB are consistent with the nearby XRD data for the nearby UE-19P1 and UE-19P (Figure A.13).

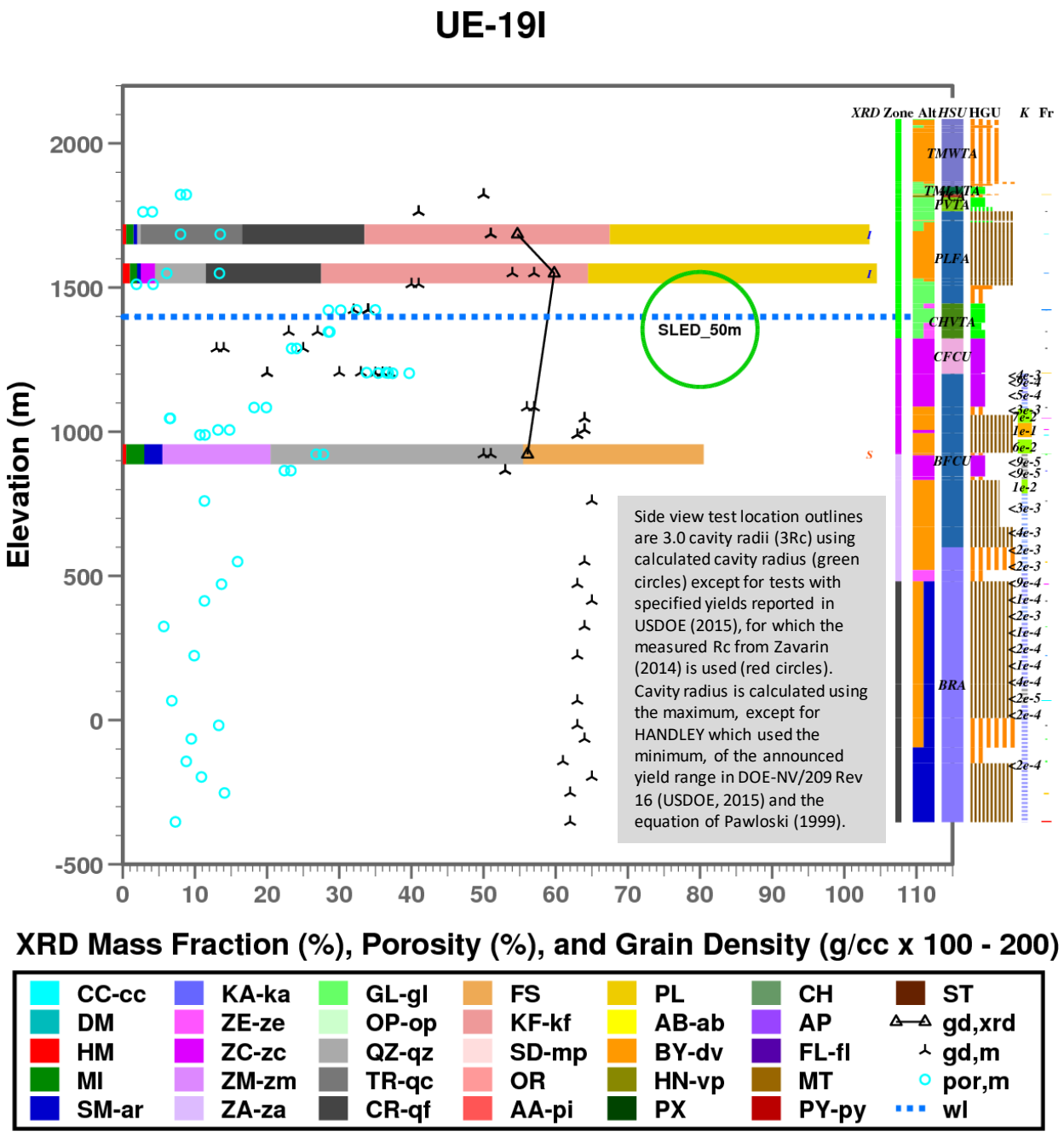

Figure A.15. Graphical representation of XRD and rock property data for borehole UE-19I, SCCC, PM, south-central Area 19, NNSS.

The SLED EZ is interpreted to be in Zones 1 and Zone 2 based on XRD and alteration description as well as HSU and HGU. Grain density data in the CFCU are consistent with zeolitized tuff.

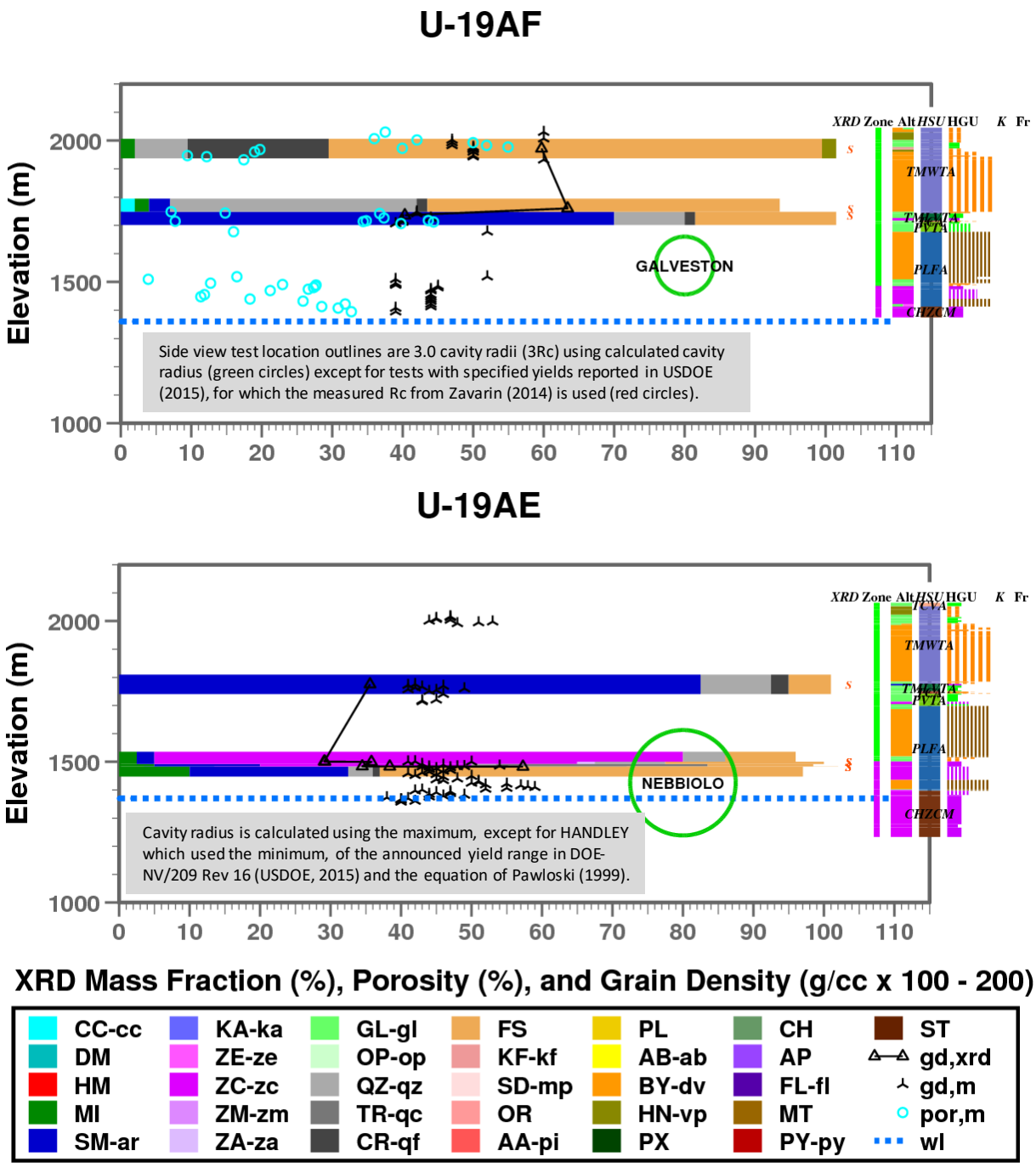

Figure A.16. Graphical representation of XRD and rock property data for boreholes U-19AF and U-19AE, SCCC, PM, southwestern Area 19, NNSS.

The GALVESTON EZ is interpreted to be in Zone 1 based on alteration, HSU, and HGU. The and NEBBIOLO EZ is interpreted to be mostly in Zone 2 and partially in Zone 1 based on XRD and alteration description.

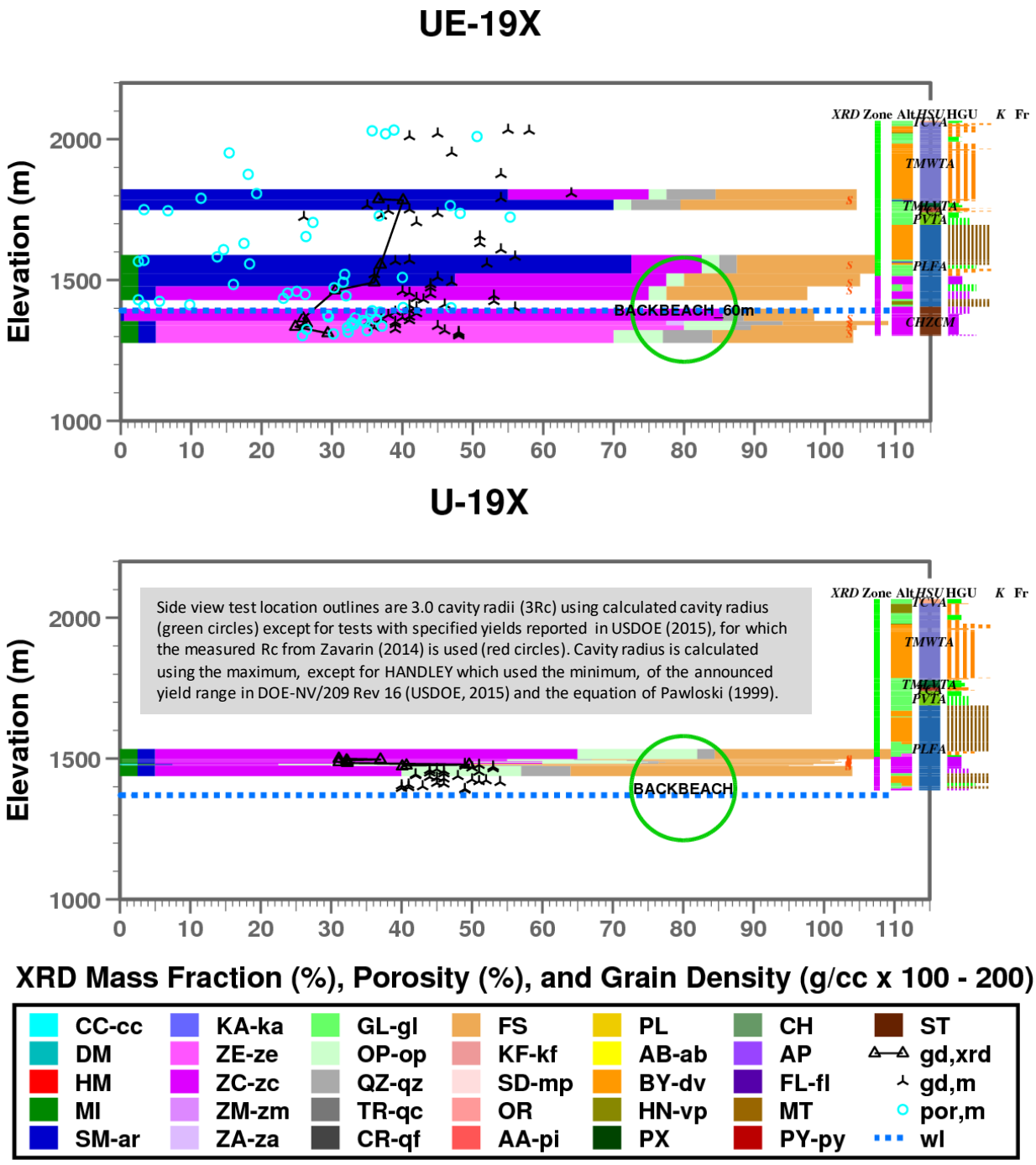

Figure A.17. Graphical representation of XRD and rock property data for boreholes UE-19X and U-19X (BACKBEACH), SCCC, PM, southwestern Area 19, NNSS.

The BACKBEACH EZ is interpreted to be mostly in Zone 2 based on XRD and alteration. In the unsaturated zone above BACKBEACH, the apparent high smectite mass fraction of over 50% is unusual in the PM area, but consistent with XRD data for the nearby GALVESTON and NEBBIOLO tests (Figure A.16).

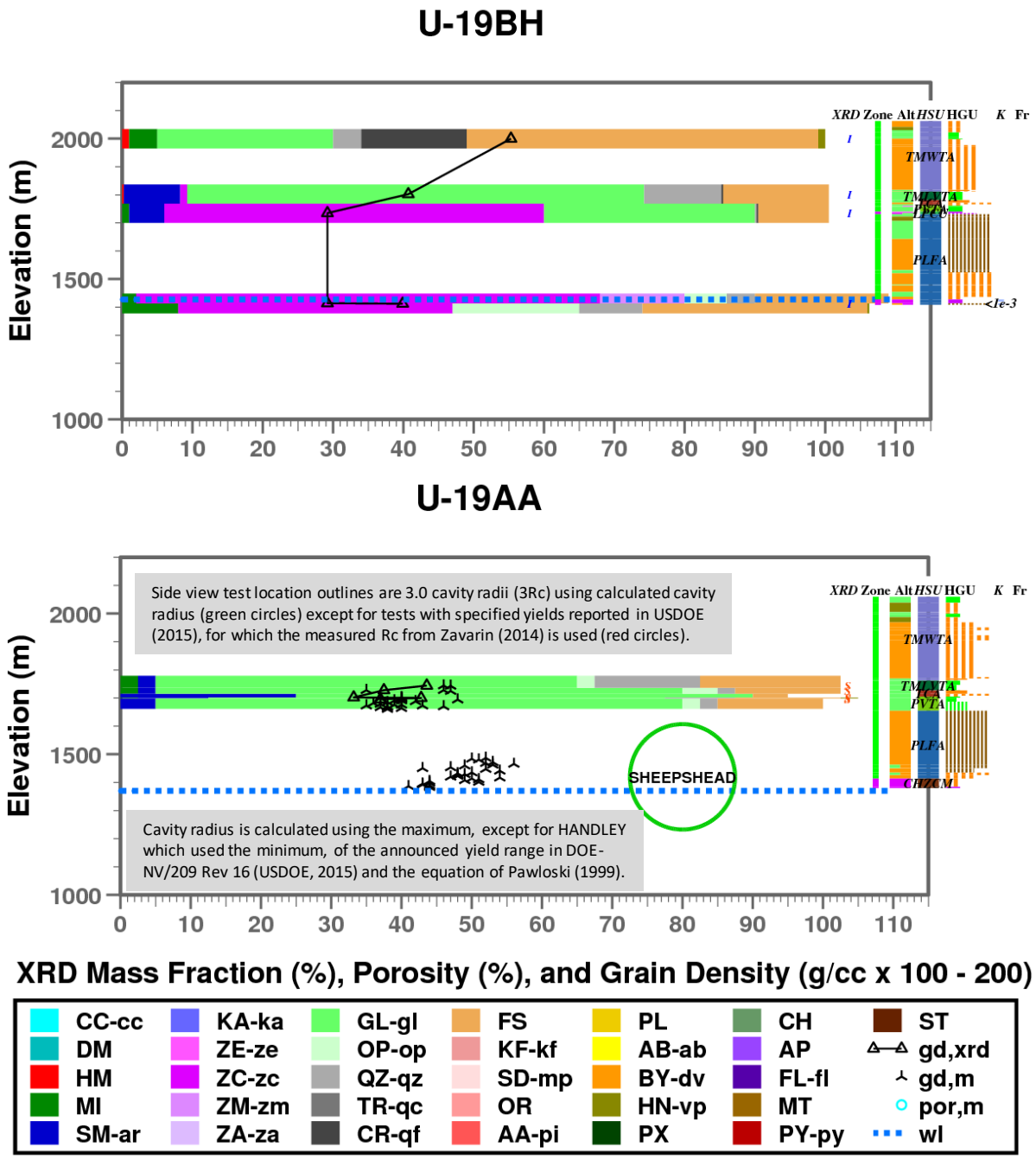

Figure A.18. Graphical representation of XRD and rock property data for boreholes U-19BH and U-19AA (SHEEPSHEAD), SCCC, PM, southwestern Area 19, NNSS.

The SHEEPSHEAD EZ is interpreted to be divided between Zones 1 and 2 based on XRD, alteration, and HSU. Zone 2 can be expected to extent through the CHZCM below SHEEPSHEAD based on XRD data at nearby UE-19X (Figure A.17). Zone 3 may occur in the IA below the CHZCM based on XRD at UE-19F-S (Figure A.19).

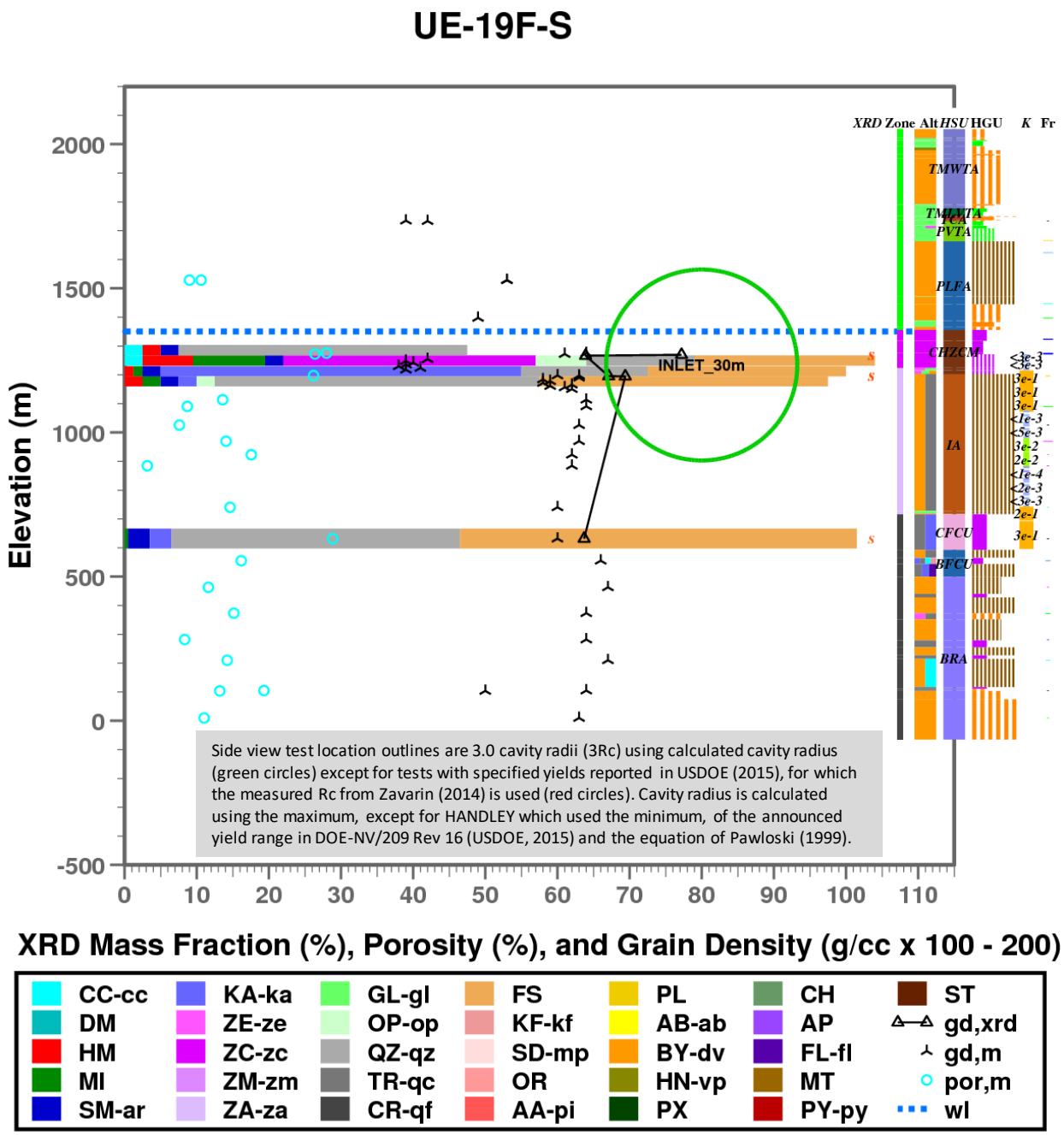

Figure A.19. Graphical representation of XRD and rock property data for borehole UE-19F-S, SCCC, PM, southwestern Area 19, NNSS.

The INLET EZ is interpreted to span in Zones 1, 2, and 3 based on XRD, alteration, HSU, and HGU. The high mass fraction of kaolinite near the topo top of the IA is unusual within the SCCC and more characteristic of high-temperature hydrothermal alteration of feldspar seen in Zone 4 at ER-EC-2A in the northwest TMCC (Figure 19, Section 3.4).

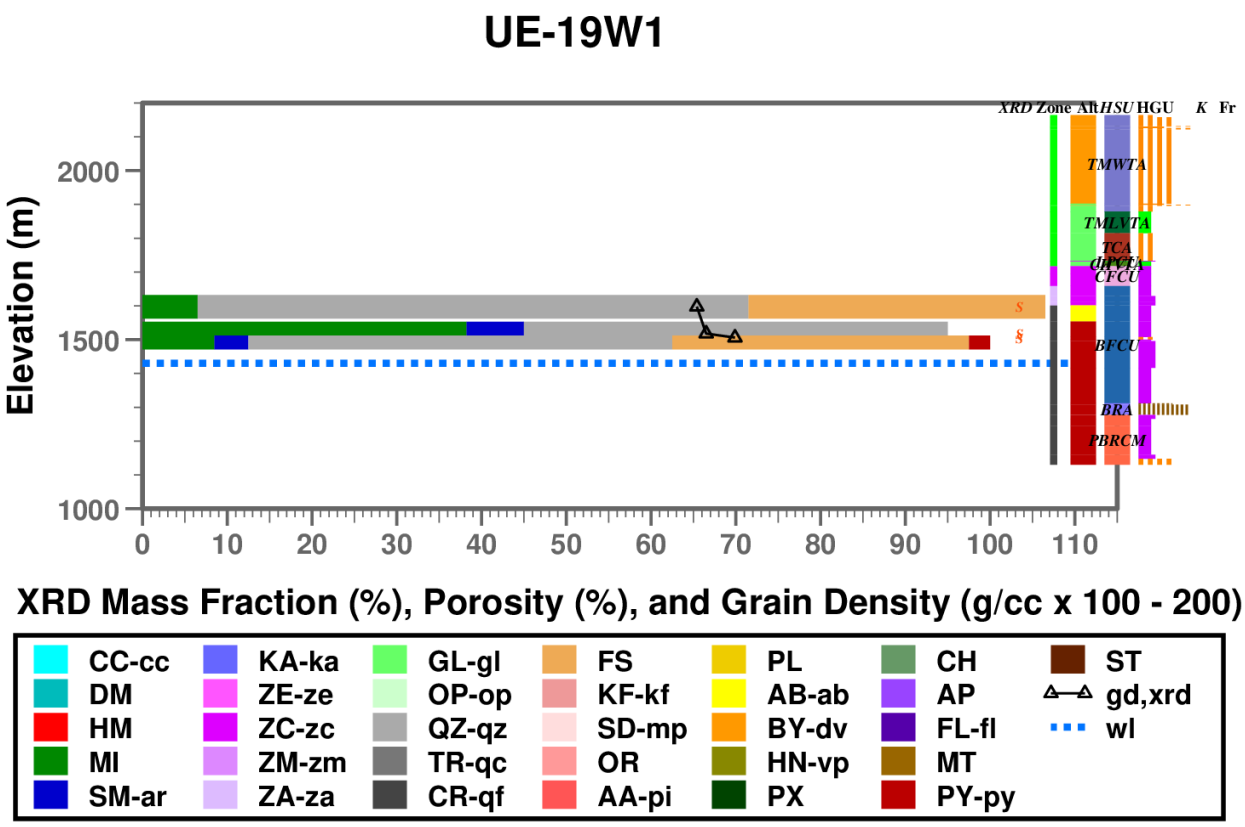

Figure A.20. Graphical representation of XRD and rock property data for borehole UE-19W1, southwest of SCCC, PM, southern Area 19, NNSS.

Borehole UE-19W1 is located in southern Area 19 about 2 km west of the southwestern margin of the SCCC. The XRD data for UE-19W1 are limited to three locations in bedded tuff of the BCU. The S XRD data indicate a prevalence of quartz and feldspar with no zeolite, characteristic of Zone 4. The alteration description indicates the CFCU and upper BFCU are zeolitic. The top of Zone 3 is interpreted to be at top of the BFCU. This limited XRD data suggests that southwest of the SCCC, the water table is within Zone 4, which is not seen anywhere else on PM. Both the XRD and alteration description indicate the presence of pyrite in what is interpreted here as Zone 4.

A.2 Area 20 Boreholes – Central Pahute Mesa CAU

This section includes XRD data from 29 boreholes located in the eastern portion of Area 20, NNSS, and the Central Pahute Mesa CAU. Almost all of the XRD data for the U-20 and UE-20 boreholes in this section were derived from the lower quality S and E methods. Included in this section are high quality XRD data obtained by the F method from boreholes ER-20-6-1 and ER-20-1. Most of the PM, U-20, and UE-20 boreholes include rock property measurements. XRD-derived grain density provides a check on the grain density measurements.

Table A.2 lists Area 20 boreholes within the Central Pahute Mesa CAU with XRD data, general location (see Figure 5 for exact locations), XRD method, adjacent PM test (if emplacement hole or nearby exploration hole), and report figure reference.

Table A.2. List of 29 boreholes with XRD data in PM Area 20, Central Pahute Mesa CAU, NNSS.

Borehole	Location in Area 20	XRD Method(s)	Adjacent PM Test (distance to)	Figure
UE-20E1	northeastern	S	JORUM (460 m)	A.21
U-20AR	northeastern	E	KERNVILLE	A.22
U-20AR1	northeastern	E	KERNVILLE (10 m)	A.22
U-20AA	northeastern	S	COLBY	A.23
U-20AJ	northeastern	S	CABRA	A.23
U-20AD	northeastern	S	PEPATO	A.24
UE-20AD	northeastern	S	PEPATO (30m)	A.24
U-20AF	northeastern	S	KASH	A.25
U-20AN	northeastern	E	SERENA	A.26
U-20AW	northeastern	E	CONTACT	A.26
PM-1	northeastern	I, S	---	A.27
UE-20H	east-central	I	REX	**7**
U-20AI	east-central	E, S	JEFFERSON	A.28
U-20AP	east-central	E	BODIE	A.28
ER-20-6-1	east-central	F, I	BULLION (170 m)	A.29
U-20BD	east-central	E	BULLION	A.29
U-20BD1	east-central	E	BULLION	A.30
U-20BD2	east-central	E	BULLION	A.30
U-20AH	east-central	S	GIBNE	A.31
U-20AC	east-central	S	COLWICK	A.31
U-20BF	east-central	E	MONTELLO	A.32
U-20A2WW	east-central	I, S	CHESHIRE (90 m)	A.33
U-20N	east-central	S	CHESHIRE	A.33
UE-20AV	southeastern	E	HARDIN (40 m)	A.34
U-20AV	southeastern	E	HARDIN	A.34
U-20AX	southeastern	E	---	A.35
U-20BE	southeastern	E	HOYA	A.35
U-20AZ	southeastern	E	BARNWELL	A.36
ER-20-2-1	southeastern	F	---	A.37

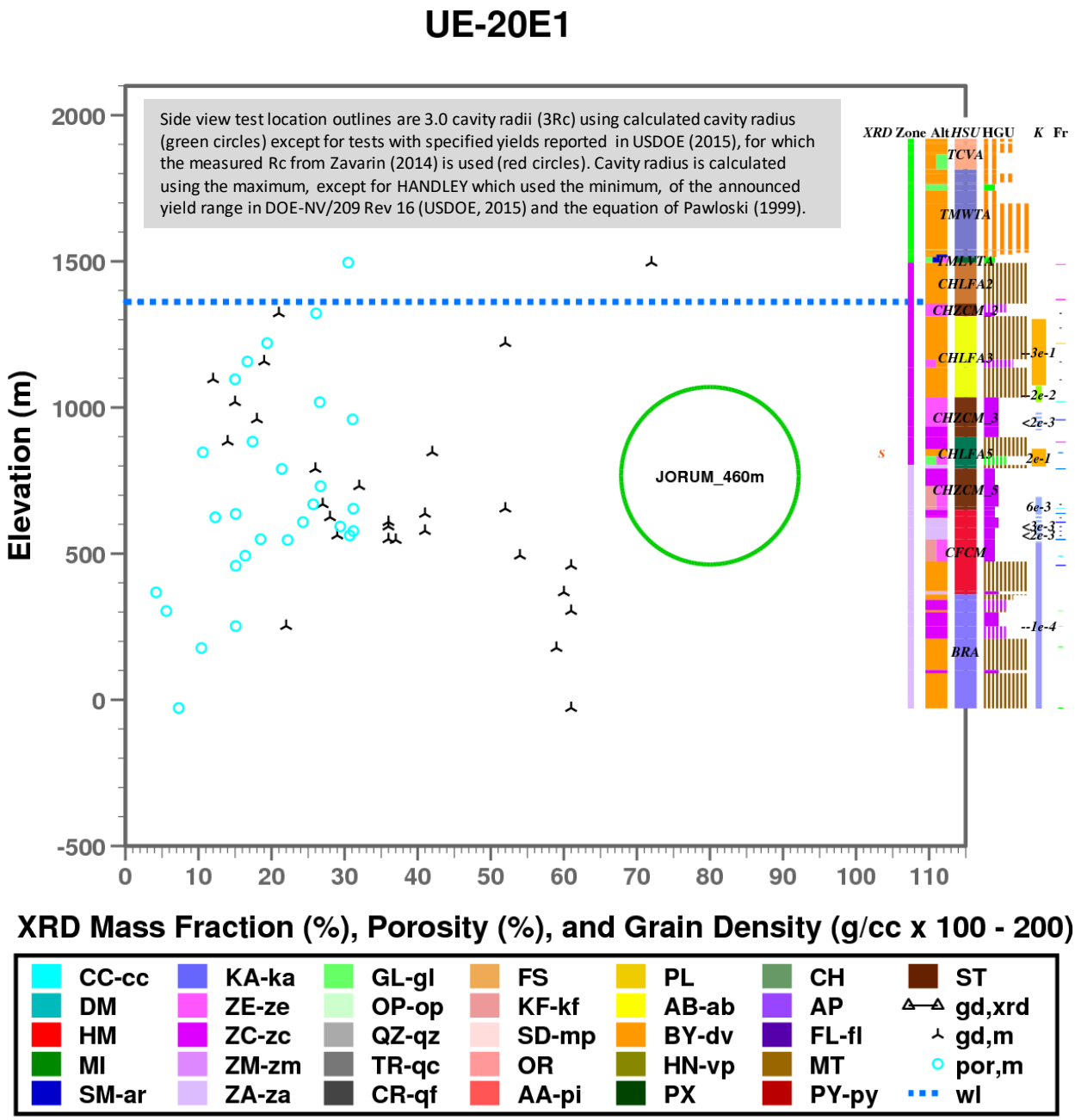

Figure A21. Graphical representation of XRD and rock property data for boreholes U-20E1 (JORUM), SCCC, PM, northeastern Area 20, NNSS.

Only one XRD data location was found for UE-20E1, apparently of non-quantitative subjective origin. The location of Zone 3 is interpreted from alteration and grain density. The JORUM EZ is interpreted to be in Zones 2 and 3.

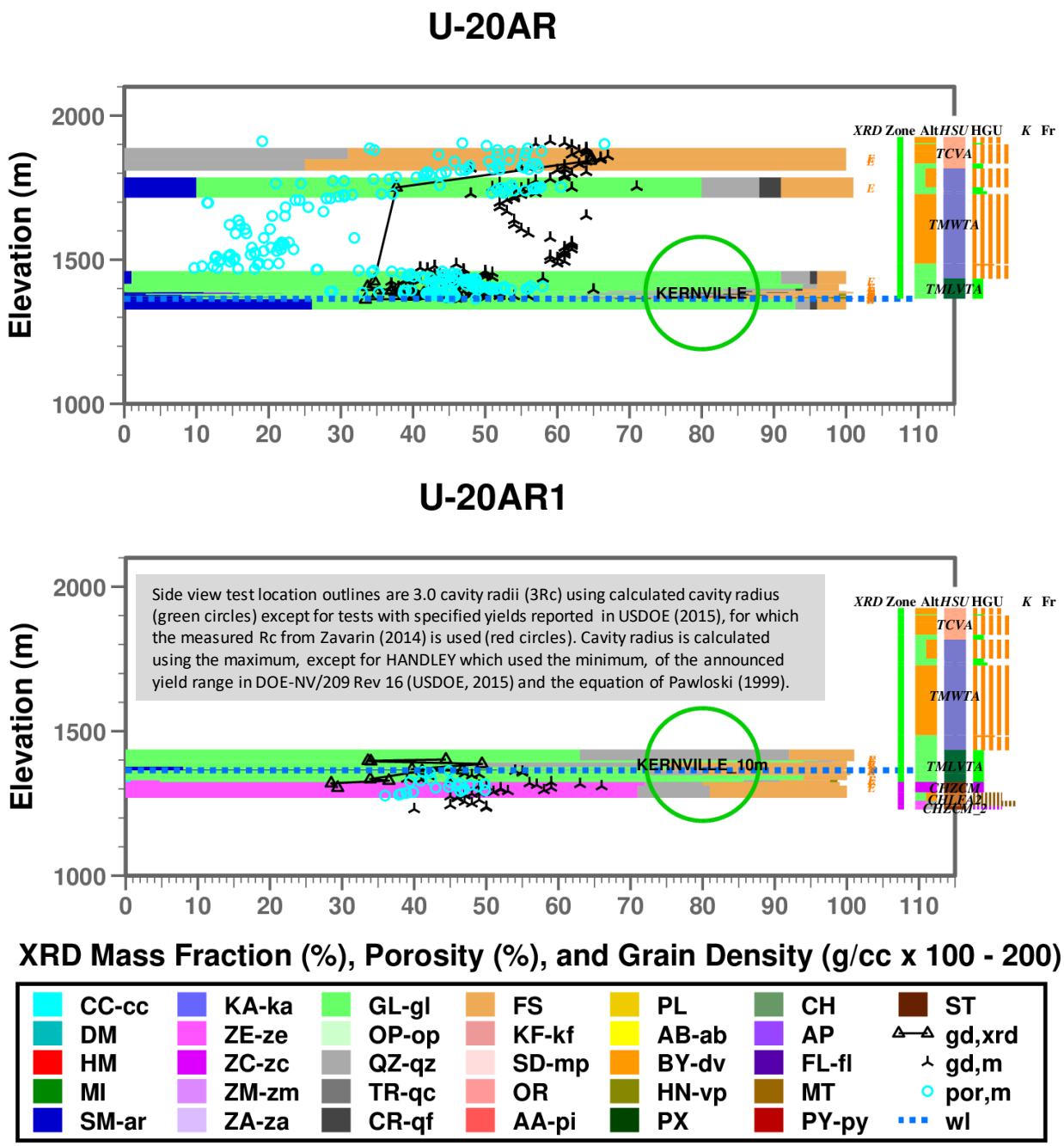

Figure A.22. Graphical representation of XRD and rock property data for boreholes U-20AR (KERNVILLE) and U-20AR1, SCCC, PM, northeastern Area 20, NNSS.

Most of the KERNVILLE EZ is located in Zone 1, with the lower portion of the EZ in Zone 2 based on XRD, alteration, HSU, and HGU. Within the highly zeolitized intervals of U-20AR1, the measured grain density appears to be overestimated by 0.2 g/cc or greater.

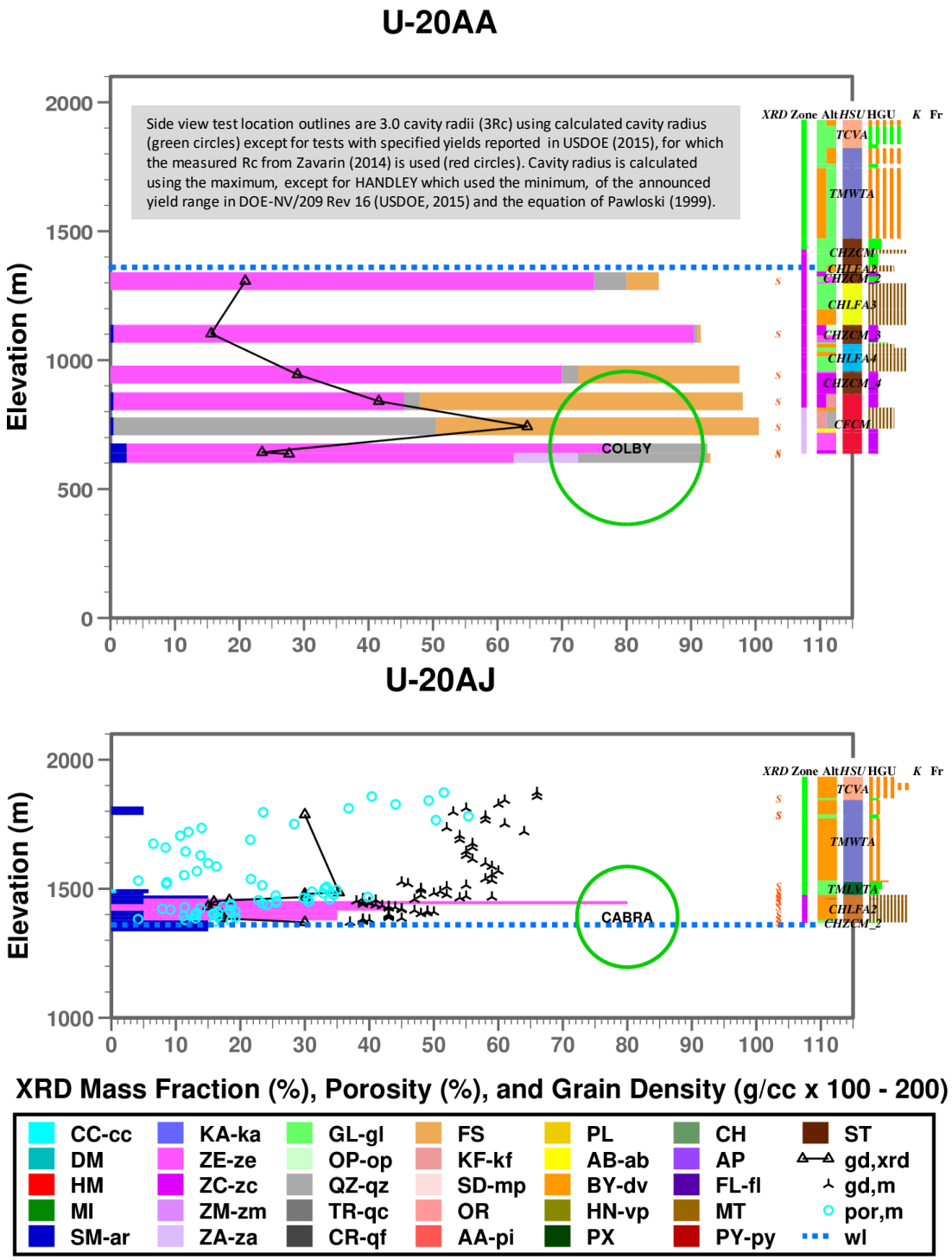

Figure A.23. Graphical representation of XRD and rock property data for borehole U-20AA (COLBY) and U-20AJ (CABRA), SCCC, PM, northeastern Area 20, NNSS.

Most of the COLBY EZ is interpreted to be Zone 3, with the upper portion of the EZ in Zone 2 based on XRD, alteration, HSU, and HGU. The XRD obtained from the S method do not differentiate zeolite minerals except for some analcime near the middle of the COLBY EZ. About 1 km to the southeast, the CABRA EZ is interpreted to be in Zones 1 and 2.

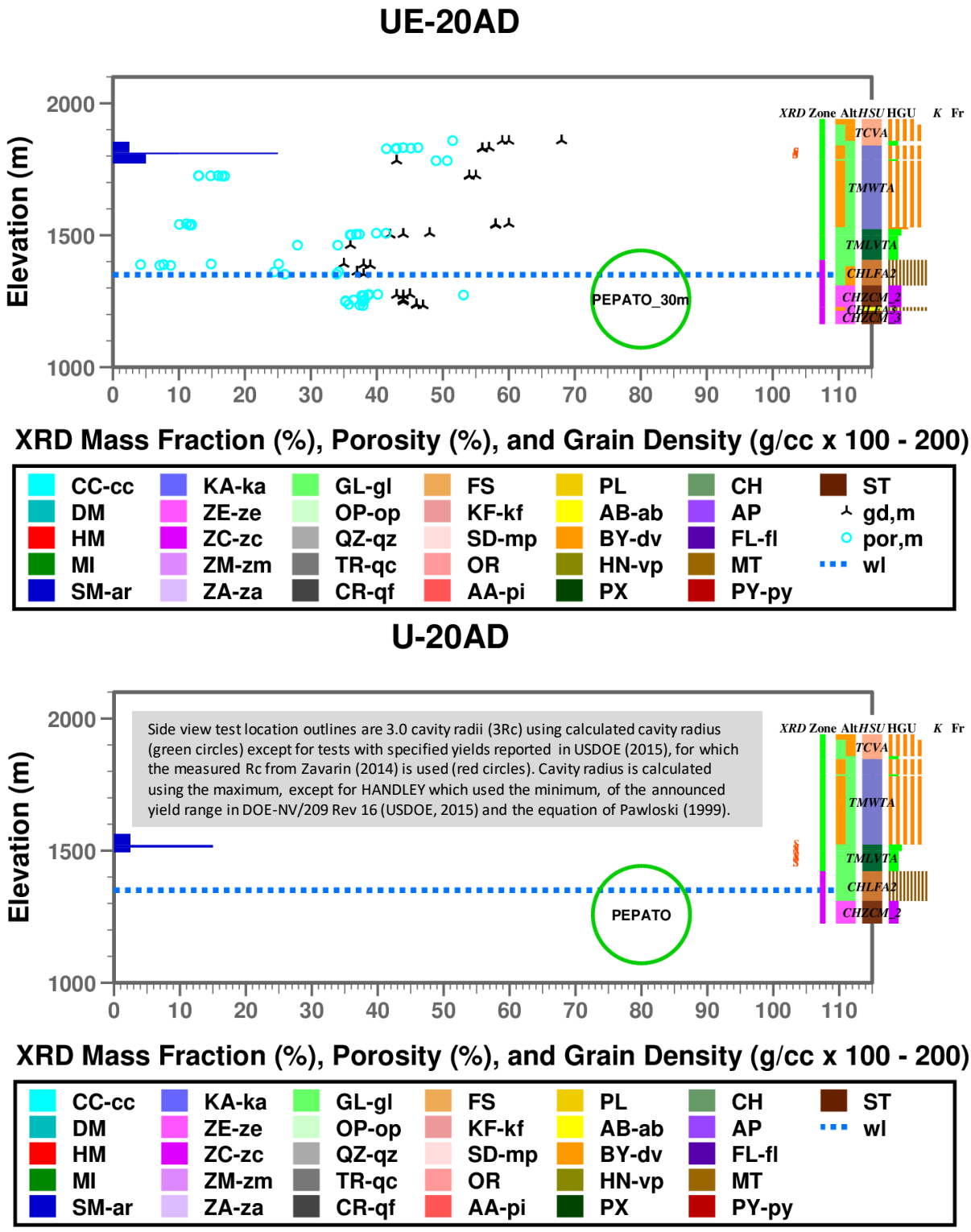

Figure A.24. Graphical representation of XRD and rock property data for boreholes UE-20AD and U-20AD (PEPATO), SCCC, PM, northeastern Area 20, NNSS.

Most of the PEPATO EZ is interpreted to be Zone 2 based on alteration, HSU, and HGU. At nearby U-20AJ (CABRA), the CHLFA2 is zeolitic based on XRD (Figure A.23).

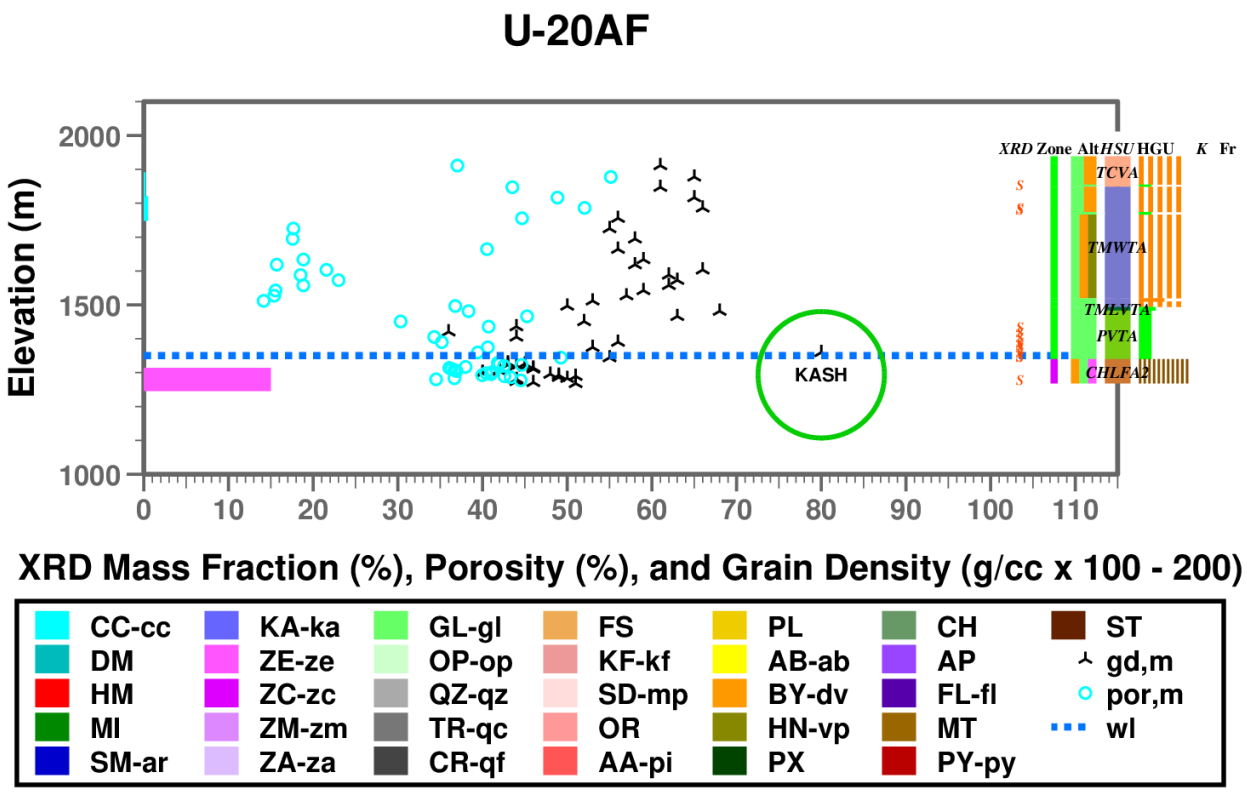

Side view test location outlines are 3.0 cavity radii (3Rc) using calculated cavity radius (green circles) except for tests with specified yields reported in USDOE (2015), for which the measured Rc from Zavarin (2014) is used (red circles). Cavity radius is calculated using the maximum, except for HANDLEY which used the minimum, of the announced yield range in DOE-NV/209 Rev 16 (USDOE, 2015) and the equation of Pawloski (1999).

Figure A.25. Graphical representation of XRD and rock property data for borehole U-20AF (KASH), SCCC, northeastern Area 20, NNSS.

THE KASH EZ is interpreted to be Zones 1 and 2 based on alteration, HSU, and HGU. The limited XRD data indicate the CHLFA2 is zeolitic, as at nearby U-20AJ (Figure A.23).

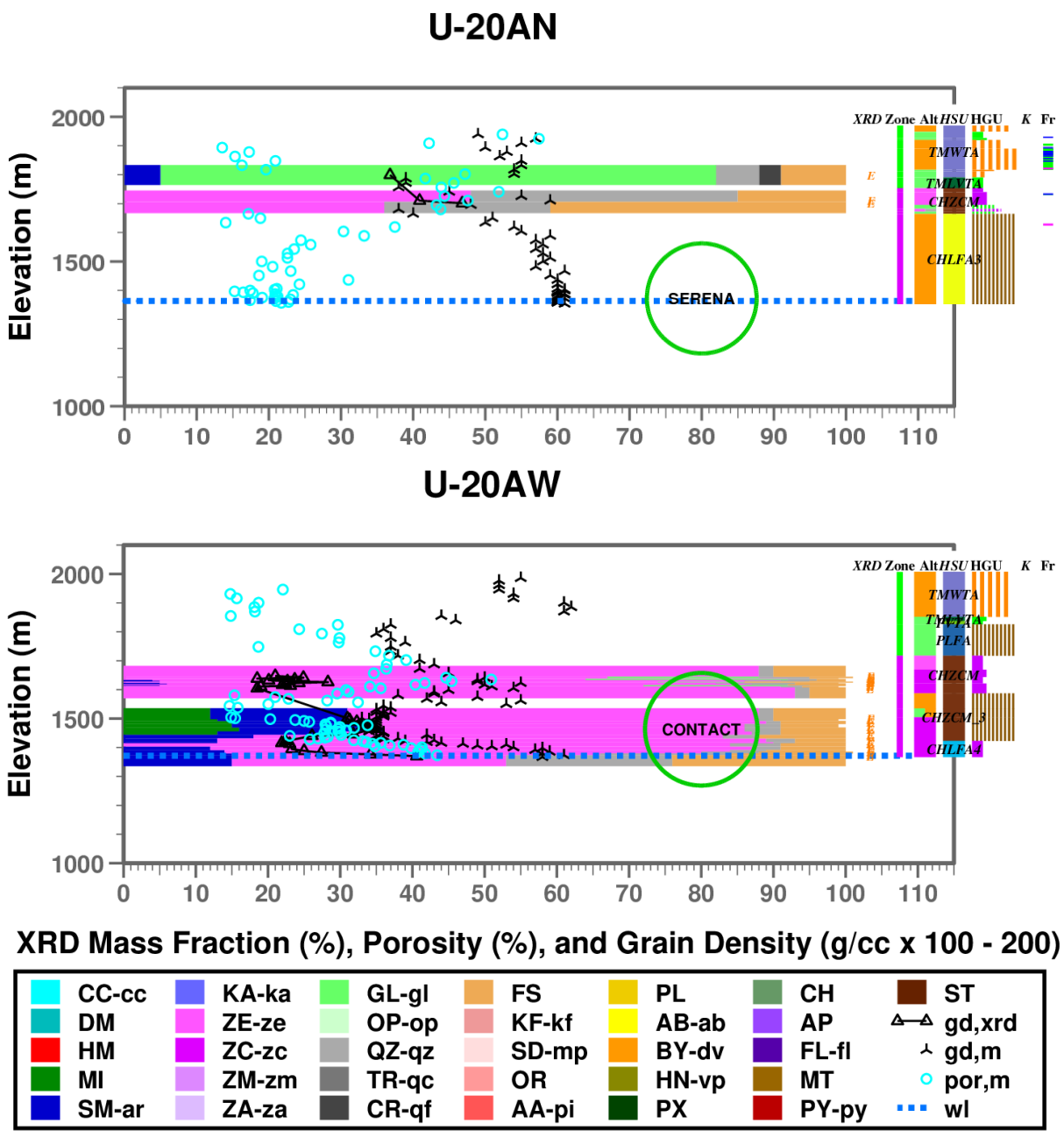

Side view test location outlines are 3.0 cavity radii (3Rc) using calculated cavity radius (green circles) except for tests with specified yields reported in USDOE (2015), for which the measured Rc from Zavarin (2014) is used (red circles). Cavity radius is calculated using the maximum, except for HANDLEY which used the minimum, of the announced yield range in DOE-NV/209 Rev 16 (USDOE, 2015) and the equation of Pawloski (1999).

Figure A.26. Graphical representation of XRD and rock property data for boreholes U-20AN (SERENA) and U-20AW (CONTACT), SCCC, PM, northeastern Area 20, NNSS.

The SERENA EZ is interpreted to be in Zone 2 based on alteration, HSU, and HGU. The CONTACT EZ is located in Zone 2 based on XRD, alteration, HSU, and HGU. Within the highly zeolitized intervals of U-20AW, the measured grain density appears to be overestimated by 0.2 g/cc or greater.

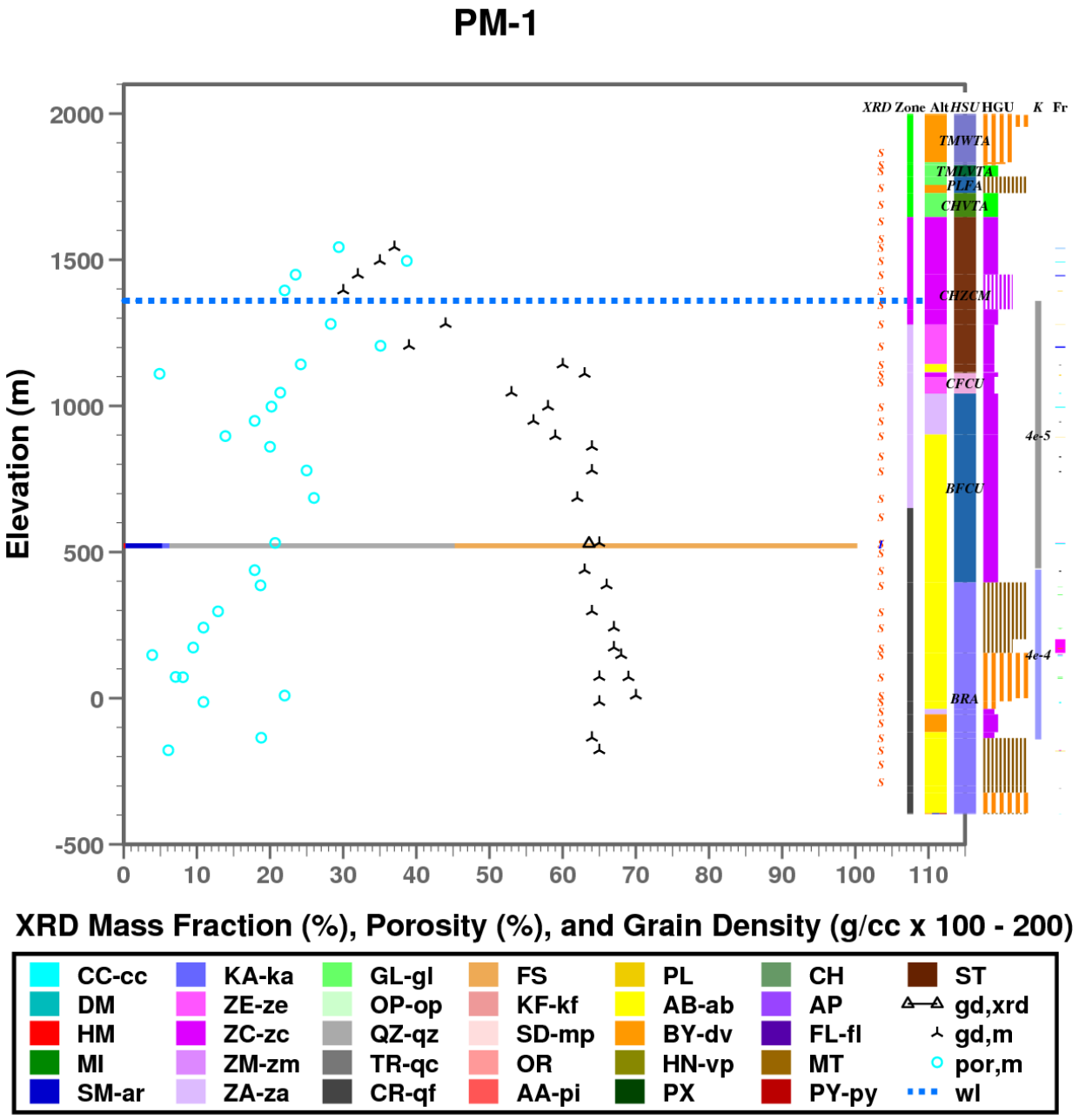

Figure A.27. Graphical representation of XRD and rock property data for borehole PM-1, SCCC, PM, northeastern Area 20, NNSS.

The PM-1 borehole was included in the original interpretation of diagenesis at PM by Moncure et al. (1981), but without presentation of any XRD data. The original PM-1 XRD data was obtained by a non-quantitative subjective method. One XRD datum obtained by the I method was added, indicating the TCU within the BFCU is quartzofeldpathic at about 500 m elevation. The interpreted location of Zone 4 is supported by the high measured grain density of over 2.6 g/cc.

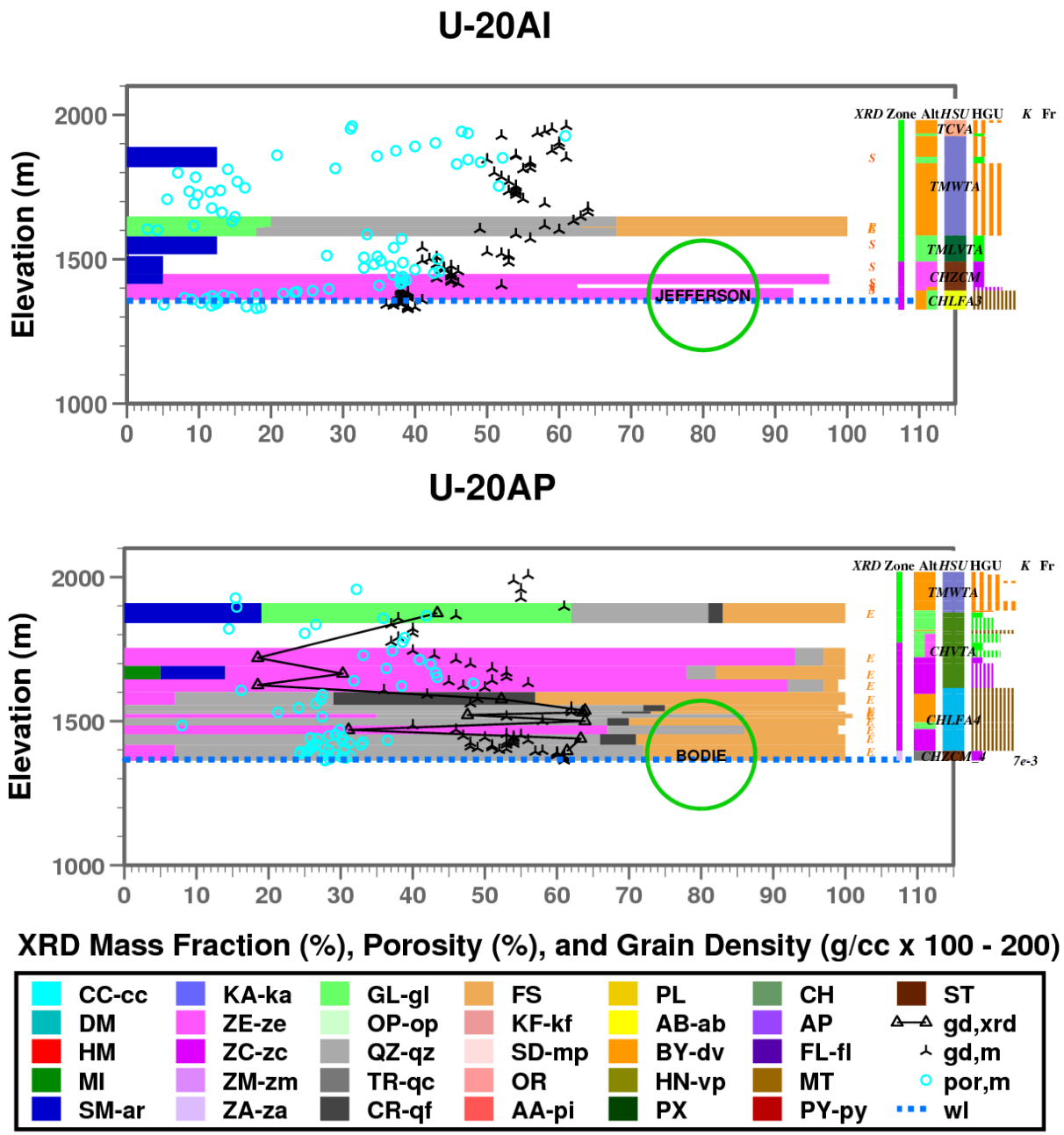

Side view test location outlines are 3.0 cavity radii (3Rc) using calculated cavity radius (green circles) except for tests with specified yields reported in USDOE (2015), for which the measured Rc from Zavarin (2014) is used (red circles). Cavity radius is calculated using the maximum, except for HANDLEY which used the minimum, of the announced yield range in DOE-NV/209 Rev 16 (USDOE, 2015) and the equation of Pawloski (1999).

Figure A.28. Graphical representation of XRD and rock property data for boreholes U-20AI (JEFFERSON) and U-20AW (BODIE), SCCC, PM, east-central Area 20, NNSS.

The JEFFERSON EZ is in Zones 1 and 2, and the BODIE EZ is interpreted to be in Zones 2 and 3 based on XRD, alteration, HSU, and HGU. Within the highly zeolitized intervals of U-20AP, the measured grain density appears to be overestimated by 0.2 g/cc or greater.

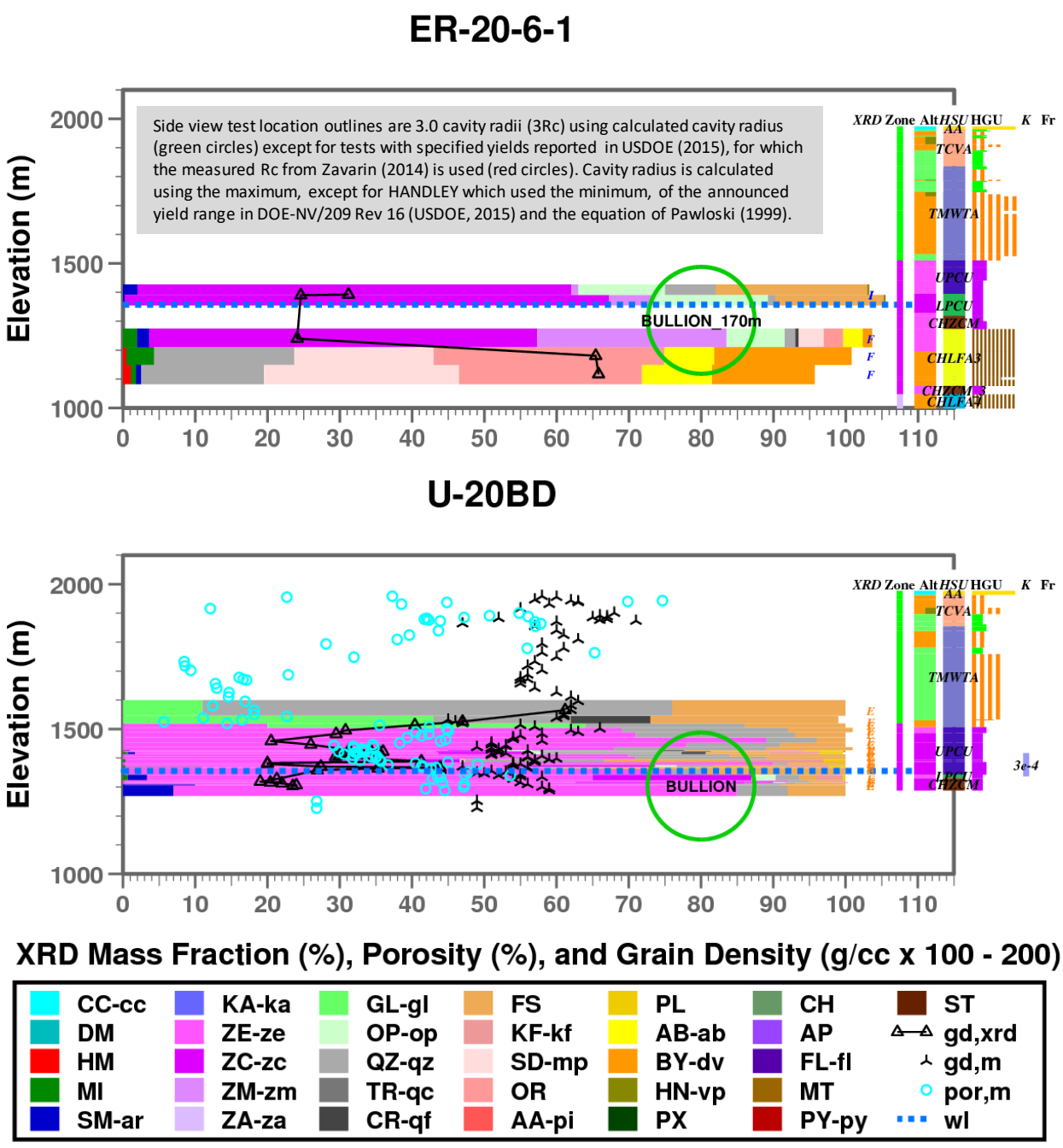

Figure A.29. Graphical representation of XRD and rock property data for boreholes ER-20-6-1 and U-20BD (BULLION), SCCC, PM, east-central Area 20, NNSS.

The BULLION EZ is located in Zone 2 based on XRD, alteration, HSU, and HGU. Within the highly zeolitized intervals of U-20BD, the measured grain density appears to be overestimated by 0.2 g/cc or greater.

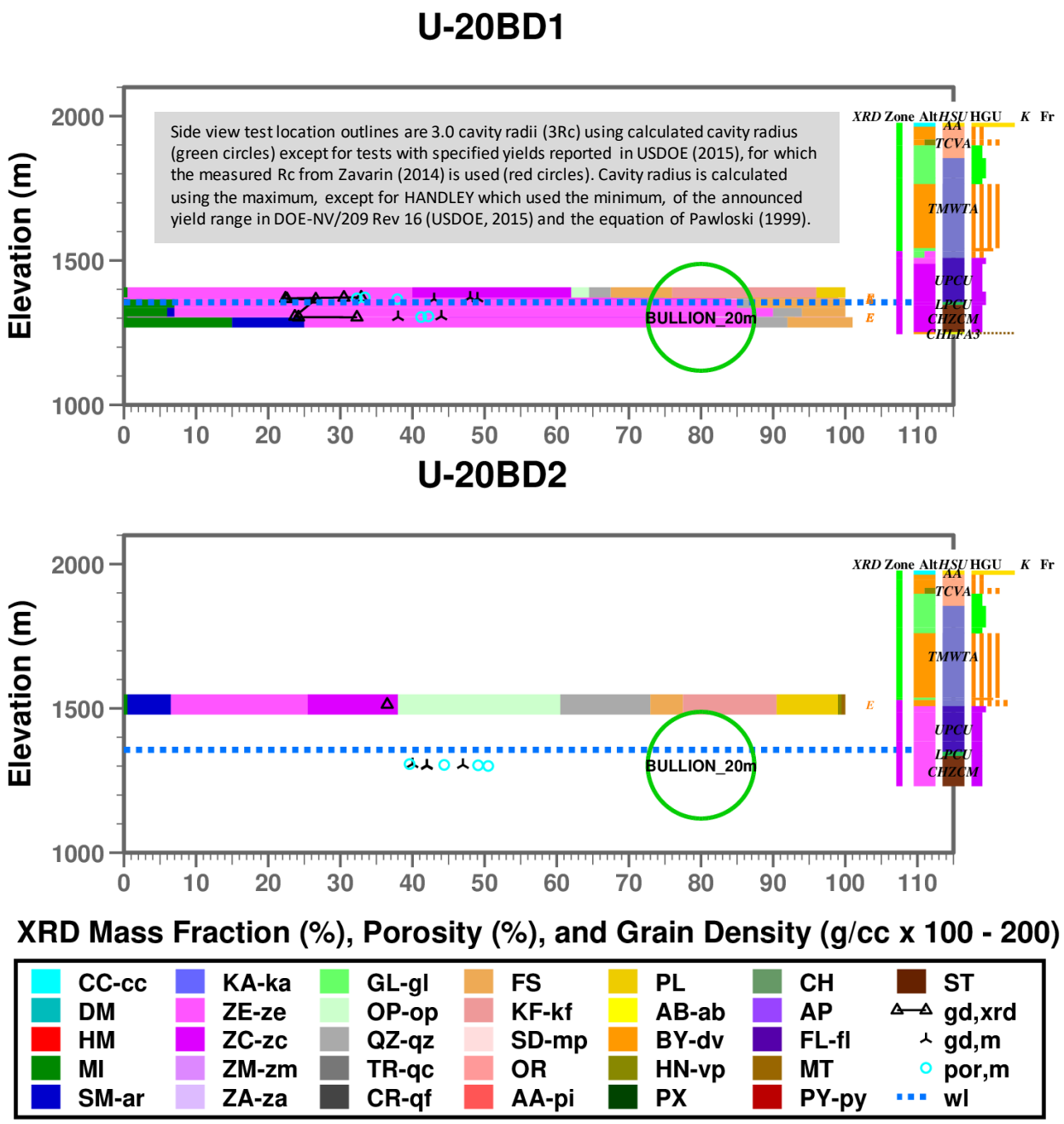

Figure A.30. Graphical representation of XRD and rock property data for boreholes U-20BD1 and U-20BD2, SCCC, PM, east-central Area 20, NNSS.

The E XRD data for boreholes U-20BD1 and U-20BD2 further support the location of the BULLION EZ in Zone 2.

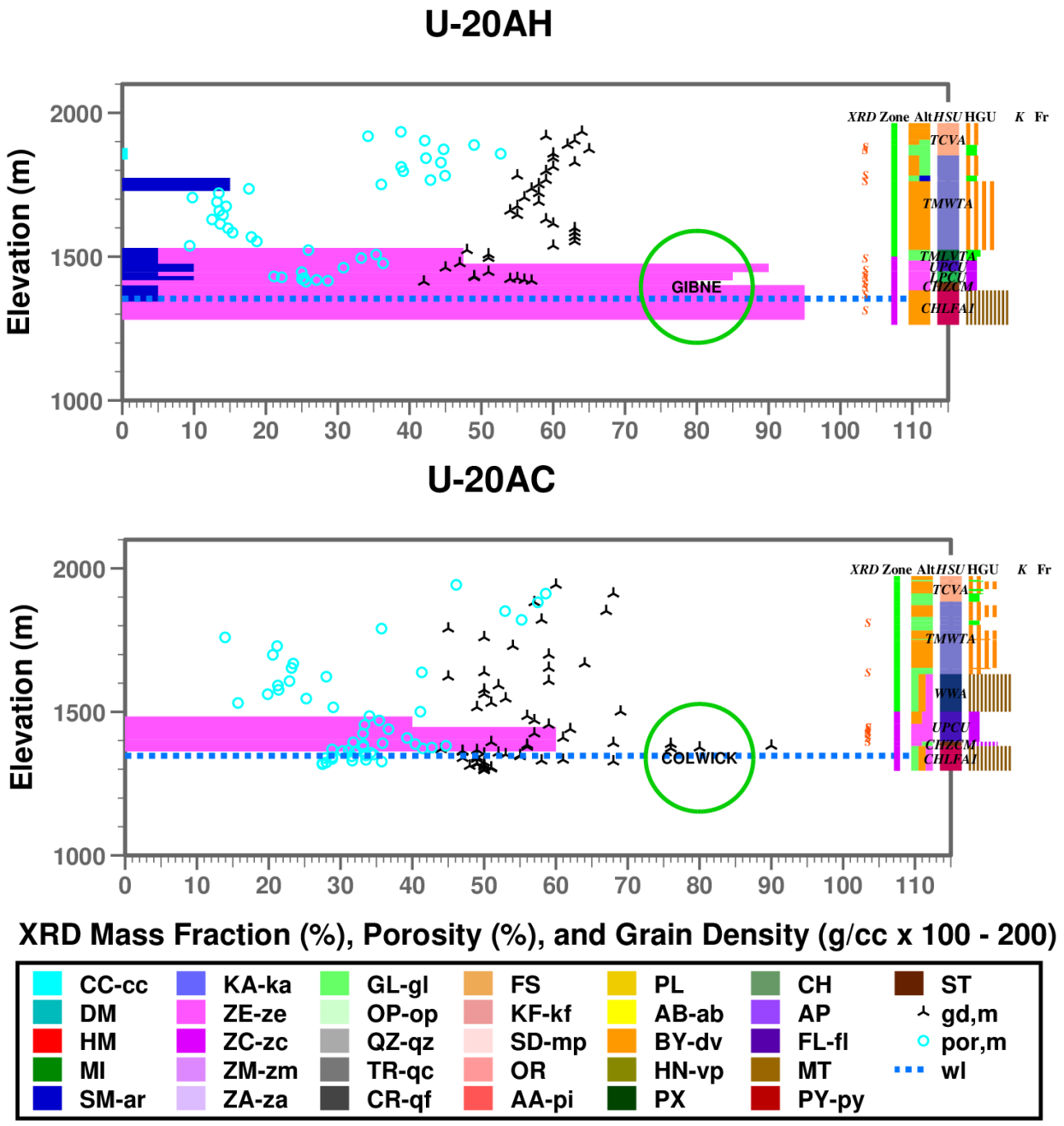

Side view test location outlines are 3.0 cavity radii (3Rc) using calculated cavity radius (green circles) except for tests with specified yields reported in USDOE (2015), for which the measured Rc from Zavarin (2014) is used (red circles). Cavity radius is calculated using the maximum, except for HANDLEY which used the minimum, of the announced yield range in DOE-NV/209 Rev 16 (USDOE, 2015) and the equation of Pawloski (1999).

Figure A.31. Graphical representation of XRD and rock property data for boreholes U-20AH (GIBNE) and U-20AC (COLWICK), SCCC, PM, east-central Area 20, NNSS.

For GIBNE and COLWICK, the EZ is mostly in Zone 2 based on the limited XRD data, alteration, HSU, and HGU.

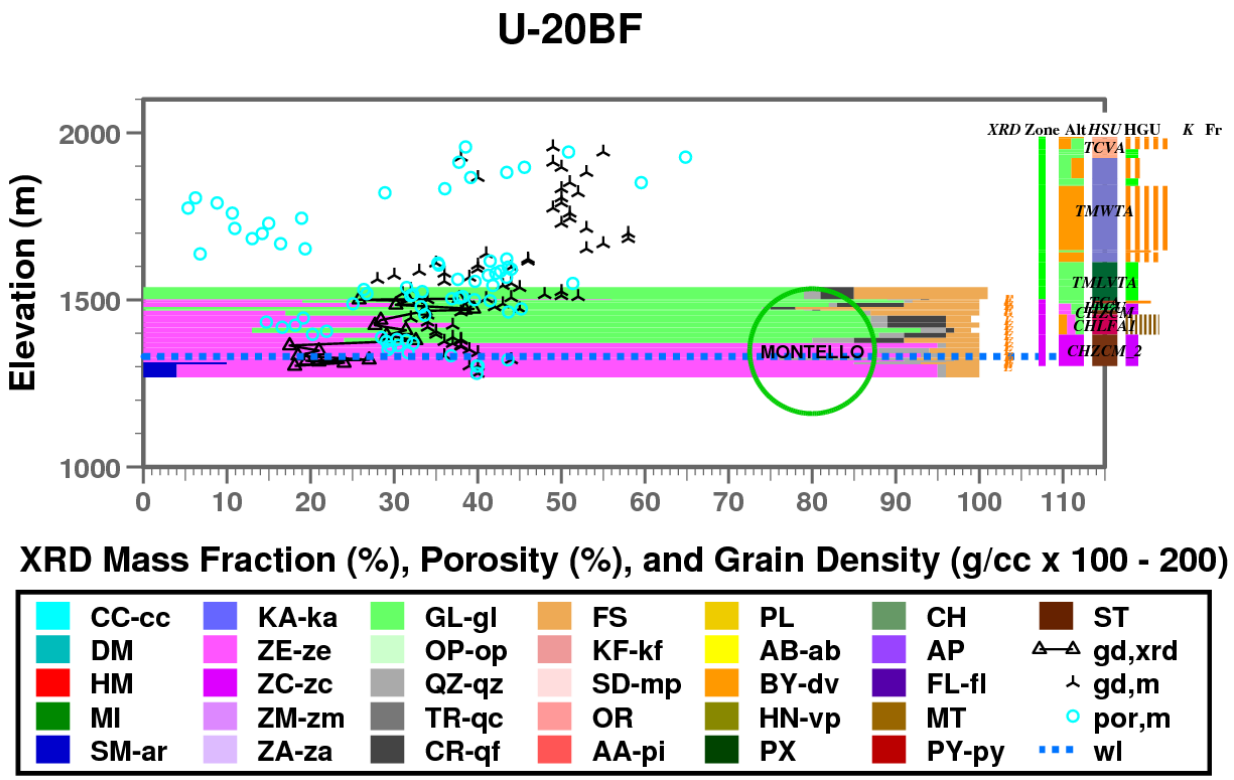

Side view test location outlines are 3.0 cavity radii (3Rc) using calculated cavity radius (green circles) except for tests with specified yields reported in USDOE (2015), for which the measured Rc from Zavarin (2014) is used (red circles). Cavity radius is calculated using the maximum, except for HANDLEY which used the minimum, of the announced yield range in DOE-NV/209 Rev 16 (USDOE, 2015) and the equation of Pawloski (1999).

Figure A.32. Graphical representation of XRD and rock property data for borehole U-20BF (MONTELLO), SCCC, PM, east-central Area 20, NNSS.

The MONTELLO EZ is mostly in Zone 2 based on XRD, alteration, HSU, and HGU. The high glass mass fraction in the upper portion of the MONTELLO EZ is transitional to Zone 1. Within the highly zeolitized intervals of U-20BF, the measured grain density appears to be overestimated by 0.2 g/cc or greater.

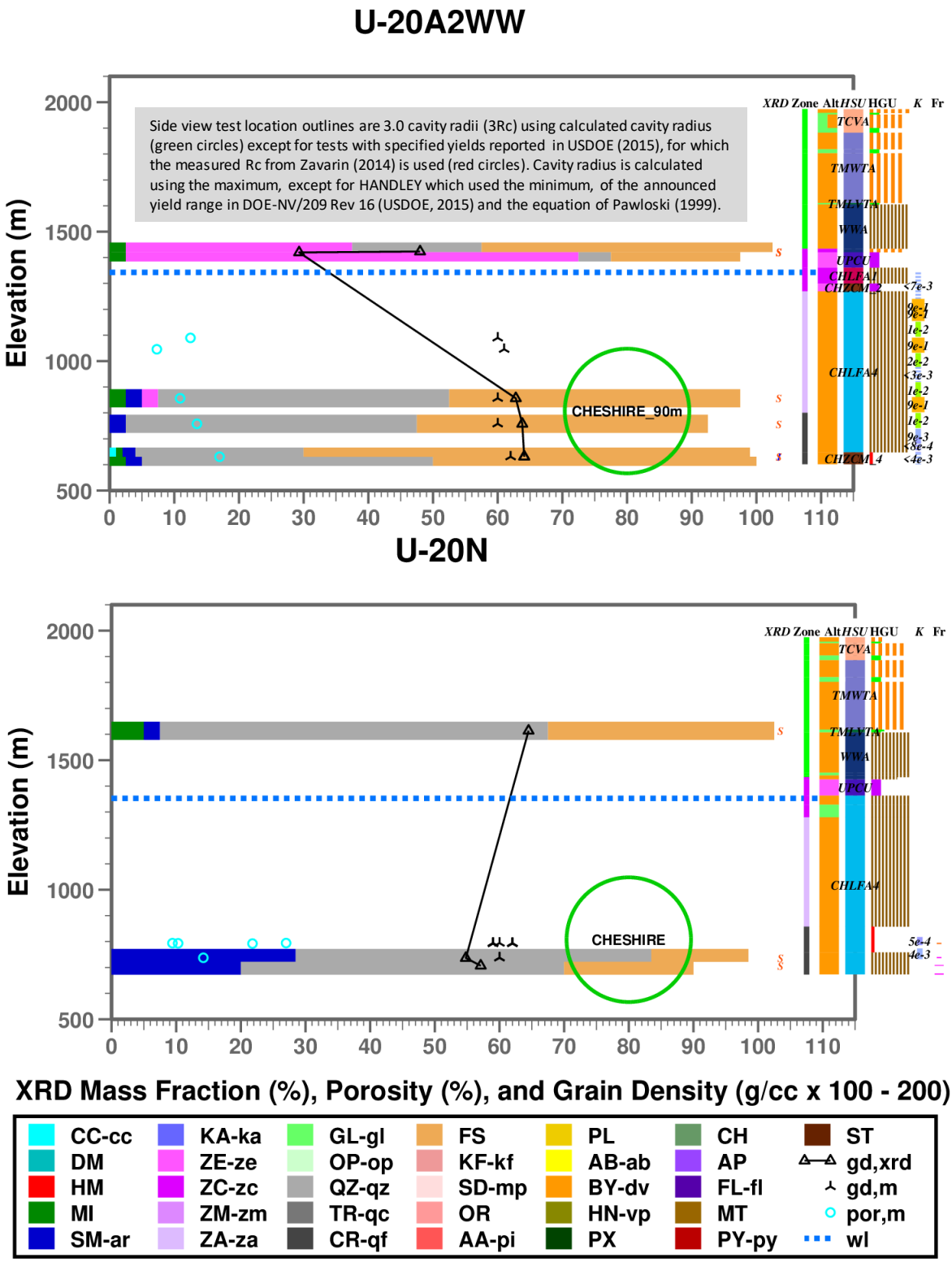

Figure A.33. Graphical representation of XRD and rock property data for boreholes U-20A2WW and U-20N, SCCC, PM, east-central Area 20, NNSS.

The CHESHIRE EZ is in Zones 3 and 4 based on interpretation of XRD and alteration. The XRD and grain density from nearby U-20A2WW support this interpretation.

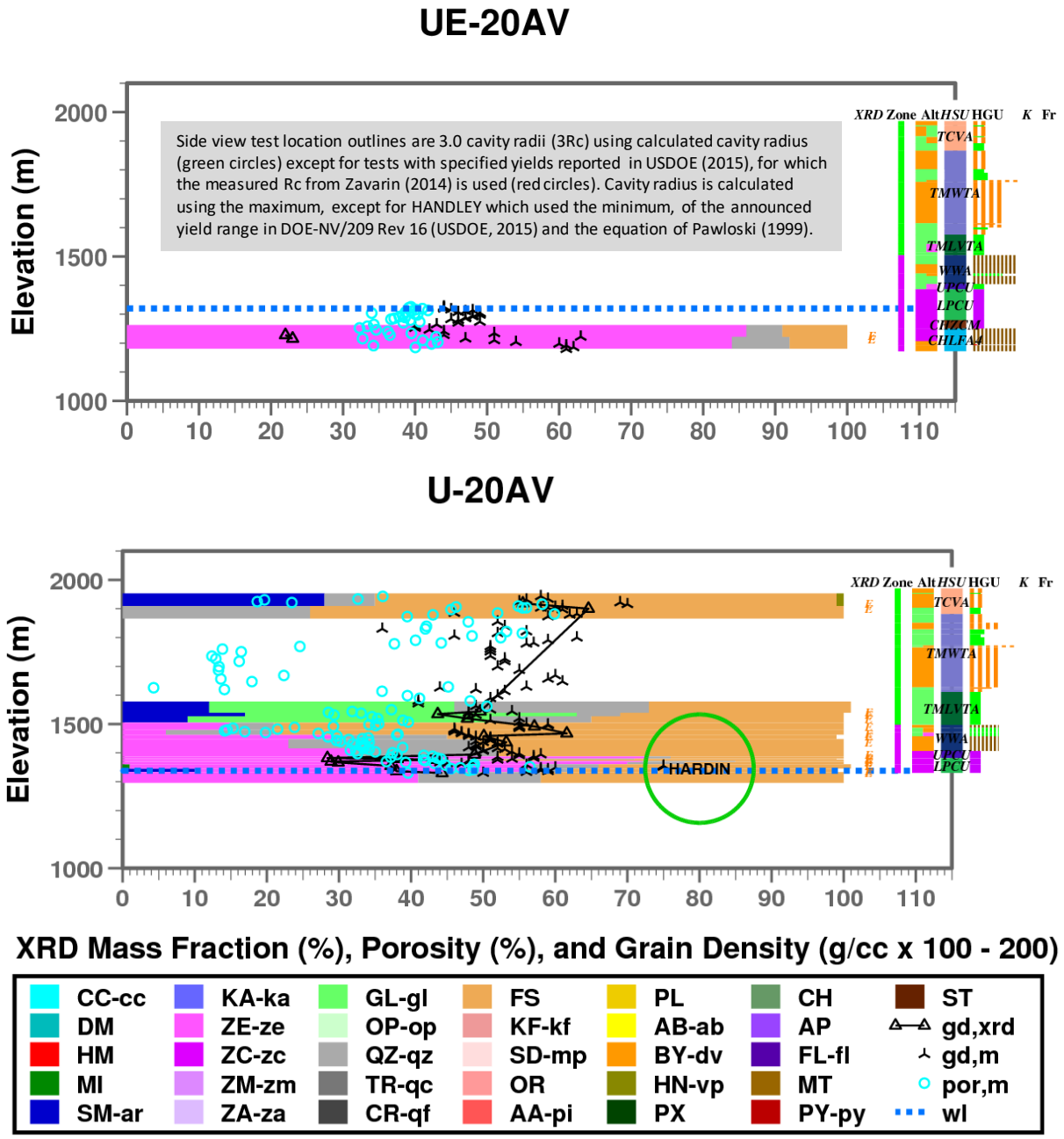

Figure A.34. Graphical representation of XRD and rock property data for boreholes UE-20AV and U-20AV (HARDIN), SCCC, PM, southeastern Area 20, NNSS.

The HARDIN EZ is located in Zone 2 based on XRD, HSU, and HGU. Within the highly zeolitized intervals of U-20AV and UE-20V, the measured grain density appears to be overestimated by 0.2 g/cc or greater.

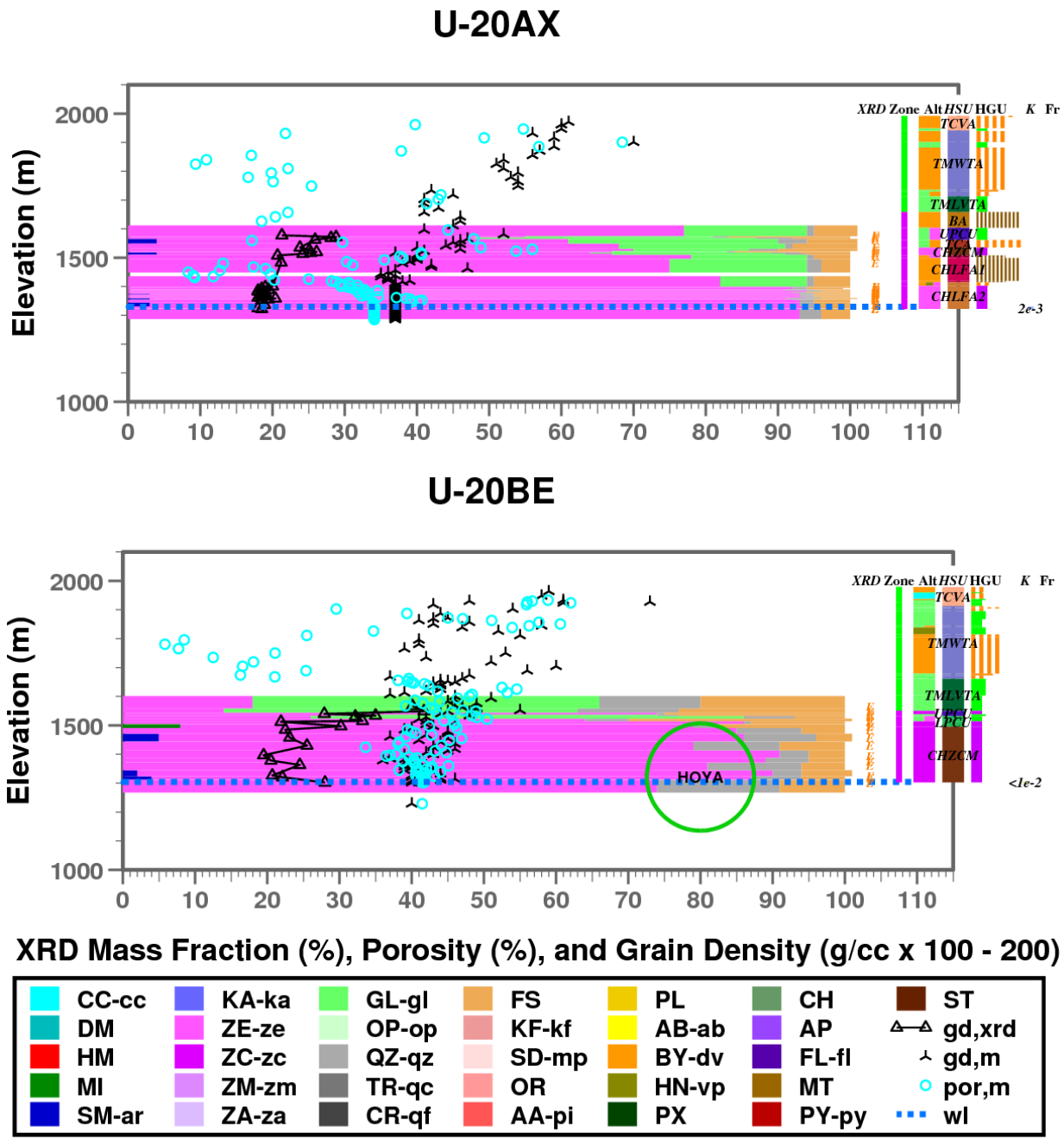

Side view test location outlines are 3.0 cavity radii (3Rc) using calculated cavity radius (green circles) except for tests with specified yields reported in USDOE (2015), for which the measured Rc from Zavarin (2014) is used (red circles). Cavity radius is calculated using the maximum, except for HANDLEY which used the minimum, of the announced yield range in DOE-NV/209 Rev 16 (USDOE, 2015) and the equation of Pawloski (1999).

Figure A.35. Graphical representation of XRD and rock property data for boreholes U-20AX and U-20BE (HOYA), SCCC, PM, southeastern Area 20, NNSS.

The HOYA EZ is located in Zone 2 based on XRD, alteration, HSU, and HGU. Within the highly zeolitized intervals of U-20AX and U-20BE, the measured grain density appears to be overestimated by about 0.2 g/cc.

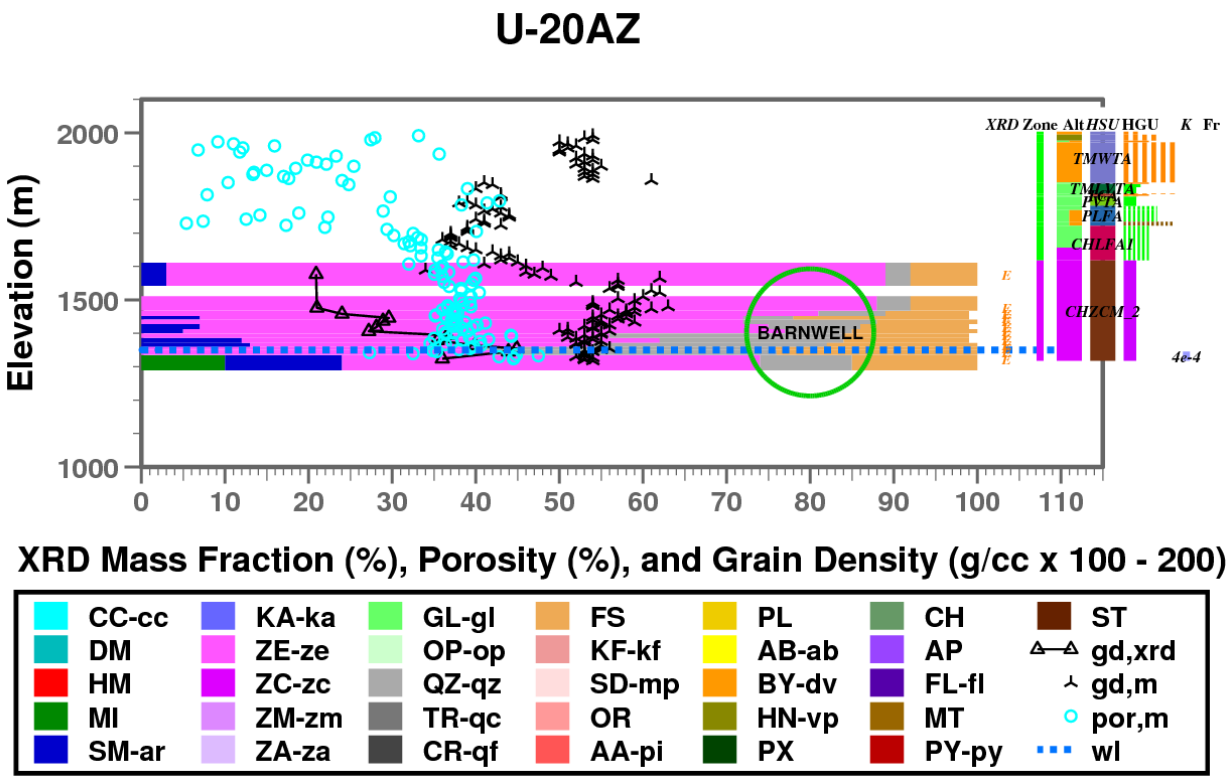

Side view test location outlines are 3.0 cavity radii (3Rc) using calculated cavity radius (green circles) except for tests with specified yields reported in USDOE (2015), for which the measured Rc from Zavarin (2014) is used (red circles). Cavity radius is calculated using the maximum, except for HANDLEY which used the minimum, of the announced yield range in DOE-NV/209 Rev 16 (USDOE, 2015) and the equation of Pawloski (1999).

Figure A.36. Graphical representation of XRD and rock property data for boreholes U-20AZ (BARNWELL), SCCC, PM, southeast Area 20, NNSS.

The BARNWELL EZ is located in Zone 2 based on XRD, alteration, HSU, and HGU. Within the highly zeolitized intervals of U-20AZ, the measured grain density appears to be overestimated by as much as 0.3 g/cc.

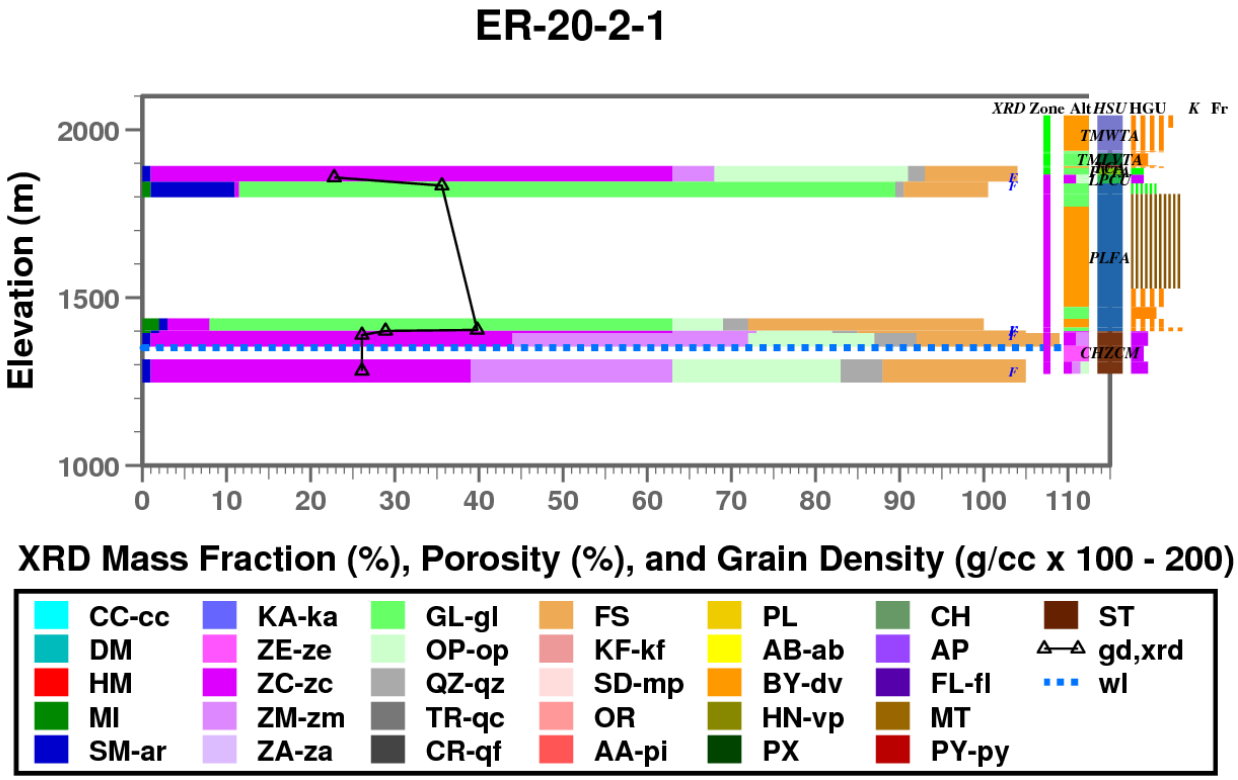

Figure A.37. Graphical representation of XRD and rock property data for borehole ER-20-2-1, SCCC, PM, southeastern Area 20, NNSS.

At ER-20-2-1 near the southern margin of the SCCC, Zone 2 extends to the top of the LPCU based on XRD, HSU, and HGU. The upper margin of the PLFA is vitric (glassy), which is typical of some lithologies (e.g. vitrophyre) within a lava flow. It is possible that the mineralogy of the tuffaceous lower portion of the PLFA is more characteristic of Zone 1.

A.3 Area 20 Boreholes – Western Pahute Mesa CAU

This section includes XRD data from 28 boreholes located in western Area 20, NNSS, and the western Pahute Mesa CAU. All of the XRD data for the U-20 and UE-20 boreholes in this section were derived from the lower quality S and E methods except for U-20F. Included in this section are high quality XRD data obtained by the F and I methods from boreholes PM-2, ER-20-12, ER-20-1, ER-20-5-3, ER-20-7, ER-20-11, ER-20-8, and ER-20-4.

Most of the PM and U-20 boreholes include rock property measurements. XRD-derived grain density provides a check on the grain density measurements.

Table A.3 lists Area 20 boreholes within the Western Pahute Mesa CAU with XRD data, general location (see Figures 5 and 6 for exact locations), XRD method, adjacent PM test (if emplacement hole or nearby exploration hole), and report figure reference.

Table A.3. List of 28 boreholes with XRD data in PM Area 20, Western Pahute Mesa CAU, NNSS.

Borehole	Location in Area 20	XRD Method(s)	Adjacent PM Test (distance to)	Figure
PM-2	northwestern	F, I	---	A.38
UE-20J	northwestern	I	HANDLEY (20 m)	**10**
U-20M	northwestern	I	HANDLEY	**11**
ER-20-12	northwestern	F	---	A.39
PM-3	west of Area 20	F	---	A.40
U-20AL	west-central	E	EGMONT	A.41
U-20F	west-central	I	FONTINA	A.41
UE-20F	west-central	F, I, S	FONTINA (50 m)	**9**
U-20AQ	west-central	E	DARWIN	A.42
U-20BC	west-central	E	HORNITOS	A.42
UE-20AE	west-central	S	TAFI (10 m)	A.43
U-20AE	west-central	S	TAFI	A.43
U-20AT	west-central	E	DELAMAR	A.44
U-20AK	west-central	E	SALUT	A.44
U-20BB1	west-central	E	TENABO (20 m)	A.45
U-20BB	west-central	E	TENABO	A.45
U-20AO	southwestern	E	GLADSTONE	A.46
ER-20-1	southwestern	I	---	A.46
U-20AG	southwestern	S	MOLBO	A.47
U-20AS	southwestern	E	BELMONT	A.47
UE-20C	southwestern	I	BENHAM (170 m)	**12**
U-20C	southwestern	I	BENHAM	**13**
ER-20-5-3	southwestern	I	TYBO (290 m)	**14**
U-20Y	southwestern	I, S	TYBO	**15**
ER-20-7	southwestern	F	---	**16**
ER-20-11	southwestern	F	---	A.48
ER-20-8	southwestern	F	---	A.48
ER-20-4	southwestern	F	---	A.49

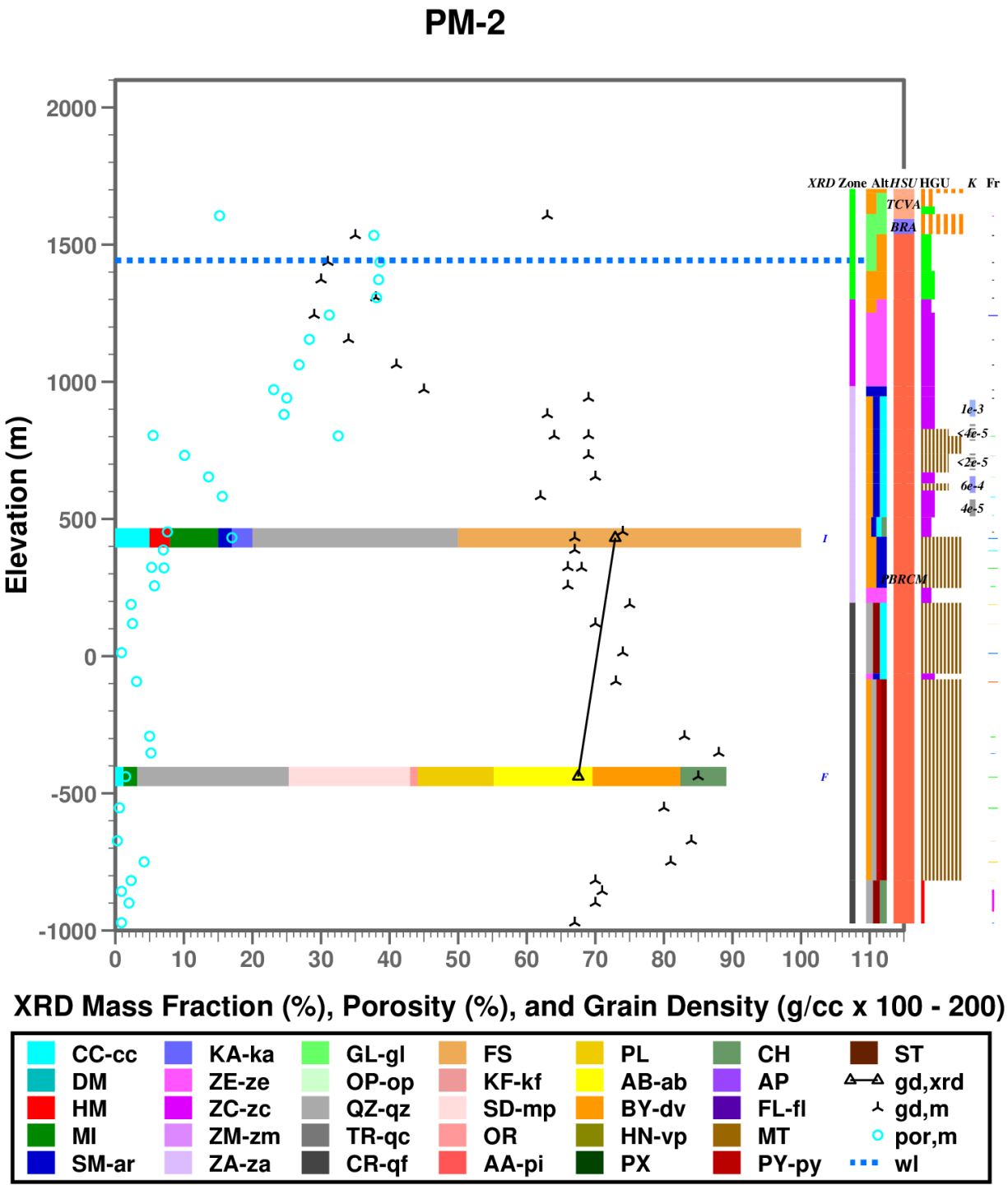

Figure A.38. Graphical representation of XRD and rock property data for borehole PM-2, PM, northwest Area 20, NNSS.

At borehole PM-2, Zones 3 and 4 are interpreted primarily by the XRD, rock property, and alteration data.

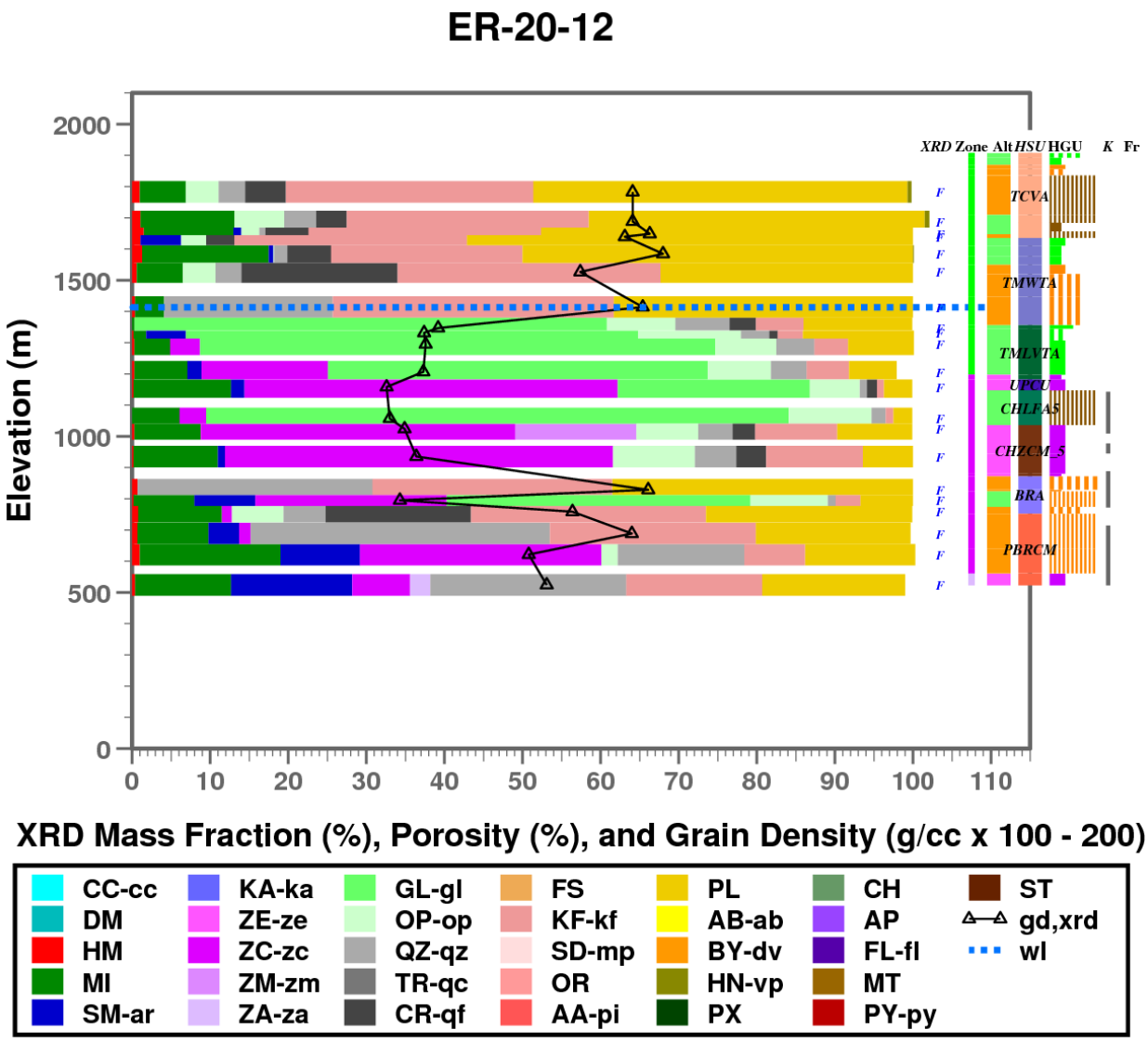

Figure A.39. Graphical representation of XRD and rock property data for borehole ER-20-12, PM, northwest Area 20, NNSS.

At borehole ER-20-12, the top of Zone 3 is interpreted by presence of analcime and decreased mass fraction of clinoptilolite in the TCU. Hematite abundance is relatively low in the Calico Hills units, as evident at UE-20H (Figure 7), UE-20F (Figure 9), and ER-20-4 (Figure A.49). The XRD data indicate mica is much more abundant at ER-20-12 as compared to the upgradient locations U-20M and UE-20J.

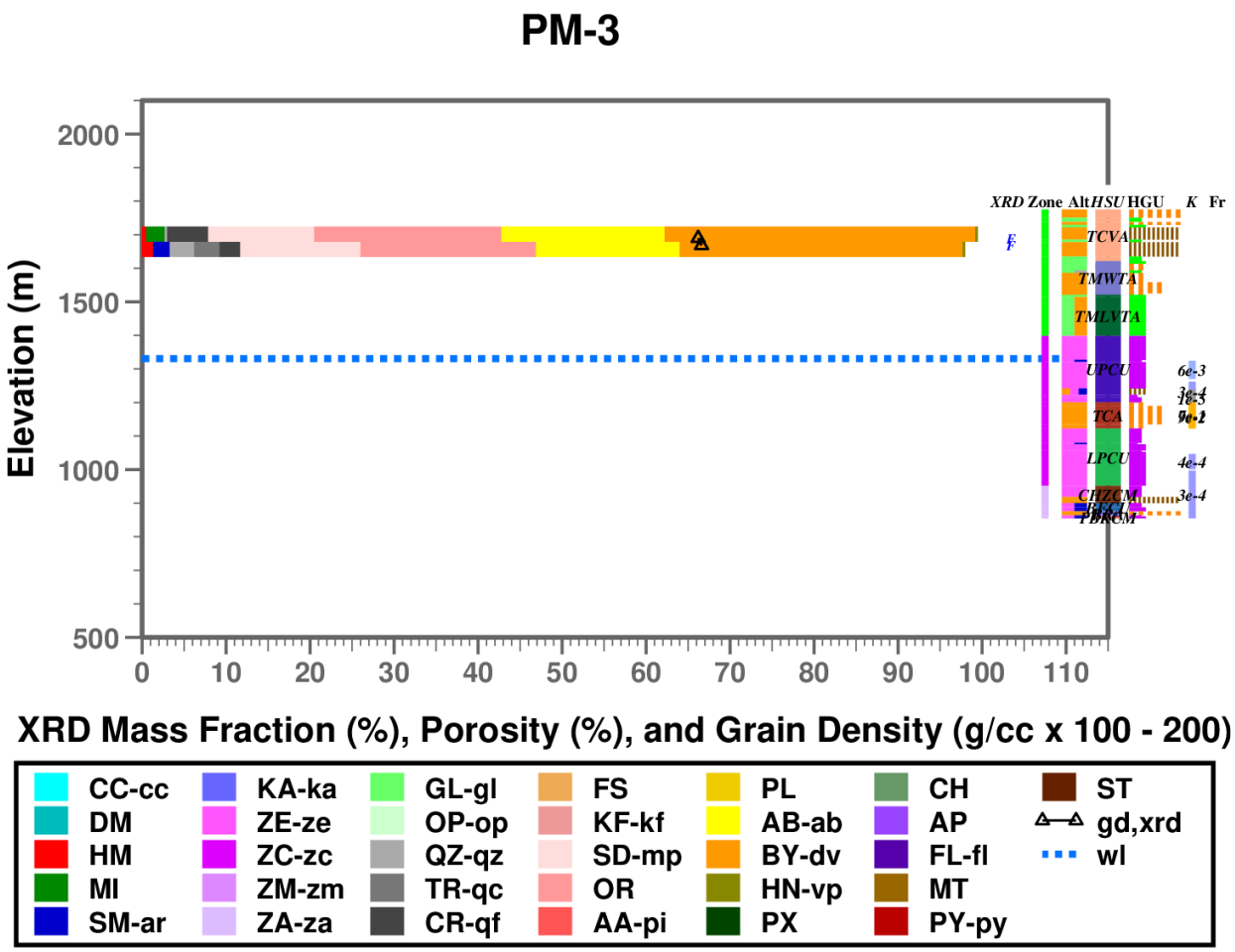

Figure A.40. Graphical representation of XRD and rock property data for borehole PM-3, PM, west of Area 20, NNSS.

Although borehole PM-3 is located west of NNSS Area 20, it is grouped with other Area 20 boreholes in the Western Pahute Mesa CAU because it is hydrologically downgradient of the HANDLEY test and ER-20-12 (Figure A.31). The top of Zone 3 is inferred at the base of PM-3 by presence of secondary calcite (Smith et al, 1999).

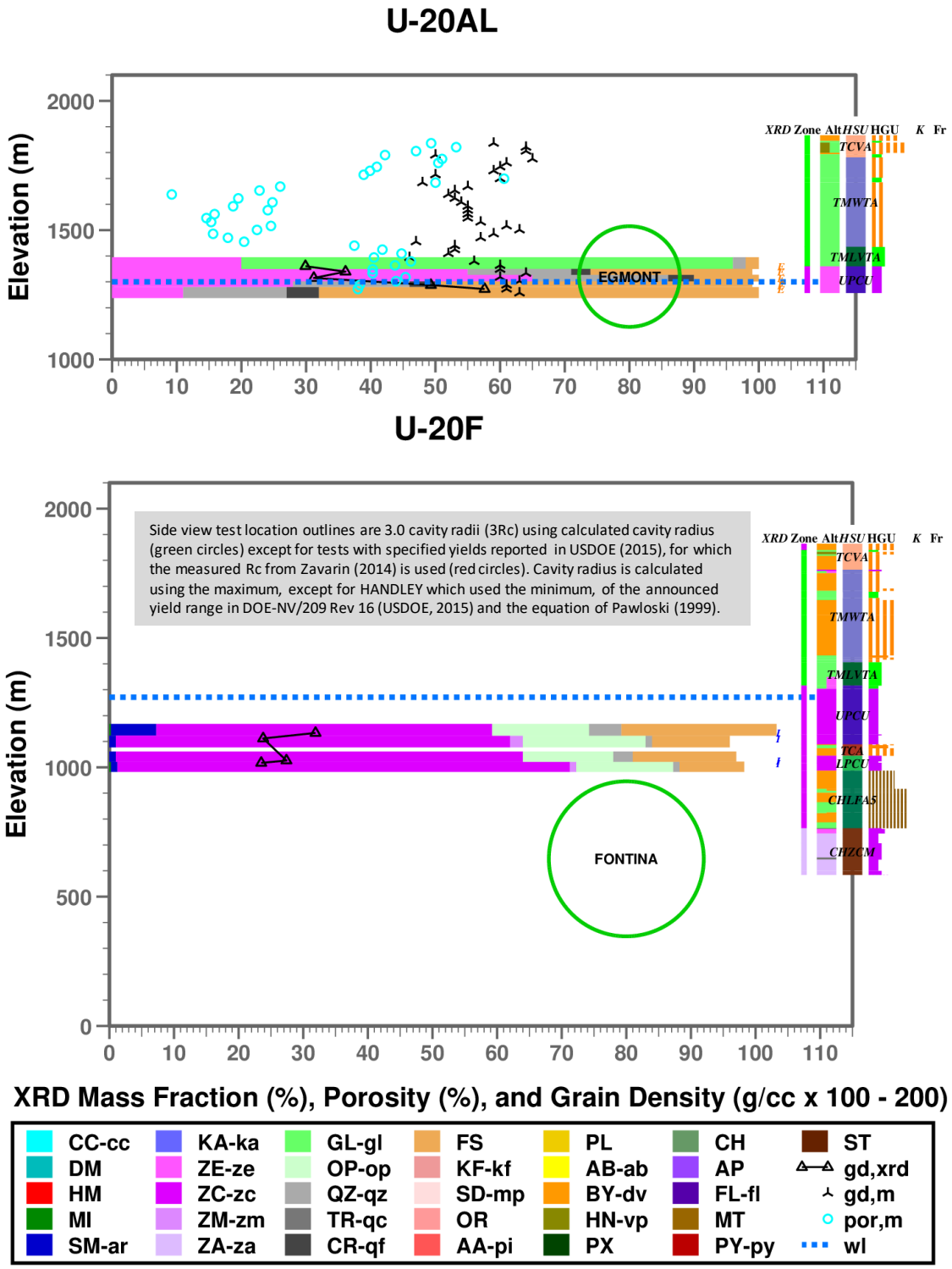

Figure A.41. Graphical representation of XRD and rock property data for boreholes U-20AL and U-20F (FONTINA), SCCC, PM, west Area 20, NNSS.

The EGMONT EZ is located in Zones 1 and 2 based on XRD, alteration, HSU, and HGU. The FONTINA EZ is located in Zones 2 and 3, as largely interpreted from XRD data for UE-20F (Figure 9).

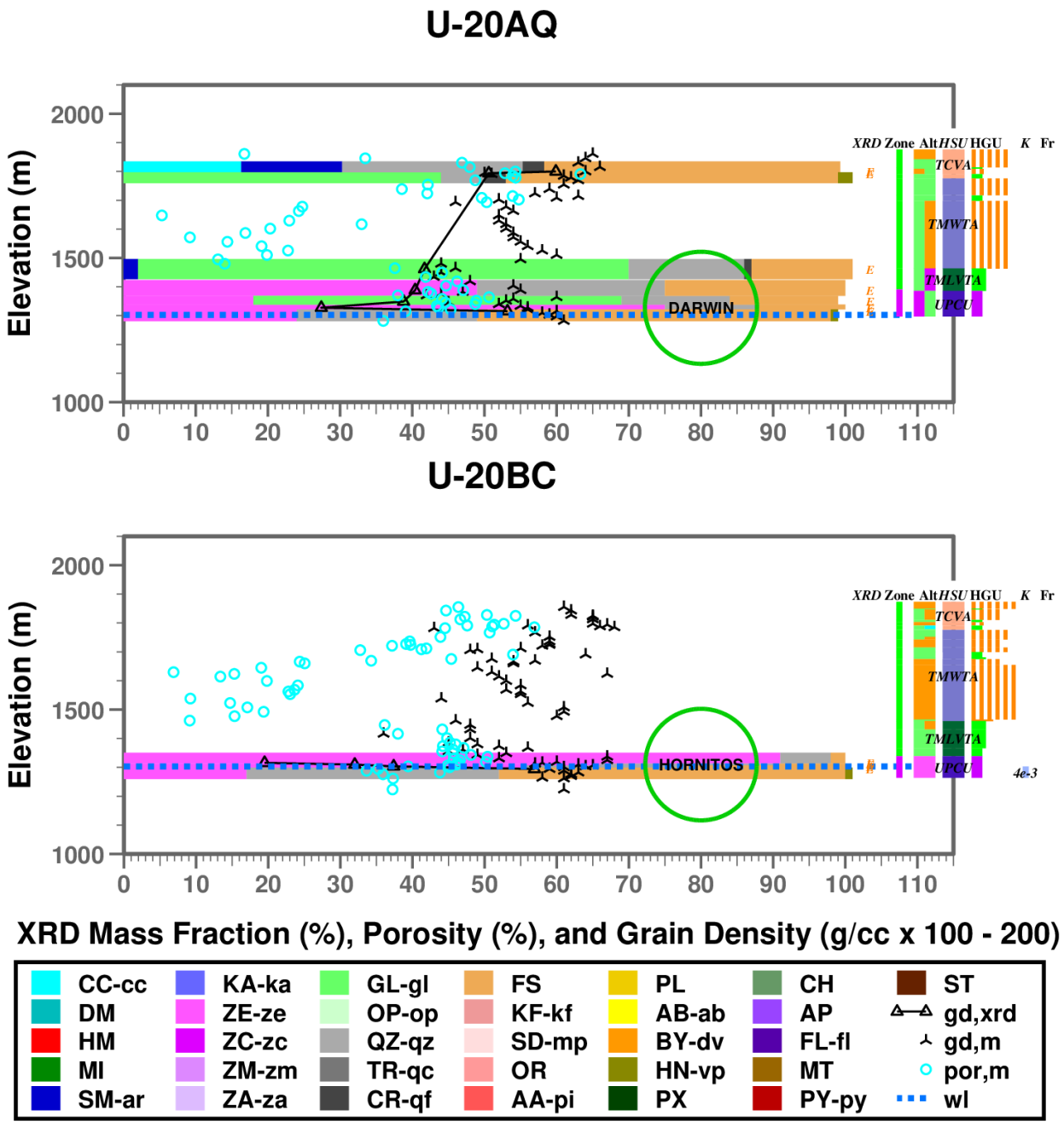

Side view test location outlines are 3.0 cavity radii (3Rc) using calculated cavity radius (green circles) except for tests with specified yields reported in USDOE (2015), for which the measured Rc from Zavarin (2014) is used (red circles). Cavity radius is calculated using the maximum, except for HANDLEY which used the minimum, of the announced yield range in DOE-NV/209 Rev 16 (USDOE, 2015) and the equation of Pawloski (1999).

Figure A.42. Graphical representation of XRD and rock property data for boreholes U-20AQ (Darwin) and U-20BC (HORNITOS), SCCC, PM, west-central Area 20, NNSS.

The GOLDSTONE EZ is located mostly in Zone 2, with Zone 1 near the top, and the HORNITOS EZ is located in Zones 1 and 2 based on XRD, alteration, HSU, and HGU. Within the highly zeolitized intervals of U-20AO and U-20BC, the measured grain density appears to be overestimated by 0.2 g/cc or greater.

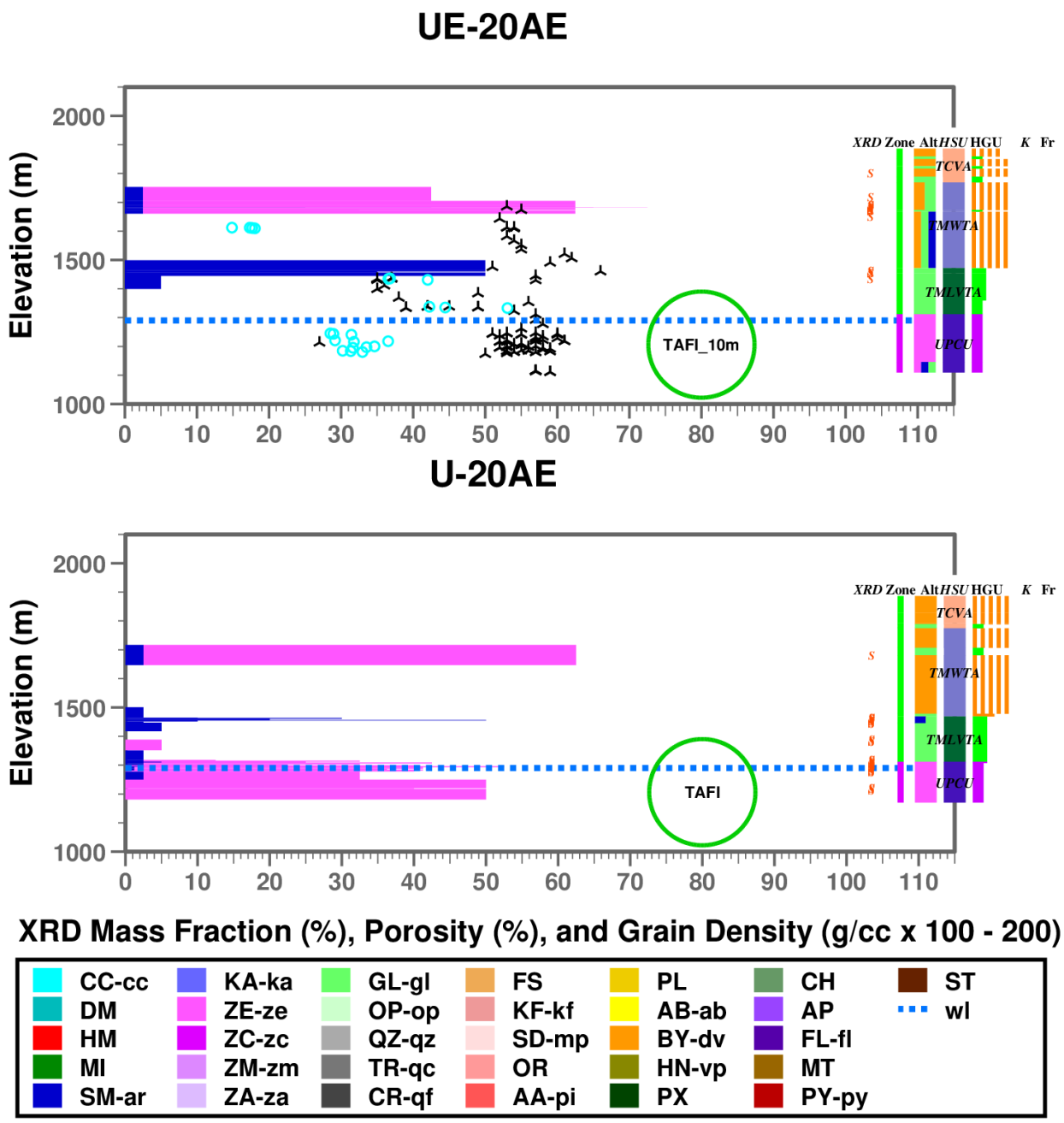

Side view test location outlines are 3.0 cavity radii (3Rc) using calculated cavity radius (green circles) except for tests with specified yields reported in USDOE (2015), for which the measured Rc from Zavarin (2014) is used (red circles). Cavity radius is calculated using the maximum, except for HANDLEY which used the minimum, of the announced yield range in DOE-NV/209 Rev 16 (USDOE, 2015) and the equation of Pawloski (1999).

Figure A.43. Graphical representation of XRD and rock property data for boreholes U-20AO (GOLDSTONE) and U-20BC (HORNITOS), SCCC, PM, west Area 20, NNSS.

The TAFI EZ is located mostly in Zone 2, with Zone 1 near the top, based XRD, alteration, HSU, and HGU. The UE-20AE and U-20AE XRD both show a zeolitic interval within the TMWTA, similar to at UE-19P1 (Figure A.13)

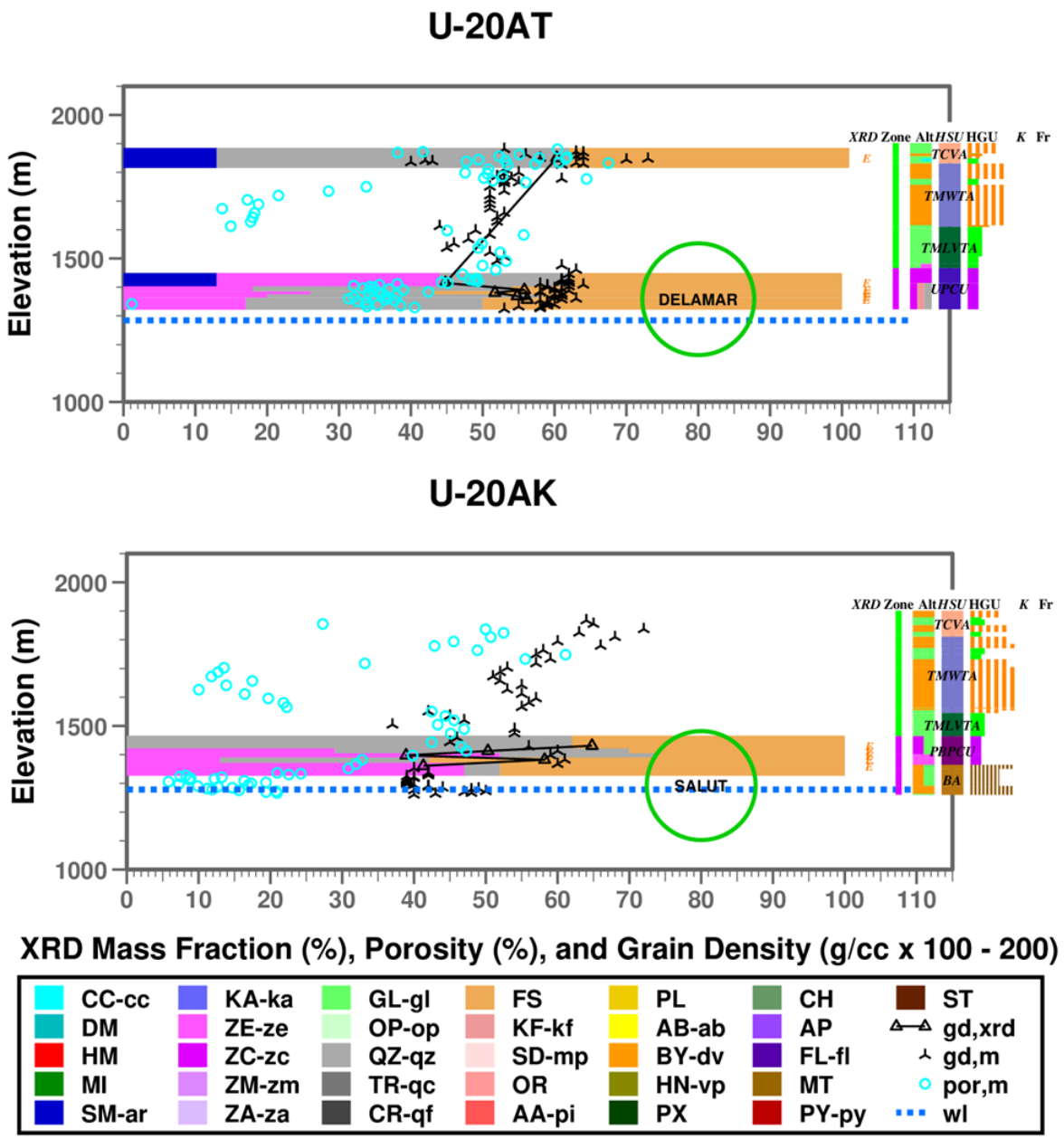

Side view test location outlines are 3.0 cavity radii (3Rc) using calculated cavity radius (green circles) except for tests with specified yields reported in USDOE (2015), for which the measured Rc from Zavarin (2014) is used (red circles). Cavity radius is calculated using the maximum, except for HANDLEY which used the minimum, of the announced yield range in DOE-NV/209 Rev 16 (USDOE, 2015) and the equation of Pawloski (1999).

Figure A.44. Graphical representation of XRD and rock property data for boreholes U-20AT (DELAMAR) and U-20AK (SALUT), SCCC, PM, west Area 20, NNSS.

The DELAMAR EZ is located mostly in Zone 2, with Zone 1 near the top, and the SALUT EZ is located almost entirely in Zone 2 based on XRD, alteration, HSU, and HGU. Within the more zeolitized intervals of U-20AT and U-20AK, the measured grain density appears to be overestimated by up to 0.2 g/cc.

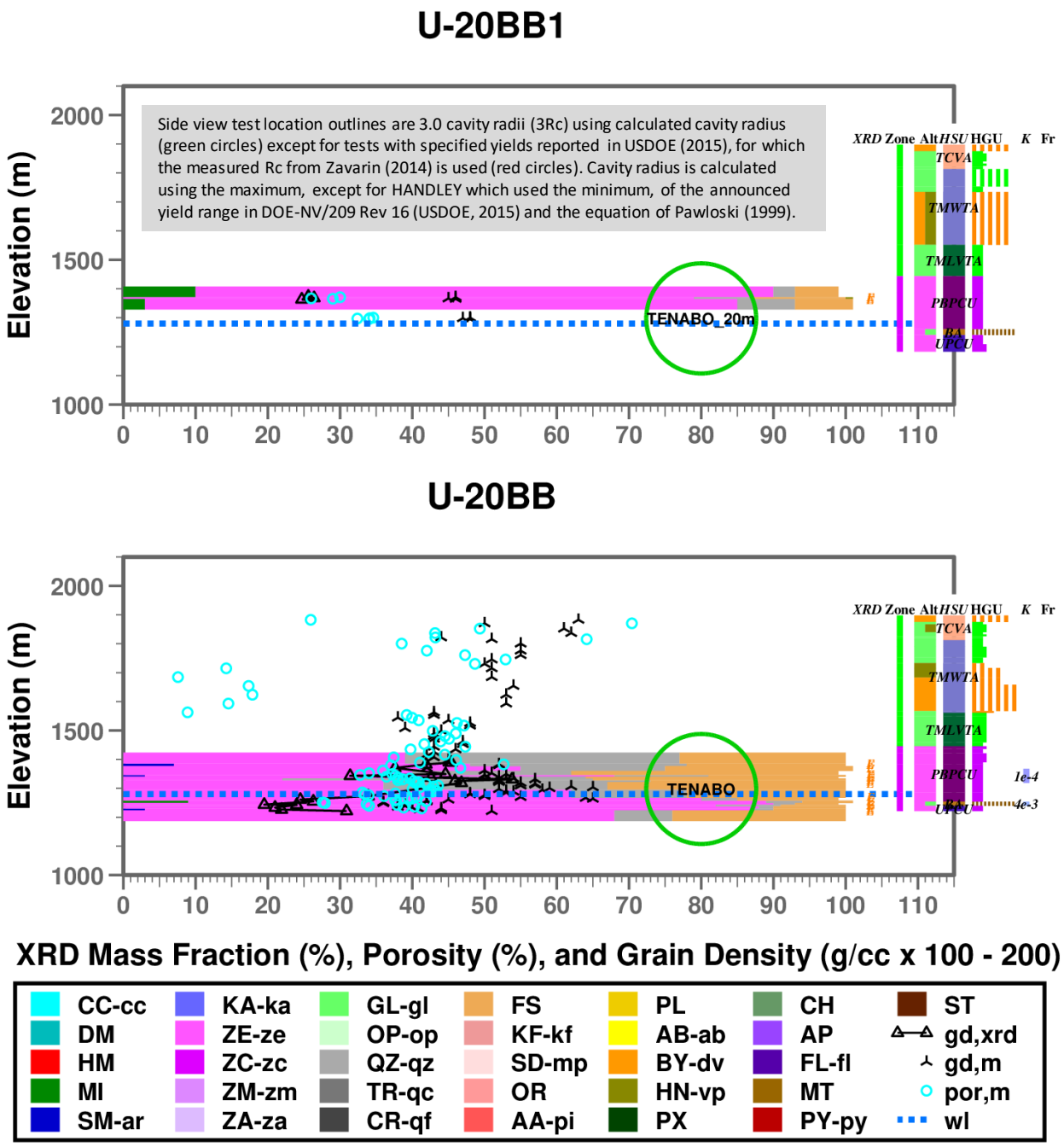

Figure A.45. Graphical representation of XRD and rock property data for boreholes U-20BB1 and U-20BB (TENABO), SCCC, PM, west Area 20, NNSS.

The TENABO EZ is located mostly in Zone 2, with Zone 1 near the top based on XRD, alteration, HSU, and HGU. Within the highly zeolitized intervals of U-20BB1 and U-20BB, the measured grain density appears to be overestimated by about 0.2 g/cc.

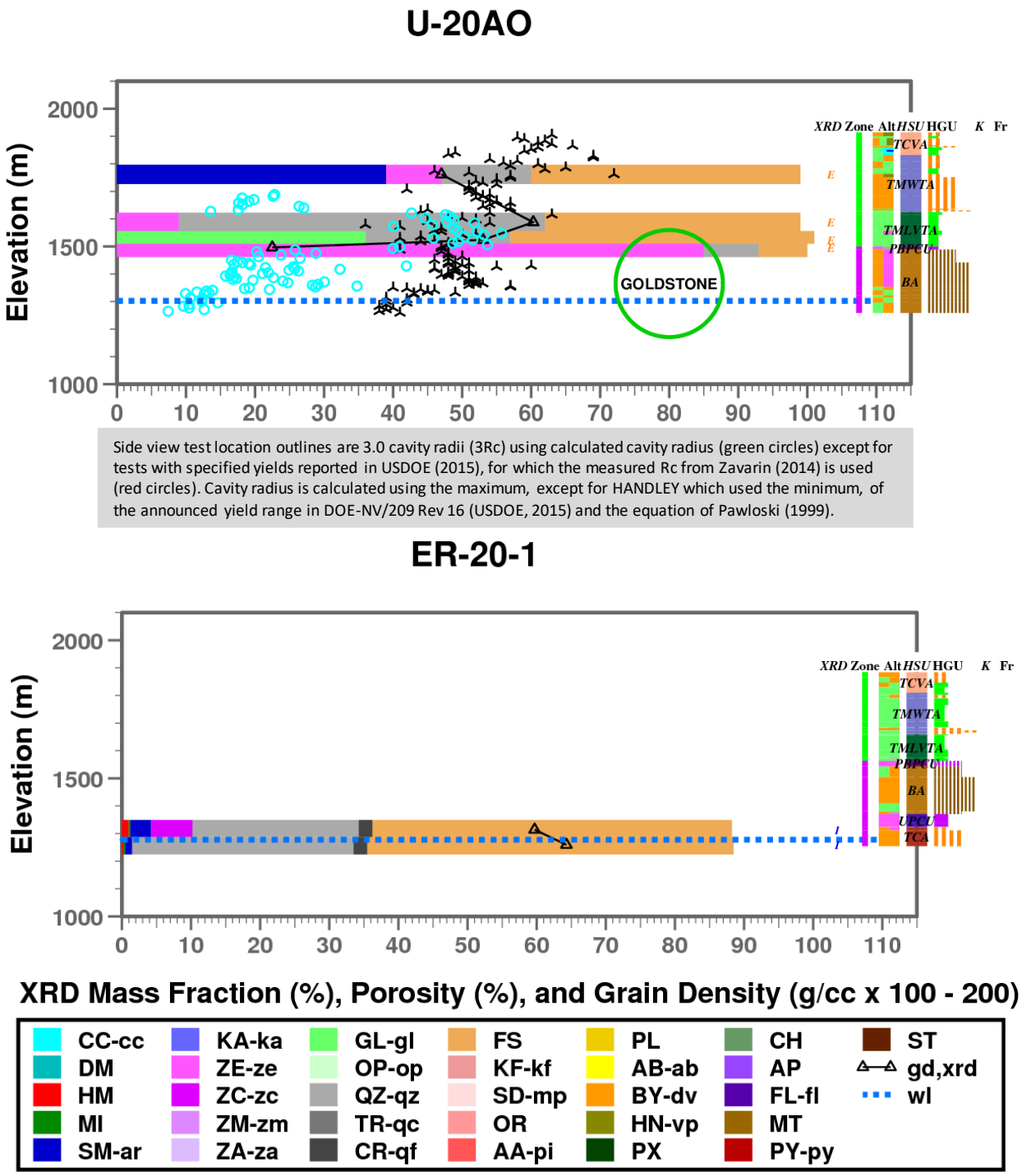

Figure A.46. Graphical representation of XRD and rock property data for boreholes U-20AO and ER-20-1, SCCC, PM, southwestern Area 20, NNSS.

The GOLDSTONE EZ is mostly in Zone 2 based on XRD, alteration, HSU, and HGU. At ER-20-1, 2 km southwest of the BENHAM test, Zone 2 extends from the base of the TMLVTA to the base of the UPCU or deeper, mostly based on alteration, HSU, and HGU. The presence of clinoptilolite in the TCA indicates Zone 2 extends down into the TCA.

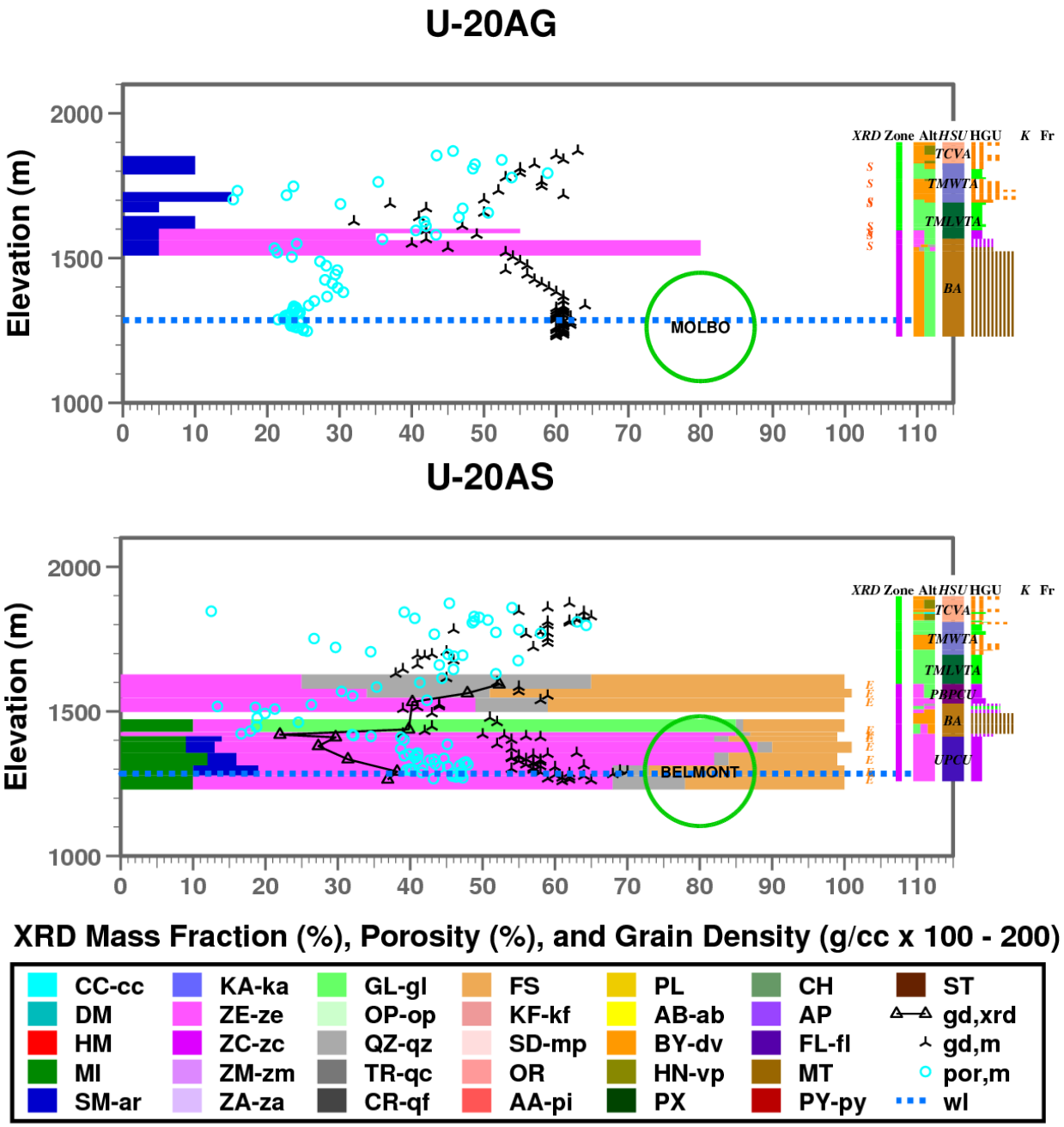

Side view test location outlines are 3.0 cavity radii (3Rc) using calculated cavity radius (green circles) except for tests with specified yields reported in USDOE (2015), for which the measured Rc from Zavarin (2014) is used (red circles). Cavity radius is calculated using the maximum, except for HANDLEY which used the minimum, of the announced yield range in DOE-NV/209 Rev 16 (USDOE, 2015) and the equation of Pawloski (1999).

Figure A.47. Graphical representation of XRD and rock property data for boreholes U-20AG (MOLBO) and U-20BC (BELMONT), SCCC, PM, southwest Area 20, NNSS.

The MOLBO EZ is interpreted to be located in Zone 2. The BELMONT EZ is located in Zone 2 based on XRD, alteration, HSU, and HGU. Within the highly zeolitized intervals of U-20AS, the measured grain density appears to be overestimated by 0.2 g/cc or greater.

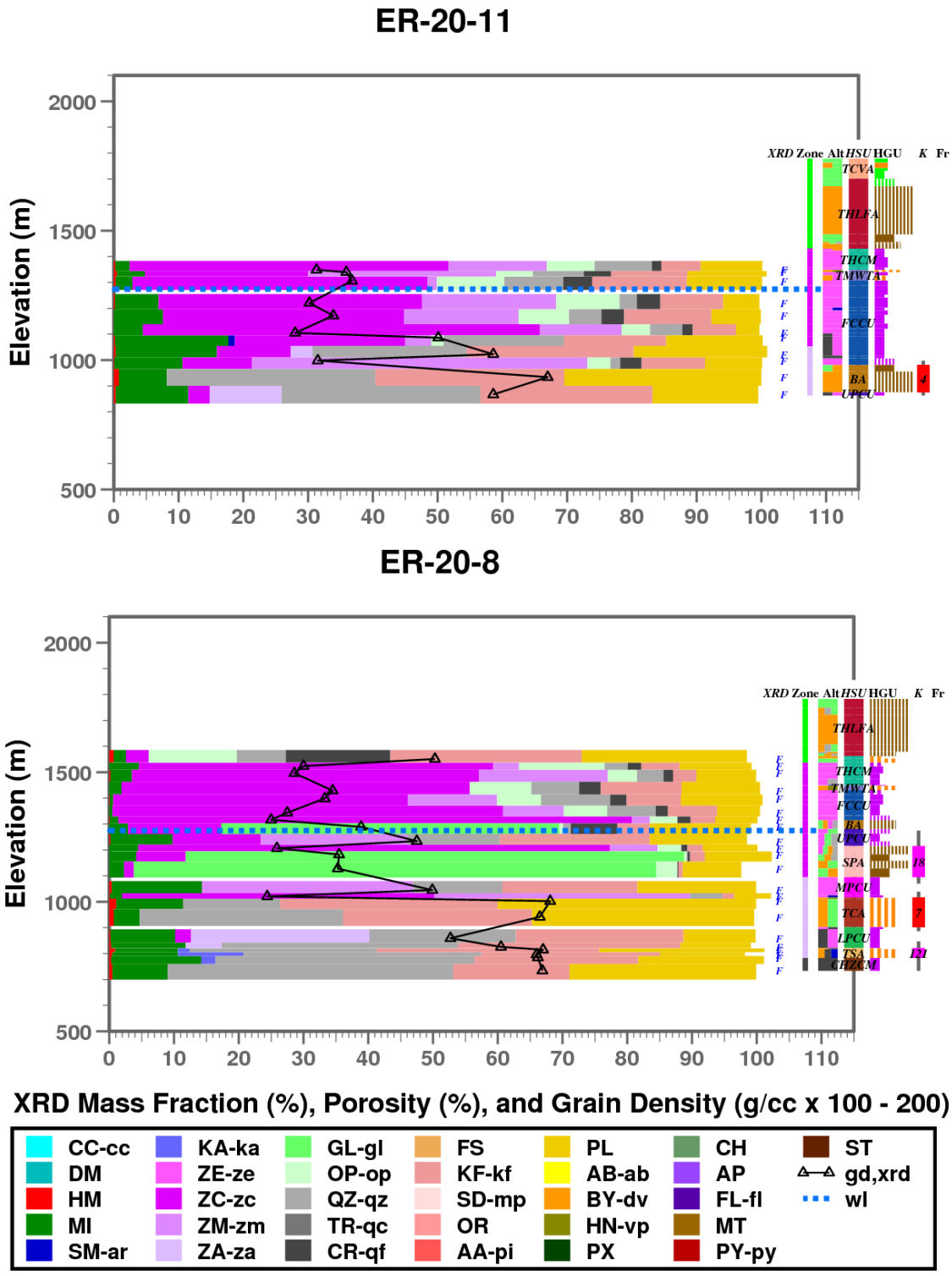

Figure A.48. Graphical representation of XRD and rock property data for boreholes ER-20-11 and ER-20-8, the Bench, SCCC, PM, southwest Area 20, NNSS.

The XRD data for boreholes ER-20-11 and ER-20-8 show distinct characteristics of Zone 2 mineralization (clinoptilolite, opal) and Zone 3 (transition to mordenite, analcime). Zone 4 is identified at ER-20-8 by quartzofeldspathic alteration in the CHZCM.

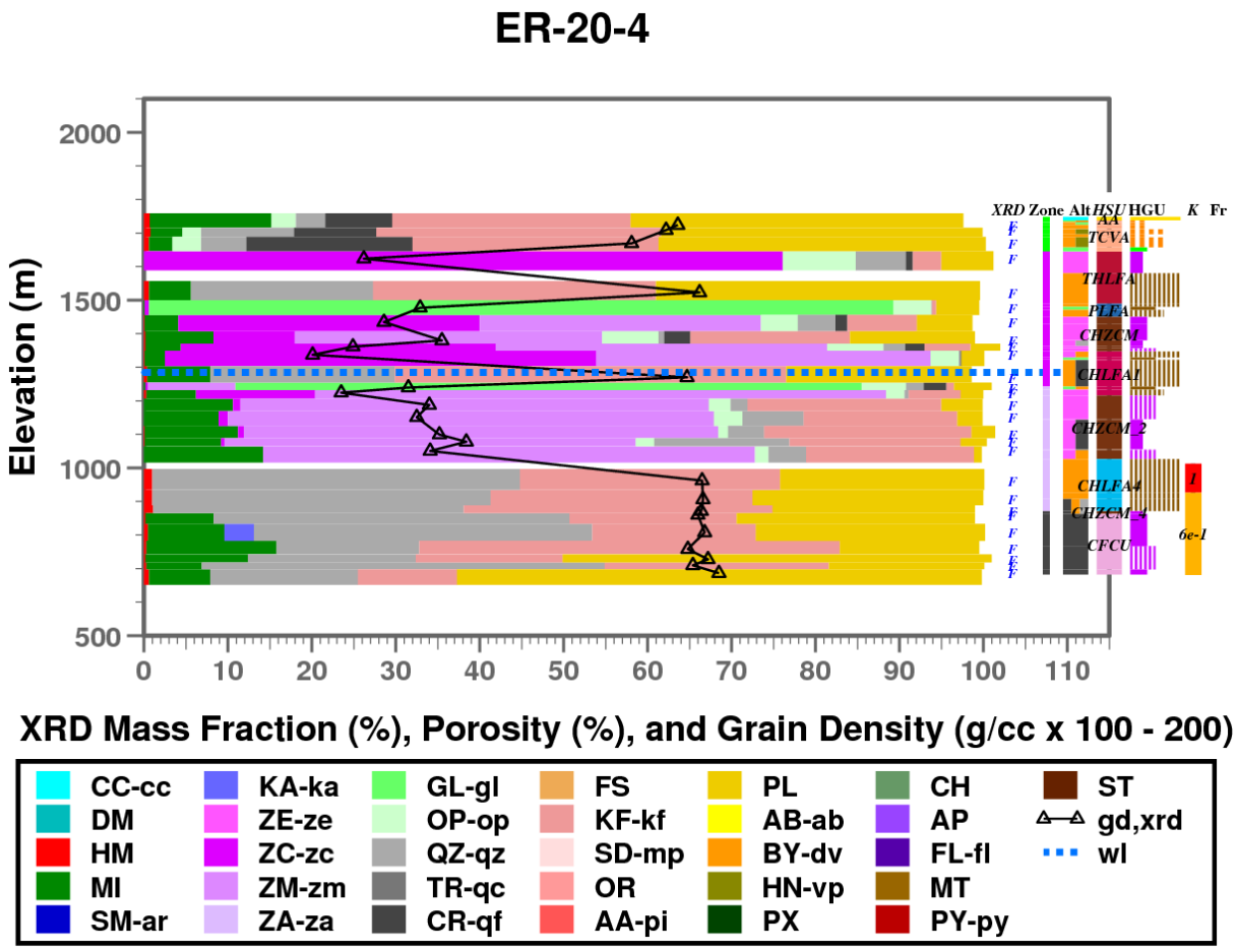

Figure A.49. Graphical representation of XRD and rock property data for borehole ER-20-4, the Bench, SCCC, PM, southern Area 20, NNSS.

The XRD data for borehole ER-20-4 shows distinct characteristics of Zone 2 mineralization (clinoptilolite, opal) and Zone 3 (transition to mordenite). Zone 4 is identified at ER-20-4 by quartzofeldspathic alteration in the CFCU. Kaolinite is present in Zone 4.

A.4 ER-EC Boreholes

The nine ER-EC boreholes with XRD data are located in areas outside of NNSS on the Bench, in the area of Thirsty Canyon, and within and along the margins of the TMCC, further down gradient from the ER boreholes. All XRD for the ER-EC boreholes were derived from high quality F or I methods.

Table A.4 lists ER-EC boreholes, general location (see Figures 5 and 6 for exact locations), XRD method, and report figure reference.

Table A.4. List of 12 ER-EC boreholes with XRD data in Thirsty Canyon and TMCC areas southwest of the NNSS.

Borehole	Location	Method	Figure
ER-EC-1	The Bench, SCCC	I	A.50
ER-EC-4	northwest of TMCC	F	A.51
ER-EC-11	The Bench, SCCC	F	**17**
ER-EC-6	The Bench, SCCC	F	**18**
ER-EC-15	The Bench	F	A.52
ER-EC-12	The Bench	F	A.53
ER-EC-13	northwestern TMCC	F	A.54
ER-EC-14	northwestern TMCC	F	A.54
ER-EC-2A	northwestern TMCC	F	**19**
ER-EC-8	western TMCC	F	A.55
ER-EC-5	western TMCC	F	A.55
ER-EC-7	southern TMCC	F	A.56

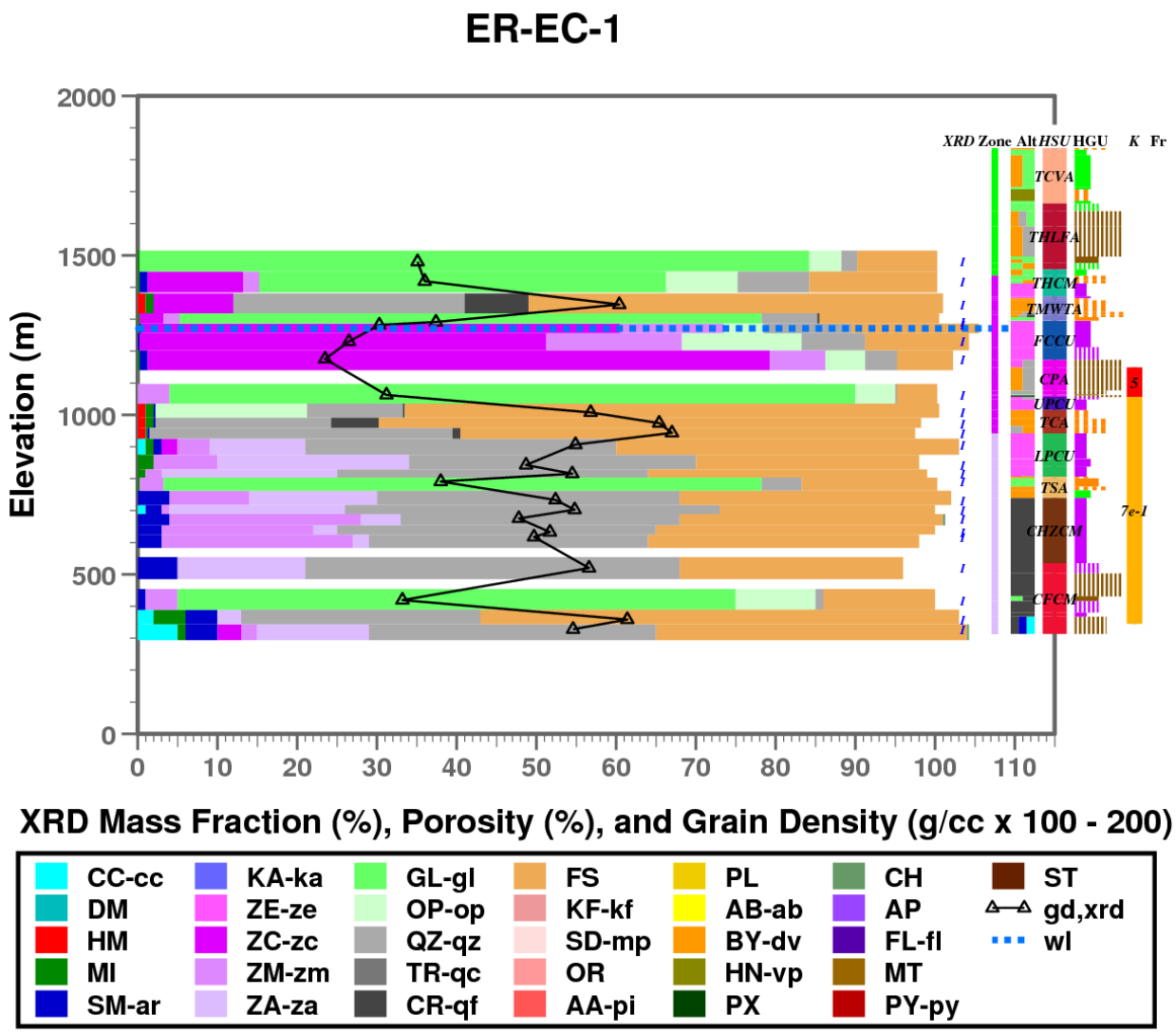

Figure A.50. Graphical representation of XRD and rock property data for borehole ER-EC-1, the Bench, SCCC, PM.

The XRD data for borehole ER-EC-1 show distinct characteristics of Zone 2 (clinoptilolite, opal) and Zone 3 (transition to mordenite, analcime). The apparent lack of mica and relatively greater abundance of smectite are similar to XRD data at ER-EC-4 (Figure A.51) and several upgradient boreholes at PM Area 20 discussed in Section 2 and 3 (UE-20H, UE-20F, U20C, UE-20C, U-20Y, ER-20-5-3).

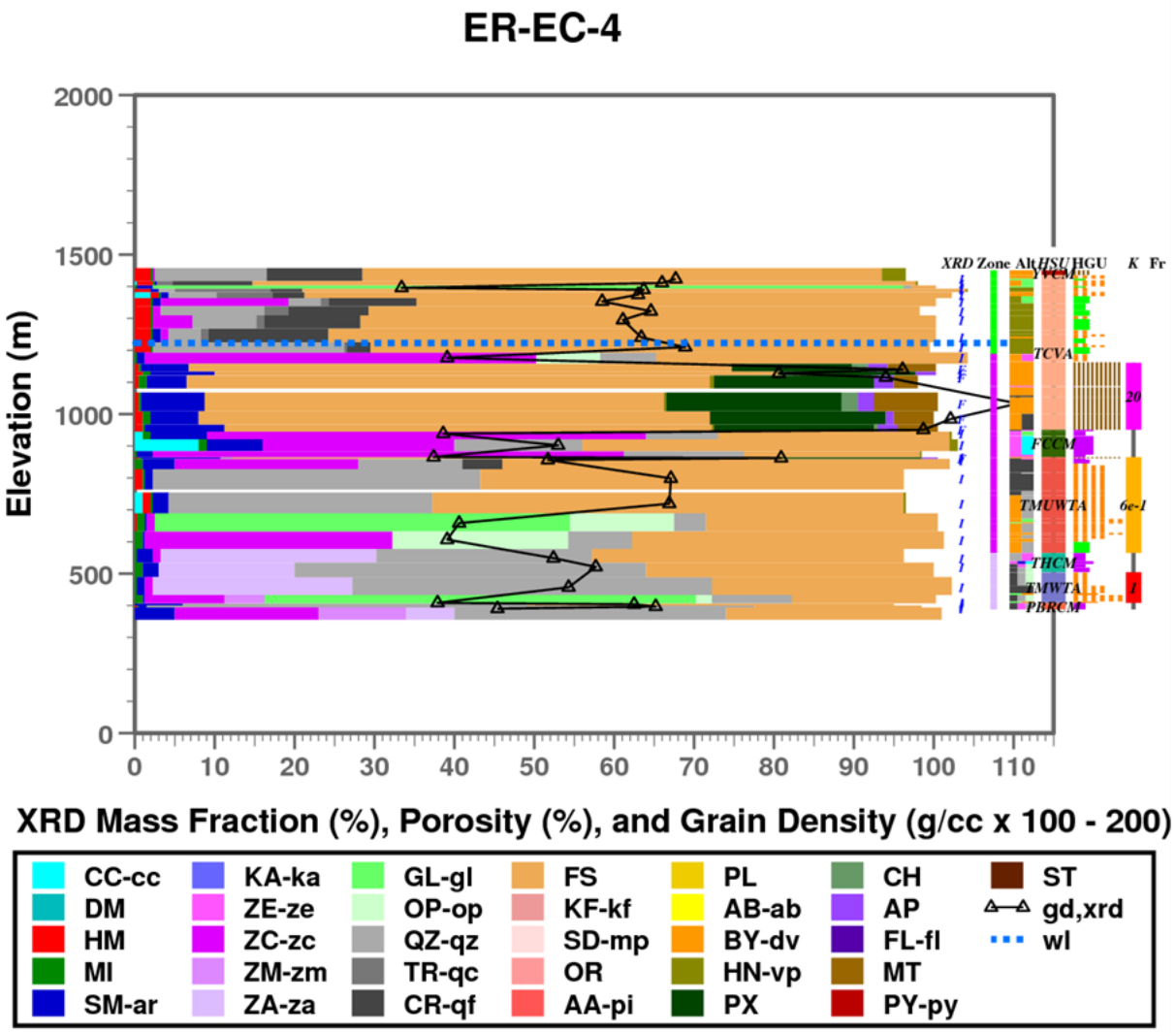

Figure A.51. Graphical representation of XRD and rock property data for borehole ER-EC-4 and ER-EC-13, about 3km west of the northwest margin of TMCC.

The XRD data for boreholes ER-EC-4 shows distinct characteristics of Zone 2 (clinoptilolite, opal) and Zone 3 (transition to mordenite, analcime). The apparent lack of mica and relative abundance to smectite are similar to XRD data for ER-EC-1 (Figure A.50).

From both a hydrologic and mineralogic perspective, a lava flow aquifer at the base of the TCVA is distinctive. The hydraulic conductivity of this interval is very high (20 m/d). The mineralogy includes rarely seen pyroxene (PX), chlorite (CH), apatite (AP), and magnetite (MT). These relatively dense minerals contribute to an unusually high grain density of about 3 g/cc.

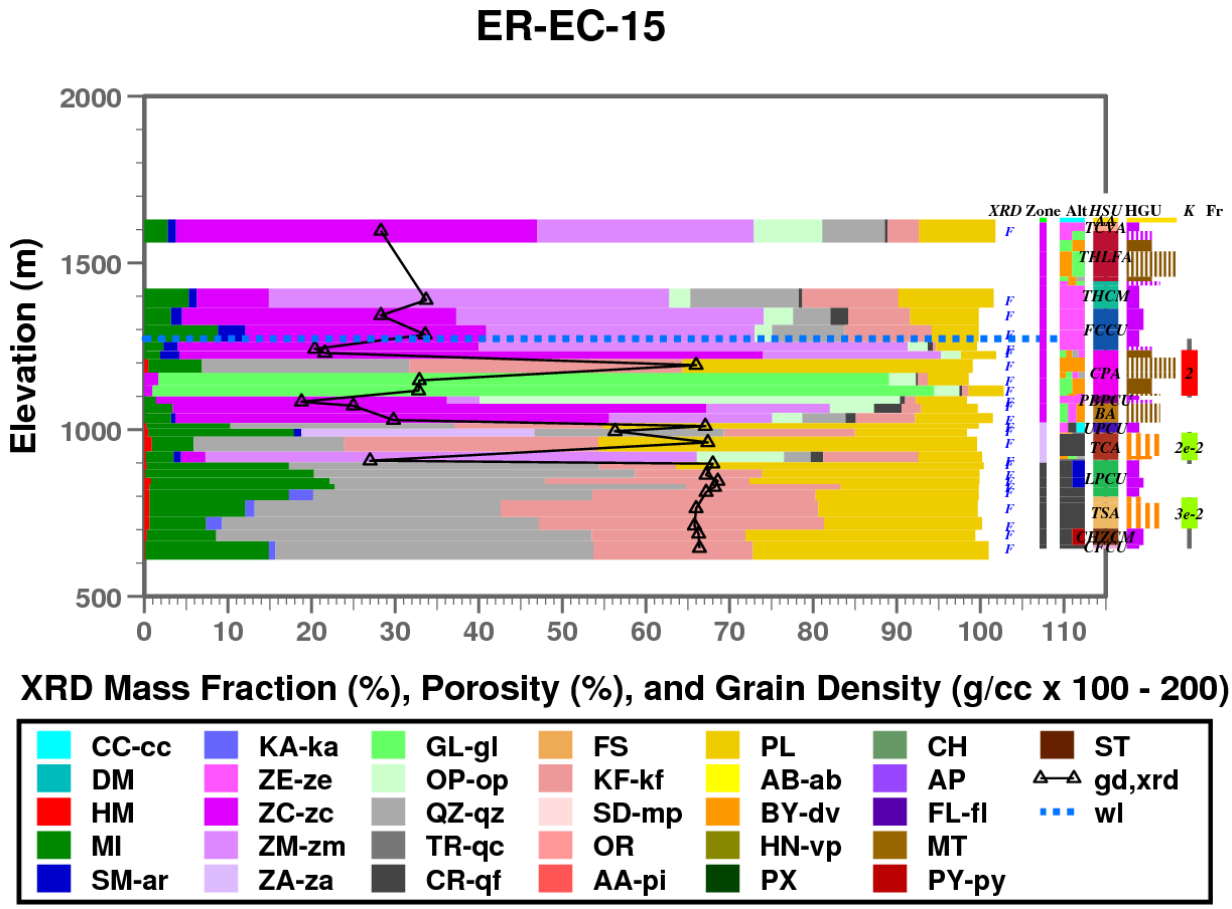

Figure A.52. Graphical representation of XRD and rock property data for boreholes ER-EC-15 and ER-EC-13, the Bench and TMCC.

The XRD data for borehole ER-EC-15 shows distinct characteristics of Zone 2 (clinoptilolite, opal), Zone 3 (transition to mordenite, analcime), and Zone 4 (quartzofeldspathic in TCUs). Kaolinite occurs in Zone 4. Relative abundance of mica, lack of smectite, and presence of kaolinite in Zone 4 are similar to XRD for ER-20-11 and ER-20-8 (Figure A.48), ER-20-4 (Figure A.49), ER-EC-12 (Figure A.53), ER-EC-13 and ER-EC-14 (Figure A.54), and ER-EC-2A (Figure 19).

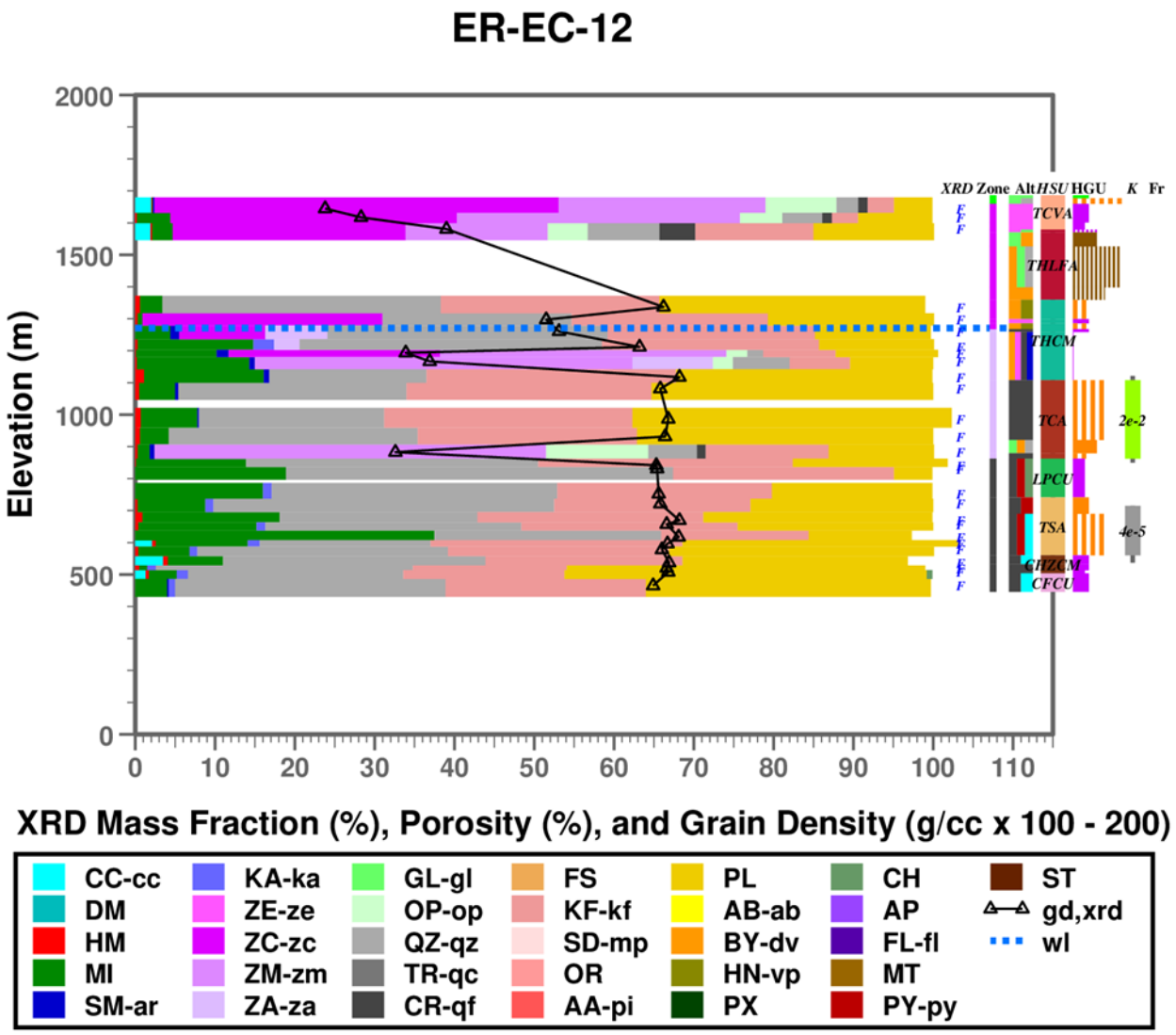

Figure A.53. Graphical representation of XRD and rock property data for borehole ER-EC-12, TMCC.

The XRD data for borehole ER-EC-12 shows distinct characteristics of Zone 2 (clinoptilolite, opal), Zone 3 (transition to mordenite, analcime), and Zone 4 (quartzofeldspathic in TCUs). Relative abundance of mica, lack of smectite, and presence of kaolinite in Zone 4 are similar to XRD for ER-20-11 and ER-20-8 (Figure A.48), ER-20-4 (Figure A.49), ER-EC-15 (Figure A.52), ER-EC-13 and ER-EC-14 (Figure A.54), and ER-EC-2A (Figure 19).

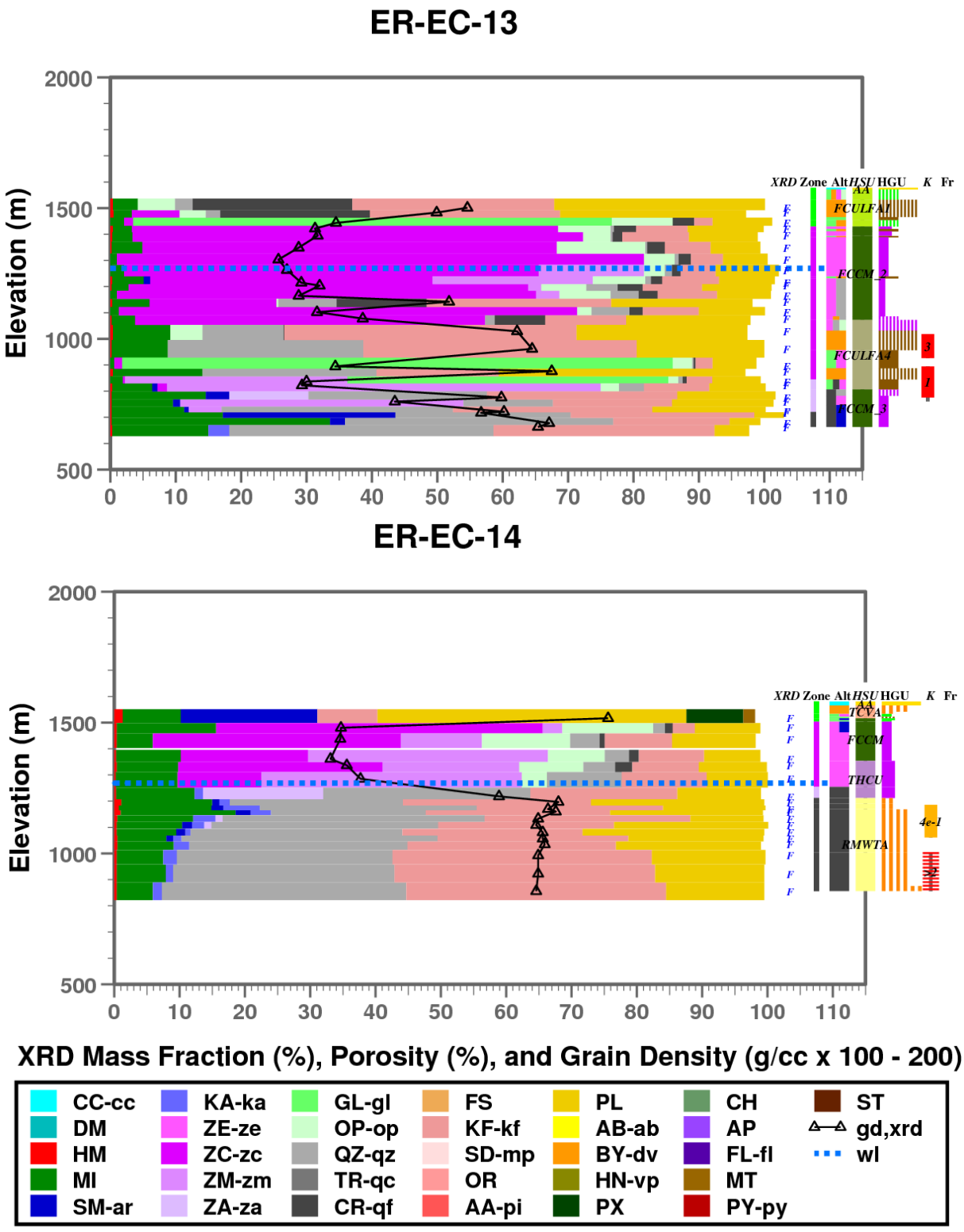

Figure A.54. Graphical representation of XRD and rock property data for borehole ER-EC-14, TMCC.

The XRD data for borehole ER-EC-14 shows distinct characteristics of Zone 2 mineralization (clinoptilolite, opal), Zone 3 (transition to mordenite, analcime), and Zone 4 (quartzofeldspathic). Kaolinite occurs in Zone 4.

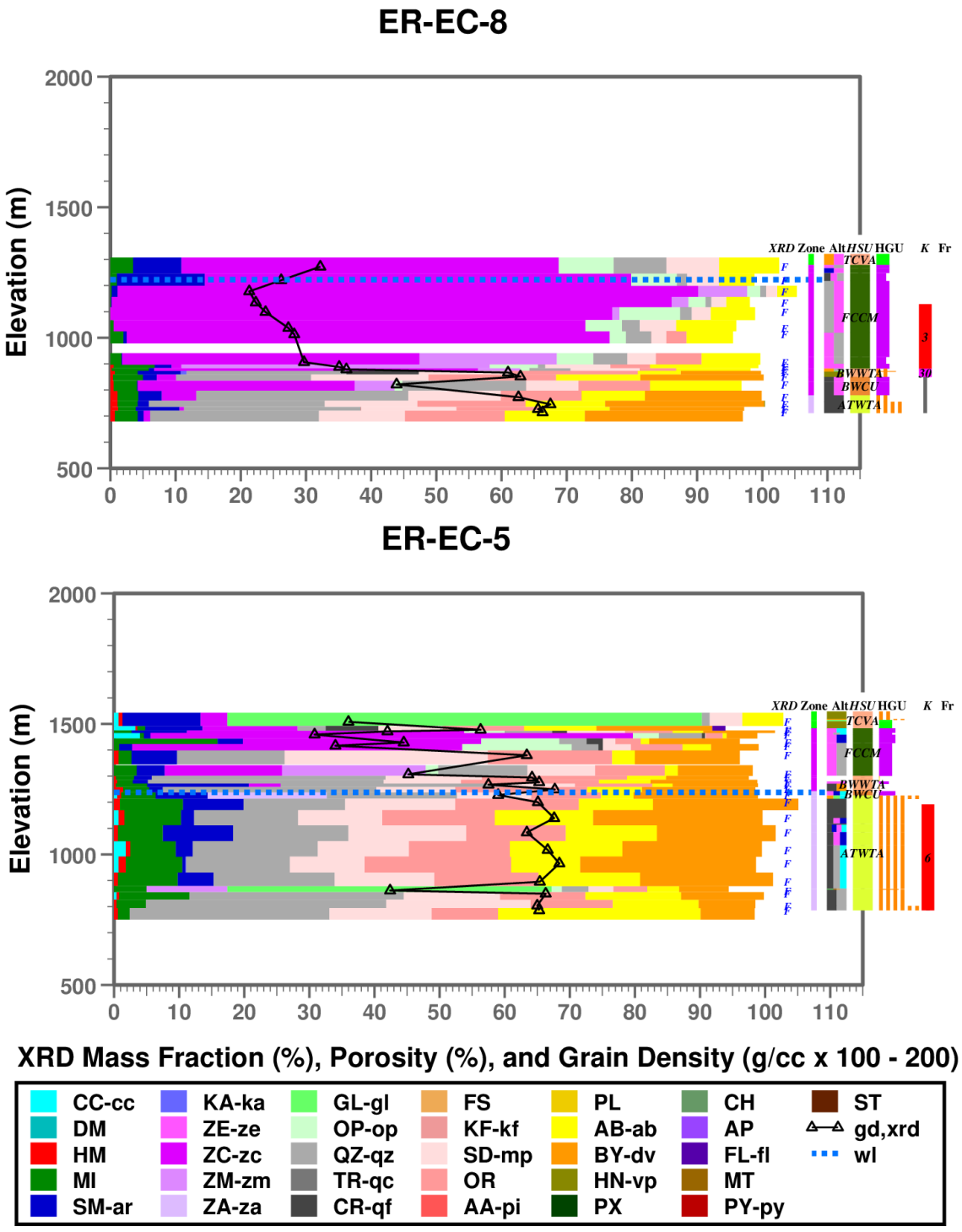

Figure A.55. Graphical representation of XRD and rock property data for boreholes ER-EC-8 and ER-EC-5, TMCC.

The XRD data for boreholes ER-EC-8 and ER-EC-5 show distinct characteristics of Zone 2 mineralization (clinoptilolite, opal). Identification of Zone 3 is less apparent. At ER-EC-5, analcime is present near the top of the ATWTA. Smectite appears to become more abundant southward through the TMCC.

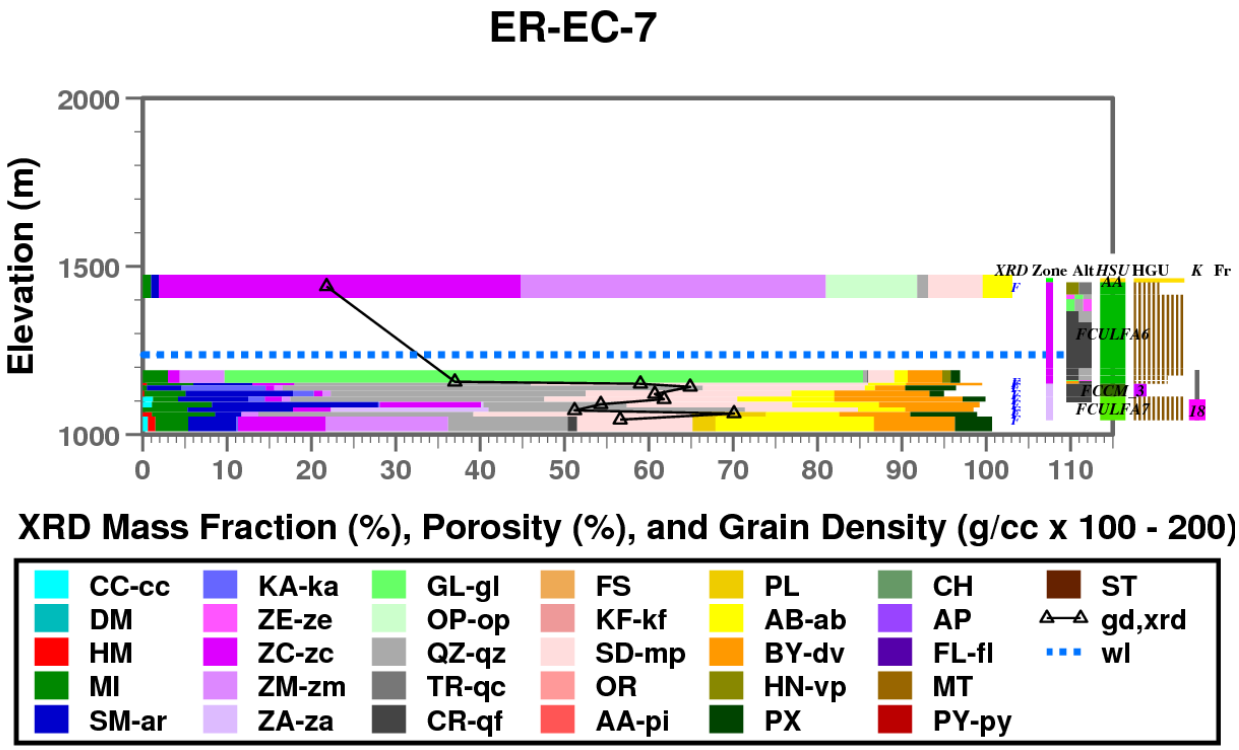

Figure A.56. Graphical representation of XRD and rock property data for borehole ER-EC-7, TMCC.

The XRD data for borehole ER-EC-7 show distinct characteristics of Zone 2 (clinoptilolite, opal) and Zone 3 (mordenite, analcime). As apparent in XRD data for ER-EC-5 and ER-EC-8 (Figure A.46), smectite appears to become more abundant southward through the TMCC.

A.5 ER-OV Boreholes

The ER-OV boreholes ER-OV-01, ER-OV-06A, ER-OV-03A2, and ER-OV-03C with XRD data are located near the discharge areas of the PM-OV groundwater basin. In the OV area, the water table is relatively shallow relative to the ground surface. Figure A.57 shows XRD and rock property data for the ER-OV boreholes. Table A.4 lists ER-EC boreholes, general location (see Figure 6 for exact locations), XRD method, and report figure reference.

Table A.5. List of 4 ER-OV boreholes with XRD data in the Oasis Valley and southwestern TMCC areas, about 25 km southwest of the NNSS.

Borehole	Location	XRD method	Figure
ER-OV-01	northern OV	F	A.57
ER-OV-6A	northern OV	F	A.57
ER-OV-03A2	southern OV	F	A.57
ER-OV-03C	southwestern TMCC	F	A.57

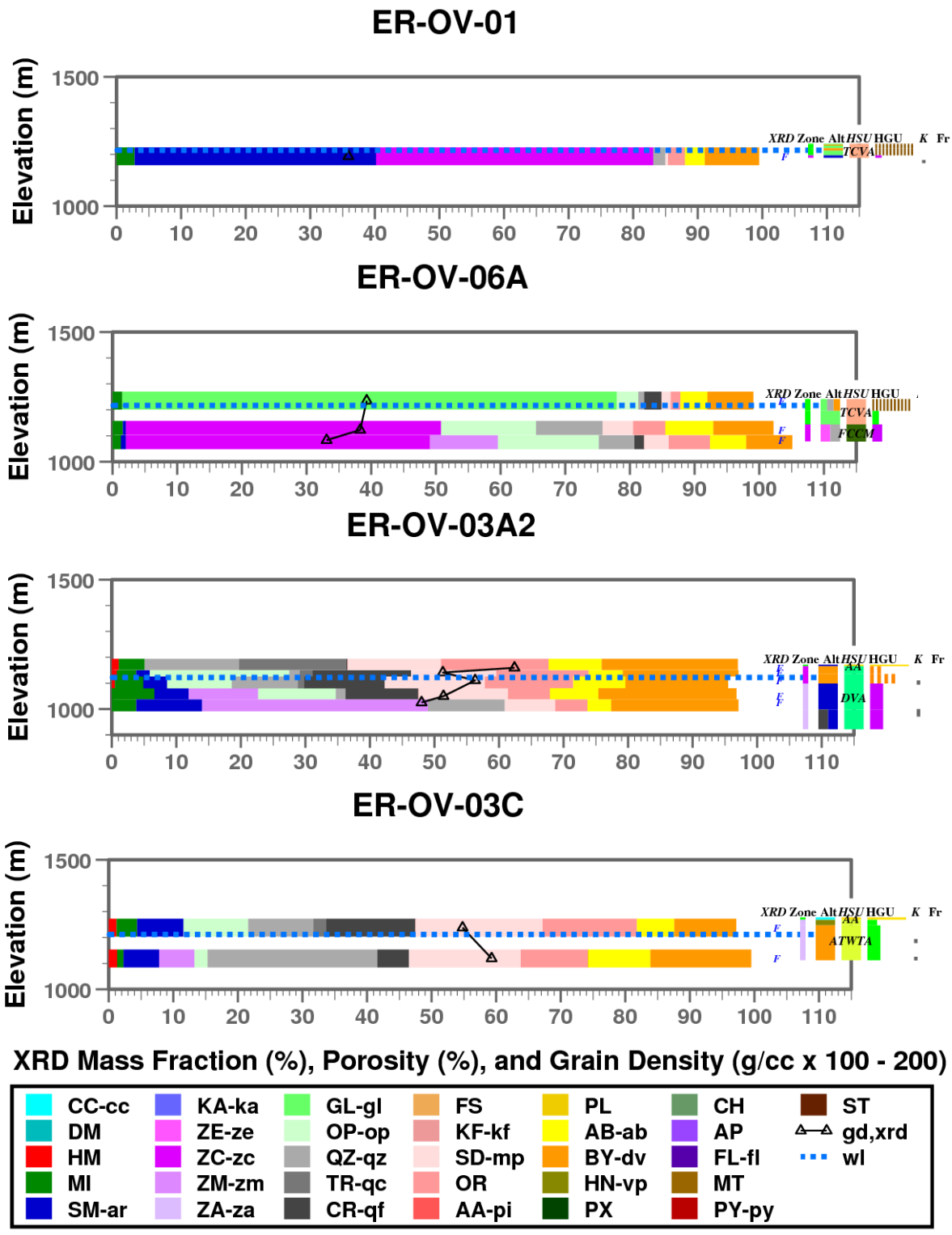

Figure A.57. Graphical representation of XRD and rock property data for boreholes ER-OV-1, ER-OV-06A, ER-OV-03A2, and ER-OV-03C, TMCC and OV.

Boreholes ER-OV-01 and ER-OV-6A are located near each other in northern Oasis Valley. Here, the upper portion of the TCVA is within Zone 1 where alteration is described as vitric.

Zone 2 occurs deeper in the TCVA or in the FCCM, where alteration is described as zeolitic, and XRD data indicate up to 50% clinoptilolite and some mordenite and opal. Smectite is present, in abundance at the base of the TCVA in ER-OV-01. Boreholes ER-OV-03A2 and ER-OV03C are located near the southeastern margin of the TMCC. Both smectite and mica appear to be pervasive.

The abundance of smectite in the ER-OV boreholes is similar to XRD data for ER-EC-8 and ER-EC-5 (Figure A.46) and ER-EC-7 (Figure A.47) in west-central TMCC. This is contrast to the lack of smectite in XRD data for boreholes ER-20-4 (Figure A.40), ER-EC-15 and ER-EC-13 (Figure A.42), ER-EC-12 (Figure A.44), and ER-EC-14 (Figure A.45), and ER-EC-2A (Figure 19) in the northwest TMCC and the Bench. The XRD data indicate a locational dependence (i.e. non-stationarity) to the abundance of smectite and mica (or illite).

A.6 Area 18 and 30 Boreholes

Boreholes UE-18R, UE-18T, ER-18-2, and ER-30-1 in Areas 18 and 30 of NNSS are located within the northeastern portion of TMCC. XRD data for these locations show similar diagenetic zonation as seen elsewhere at PM-OV. The increased abundance of smectite is similar to XRD data for boreholes in west-central and the southwest portions of TMCC (different from the northwest TMCC and the Bench).

Table A.6 lists the four Area 18 and 30 boreholes with XRD data, general location (see Figure 6 for exact locations), XRD method, and report figure reference.

Table A.6. List of 4 boreholes with XRD data in Areas 18 and 30 of the NNSS.

Borehole	Location	XRD	Figure
UE-18R	northern TMCC	F	A.58
UE-18T	northeastern TMCC	F, S	A.59
ER-18-2	northeastern TMCC	I	A.60
ER-30-1	eastern TMCC	F	A.61

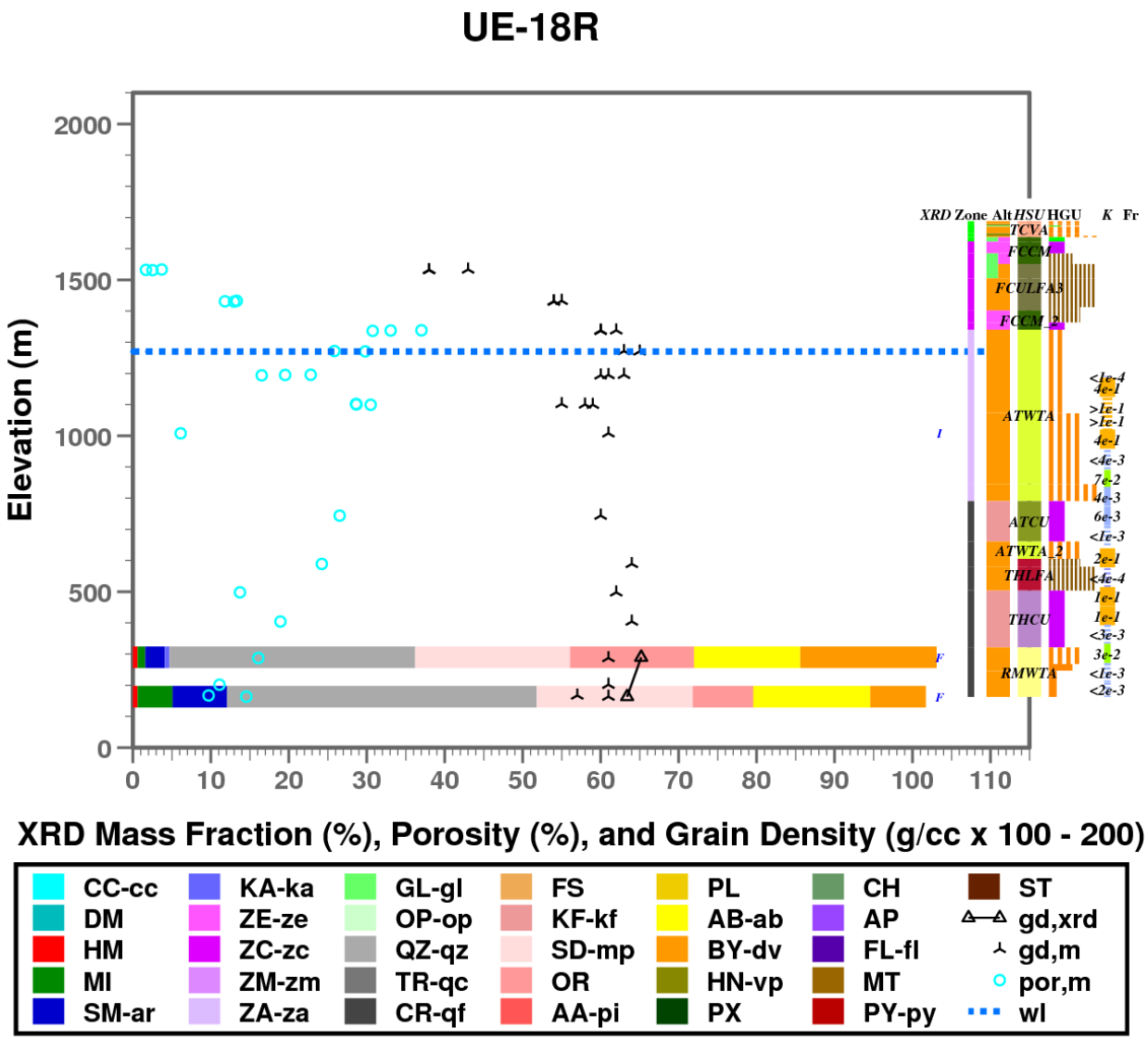

Figure A.58. Graphical representation of XRD and rock property data for borehole UE-18R, northern TMCC.

The two XRD data locations in UE-18R are near the base of the borehole. XRD data are consistent with quartzofeldspathic alteration of Zone 4, which appears to extend upward to at least the top of the ATCU based on grain density measurements over 2.60 g/cc. Considering XRD data at the nearest locations ER-EC-14 (Figure A.53), UE-18T (Figure A.59), and ER-18-2 (Figure A.60), Zone 4 may extend higher into the ATWTA. Zone 2 is identified by the zeolitic alteration description.

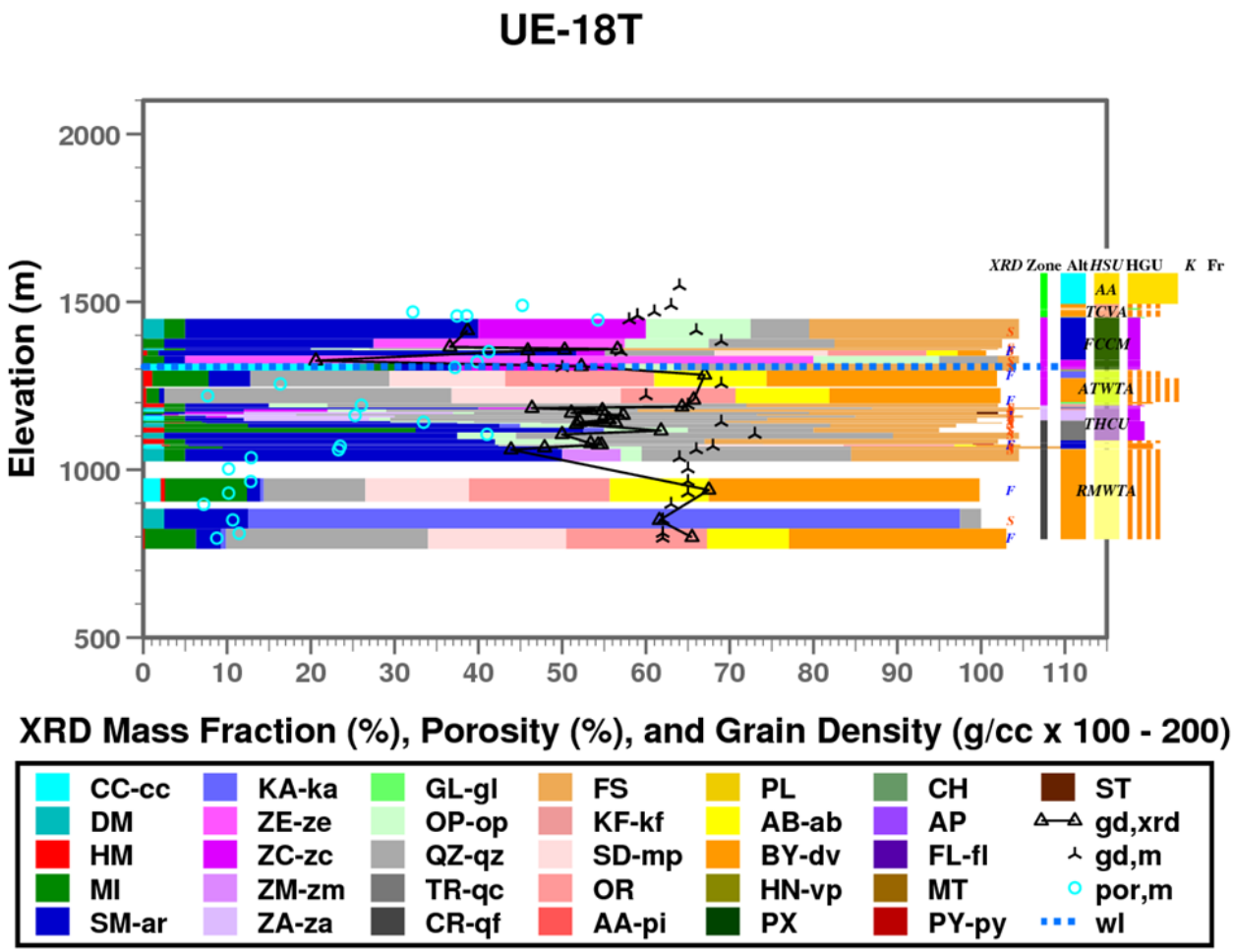

Figure A.59. Graphical representation of XRD and rock property data for borehole UE-18T, northwestern TMCC

XRD data for borehole UE-18T, located on the northeastern margin of the TMCC XRD, show distinct diagenetic zonation seen elsewhere at PM-OV, but with unusually high smectite. The high smectite abundance is similar to U-19AK located on the northeastern margin of the SCCC (Figure A.1). This is further evidence that smectite may be more abundant along caldera margins.

The XRD data derived from the S method at about 850 m elevation indicate a very high mass fraction of kaolinite (> 80%) at one location in Zone 4. Kaolinite is common in Zone 4 in the northwest TMCC, but never above about 15% (e.g. at ER-EC-2A, Figure 19).

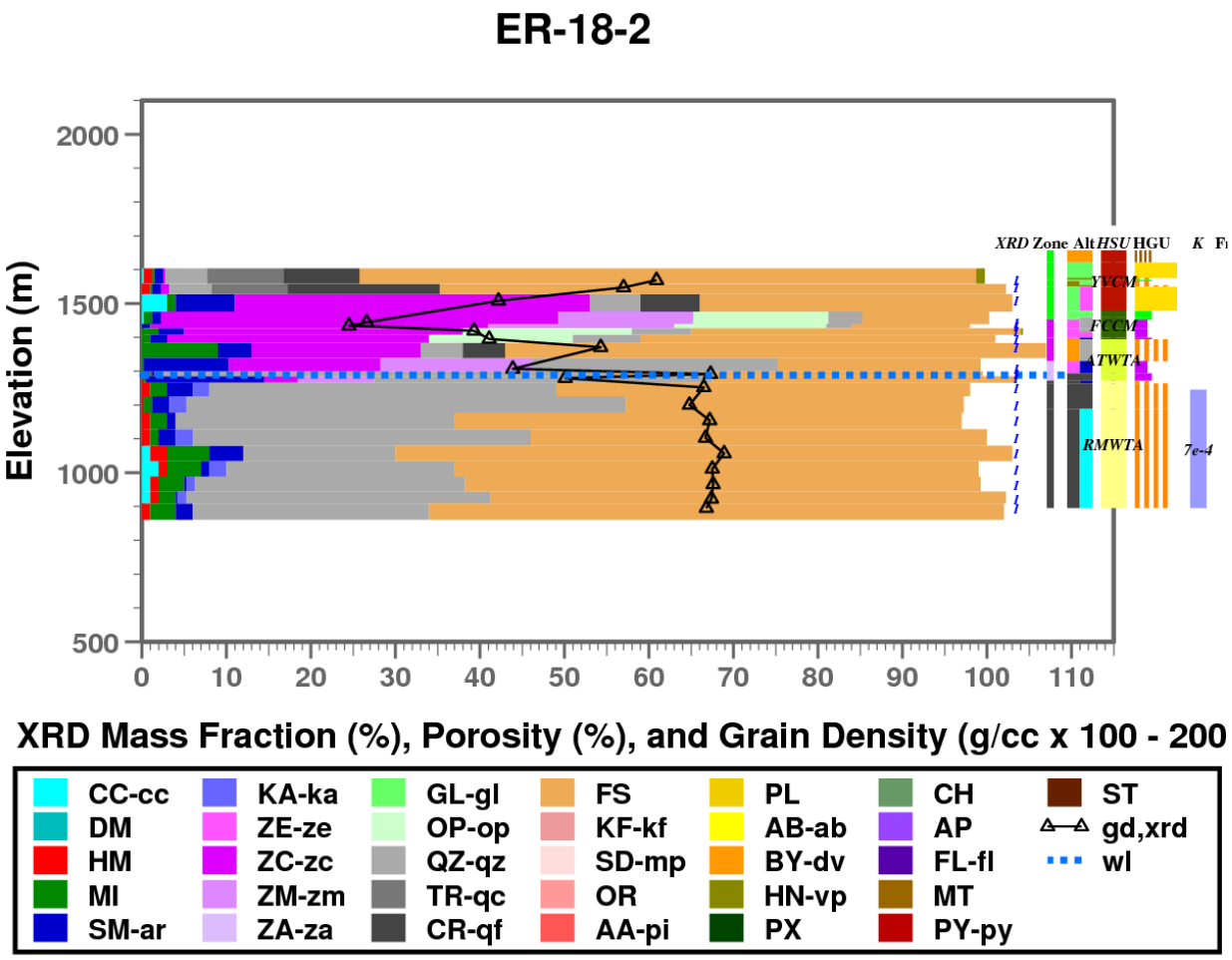

Figure A.60. Graphical representation of XRD and rock property data for boreholes ER-18-2 and ER-30-1, northeastern TMCC.

XRD data for borehole ER-18-2 show distinct occurrence of Zone 2 evident by a high mass fraction of clinoptilolite and presence of opal and mordenite. Zone 2 appears to extend from the upper half of the ATWTA to the lower half of the YVCM. Zone 3 is apparently thin and occurs at the base of the ATWTA. Kaolinite in the RMWTA is characteristic of Zone 4. The short transition from Zone 2 to Zone 4 is similar to ER-EC-6 (Figure A.18) and ER-EC-14 (Figure A.54)

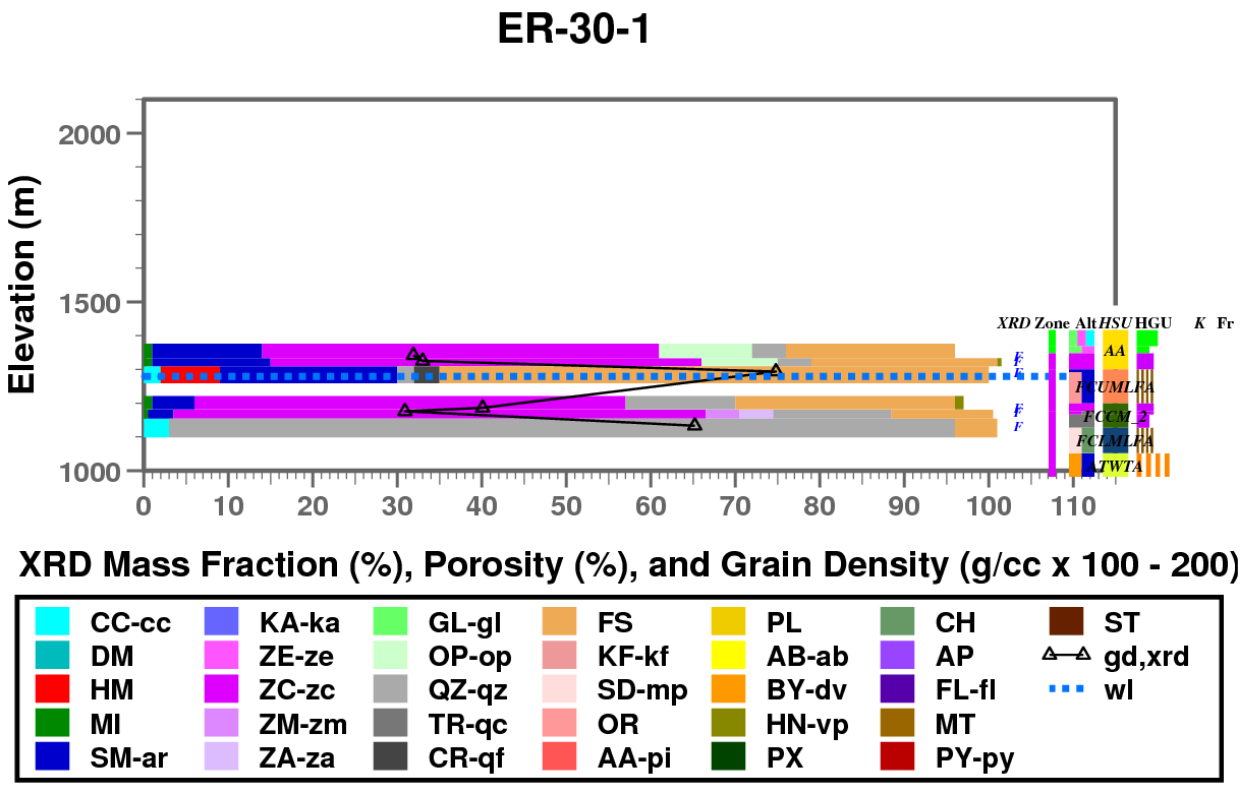

Figure A.61. Graphical representation of XRD and rock property data for boreholes ER-18-2 and ER-30-1, northeastern TMCC.

XRD data for borehole ER-30-1 shows distinct occurrence of Zone 2 evident by a high mass fraction of clinoptilolite and presence of opal. A transition to Zone 3 could be interpreted near the base of the FCCM_2 based on presence of analcime and calcite.